Dissertation

Cooling of the End-Windings in Electrical Traction Machines

Dipl.-Ing. Martin Hettegger

Institut für Grundlagen und Theorie der Elektrotechnik

Technische Universität Graz

TU Graz

Graz University of Technology

Betreuer: Univ.-Prof. Dipl.-Ing. Dr. techn. Oszkár Bíró

Graz, im Oktober 2012

Preface

Many people have been encouraging me in the work leading to my PhD thesis. I would like to appreciate everyone for their contributions during my time as a PhD student.

First and foremost, I would like to express my sincere gratitude to my supervisor, Univ.-Prof. Dipl.-Ing. Dr. Oszkár Bíró for the valuable guidance. The advice and support received from him was vital for the success of this thesis.

Deepest gratitude goes also to Dipl.-Ing. Dr. Bernhard Streibl who was an inspiring counterpart at my industrial partner, the Traktionssysteme Austria GmbH. I very much appreciate his contributions during the measurements and his encouragement and collaboration in writing the publications.

I am very grateful to the staff of the Traktionssysteme Austria GmbH for supporting my work and for providing the measuring facility. Special thanks also to the head of the product development and design team Dipl.-Ing. Dr.phil. Dr.techn. habil. Harald Neudorfer, who gave the permission to present the measured results in this thesis.

I would also like to express my gratitude to Dipl.-Ing. Dr. Georg Ofner and Univ.-Doz. Dipl.-Ing. Dr. Bernhard Brandstätter from ELIN Motoren GmbH for their support.

I sincerely appreciate the Christian Doppler Association for providing the productive working environment of the Christian Doppler Laboratory.

Finally, I would like to express my deep gratitude to my family and friends for being there for me and, whenever it was necessary, taking my mind off the subject.

Martin Hettegger

Abstract

Simulation of the heat transfer at the end-windings of an electric machine is often restricted by the quality of the coefficients used in the simulation model. This thesis presents a method of obtaining correlations between the convective wall heat transfer coefficient and parameters of the end-region of an electrical machine and its operational conditions. The data have been evaluated by computational fluid dynamics and validated by measurements. Dimensionless numbers for the convective wall heat transfer coefficients have been correlated to the operating conditions by the Gauss-Newton method. This characterization provides a way of calculating values for the convective wall heat transfer coefficient depending on the rotational speed and the end-shield geometry. Due to the used dimension analysis, the result is adaptable on scaled geometries. It is not an exact method for calculating the convective convective wall heat transfer coefficient, but provides a tool with sufficient accuracy for most engineering purposes.

Kurzfassung

Die Genauigkeit der Wärmefluss-Simulation am Wickelkopf einer elektrischen Maschine wird von der Qualität der verwendeten Koeffizienten im Simulationsmodell bestimmt. Diese Arbeit stellt eine Methode vor, die zur Gewinnung von Korrelationen zwischen den konvektiven Wärmeübergangskoeffizient und geometrischen Parameter der Endzone einer elektrischen Maschine, sowie deren Betriebsbedingungen dient. Die Daten zur Korrelation wurden mithilfe von Computational Fluid Dynamics erzeugt und mit Messungen validiert. Dimensionslose Kennzahlen für den konvektive Wärmeübergangskoeffizienten wurden mit den Betriebsbedingungen anhand des Gauss-Newton-Verfahren korreliert. Diese Charakterisierung bietet die Möglichkeit die konvektiven Wärmeübergangskoeffizienten in Abhängigkeit von der Drehzahl und Lagerschild-Geometrie zu approximieren. Aufgrund der verwendeten dimensionslosen Kennzahlen ist die Approximation auch für skalierte Geometrien anwendbar. Es handelt sich hierbei nicht um eine exakte Methode zur Berechnung des konvektiven Wärmeübergangskoeffizient, sondern bietet ein Werkzeug welches Wärmeübergangskoeffizienten des Wickelkopfes sehr schnell und für die meisten technischen Zwecke mit hinreichender Genauigkeit ermittelt.

Statutory Declaration

I declare that I have authored this thesis independently, that I have not used other than the declared sources / resources and that I have explicitly marked all material which has been quoted either literally or by content from the used sources.

Eidesstattliche Erklärung

Ich erkläre an Eides statt, dass ich die vorliegende Arbeit selbstständig verfasst, andere als die angegebenen Quellen/Hilfsmittel nicht benutzt und die den benutzten Quellen wörtlich und inhaltlich entnommenen Stellen als solche kenntlich gemacht habe.

_____   _____   _____
        Ort   Datum   Unterschrift

Contents

Nomenclature

Latin symbols:

A	area in m^2		m	mass in kg
a	radiation absorption coefficient		n	rotational speed in rev/min
a_1	SST turbulence model constant		n	surface normal
a_i	Pi-Theorem variable		n_λ, n_μ	Sutherland exponents
a_t	specific technical work in J/kg		$O(.)$	order of (.)
A_t	technical work in J		P	power in W
A_h	wetted crossectional area in m^2		P_k	production of turbulence kinetic energy in kg/ms^3
B	constant value			
C	constant value		p	pressure in Pa
c_p	specific heat capacity in J/kgK		$q_1 \ldots q_4$	characterization parameters
d	diameter in m		Q	heat energy in J
d_h	hydraulic diameter in m		$\dot{Q}$	heat flux in W
D_{or}	outer rotor diameter in m		$\dot{q}$	heat flux density in W/m^2
e_o	specific outer energy in J/kg		$\dot{q}_w$	convection heat flux density in W/m^2
E_o	outer energy in J		$\dot{q}_r$	radiation heat flux density in W/m^2
E	absolute error		$\dot{\mathbf{q}}$	heat flux density vector in W/m^2
E_{Nu}	absolute error of Nusselt number		Q_o	outer heat energy in J
e_{Nu}	relative error of Nusselt number		q_o	specific outer heat energy in J/kg
e	relative error in %		r_{th}	specific thermal resistance in Km^2/W
f	frequency in Hz		R	electrical resistance in Ω
F	force in N		R_s	specific gas constant in J/kgK
F_1, F_2	SST turbulence model blending functions		R_{th}	thermal resistance in K/W
$\mathbf{F}$	force vector in N		s_f	geometry scaling factor
f^B	specific force per unit volume in N/m^3		S	magnitude of strain rate in 1/s
$\mathbf{f}$	specific force vector per unit volume in N/m^3		S_λ, S_μ	Sutherland constant in K
			T	temperature in K
$f(.), F(.)$	function of (.)		T_e	environmental temperature in K
$g(.)$	function of (.)		T_w	wall temperature in K
$\mathbf{g}$	acceleration vector in m/s^2		T_∞	fluid temperature beyond the wall in K
h	specific enthalpy in J/kgK		t	time in s
h_y	height in m		U	inner energy in J
H	enthalpy in J		U_B	electrical potential at the brushes in V
I	current in A		U_h	wetted cross-sectional circumference in m
$\mathbf{I}$	identity tensor		U_i	inner energy in J
I_t	turbulence intensity		u_i	specific inner energy in J/kg
k	turbulence kinetic energy per unit mass in m^2/s^2		u_τ	friction velocity in m/s
			u^+	dimensionless velocity
k_s	surface roughness in m		u, v, w	velocity in m/s
K_{HFS}	sensitivity of heat flux sensor in $\mu V/(W/m^2)$		$\mathbf{v}$	velocity vector in m/s
			V	volume in m^3
L	characteristic length in m		V	Euclidean norm of velocity vector in m/s
L_x, L_y	finite-differences for Cartesian coordinates		W_m	test function of weighted residual method
l	mixing length in m		x	Cartesian direction in m
l_x	geometry length in m		$\mathbf{x}$	direction vector in m
l_h	length in m		y	Cartesian direction in m
			y	distance to the wall in m
			y_0	initial finite volume cell height

	next to the wall in m	z	Cartesian direction in m
y^+	dimensionless distance to the wall		

Greek symbols:

α	heat transfer coefficient in W/m²K	μ	molecular viscosity in m²/s
α_S	heat transfer coefficient by radiation in W/m²K	μ_t	turbulent viscosity in m²/s
β	volumetric thermal expansion coefficient in 1/K	ν	kinematic viscosity in m²/s
		ν_t	turbulence eddy viscosity in m²/s
ϵ	radiation emission-coefficient	ω	turbulence frequency in 1/s
ε	turbulence eddy dissipation in m²/s³	Π_i	Pi-Theorem dimensionless values
η	Kolmogorov microscale in m	π	constant value
Φ	angle in °	ρ	density in kg/m³
ΔT	temperature difference in K	$\boldsymbol{\sigma}$	stress tensor in Pa
δ	thickness of velocity boundary layer m	σ	Stefan-Boltzmann constant in W/m²K⁴
δ_{ij}	Kronecker delta	σ_{ii}	principal stress in Pa
δ_t	thickness of thermal boundary layer m	Θ^+	dimensionless near wall temperature profile
Γ_t	eddy diffusivity Pa	τ_{ij}	shear stress in Pa
κ	von Kármán constant	τ_t	turbulent wall shear stress in Pa
λ	thermal conductivity of air W/mK	τ_w	wall shear stress in Pa
$\boldsymbol{\lambda}$	anisotropic thermal conductivity W/mK	$\tilde{\tau}$	total shear stress in Pa
λ_f	Darcy friction factor	$\boldsymbol{\tau}$	viscose stress tensor in Pa
λ_t	turbulence thermal conductivity W/mK		

Dimensionless numbers:

Bi	Biot number	Gr	Grashof number	Re	Reynolds number
Ec	Eckert number	Nu	Nusselt number		
Eu	Euler number	Pr	Prandtl number		

Subscripts:

a	ambient	i, j, k	alternating Cartesian coordinates in index notation	s	surface
ab	absorption			tot	total
avg	average			vis	viscose sublayer
aprx	approximation	log	logarithmic layer	w	wall
D	diameter as char. length	max	maximum	ref	reference
DE	drive end	min	minimum	x, y, z	Cartesian coordinates
e	environment	mon	monitor	∞	beyond the wall
em	emission	nc	natural convection		
f	fluid	NDE	non drive end		
fc	forced convection	r	radiation		

Superscripts:

(i, j, k)	iteration step	$+, *$	dimensionless
B	body force	log	logarithmic layer
S	surface force	vis	viscose sublayer

Chapter 1

Introduction

1.1 Motivation

Electric traction motors are steadily gaining importance in the drive-train as means of transportation. Especially, public transport already uses electric traction motors to a large extent. Due to the long operating times of the electric motor in such applications, even a small improvement has evident consequences on operating costs.

Higher efficiency can be reached by customized machines exactly fitting the requirements of the customer. The consequence is lower production numbers of the same motor type and less capability for expensive prototypes. On the other hand, there is an advantage in less weight and less energy consumption saving resources in terms of copper, iron and hence weight and money.

Self ventilated traction motors have the problem of worse cooling at low revolution speeds. Especially for start/stop scenarios, it is necessary for the motor to store (buffer) the heat energy caused by the electric and iron losses within the machine, due to the high torque and high current at low or zero velocity.

Electric traction motors are being used in both directions of rotation and in a wide range of rotational speed. Therefore it does not make sense to optimize them for one certain revolution speed or direction, which complicates the optimization of the motor as regards efficiency.

To investigate this problem, it is necessary to simulate one operational cycle of the vehicle. This involves a transient analysis with the energy balance of supplied, buffered, converted and transported energy considered. No matter whether the calculation is carried out by numerical simulation, derived by empirical formulas or a thermal circuit method [30], a good description of the boundary conditions is mandatory to predict the temperatures inside the motor with sufficient accuracy.

Since the thermal conductivity is generally constant, the conductive heat transport within solids can be derived reliably. The problem becomes more complicated at the surface where the convective and radiation heat transfer transports the heat energy from the solid material into the surrounding space.

A reliable prediction of the temperature distribution in an electrical machine during the design process depends basically on the used boundary conditions, heat sources and heat sinks. The convective wall heat transfer coefficient appears in a boundary condition of high importance for any type of thermal simulation of electrical machines. It is a fundamental value which directly influences the calculated energy transport over the system boundary, and thus defines the level of the inner temperature field. It is not a constant value but depends on temperature-dependent fluid properties and factors which are affected by the flow conditions of the surrounding fluid (air). These factors can be geometry of the end-windings, geometry of the end-shield, ventilation flow rate and revolution speed. Therefore, it is obligatory to adjust the wall heat transfer coefficient for each time step in a transient simulation.

The magnitude of the wall heat transfer coefficient α in an environment with air and forced convection ranges between 30 and about 300 W/m²K [48]. This wide range entails the risk of non-negligible errors if transient calculations are carried out with a constant wall heat transfer coefficient.

With analytical investigations known from the established literature, many machine parameters have been predictable for years, but there are still parameters like the convective wall heat transfer coefficients at the end-windings, which depend highly on the complex geometry and cannot be calculated analytically [42].

An exact, analytical derivation of the wall heat transfer coefficient is possible for very simple geometric setups under certain flow conditions, but due to the convoluted shape it is not feasible for the end-windings of an electric machine. The value of the local wall heat transfer coefficient α_x has a linear dependence on the difference of wall and fluid temperature $\Delta T = T_W - T_f$, only in the case of forced convection with constant wall temperature or radiation with a vanishing temperature difference ΔT. For any other case of convection, condensation or radiation the dependence is much more sophisticated [33]. On this account, only the average value of the wall heat transfer coefficient over a certain area makes sense for the use in boundary conditions in thermal field calculations. Nevertheless, the derivation of the local wall heat transfer coefficient by computational fluid dynamics (CFD) is necessary, in order to validate the simulations with measurements. Therefore, it has been necessary to obtain convective wall heat transfer coefficients by measurements until other approaches become reliable [42].

As sketched in Fig. 1.1 the convective wall heat transfer coefficient α can either be calculated by empirical formulas, measured on existing machines or obtained by CFD. Measurements demand the actual geometry and application of sensors, which can be time consuming and requires operational resources. With CFD simulations it is possible to investigate any kind of shape but it can become very tedious with a rising level of detail. Empirical formulas on the other hand are easy to use and fast in calculation. They can even be used in transient simulations of traction motor drive cycles, with changing rotational velocities and thus changing convective wall heat transfer coefficient inside the electrical machine in each time step. Therefore it is beneficial to have empirical formulas for the examined geometry, which are available
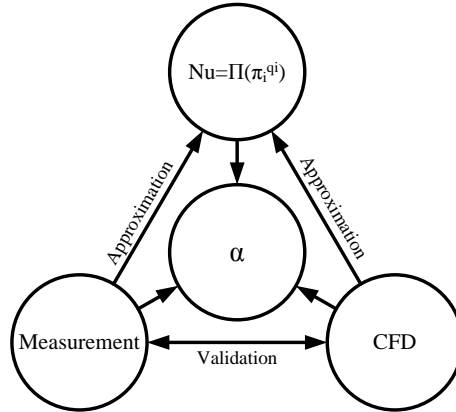
Figure 1.1: Approaches of deriving the heat transfer

in literature for typical geometries [88] but not for sophisticated shapes like the end-windings of electrical machines.

On the one hand, the data from measurements can be used to validate the CFD simulations (and vice versa), on the other hand the data can be taken to approximate the convective wall heat transfer coefficient with empirical formulas by means of dimensional analysis and similitude theory as explained in [15] and [96]. In the present investigation all data for the convective wall heat transfer coefficients have been obtained by CFD and validated by measurements.

1.2 Literature review

Due to their elementary geometric shape an analytical description of the wall heat transfer coefficient for cooling ducts and cooling fins has already done by [72]. Textbooks as [62, 78] and [29] introduce the conductive and the convective heat transport but do not discuss the cooling characteristics of the end-windings or end-region. Since the results of the temperature field analysis in an electric motor depend on the accuracy of the convective wall heat transfer coefficient, as explained in [50], the prediction of such values is an essential part of the design process. Several researches on the issue about heat transfer on end-windings of electric machines have been carried out in the last decades. Recent publications concerning convective air cooled electrical machines are mainly focused on smaller machines in a power class of a few kVA and with simple cooling strategies.

A calculation of the convective wall heat transfer coefficients of totally enclosed fan cooled (TEFC) motors has been established in [8], based on measured temperatures at the end-windings and the end-shield, as well as calculated thermal resistances. Detailed information about temperature measurements at the end-region of two types of induction machines has been shown in [8], and hence a method for calculating the convective wall heat transfer coefficient of the end-windings. This method has been

tested on different motor-power classes in [9] and compared to a commercial thermal analysis software in [11]. Since the convective wall heat transfer at the end-windings depends highly on the geometry of the end-region and on the angular velocity of the rotor, the values for the convective wall heat transfer coefficient can be distributed over a wide range, depending on the type of machine, as outlined on a set of TEFC motors in [81]. A summary of end-region convection correlations have been prepared in [82], in addition to other heat transfer problems in electric machines. Different formulas for the determination of the convective wall heat transfer coefficient of the end-windings have been compared in [28] for a motor similar to the TEFC type. A scalability with dimensionless numbers would be beneficial to the calculation of the convective wall heat transfer coefficient of similar geometries.

Measured convective wall heat transfer coefficients at the end-region and cooling ducts of through-ventilated induction motors have been published in [69] and [70]. These publications also investigate the differences of the end-windings' heat transfer between lap wound and concentric wound induction motors by using heat flux sensors to determine local convective wall heat transfer coefficients and pitot-static tubes to measure the velocity of the coolant. Since these measurements have been carried out on specific locations at the end-windings an averaged heat transfer coefficient cannot be determined accurately, which would be beneficial to a thermal network model.

An early numerical approach to solve the temperature distribution inside the stator core with FEM has been published in [5]. Results of research about thermal management in turbo or hydro generators have been published in [16, 32, 84, 85, 90–92]. The key topics in these publications are the temperature fields inside specific parts of the stator and rotor, dependence of the wall heat transfer coefficient on environmental pressure, air mass flow and distribution of pressure but do not deal with the derivation of the wall heat transfer coefficient on the end-windings itself.

A possible way of obtaining the convective wall heat transfer coefficients of complex geometries is by numerical simulation of fluid flow with software for computational fluid dynamics (CFD). The investigations in [65] and [64] have applied this method to a TEFC type motor and have also identified some limits of this approach. CFD simulations have been compared to measurements with heat flux sensors applied to an experimental test rig in [61]. In [81], CFD has been introduced as a tool for the flow visualizations. An optimization of the air mass flow inside an TEFC motor has been investigated in [68] by comparing CFD simulations with differently modeled ventilators. A comparison of the flow conditions in the end-region of a TEFC motor between the original complex end-windings and simplified end-windings has been illustrated in [60]. The cooling effects in radially ventilated stator ducts in an air cooled turbo generator have been investigated in [52, 53], using CFD for the calculation of the heat transfer but without any details about the used simulation setup. A very comprehensive and detailed investigation about CFD for rotating electrical machinery has been published in [21]. This work contains measurements and CFD simulations of heat flux and pressure loss on the example of the ventilation system of a salient pole generator, including dimensionless correlations.

Progress in the fields of computational power and numerical calculation of fluid flow in the last decades offers the possibility to obtain certain motor parameters by a numerical approach. Especially recent improvements of turbulence models [56, 57] and transition models [49, 55] are of great value to the accuracy of the convective wall heat transfer coefficient, predicted by CFD. Even though a CFD simulation of the convective wall heat transfer of a whole machine is hardly possible with reasonable computational effort [87], it is still possible to solve sub-problems of the fluid flow with the known boundary conditions.

Due to the different size and different winding types, the heat transfer values for the investigated double air cooled system (DACS) induction motor cannot be compared directly to the investigated TEFC motors presented in [11] and [82]. Basic differences in the power class and the cooling system prevent a reasonable comparison with the results obtained in this thesis.

1.3   Current practice

Prototypes are mostly uneconomic in the design process of a machine, if production numbers of a certain machine type are small. Designing electrical motors by prior numerical simulations is a state of the art method in industry. A survey of present approaches for thermal analysis as well as a comprehensive list of references can be found in [10].

Due to the high computational effort, CFD simulations of whole electrical machines are more the topic of academic research than the daily business in machine development. With today's computational power, the simulation of subproblems is more common in industry. Most manufacturers of electric machines have a history which goes back several decades. Their methods of machine development have grown over years, improved step-by-step by some generations of engineers. The core-principle of the thermal calculation is a thermal network model [31] as it has been used since the early beginnings of electrical machine development. The early employment of computers has been very useful in accelerating the calculations with sometimes higher level of detail and thus higher accuracy, but the method itself did not change much. Due to simple calibration with measurements of manufactured machines within decades of development these thermal network models satisfy the requested accuracy and savor the confidence of manufacturers. Furthermore, these models are cheap and with today's computational power, able to solve transient problems, e.g. for vehicle drive cycles. This grown method works well as long as the manufactured machines are within known power classes, have similar shapes and known cooling methods. For any other machine with an 'out of line' cooling strategy, these individually calibrated thermal network models might fail.

For novel concepts of electrical machines, a more flexible approach is required for thermal calculation and for the calibration of thermal network models. Today's models in CFD can predict the convective wall heat transfer coefficient with acceptable

accuracy, allowing a calibration of thermal and fluid flow network models. A derivation of the thermal management by a thermal network model coupled with a fluid flow network model has been presented by Traxler-Samek et. al [86]. In this paper the authors examine the cooling process as an interaction of convective and conductive heat transfer, as it appears in reality. A state of the art method for the design of hydro generator ventilation has been introduced in [20], combining the benefits of the simulation techniques CFD and fluid flow network.

1.4   Approach in this thesis

Modern electrical machines have to satisfy many requirements regarding the electrical, mechanical and thermal behavior. Sometimes the improvement on one requirement has to be carried out at the cost of another requirement and the determination of the application-oriented ideal configuration becomes a challenging task. The design of a new machine is often based on values for similar machines but marginal changes of geometry. Even small changes in the geometry can have noticeable consequences in the thermal behavior of a machine. Therefore a method is required, which allows an interpolation between similar machine types or an extrapolation within a specific range.

The aim of the present thesis is the prediction of the convective wall heat transfer coefficient at the end-windings inside an electrical machine depending on known operating conditions and geometric dimensions of the end-shield and end-windings. Due to the large number of different cooling methods for electrical machines, one specific cooling type has been chosen for the investigations. Nevertheless, the presented method of characterization can be used for any type of machine by combining and enhancing the investigations in [35–42].

In [37–39, 41, 42], a proper configuration setup for CFD simulations has been investigated to achieve accurate values for the convective wall heat transfer coefficients and have been validated by measurements. The flow conditions next to the end-windings depend primarily on the rotational speed of the machines rotor and the ventilation characteristics of the fan. Both have been considered in the characterization of the end-windings' heat transfer in [36] by means of dimensional analysis and theory of similitude. Another important factor to the flow conditions next to the end-windings is the shape of the inner side of the end-shield. By varying basic geometric dimensions of the end-shield in two dimensional models, the end-windings' heat transfer has been changed and correlated to the geometric variations in [40]. This work has been combined with [36] additionally to a set of scaled geometries on three dimensional models in [35], allowing the characterization of the end-windings' convective wall heat transfer coefficient depending on the rotational speed, the fan characteristics, some basic geometric dimensions and a geometry scale factor.

The investigations in this work have been carried out under steady state conditions for specific operating points. Based on the results for these operating points, a

characteristic function for the transient behavior has been obtained by approximation.

1.5 Structure of the thesis

The following Chapter 2 presents physical basics and tools which appear in or have been used in this thesis. The accuracy of CFD calculations depends on the right configuration of the fluid flow calculation. Different turbulence models have been tested regarding the quality of the derived convective wall heat transfer coefficient. Their configuration has been validated with empirical values of the heat transfer on cylinders in a cross flow as explained in Chapter 3. In the same chapter the global-local domain decomposition method has been introduced allowing the prediction of local wall heat transfer coefficients of larger models with reasonable computational effort. Chapter 4 presents measurements on an induction motor's cooling system which have been used for the validation and for the identification of operational conditions. These operational conditions and the simulation setup of Chapter 3 have been employed for the simulation of the heat transfer at end-windings in Chapter 5. With this validated configuration setup, an analysis has been carried out in Chapter 6 which characterizes the convective wall heat transfer coefficient in correlation to geometric variations and changing operational conditions. The operational conditions used for the simulation setup in Chapters 5 and 6 have been measured on a particular motor, introduced in Chapter 4. This chapter also includes measurements of temperatures and heat fluxes, which are compared to the simulated results followed by the conclusion and comments on the scientific value in Chapter 7.

1.6 Employed commercial software packages

All CFD calculations which are presented in this work or have been accomplished with the CFD software *CFX* from the software package *ANSYS Academic Research* v12.1 and v13.0. The meshes used for the CFD calculations have been created with the *ANSYS Mechanical* 13.0 software and with *ANSYS ICEM CFD* 13.0. Calculations and diagrams have been created with *MATLAB* R 2009b.

Chapter 2

Fundamentals

2.1 Heating and cooling of electrical machines

2.1.1 Heating process

Conversion of electrical into mechanical power (and vice versa) inside an electrical machine is always linked to a conversion into heat to some extent. Heat is usually not the intended purpose of the conversion process and is therefore denoted as power loss, causing a rise in temperature inside the machine. At the beginning, all parts of the machine have uniform temperature. The heating of different parts of the machine depends on the local loss density and heat capacity of the material. With differently rising temperatures in different parts of the machine, the arising temperature gradient causes heat flux between the machine parts. Heat always follows the negative temperature gradient and finally reaches a cooling medium which discharges the heat energy to the environment. Temperatures and heat fluxes are rising inside the machine until the discharged heat equals the generated heat caused by the loss density in every part of the machine. Once the discharged and generated heat are balanced, the machine as a whole discharges the same amount of power as the losses occurring inside are and no more heat is stored inside the machine. Consequently, the temperatures inside the machine remain at a steady state value, if the operating conditions stay constant.

The temperature difference between the coolant at the beginning of the cooling cycle and a specific location in the machine is known as the over-temperature of this location. The maximal over-temperature in an electrical machine is primarily limited by the thermal stability of the windings' insulation material, which is classified into insulation classes regarding thermal stability. The average over-temperature of the windings is usually determined by measuring their electrical resistance, a procedure known as resistance-method. Depending on the winding-type, an additional 5 to 15K [63] are added to the average over-temperature, in order to get the maximum over-temperature of the winding. If the winding temperature is measured by a thermometer (thermometer-method) different values have to be added, in order to get the maximum over-temperature. The maximal allowable over-temperatures for specific

8

parts of the machine are known as over-temperature limits and are listed in the IEC 60034-1 standard, as shown in Tab. 2.1.

Insulation class	130 (R)	155 (P)	180 (H)
Over-temperature limits (in K)	80	105	125

Table 2.1: Over-temperature limits of the windings of a rotating electrical machine in a power class of less than 200 kVA and more than 600 VA cooled by air, evaluated by the resistance method (IEC 60034-1) [63]

The steady state can be achieved with a long operation time. Due to the heat capacity of materials, the machine can be overloaded for short periods of time. Respecting the required relaxing periods for cooling, the over-temperature limit of the windings will not be exceeded. Since such operating conditions exist on a regular basis, the ten ideal operation-modes from S1 (continuous running duty) to S10 (duty with discrete constant loads) have been standardized in IEC 60034-1 [45]. This standard defines operation modes with cyclic periods of load, non-load or down time conditions. [63].

2.1.2   Balance of energy

The cooling process of an electrical machine should also be considered from a thermodynamic point of view. The energy state of an electrical machine at a specific point of time can be explained by the first law of thermodynamics for a closed system

$$dQ + dA_t = dE_o + dU_i \, , \tag{2.1}$$

with the supplied external energy on the left-hand side and the stored energy at the right-hand side [71]. In equation (2.1) Q and A_t stand for variables of the energy transport and E_o and U_i stand for variables of the energy state and d denotes the differential change. Considering the electrical machine as one system within a system boundary, the transport variables dQ and dA_t denote the energy transport across the system boundary and the state variables dE_o and dU_i stand for the differential change of energy change inside the system.

The types of externally supplied energy are heat Q and work A_t, which both have to be positive when added to, or negative when taken away from the system. Since reversible heat cannot be stored in an electrical machine, all the heat energy Q is usually taken away from the system via the cooling process and is therefore negative in (2.1). Any outer thermal energy Q_o which is transferred across system boundaries to the machine needs to be added (i.e. radiation, sunlight). The work A_t which is transported across the system boundary can be split into mechanical work A_{tm} and electrical work A_{te}. Assuming the machine is in motor operation mode, the electrical work has to be positive and the mechanical work, which is taken away from the system, has to be negative. In generator operation mode of the machine, the mechanical work has to be positive and the electrical work has to be negative in (2.1).

Energy stored inside the system is separated into outer energy dE_o and inner energy dU_i. Since there are no relevant chemical processes which can store energy on a molecular level, the stored heat energy is the only existing inner energy U_i.

Outer energy can be stored as kinetic energy $dE_{o\ kin}$, potential energy $dE_{o\ pot}$, electrical energy $dE_{o\ el}$ or magnetic energy $dE_{o\ mag}$. The magnetic energy is high in comparison to the electrical energy and would be the only outer energy in the case of a transformer, but in the case of a rotating electrical machine the kinetic energy is the dominating outer energy. The potential energy is usually not relevant. Electrical energy can be stored in a battery, which is usually not present inside the machine, or in an electrical field. Capacitors inside the electrical machine are able to store electrical energy, but its value is usually much smaller than the values of kinetic or magnetic energy and can also be neglected. Nevertheless, the electrical energy and the magnetic energy can become relevant for the outer energy at zero speed of rotation.

In the cooling process of an electrical machine, the transported energy is more relevant than the stored energy, hence the system can be described in more detail with the first law of thermodynamics for an open system [71]:

$$dA_t + dQ_o + \sum dm_i(h_i + e_{oi}) = dU_i + dE_o \qquad (2.2)$$

with the transported energy at the left- and the stored energy at the right-hand side. Since the derivative of the stored energy with respect to time is zero in steady state, the energy balance can be expressed as:

$$dA_{te} + dA_{tm} + dQ_o + \sum dm_i(h_i + e_{oi}) = 0 \ , \qquad (2.3)$$

with specific enthalpy h_i, specific energy e_{oi} and mass m_i for the i'th transport across the system boundary. Considering a single coolant only with one transport into $(h_1 + e_{o1})$ and one transport out of $(-h_2 - e_{o2})$ the system, the steady state flow process

$$a_t = h_2 - h_1 + e_{o2} - e_{o1} - q_o \qquad (2.4)$$

covers all variables relevant to cooling, which is, in most cases, sufficient to describe the process. All variables in (2.4) are given as specific energy per unit mass: technical work $a_t = \frac{A_t}{m}$, enthalpy $h_i = \frac{H_i}{m}$, outer energy $e_{oi} = \frac{E_{oi}}{m}$ and heat energy $q_o = \frac{Q_o}{m}$. The enthalpy H includes the inner energy U and the energy stored in the pressure p for the volume V, and can be expressed as:

$$H = U_i + pV \ , \qquad (2.5)$$

or, for specific values, with the density ρ:

$$h = u_i + \frac{p}{\rho} \ . \qquad (2.6)$$

2.1.3 Heat sources

All the power provided to an electrical motor, which is not converted from electrical to mechanical output power, is converted into heat Q and its derivative with respect to time t can be considered as losses P:

$$P = \frac{dQ}{dt} = \dot{Q} \; . \tag{2.7}$$

From the thermal calculation point of view, the losses are considered as heat sources and the coolant as a heat sink.

The geometric dimensions change in correspondence with the power class of the machine. The crucial origin of heat in an electrical machine lies in the volume of conductors and iron sheets. The process of cooling depends on the surface area of the interface to the coolant. Since volume increases by the third power, while surface area increases by second power of geometric dimensions, the problem of cooling is more relevant to higher power classes and hence larger machines.

The internal arrangement of losses depends on the type of the machine. In order to give a general overview, the losses are classified according to their physical origin as ohmic losses P_{cu}, iron losses P_{fe}, friction losses P_{fr} and other losses. Ohmic losses occur due to electrical current I in conductors like windings and brushes. Since brushes do not have a current dependent voltage difference U_B, the ohmic resistance of the brushes is not linear and the brush losses P_{br} are separate from the rotor winding losses.

$$P_{br} = U_B \cdot I \tag{2.8}$$

Other ohmic losses like rotor and stator winding losses and excitation losses can be calculated using the ohmic resistance and the applied current.

$$P_{cu} = I^2 \cdot R \tag{2.9}$$

Iron losses P_{fe} can be divided into hysteresis losses P_{hy}, eddy current losses P_{ed} and anomalous losses (or excess losses) P_{ex}. Both occur in the iron core due to alternating magnetization and depend on the frequency f of alternation. The dependence of hysteresis losses is linear on frequency: $P_{hy} \sim f$. Since the eddy current losses depend on the square of the frequency, $P_{ed} \sim f^2$, the use of converters can have a high impact on this type of losses. Friction losses P_{fr} are brush friction or bearing losses caused by sliding contacts and windage losses caused by ventilation. These windage losses P_w are caused by the fan and the rotor which convey the coolant through the machine's cooling system.

Except for windage losses of the ventilation process, almost all the energy from electrical and mechanical losses have to pass the boundaries of the heated bodies for the heat transport. The share of windage losses also known as dissipation losses is usually small. Dissipation is a process which occurs in the fluid (coolant) when the kinetic energy of eddies in the fluid gradually collapses into smaller eddies and

finally turns into heat energy due to the internal friction and viscosity of the fluid. Since dissipation losses are generated directly in the cooling fluid, there is no need to transport these losses across the boundary.

The diagram in Fig. 2.1 shows a classification of losses in an induction motor according to the sequence of the power flow. The windings in the stator, which are connected to the electrical network, cause losses due to the ohmic resistance of the conducting material. Since in most cases this material is copper, these ohmic losses are also known as copper losses P_{cus}. Due to the alternating current in the stator
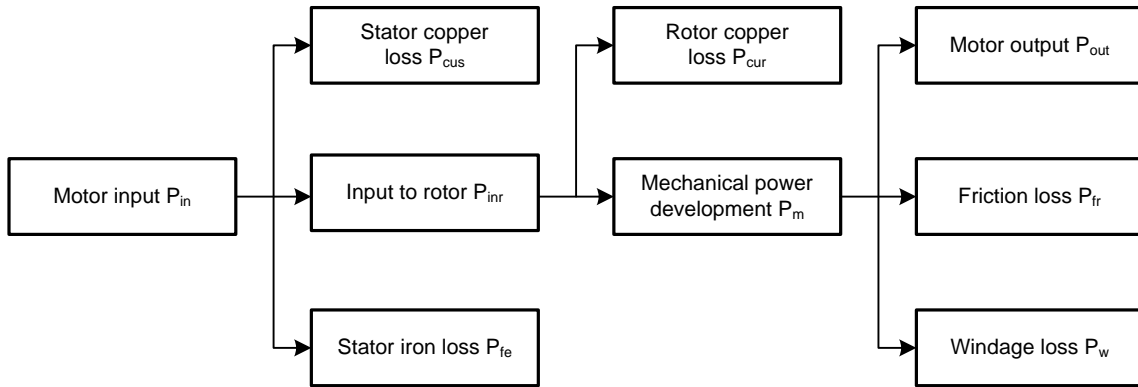

Figure 2.1: Power flow diagram of an induction motor including the sequence of appearance in the energy flow.

windings and to the rotating magnetic field of the rotor, the alternating and rotating magnetic field in the stator causes eddy current losses, hysteresis losses and anomalous losses P_{fe}. The power from the stator is transmitted to the rotor over the air gap by magnetic excitation of stator and rotor iron, similarly to the process occurring in a transformer. This converted power is denoted as P_{inr} in Fig. 2.1 and can be interpreted as the input power the rotor receives from the stator. Since the rotor revolves with almost the same speed as the rotating magnetic field of the stator, the frequency in the rotor conductors is only a few Hz at steady state operation, after the speed-up phase. Due to the low frequency in the rotor, the eddy current losses can be neglected and the ohmic losses P_{cur} dominate. The rest of the power is transformed to mechanical power P_m which has to be reduced by the friction losses P_{fr} and windage losses P_w in order to obtain the mechanical output power of the motor P_{out}.

2.1.4   Cooling methods

The heat energy of an electrical machine is discharged to the environment either directly by a coolant or indirectly through a heat exchanger. The over-temperature in a machine can be controlled by the cooling method, the type of coolant, the coolant streaming velocity, the distance and material between the heat source and the heat sink.

Numerous methods of cooling are available, which can be categorized by the number of cooling circuits arranged together, the type of coolant, the design of cooling circuit and the conveying method of the coolant. When two cooling circuits arranged in series, they are denoted as a primary and a secondary cooling cycle with a primary coolant which passes the heat energy to the secondary coolant with the aid of a heat exchanger. An open cooling cycle takes the coolant from direct or close environment (e.g. ambient air or nearby water reservoir) and discharges the heated coolant to the same environment. The primary cooling cycle is usually separated from the environment and therefore has to be a closed cooling cycle. Machines without any cooling pipes or cooling ducts for air inlet and outlet can either take and discharge the coolant from a direct environment in a free cooling circuit, or use the direct contact with the environment for surface cooling.
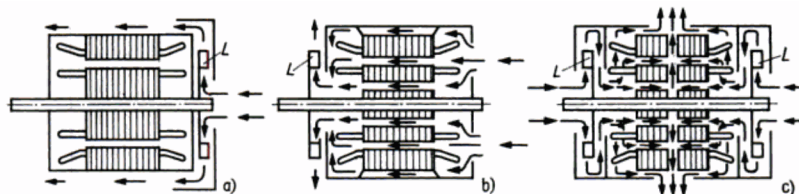

Figure 2.2: Ventilation methods for small and medium size machines: (a) closed machine with surface cooling and outer radial flow fan L (cooling method IC 4A1A1 or IC 411), (b) machine with open cooling cycle, axial cooling ducts and one radial flow fan L (cooling method IC 0A1 or IC 01); (c) machine with open cooling cycles, two radial flow fans L, axial and radial ducts in the stator (cooling method IC 0A1 or IC 01) [63]

Depending on the type of coolant, cooling methods can be separated into gas-cooled and liquid-cooled methods. For gaseous coolants, the conveying process can be carried out by a shaft mounted fan or an externally driven fan. Liquids require a pump usually driven externally. In small and medium sized machines the gas-cooled methods with surface cooling are more frequently used. In order to protect machines from contaminating dust or moisture, large-scaled machines are often built with a closed primary cooling cycle. Machines which have a high circumferential velocity use hydrogen (or sometimes helium) as coolant in a closed and pressure-resistant primary cooling circuit. Beside the benefit of lower dissipation losses, the wall heat transfer coefficient in hydrogen cooled machines is about 50% higher [63] than in air cooled machines and they can operate in a protective atmosphere reducing oxidation. The secondary coolant for such an assembly is usually water.

Water is the prevailing medium for liquid-cooled methods due to its high specific heat capacity. This permits good cooling properties with small amounts (volumes) of coolant, small cooling duct cross sections and low coolant flow velocities. In the case of directly cooled conductors where the coolant flows directly inside hollow conductors or in pipes next to the conductors, a liquid coolants such as water have a great benefit.

A standard for designation of cooling methods has been defined in IEC 60034-6 [46]. The standard describes the cooling arrangement and the types of coolants

using specific codes:

$$IC\,5\,A\,1\,A\,1\,,$$

with IC for International Coding and subsequent code letters and numbers. In this example 5, denotes the cooling arrangement of an integrated heat exchanger between the primary and secondary cooling circuit with air (A) as coolant for both cooling cycles. Self ventilation depending on the speed of rotation of the machine (1) has been chosen for the movement (conveying) type of the primary and secondary coolant. The codes for cooling arrangement, type of coolant and conveying type are listed and briefly explained in the appendix (Tab. A.1, A.2 and A.3). A more detailed description of the nomenclature can be found in the IEC 60034-6 standard. The following Fig. 2.3 demonstrates the explained cooling method.
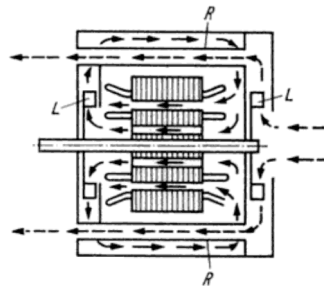
Figure 2.3: Ventilation of a machine with a closed primary and an open secondary cooling circuit (cooling method IC 5A1A1 or IC 511) [63]

The different constructions of the drive-train of vehicles require different types of traction-motors. The weight of the vehicle and the number of wheels which are driven directly by the traction-motors have an influence on the cooling-type. Other influencing factors are the properties of the gear-box, the vehicles' maximum speed and the maximum traction torque, especially at zero speed. Depending on these properties, various types of cooling systems have been developed to meet the desired requirements of the vehicle manufacturer.

A common practice for describing the cooling method of an electrical motor is the acronym of the cooling system itself, as shown in the first column in Tab. 2.2. Some acronyms fit to IEC standards listed in the third column. Although this is a commonly used nomenclature, it is not part of a recognized standard. Due to the large number of different cooling strategies, only a few types are randomly listed in Tab. 2.2, without any preference on technical properties. Some of them are considered in this work.

Due to limited space and weight, air is usually used as a coolant in electrical traction motors. Optimizing the cooling process means optimizing the pressure driven air flow through the machine. Efficient ventilators which provide this pressure can be conveniently designed for one single speed of rotation and a specified rotating direction. Due to the changing operational conditions, the ventilation of an electrical traction motor is more challenging compared to motors with fixed operational conditions [63].

Acronym	Explanation	IEC 60034-6 standard
TEFC	Totally Enclosed Fan Cooled	IC 4A1A1, IC 4A1A6
TESC	Totally Enclosed Self Cooled	
DACS	Double Air Cooled System	
TEAOM	Totally Enclosed Air Over Motor	
TETV	Tube Ventilated	IC 5A1A1, IC 5A1A6
SPDP	Open Air type	IC 0A1, IC 0A6
CACW	Water Cooled	IC 8A1W7
CACA	Air Cooled	IC 6A1A1, IC 6A1A6, IC 6A6A6
DPFC	Drip Proof Fan Cooled	
TENV	Totally Enclosed Non-Ventilated	

Table 2.2: Acronyms of cooling methods and the corresponding IEC standards

2.2 Heat transfer

As shown in [7], the transport of heat energy can rely on different physical effects such as diffusion in materials, spatial movement of materials or electromagnetic radiation between materials. Depending on the effect, three different means of heat transfer are distinguished: conductive heat transfer, heat transfer by convection and radiation. The descriptions of the following subsections are mainly abstracted from [7].

2.2.1 Conductive heat transfer

Conductive heat transfer is the transport of heat energy by the vector heat flux density $\dot{\mathbf{q}}$ as a function of the direction vector $\mathbf{x}$ and time t [7]:

$$\dot{\mathbf{q}} = \dot{\mathbf{q}}(\mathbf{x}, \mathsf{t}) \ . \tag{2.10}$$

The heat flux direction is perpendicular to the isothermal lines, from higher to lower magnitude of temperature. This direction coincides with that of the negative gradient of temperature describing the fundamental law of heat conduction discovered by Jean-Baptiste-Joseph Fourier:

$$\dot{\mathbf{q}} = -\lambda \cdot \nabla \mathsf{T} \ , \tag{2.11}$$

where the temperature T and the thermal conductivity λ especially for fluids, depend on local temperature and pressure. The thermal conductivity describes the amount of heat per unit surface area which can be transported through a specific material. For solid materials and for small changes in temperature and pressure the thermal conductivity can be assumed as constant. The thermal conductivities of some selected, technically relevant or exceptional materials are listed in Tab. 2.3. The thermal conductivity is usually an isotropic material property with equal values in each direction. For composite or laminated materials which consist of two or more materials with different thermal conductivities, a homogenization of the thermal conductivity does make sense, in order to simplify calculation. Such homogenization of materials can

Material	λ in W/mK	Material	λ in W/mK
Nanotubes	≈ 8000	Casted iron	$41 \ldots 55$
Silver	427	Steel	$13 \ldots 48$
Copper	399	Water	0.598
Aluminum 99.2%	209	Air	0.0257

Table 2.3: Thermal conductivity of some materials at a temperature of 20°C [6, 48]

lead to an anisotropic thermal conductivity:

$$\boldsymbol{\lambda} = \begin{pmatrix} \lambda_x \\ \lambda_y \\ \lambda_z \end{pmatrix} . \tag{2.12}$$

According to the second law of thermodynamics, the conductive heat flux describes a non-reversible process flowing from the higher to the lower temperature against the temperature gradient and has, for that reason, a negative sign. For a flat plate with thickness b, surface area A and different temperatures T_{w1} and T_{w2} on the two surfaces, the heat flux is

$$\dot{Q} = \frac{\lambda \, A}{b}(T_{w1} - T_{w2}) . \tag{2.13}$$

2.2.2   Convective heat transfer

In contrast to solid bodies, the transport of heat inside a fluid is not restricted to conductive heat transport. On the account of macroscopic fluid movements relative to the heat source, heat energy is also transported by local fluid exchange. Hence the convective heat transport depends not only on the fluid properties but also on the local flow conditions next to the energy source.

Since a fluid typically adheres to the surface ($y = 0$) of a solid body, as sketched in Fig. 2.8 on page 29, the velocity of the fluid relative to the surface is zero, which is known as the non-slip-condition. The heat transport from the solid material to the fluid starts with conductive heat transport and consequently Fourier's fundamental law of heat conduction is valid at the boundary from solid to fluid material. Hence convective heat transport depends on the value of the fluid's thermal conductivity λ and the heat flux density $\dot{q}_w$ directly at the surface can be expressed as:

$$\dot{q}_w = -\lambda \left(\frac{\partial T}{\partial y} \right)_{y=0} . \tag{2.14}$$

The heat flux density depends on the difference between the surface temperature T_w and the temperature of the fluid T_∞

$$\dot{q}_w = \alpha(T_w - T_\infty) , \tag{2.15}$$

where the wall heat transfer coefficient α can be calculated analytically for very simple geometries under certain flow conditions. An analytical way of calculation for convoluted surfaces and/or turbulent flow conditions does not exist. Therefore α has to be

found empirically or by numerical methods. Using the equality of (2.14) and (2.15) leads to:

$$\alpha = -\lambda \frac{\left(\frac{\partial \mathsf{T}}{\partial y}\right)_\mathsf{w}}{\mathsf{T_w} - \mathsf{T}_\infty} \ . \tag{2.16}$$

The ratio λ/α is illustrated in Figure 2.4 as the slope of the temperature profile next to the surface [6].
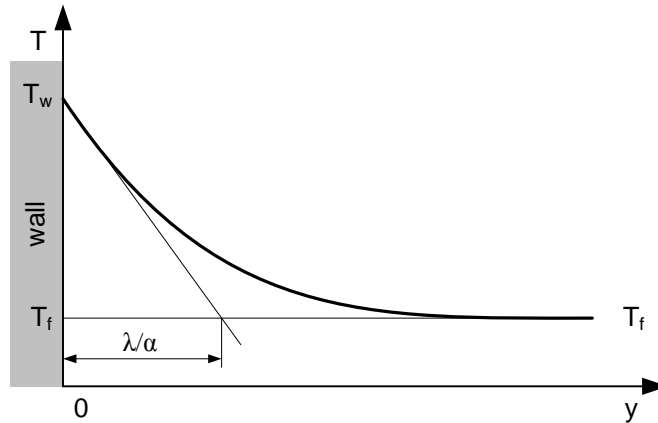
Figure 2.4: Temperature profile of the fluid for convective heat transport from the solid surface to the fluid

The wall heat transfer coefficient depends basically on the fluid properties and on the flow conditions. Some examples for the magnitude of the wall heat transfer coefficient are shown in Tab. 2.4. The wall heat transfer coefficient α is usually used

Fluid	Flow condition	α in W/m^{2}K
Air	free convection	6 - 30
Superheated steam or air	forced convection	30 - 300
Oil	forced convection	60 - 1.800
Water	forced convection	300 - 18.000
Water	boiling	3.000 - 60.000
Steam	condensing	6.000 - 120.000

Table 2.4: Order of magnitude of convection heat transfer coefficients [48]

as a mean value for a specific surface. If the coefficient is used as a value for a specific location at the surface it is very often designated as local wall heat transfer coefficient α_x.

2.2.3 Heat transfer by radiation

Besides convective heat transfer and heat transfer by conduction, every surface can transfer heat energy by radiation of electromagnetic waves in and close to the infrared

spectrum of light. The heat flux density $\dot{q}_r$ which is caused by radiation can be expressed as

$$\dot{q}_r = \sigma T^4 \ , \tag{2.17}$$

rising with the fourth power of the surface temperature T and $\sigma = 5.671 \cdot 10^{-8} \ \text{W/m}^2\text{K}^4$ for an ideally absorbed radiation. This correlation was first discovered by Josef Stefan and Ludwig Boltzmann hence σ is called the Stefan-Boltzmann constant. Since most bodies do not ideally emit or absorb radiation, the material property of the surface has to be considered with the inclusion of the emission-coefficient ϵ

$$\dot{q}_{r\ em} = \epsilon(T)\sigma T^4 \tag{2.18}$$

for emitted radiation and the absorption-coefficient a

$$\dot{q}_{r\ ab} = a\sigma T^4 \ , \tag{2.19}$$

for absorbed radiation, respectively. The total emitted or absorbed power can be expressed with the surface area A as $\dot{Q}_{em} = A\epsilon\sigma T^4$ and as $\dot{Q}_{ab} = Aa\sigma T_e^4$. Since the process of emission and absorption appear simultaneously in most technical applications, the total balance of exchanged power is of interest. For an emitting body with temperature T in an environment with temperature T_e the resulting balance of power is:

$$\dot{Q} = \dot{Q}_{em} - \dot{Q}_{ab} = A\sigma(\epsilon T^4 - aT_e^4) \ . \tag{2.20}$$

The use of a so called gray body in a black environment is sufficient in many technical calculations. For such conditions, the absorption coefficient a can be assumed to the equal to the emission coefficient ϵ:

$$\dot{Q} = \dot{Q}_{em} - \dot{Q}_{ab} = A\sigma\epsilon(T^4 - T_e^4) \ . \tag{2.21}$$

In contrast to conduction and convection, radiation is also possible in vacuum. If the heated body is surrounded by a fluid, convective heat transfer occurs simultaneously with radiation and has to be considered in the overall heat flux density. Therefore $\dot{q} = \dot{q}_c + \dot{q}_r$ and

$$\dot{q} = \alpha(T - T_\infty) + \epsilon\sigma(T^4 - T_e^4) = (\alpha + \alpha_r)(T - T_e) \ , \tag{2.22}$$

with the temperature of environmental surfaces T_e and the temperature of air T_∞, which can be assumed to be equal in many cases. This leads to a mathematical description of the heat transfer coefficient by radiation:

$$\alpha_r = \epsilon\sigma\frac{T^4 - T_e^4}{T - T_e} \ . \tag{2.23}$$

One important property of heat radiation becomes evident from this equation. Since the radiation heat flux depends on the fourth power of the temperature difference, it has to be considered if the surface temperature is very high or if the simultaneously existing heat flux by convection is very small, e.g. free buoyant convection [6].
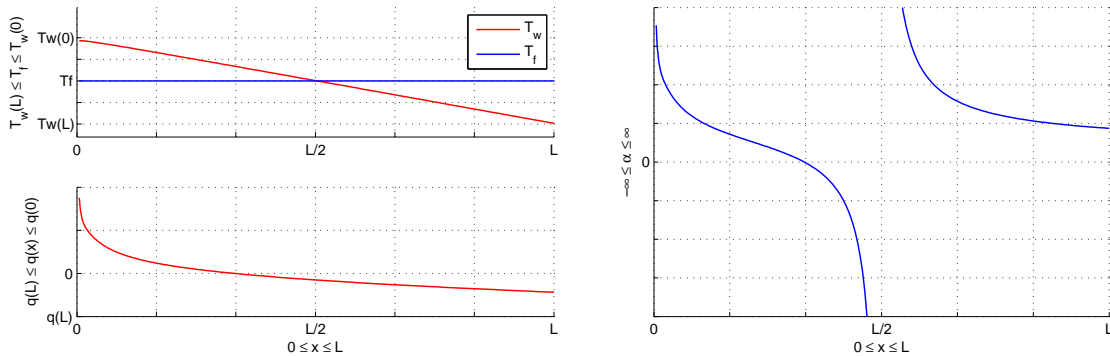
2.2.4 The wall heat transfer coefficient

The majority of English textbooks dealing with the topic of heat transfer denote (2.15) as Newton's law of cooling. According to [1], this is a widespread misconception. In the year of 1701, Newton commented the cooling process of red glowing hot iron as follows: *Therefore if the Times of cooling are taken equal, the Heats will be in Geometrical Ratio, and therefore are easily found by a Table of Logarithms* [66]. As pointed out in [1], Newton's paper was originally written in Latin and he used the word 'calor', which was translated to the word 'heat' in the 18th century, since the word 'temperature' had not yet been established. He explained the change in the temperature of a hot body over time in the form of:

$$\frac{\mathsf{d}\Delta\mathsf{T}}{\mathsf{d}t} \sim -\Delta\mathsf{T}, \tag{2.24}$$

which describes a cooling curve. Newton was dealing with the process of cooling but did not define a coefficient as we do today. Furthermore, he assumed that the whole body had a uniform temperature and did not consider the surface of the body or heat flux. Since the influence of area is crucial to the convective wall heat transfer coefficient, it is questionable that Newton was the creator of this coefficient. The concept of the wall heat transfer coefficient was most likely developed a whole century later by Fourier. In 1822 he published an awarded earlier version of Analytical Theory of Heat [26], which seems to be the first profound evidence of the wall heat transfer coefficient [1].

The textbook interpretation of Newton's law of cooling (2.15) adopts a very simple approach which meets the requirements in many cases. On the other hand, this approach can fail on a quite simple example, as shown in [33] :

(a) Wall temperature $\mathsf{T_w}$, fluid temperature $\mathsf{T_\infty}$ and resulting heat flux $\dot{\mathsf{q}}$

(b) Local wall heat transfer coefficient α

Figure 2.5: Example of a heat transfer scenario with non-physical behavior of the convective wall heat transfer coefficient as described in [33] and calculated by CFD

Assume a flat plate with the length L and a linearly declining surface temperature $\mathsf{T_w(x)} > \mathsf{T_f}$ from the leading edge at $\mathsf{x} = 0$, with $\mathsf{T_w(x)} = \mathsf{T_f}$ at $\mathsf{x} = \mathsf{L}/2$ to $\mathsf{T_w(x)} < \mathsf{T_f}$

at the tailing edge $x = L$, as sketched in Fig. 2.5(a). The cooling fluid with temperature T_f flows parallel to the plate, cooling the leading part and heating the tailing part. Investigations in [75] have shown that the heat flux density $\dot{q}$ becomes zero at $x \approx L/3$ due to the already heated air flowing next to the surface in down-stream direction. In this scenario the wall heat transfer coefficient is positive at the leading part, zero at $x = L/3$, switches from $-\infty$ to ∞ at $x = L/2$ due to the vanishing temperature gradient and is positive again at the tailing part of the plate, as shown in Fig. 2.5(b). Next to the position $x = L/2$ the wall heat transfer coefficient suggests an unrealistically high magnitude, which is physically not valid.

The complex process of energy exchange between a solid body and the surrounding fluid, cannot be described for each case with one single equation, e.g. cases of free convection and forced convection can not be described with the same equation. A closer look at the principle of cooling reveals some relevant details, as presented by O'Sullivan [67] and Bohren [12]. The authors categorize the cooling process by historically different approaches in Newtonian cooling, Dulong-Petit cooling and Newton-Stefan cooling. The classifications by O'Sullivan can be found in Appendix A.1.

A different classification was published by Herwig in [33], categorizing cooling into the physical principles of free convection, forced convection, condensing and radiation. In the case of free convection a linear correlation between $\dot{q}$ and ΔT does not exist. The flow condition is a function of the temperature dependent density $\rho(T)$ of the fluid. On a vertical plate with a constant wall temperature T_w, characteristic length L, position $0 \leq x \leq L$, thermal conductivity λ and laminar flow conditions, the wall heat transfer coefficient is

$$\alpha = F_{\mathrm{nc}}(\mathrm{Pr}) \ \mathrm{Gr}^{1/4} \ \lambda \ (x \ L^3)^{-1/4} \ , \tag{2.25}$$

with the Grashof number Gr and Prandtl number Pr, both described in Subsection 2.3.9. $F_{\mathrm{nc}}(\mathrm{Pr})$ is a function for free (natural) convection depending on the Prandtl number Pr. The Grashof number rises linearly with the characteristic temperature difference ΔT, hence the wall heat transfer coefficient corresponds to $\alpha \sim \Delta T^{-1/4}$. Consequently the heat flux density corresponds to the characteristic temperature difference ΔT with $\dot{q} \sim \Delta T^{5/4}$ for laminar flow and $\dot{q} \sim \Delta T^{4/3}$ for turbulent flow conditions.

Forced convection, on the other hand, can be described for laminar flow conditions on a plate with constant wall temperature T_w as

$$\alpha = F_{\mathrm{fc}}(\mathrm{Pr}) \ \mathrm{Re}^{1/2} \ \lambda \ (x \ L^3)^{-1/2} \ . \tag{2.26}$$

with the function $F_{\mathrm{fc}}(\mathrm{Pr})$ for forced convection dependent on the Prandtl number Pr and the Reynolds number Re which is also described in Subsection 2.3.9. Since (2.26) does not depend on the characteristic temperature difference ΔT, a linear dependence as described in (2.15) is valid. In the case of turbulent flow conditions, the right hand side of (2.26) changes, but remains independent of ΔT. Thus the linear dependence of the wall heat transfer coefficient α on the characteristic temperature difference ΔT remains linear for the mentioned conditions [33].

2.3 Fluid dynamics

The heat transport by convection depends on the properties of the fluid and the state of fluid flow. In order to express the quantity of the convective heat transfer, it is essential to know what the flow conditions are. With regard to the flow simulation, some fundamental basics of fluid dynamics are described in this section.

2.3.1 Fluid and viscosity

Matter which cannot sustain shear stress under resting conditions but is deforming its shape is referred to as fluid [14]. A fluid is considered as a continuum and can be either liquid or gaseous.
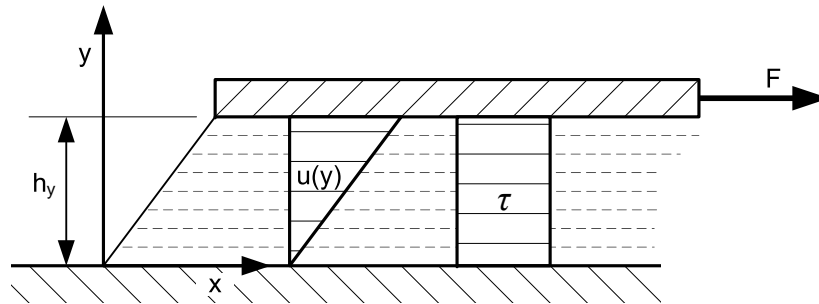
Figure 2.6: Shear of fluid between two horizontal plates with profiles of velocity $u(y)$ and shear stress τ

Consider a fluid between two parallel flat plates with constant distance $y = h_y$, as sketched in Fig. 2.6. On one plate, a force F is acting in parallel direction to the plates and the other plate is fixed. Due to the constant force, the plate moves with constant velocity u in the same direction and causes a shear stress τ in the fluid. Since no other forces are acting on the fluid or the plates, the shear stress in the fluid is constant in every plane parallel to the plates from $y = 0$ to h. Experiments on technically important fluids (e.g. air and water) show that shear stress and velocity gradient are proportional:

$$\tau = \mu \frac{du}{dy} \; , \tag{2.27}$$

with the dynamic viscosity μ as a property of the relevant material. This also implies that the fluid cannot sustain shear stress at rest. All fluids which meet this condition are Newtonian Fluids [34].

2.3.2   Conservation of mass

The theory of fluid dynamics assumes that mass cannot be produced or destroyed. This axiom leads to the equation of conservation of mass [80]:

$$\frac{\partial \rho}{\partial t} + \nabla \cdot (\rho \mathbf{v}) = 0 \tag{2.28}$$

with velocity vector $\mathbf{v} = \mathbf{v}(u, v, w)$ and density ρ. The conservation of mass in (2.28) is written in the conservative form or divergence form. In the conservative form, the exactly same amount of mass flows into a certain volume as it flows out on the other side, if the volume is free of any sources or sinks. On the other hand the non-conservative form or quasi-linear form of (2.28) is

$$\frac{\partial \rho}{\partial t} + (\mathbf{v} \cdot \nabla)\rho + (\rho \nabla \cdot \mathbf{v}) = 0 \ . \tag{2.29}$$

Without taking the density into account properly, the mass-flux through the boundaries of adjacent cells will not be canceled. Hence the conservative form of the conservation equations is important to keep the total mass constant in numerical calculations. In many applications, the density can be assumed as incompressible, which means that it does not change during transport between locations $\mathbf{x} = \mathbf{x}(x, y, z)$ or in time t. On this account, the equation of continuity can be reduced to the conservative form for incompressible fluids

$$\nabla \cdot (\rho \mathbf{v}) = 0 \tag{2.30}$$

and to the divergence free condition for the velocity

$$\nabla \cdot \mathbf{v} = 0 \ , \tag{2.31}$$

respectively [22, 43].

2.3.3   Conservation of momentum

The axiom of momentum from classical mechanics can be applied to liquid or gaseous fluids [34]:

$$\frac{d}{dt}(\Delta m \mathbf{v}) = \sum_i \mathbf{F}_i \ . \tag{2.32}$$

This derivative on the left hand side is $\mathbf{v}\frac{d\Delta m}{dt} + \Delta m \frac{d\mathbf{v}}{dt}$. Due to the conservation of mass (2.32), $\frac{d\Delta m}{dt}$ becomes zero and (2.32) can be expressed by

$$\Delta m \frac{d\mathbf{v}}{dt} = \sum_i \mathbf{F}_i \ . \tag{2.33}$$

With the expression of mass per unit volume $\frac{\Delta m}{\Delta V} = \rho$ and force per unit volume $\frac{\mathbf{F}_i}{\Delta V} = \mathbf{f}_i$, (2.32) can be written as

$$\rho \frac{d\mathbf{v}}{dt} = \sum_i \mathbf{f}_i \ . \tag{2.34}$$

The forces applied to a fluid are separated into mass or body forces and contact or surface forces. Body forces $\mathbf{f}_i^B$ occur due to centrifugal forces, Lorenz forces or gravitational force

$$\mathbf{f}_i^B = \rho\mathbf{g} , \tag{2.35}$$

with the acceleration $\mathbf{g}_x$, $\mathbf{g}_y$ and $\mathbf{g}_z$ in the direction of x, y and z, respectively.

The surface forces $\mathbf{f}_i^S$ on a cubic control volume $\Delta V = \Delta x \Delta y \Delta z$ occur in the form of tension forces. Considering that fluids can not accommodate shear stress at rest and are able to accommodate compressive stress but not tension stress, the surface forces in direction x can be written as

$$\left(\frac{\partial\sigma_{xx}}{\partial x}\Delta x\right)\Delta y\Delta z \quad , \quad \left(\frac{\partial\tau_{yx}}{\partial x}\Delta y\right)\Delta x\Delta z \quad \text{and} \quad \left(\frac{\partial\tau_{zx}}{\partial x}\Delta z\right)\Delta x\Delta y , \tag{2.36}$$

which, expressed per unit volume, become $\frac{\partial\sigma_{xx}}{\partial x}$, $\frac{\partial\tau_{yx}}{\partial x}$ and $\frac{\partial\tau_{zx}}{\partial x}$. The principal stress σ_{xx} is defined perpendicularly to the control volumes face in the yz plane and the shear stresses τ_{yx} and τ_{zx} in the yx plane and zx plane, respectively. All tensions occurring on the cubic control volume are usually written in the stress tensor

$$\boldsymbol{\sigma} = \begin{pmatrix} \sigma_{xx} & \tau_{yx} & \tau_{zx} \\ \tau_{xy} & \sigma_{yy} & \tau_{zy} \\ \tau_{xz} & \tau_{yz} & \sigma_{zz} \end{pmatrix} . \tag{2.37}$$

If the fluid is in rest with $\mathbf{v} = 0$, then the shear stress is zero and the principal stress remains at the value of the hydrostatic pressure p, which can be separated from the principal stresses σ_{xx}, σ_{yy}, σ_{zz} in the stress tensor $\boldsymbol{\sigma}$ and the viscose stress tensor $\boldsymbol{\tau}$ remains

$$\boldsymbol{\tau} = \boldsymbol{\sigma} - p\mathbf{I} = \begin{pmatrix} \sigma_{xx} & \tau_{yx} & \tau_{zx} \\ \tau_{xy} & \sigma_{yy} & \tau_{zy} \\ \tau_{xz} & \tau_{yz} & \sigma_{zz} \end{pmatrix} - \begin{pmatrix} p & 0 & 0 \\ 0 & p & 0 \\ 0 & 0 & p \end{pmatrix} = \begin{pmatrix} \tau_{xx} & \tau_{yx} & \tau_{zx} \\ \tau_{xy} & \tau_{yy} & \tau_{zy} \\ \tau_{xz} & \tau_{yz} & \tau_{zz} \end{pmatrix} , \tag{2.38}$$

where $\mathbf{I}$ denotes the identity tensor. Combining (2.34), (2.35) and (2.38) as

$$\mathbf{f}_i^S = \boldsymbol{\tau}\nabla = \boldsymbol{\sigma}\nabla - \nabla p \tag{2.39}$$

the conservation of momentum can be written in vector notation

$$\rho\frac{d\mathbf{v}}{dt} = -\nabla p + \boldsymbol{\sigma}\nabla + \mathbf{f}^B , \tag{2.40}$$

or in the coordinate-wise form [2]

$$\begin{aligned} \frac{\partial(\rho u)}{\partial t} + (\nabla \cdot \rho u\mathbf{v}) &= -\frac{\partial p}{\partial x} + \frac{\partial\tau_{xx}}{\partial x} + \frac{\partial\tau_{yx}}{\partial y} + \frac{\partial\tau_{zx}}{\partial z} + f_x^B \\ \frac{\partial(\rho v)}{\partial t} + (\nabla \cdot \rho v\mathbf{v}) &= -\frac{\partial p}{\partial y} + \frac{\partial\tau_{xy}}{\partial x} + \frac{\partial\tau_{yy}}{\partial y} + \frac{\partial\tau_{zy}}{\partial z} + f_y^B \\ \frac{\partial(\rho w)}{\partial t} + (\nabla \cdot \rho w\mathbf{v}) &= -\frac{\partial p}{\partial z} + \frac{\partial\tau_{xz}}{\partial x} + \frac{\partial\tau_{yz}}{\partial y} + \frac{\partial\tau_{zz}}{\partial z} + f_z^B \end{aligned} \tag{2.41}$$

with mass acceleration $\frac{\partial(\rho u)}{\partial t} + \nabla \cdot \rho u \mathbf{v}$, pressure force $-\frac{\partial p}{\partial x}$, viscose forces $\frac{\partial \tau_{xx}}{\partial x} + \frac{\partial \tau_{yx}}{\partial y} + \frac{\partial \tau_{zx}}{\partial z}$ and body forces f_x^B, each per unit volume [17].

2.3.4   Conservation of energy

Similarly to the conservation of mass, the energy in a system cannot be created or destroyed. The temporal change of a body's energy equals the sum of the power of all applied forces plus all the supplied energy per unit of time [80]. This can be expressed mathematically as:

$$
\frac{\partial}{\partial t}\left[\rho\left(e + \frac{V^2}{2}\right)\right] + \left[\nabla \cdot \rho\left(e + \frac{V^2}{2}\right)\mathbf{v}\right] = \rho \mathbf{f}^B \cdot \mathbf{v} - (\nabla p \mathbf{v})
$$

$$
+ \quad \frac{\partial}{\partial x}(u\tau_{xx} + v\tau_{xy} + w\tau_{xz}) + \frac{\partial}{\partial y}(u\tau_{yx} + v\tau_{yy} + w\tau_{yz}) + \frac{\partial}{\partial z}(u\tau_{zx} + v\tau_{zy} + w\tau_{zz})
$$

$$
- \quad (\nabla \cdot \mathbf{q}) + \dot{q}_Q \, , \tag{2.42}
$$

with the total energy per unit volume

$$
E_t = \rho\left(e + \frac{V^2}{2}\right) \tag{2.43}
$$

containing the inner energy ρe, the kinetic energy $\rho \frac{V^2}{2}$ and the Euclidean norm of the velocity vector $V = ||\mathbf{v}||_2$ on the left-hand side [2]. The right-hand side of the equation includes the power of the body forces $\rho \mathbf{f}^B \cdot \mathbf{v}$, the surface forces $-\nabla p \mathbf{v} + \frac{\partial}{\partial x}(.) + \frac{\partial}{\partial y}(.) + \frac{\partial}{\partial z}(.)$, all heat energy transported over the system boundaries $\nabla \cdot \mathbf{q}$ and the inner energy sources $\dot{q}_Q$.

2.3.5   Navier-Stokes equations

The flow conditions cannot be calculated with the equations on conservation of momentum (2.41) and mass of incompressible fluids (2.31), because the number of unknowns is higher than the number of equations. For constant density ρ, the momentum equation for direction x can be written as

$$
\frac{\partial(\rho u)}{\partial t} + (\nabla \cdot \rho u \mathbf{v}) = -\frac{\partial p}{\partial x} + \frac{\partial \tau_{xx}}{\partial x} + \frac{\partial \tau_{yx}}{\partial y} + \frac{\partial \tau_{zx}}{\partial z} + f_x^B \tag{2.44}
$$

By introducing Stokes' law for frictional force

$$
\tau_{xx} = 2\mu\left(\frac{\partial u}{\partial x}\right) \quad , \quad \tau_{yx} = \mu\left(\frac{\partial v}{\partial x} + \frac{\partial u}{\partial y}\right) \quad \text{and} \quad \tau_{zx} = \mu\left(\frac{\partial w}{\partial x} + \frac{\partial u}{\partial y}\right), \tag{2.45}
$$

the tensions in (2.44) can be replaced by derivatives of velocities:

$$
\frac{\partial(\rho u)}{\partial t} + (\nabla \cdot \rho u \mathbf{v}) = -\frac{\partial p}{\partial x} + \mu\left(\frac{\partial^2 u}{\partial x^2} + \frac{\partial^2 u}{\partial y^2} + \frac{\partial^2 u}{\partial z^2}\right) + f_x^B \tag{2.46}
$$

where μ is the dynamic viscosity of the fluid. Hence:

$$\frac{\partial(\rho\mathsf{u})}{\partial\mathsf{t}} + (\nabla \cdot \rho\mathsf{u}\mathbf{v}) = -\frac{\partial\mathsf{p}}{\partial\mathsf{x}} + \mu\Delta\mathsf{u} + \mathsf{f}_\mathsf{x}^\mathsf{B}$$

$$\frac{\partial(\rho\mathsf{v})}{\partial\mathsf{t}} + (\nabla \cdot \rho\mathsf{v}\mathbf{v}) = -\frac{\partial\mathsf{p}}{\partial\mathsf{y}} + \mu\Delta\mathsf{v} + \mathsf{f}_\mathsf{y}^\mathsf{B}$$

$$\frac{\partial(\rho\mathsf{w})}{\partial\mathsf{t}} + (\nabla \cdot \rho\mathsf{w}\mathbf{v}) = -\frac{\partial\mathsf{p}}{\partial\mathsf{z}} + \mu\Delta\mathsf{w} + \mathsf{f}_\mathsf{z}^\mathsf{B} \ , \tag{2.47}$$

The equations for continuity of momentum are along with the continuity of mass and continuity of energy called the Navier-Stokes equations. With the help of the Navier-Stokes equations, an exact solution can be achieved for specific cases of laminar fluid flow and constant density.

2.3.6 Variables of the turbulent flow

Turbulent flow can be a desired flow condition, since convectional processes such as heat or mass transport are more pronounced in comparison with laminar flow conditions. Although the Navier-Stokes equations can be used to calculate laminar flow under various conditions, they fail when the fluid flow is turbulent. On the other hand, a turbulent flow always requires additional power to sustain the permanent fluctuation of the fluid. Under turbulent flow conditions, the velocity $\mathbf{v}$ can be split into a time average value $\bar{\mathbf{v}}$ and a fluctuating value $\mathbf{v}'$ in the form of $\mathbf{v} = \bar{\mathbf{v}} + \mathbf{v}'$. The average
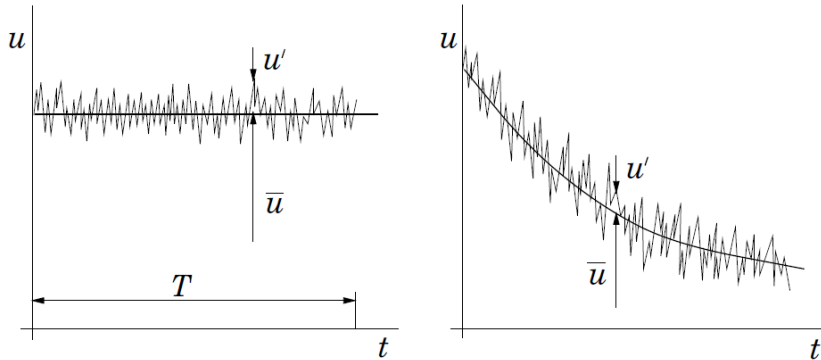
Figure 2.7: Time averaged values for (left) steady state flow and (right) transient flow conditions [22]

and fluctuating components of the velocity vector $\mathbf{v}$ exist for each component u, v and w in the appropriate directions x, y and z. As sketched in Fig. 2.7, only the u part is shown in the direction x from the vector $\mathbf{v}$ if this behavior affects all dimensions independently:

$$\mathsf{u}(\mathsf{x},\mathsf{t}) = \bar{\mathsf{u}}(\mathsf{x},\mathsf{t}) + \mathsf{u}'(\mathsf{x},\mathsf{t}) \ . \tag{2.48}$$

Due to turbulence, stochastic oscillating lateral and longitudinal movements relative to the mean flow of fluid particles require mechanical energy for permanent acceleration

and deceleration. The exchange of momentum and recurrent partial elastic deformation of fluid particles in a streaming fluid cause a transformation from kinetic into thermal energy called dissipation. The isotropic dissipation rate with the unit $\mathsf{m}^2/\mathsf{s}^3$ is defined in [76] by:

$$\varepsilon = \nu \overline{\frac{\partial \mathsf{u}_\mathsf{i}'}{\partial \mathsf{x}_\mathsf{k}} \frac{\partial \mathsf{u}_\mathsf{i}'}{\partial \mathsf{x}_\mathsf{k}}} \ , \tag{2.49}$$

with index notation which is equivalent to

$$\begin{aligned} \varepsilon \ = \ & \frac{\mu}{\rho} \left[\overline{\left(\frac{\partial \mathsf{u}'}{\partial \mathsf{x}}\right)^2} + \overline{\left(\frac{\partial \mathsf{v}'}{\partial \mathsf{x}}\right)^2} + \overline{\left(\frac{\partial \mathsf{w}'}{\partial \mathsf{x}}\right)^2} \right. \\ + \ & \overline{\left(\frac{\partial \mathsf{u}'}{\partial \mathsf{y}}\right)^2} + \overline{\left(\frac{\partial \mathsf{v}'}{\partial \mathsf{y}}\right)^2} + \overline{\left(\frac{\partial \mathsf{w}'}{\partial \mathsf{y}}\right)^2} \\ + \ & \left. \overline{\left(\frac{\partial \mathsf{u}'}{\partial \mathsf{z}}\right)^2} + \overline{\left(\frac{\partial \mathsf{v}'}{\partial \mathsf{z}}\right)^2} + \overline{\left(\frac{\partial \mathsf{w}'}{\partial \mathsf{z}}\right)^2} \right] . \end{aligned} \tag{2.50}$$

With the resulting additional flow resistance, the fluid seems to have a higher shear stress and hence a higher viscosity than under laminar flow conditions. According to (2.27), this additional turbulent wall shear stress τ_t can be expressed for the fluid flow with velocity u in direction x as:

$$\tau_\mathsf{t} = \mu_\mathsf{t} \cdot \frac{\partial \mathsf{u}}{\partial \mathsf{y}} \tag{2.51}$$

where μ_t is the turbulent viscosity and y the direction perpendicular to the flow direction and the wall surface. The turbulent viscosity μ_t depends on the local flow conditions and is therefore a parameter of momentum exchange and not of fluid properties. The eddy viscosity which is widely used for numerical calculations is defined by:

$$\nu_\mathsf{t} = \frac{\mu_\mathsf{t}}{\rho} \ . \tag{2.52}$$

Due to the dependence on turbulence, a universally valid expression of eddy viscosity is not available [79]. As shown in Subsection 2.4.4, basic turbulence models use the eddy viscosity to define the Reynolds stress tensor for the calculation of turbulent flow. The permanent acceleration of fluid particles is a form of energy, which can be expressed per unit mass by the turbulence kinetic energy k:

$$\mathsf{k} = \frac{\overline{\mathsf{u}'^2} + \overline{\mathsf{v}'^2} + \overline{\mathsf{w}'^2}}{2} \tag{2.53}$$

with the averaged fluctuating velocities for each Cartesian direction. Consequently, the unit of the turbulence kinetic energy is $\mathsf{m}^2/\mathsf{s}^2$. For fluid boundary conditions (e.g. inlet and outlet) a frequently used expression is the turbulence intensity I_t with isotropic turbulence $\mathsf{u}' = \mathsf{v}' = \mathsf{w}'$:

$$\mathsf{I}_\mathsf{t} = \frac{\mathsf{u}'}{\overline{\mathsf{u}}} \ , \tag{2.54}$$

which is calculated for the flow in direction x by the isotropic fluctuating part and the mean velocity $\bar{\mathsf{u}}$ [4]:

$$\mathsf{u}' = \sqrt{\frac{2}{3}}\mathsf{k} \; . \tag{2.55}$$

An intensity above 10% can be considered as high and, if it is below 1%, as low turbulence intensity. For the flow conditions in a cooling duct, the intensity in the core of the flow can be described with the Reynolds number $\mathsf{Re_{Dh}}$ for the hydraulic diameter $\mathsf{D_h}$ as [25]:

$$\mathsf{I_t} = 0.16 \; (\mathsf{Re_{Dh}})^{-1/8} \tag{2.56}$$

2.3.7   Reynolds Averaged Navier-Stokes (RANS) equations

The velocities for laminar flow in the Navier-Stokes equations in (2.47) can be replaced by the time-averaged and fluctuating velocities as shown in (2.48). Assuming that the time-average of the fluctuating value $\overline{\mathsf{a}'} = 0$ is zero, the rules for calculating with averaged values are:

$$\overline{\mathsf{a} + \mathsf{b}} = \bar{\mathsf{a}} + \bar{\mathsf{b}} \qquad \bar{\bar{\mathsf{a}}} = \bar{\mathsf{a}} \qquad \overline{\bar{\mathsf{a}}\mathsf{b}} = \bar{\mathsf{a}}\bar{\mathsf{b}} \qquad \overline{\frac{\partial \mathsf{a}}{\partial \mathsf{s}}} = \frac{\partial \bar{\mathsf{a}}}{\partial \mathsf{s}}$$

As seen in (2.47), the Navier-Stokes equation for the x direction is

$$\frac{\partial(\rho\mathsf{u})}{\partial\mathsf{t}} + (\nabla \cdot \rho\mathsf{u}\mathbf{v}) = -\frac{\partial\mathsf{p}}{\partial\mathsf{x}} + \mu\Delta\mathsf{u} + \mathsf{f}_\mathsf{x}^\mathsf{B} \; . \tag{2.57}$$

Resolving $(\nabla \cdot \rho\mathsf{u}\mathbf{v})$, the left hand side of this equation is:

$$\frac{\partial(\rho\mathsf{u})}{\partial\mathsf{t}} + \frac{\partial(\rho\mathsf{u}^2)}{\partial\mathsf{x}} + \frac{\partial(\rho\mathsf{u}\mathsf{v})}{\partial\mathsf{y}} + \frac{\partial(\rho\mathsf{u}\mathsf{w})}{\partial\mathsf{z}} = \dots \tag{2.58}$$

and replacing the velocities by the mean and the fluctuating part as shown in (2.48) leads to:

$$\frac{\partial(\rho(\bar{\mathsf{u}} + \mathsf{u}'))}{\partial\mathsf{t}} + \frac{\partial(\rho(\bar{\mathsf{u}} + \mathsf{u}')^2)}{\partial\mathsf{x}} + \frac{\partial(\rho(\bar{\mathsf{u}} + \mathsf{u}')(\bar{\mathsf{v}} + \mathsf{v}'))}{\partial\mathsf{y}} + \frac{\partial(\rho(\bar{\mathsf{u}} + \mathsf{u}')(\overline{\mathsf{w}} + \mathsf{w}'))}{\partial\mathsf{z}} = \dots \; . \tag{2.59}$$

The whole equation can be averaged by averaging the single terms according to the rule $\overline{\mathsf{a} + \mathsf{b}} = \bar{\mathsf{a}} + \bar{\mathsf{b}}$ after resolving the products in the derivatives in (2.59):

$$\begin{aligned}
\frac{\overline{\partial(\rho\bar{\mathsf{u}})}}{\partial\mathsf{t}} + \frac{\overline{\partial(\rho\mathsf{u}')}}{\partial\mathsf{t}} \quad &+ \quad \frac{\overline{\partial(\rho\bar{\mathsf{u}}^2)}}{\partial\mathsf{x}} + 2\frac{\overline{\partial(\rho\bar{\mathsf{u}}\mathsf{u}')}}{\partial\mathsf{x}} + \frac{\overline{\partial(\rho\mathsf{u}'^2)}}{\partial\mathsf{x}} \\
&+ \quad \frac{\overline{\partial(\rho\bar{\mathsf{u}}\bar{\mathsf{v}})}}{\partial\mathsf{y}} + \frac{\overline{\partial(\rho\bar{\mathsf{u}}\mathsf{v}')}}{\partial\mathsf{y}} + \frac{\overline{\partial(\rho\mathsf{u}'\bar{\mathsf{v}})}}{\partial\mathsf{y}} + \frac{\overline{\partial(\rho\mathsf{u}'\mathsf{v}')}}{\partial\mathsf{y}} \\
&+ \quad \frac{\overline{\partial(\rho\bar{\mathsf{u}}\overline{\mathsf{w}})}}{\partial\mathsf{z}} + \frac{\overline{\partial(\rho\bar{\mathsf{u}}\mathsf{w}')}}{\partial\mathsf{z}} + \frac{\overline{\partial(\rho\mathsf{u}'\overline{\mathsf{w}})}}{\partial\mathsf{z}} + \frac{\overline{\partial(\rho\mathsf{u}'\mathsf{w}')}}{\partial\mathsf{z}} = \dots \; . \quad (2.60)
\end{aligned}$$

Applying the rules $\overline{a'} = 0$ and $\overline{\frac{\partial a}{\partial s}} = \frac{\partial \overline{a}}{\partial s}$, the equation can be reduced to:

$$\frac{\partial(\rho\overline{u})}{\partial t} \quad + \quad \frac{\partial(\rho\overline{u}^2)}{\partial x} + \frac{\partial(\rho\overline{u}\overline{v})}{\partial y} + \frac{\partial(\rho\overline{u}\overline{w})}{\partial z}$$
$$+ \quad \frac{\partial(\rho\overline{u'^2})}{\partial x} + \frac{\partial(\rho\overline{u'v'})}{\partial y} + \frac{\partial(\rho\overline{u'w'})}{\partial z} = -\frac{\partial\overline{p}}{\partial x} + \mu\Delta\overline{u} + f_x^B \ , \qquad (2.61)$$

which can be abbreviated in index notation for the Cartesian coordinates:

$$\frac{\partial(\rho\overline{u_i})}{\partial t} + \frac{\partial}{\partial x_j}\left(\rho\overline{u_i u_j} + \rho\overline{u_i' u_j'}\right) = -\frac{\partial\overline{p}}{\partial x_i} + \mu\frac{\partial^2\overline{u_i}}{\partial x_j^2} + f_i^B \ . \qquad (2.62)$$

For all three coordinates of the Cartesian coordinate system the Reynolds Averaged Navier-Stokes can be written as:

$$\frac{\partial\overline{u}}{\partial t} + \overline{u}\frac{\partial\overline{u}}{\partial x} + \overline{v}\frac{\partial\overline{u}}{\partial y} + \overline{w}\frac{\partial\overline{u}}{\partial z} \ = \ -\frac{1}{\rho}\frac{\partial\overline{p}}{\partial x} + \nu\Delta\overline{u} - \frac{\partial\overline{u'^2}}{\partial x} - \frac{\partial\overline{v'u'}}{\partial y} - \frac{\partial\overline{w'u'}}{\partial z} + g_x$$

$$\frac{\partial\overline{v}}{\partial t} + \overline{u}\frac{\partial\overline{v}}{\partial x} + \overline{v}\frac{\partial\overline{v}}{\partial y} + \overline{w}\frac{\partial\overline{v}}{\partial z} \ = \ -\frac{1}{\rho}\frac{\partial\overline{p}}{\partial y} + \nu\Delta\overline{v} - \frac{\partial\overline{u'v'}}{\partial x} - \frac{\partial\overline{v'^2}}{\partial y} - \frac{\partial\overline{w'v'}}{\partial z} + g_y$$

$$\frac{\partial\overline{w}}{\partial t} + \overline{u}\frac{\partial\overline{w}}{\partial x} + \overline{v}\frac{\partial\overline{w}}{\partial y} + \overline{w}\frac{\partial\overline{w}}{\partial z} \ = \ -\frac{1}{\rho}\frac{\partial\overline{p}}{\partial z} + \nu\Delta\overline{w} - \frac{\partial\overline{u'w'}}{\partial x} - \frac{\partial\overline{v'w'}}{\partial y} - \frac{\partial\overline{w'^2}}{\partial z} + g_z (2.63)$$

with the kinematic viscosity $\nu = \mu/\rho$. A detailed derivation of the RANS equations can be found e.g. in [34, 79]. These equations represent the basis of most fluid dynamic simulation tools designed for engineering purposes. Due to the consideration of fluctuating flow conditions, additional strains also known as Reynolds stress are included on the right-hand side of the equation (2.63). Since the determination of the Reynolds stress is computationally time-consuming, these additional strains are usually replaced by special models in CFD simulations [25, 80].

2.3.8   The boundary layer

Assume an impermeable surface (wall) parallel to the mean flow direction x of a fluid (as shown in Figure 2.8). The fluid flow is considered laminar and in steady state. Since the non-slip-condition is valid at the boundary, the relative velocity of the fluid to the surface is zero directly at the surface $(y \to 0)$.

Examining the flow field next to the surface, it is evident that the velocity $u_{(y)}$ rises with the increase of the distance y to the surface, until it reaches the velocity u_∞. In the outer fluid flow, at a fictitious infinite distance perpendicular to the considered surface, flow conditions are assumed to be not influenced by the examined surface. The margin of the velocity boundary layer $\delta(x)$ is defined by the position where the velocity profile $u_{(y)}$ reaches the value of the outer flow u_∞.

The thermal boundary layer $\delta_t(x)$ is defined in a similar manner. The fluid temperature T_f at the surface equals the surface temperature $T(y \to 0) = T_w$. As shown in
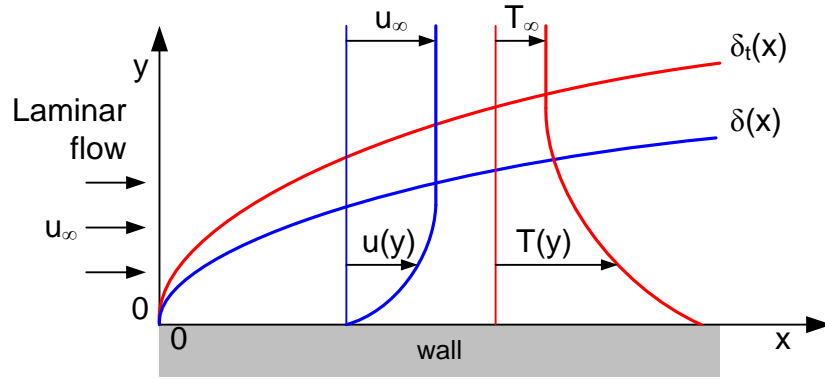
Figure 2.8: Boundary layers of velocity and temperature in a laminar flow

Figure 2.8 for the condition $T_w > T_\infty$, the fluid temperature reaches the temperature of the outer flow T_∞ asymptotically.

The thermal and the velocity boundary layers do not necessarily have the same thickness, but can have approximately the same size for monoatomic gases. For polyatomic gases, liquids and liquid metals, the velocity and thermal boundary layers are typically of different sizes. The ratio of the thicknesses of the boundary layers is proportional to the square root of the Prandtl number (see Subsection 2.3.9) [80]:

$$\frac{\delta}{\delta_t} \sim \sqrt{Pr} \tag{2.64}$$

From the relation in (2.64), it is evident that a Prandtl number of less than one corresponds to a thicker thermal boundary layer δ_t, compared to the velocity boundary layer δ. The Prandtl number of air in the temperature range from 0°C to 500°C rises from $Pr=0.71$ to $Pr=0.72$, and can be assumed to be constant in most cases related to electrical machines.

The physically and mathematically exact assumption for the boundary layer is the asymptotic approach of $u(y \to \infty) = u_\infty$. Since the exact boundary layer would not be in a finite range when using the exact assumption, an arbitrarily determined value of $0.99 \cdot u_\infty$ has been defined as a practical margin of the boundary layer [80].

2.3.9 Dimensionless numbers in fluid dynamics

Experimental research has determined that fluids with low viscosity and large characteristic length scales have similar flow conditions to fluids with high viscosity and small characteristic length scales [7].

This relation is not arbitrary, but rather complies with a physical law, which is the basis of several dimensionless numbers in fluid dynamics, e.g. the Reynolds-number. The Reynolds number is proportional to the ratio of inertial forces to viscous forces [71] and is defined by the velocity u_∞, the characteristic length L and the kinematic viscosity

of the fluid ν.

$$\mathsf{Re} = \frac{\mathsf{u}_\infty\,\rho\,\mathsf{L}}{\mu} = \frac{\mathsf{u}_\infty\,\mathsf{L}}{\nu} \; . \tag{2.65}$$

It indicates whether the flow condition is turbulent or laminar, e.g. in the case of a pipe flow a Reynolds number $\mathsf{Re} < 2300$ indicates a laminar pipe flow [79].

The Prandtl number defines the relation between flow field and temperature field [7] and is defined as:

$$\mathsf{Pr} = \frac{\mu\,\mathsf{c}_\mathsf{p}}{\lambda} = \frac{\nu}{\mathsf{a}} \; , \tag{2.66}$$

with specific heat capacity c_p and thermal conductivity λ.

The Eckert number Ec is a ratio describing the temperature field, e.g. for supersonic flows or flow conditions with noteworthy internal friction (dissipation), with temperature difference $\Delta\mathsf{T}$ between the surface and the environment.

$$\mathsf{Ec} = \frac{\mathsf{u}_\infty^2}{\mathsf{c}_\mathsf{p}\,\Delta\mathsf{T}} \tag{2.67}$$

In contrast to the Eckert number, the Grashof number Gr gains importance for slow and buoyant flows driven by acceleration of gravity g and local change of density, which can be characterized by the volumetric thermal expansion coefficient β:

$$\mathsf{Gr} = \frac{\mathsf{g}\,\beta\,\mathsf{L}^3\,\Delta\mathsf{T}}{\nu^2} \tag{2.68}$$

On the other hand, the Grashof number is usually negligible for mechanically generated flows.

A very important number for problems of heat transfer is the Nusselt number Nu, which characterizes the ratio between the existing heat flux density and the theoretical heat flux density caused by simple conductive heat transfer [13]. In general the Nusselt number depends on the four numbers mentioned above:

$$\overline{\mathsf{Nu}} = F(\mathsf{Re}, \mathsf{Pr}, \mathsf{Ec}, \mathsf{Gr}) = \frac{\overline{\alpha}\,\mathsf{L}}{\lambda} \; , \tag{2.69}$$

where $\overline{\mathsf{Nu}}$ and $\overline{\alpha}$ are the surface averaged values of the local Nusselt number Nu_x and of the local wall heat transfer coefficient α_x, respectively. Replacing the wall heat transfer coefficient with the wall heat flux and temperature difference leads to the frequently used expression

$$\mathsf{Nu} = \frac{\dot{\mathsf{q}}_\mathsf{w}\,\mathsf{L}}{\lambda\,\Delta\mathsf{T}} \; . \tag{2.70}$$

Due to the reasons mentioned above, the Eckert number and, in most cases, the Grashof number can be neglected in the investigations of the present work. The Prandtl number for air can be assumed to be constant in the considered range of temperature. The only influencing factor in this investigation is the Reynolds number.

In problems related to conductive heat transfer and sometimes also convective heat transfer, the Biot number can give useful information about the temperature

field inside solid material. Like the Nusselt number, the Biot number is defined by the heat transfer coefficient α, the characteristic length L and the thermal conductivity λ:

$$\mathsf{Bi} = \frac{\alpha\,\mathsf{L}}{\lambda}\;.\tag{2.71}$$

In contrast to the Nusselt number, the thermal conductivity of the solid material is used for the Biot number. If the value of the Biot number in a specific problem is below 2, an almost homogeneous temperature field inside the solid material can be assumed [7].

The ratio between compressive force (pressure) and inertial force is known as the Euler number Eu [79], determined by pressure p, density ρ and velocity u_∞:

$$\mathsf{Eu} = \frac{\mathsf{p}}{\rho\mathsf{u}_\infty^2}\;.\tag{2.72}$$

2.3.10 Turbulent flow in wall-proximity

This subsection is based on derivations of turbulent flow in [80]. In technical applications for convective cooling, the flow conditions are usually turbulent and laminar flows are exceptions. The laminar behavior of fluid flow parallel to the wall can be explained by the Navier-Stokes equation (2.47) with the conditions $\mathsf{u} = f(\mathsf{y})$ and $\mathsf{v} = \mathsf{w} = 0$ by

$$0 = \mu\frac{\mathsf{d}^2\mathsf{u}}{\mathsf{d}\mathsf{y}^2}\;.\tag{2.73}$$

The vanishing second derivative of velocity indicates a constant shear stress τ_{yx} and a linear dependence of velocity u on the distance to the wall y. For the same conditions, the turbulent behavior of fluid flow parallel to the wall can be described by introducing the Reynolds equation

$$\rho\bar{\mathsf{v}}\frac{\partial\bar{\mathsf{u}}}{\partial\mathsf{y}} = \frac{\partial\tilde{\tau}_{\mathsf{yx}}}{\partial\mathsf{y}}\;.\tag{2.74}$$

Since $\bar{\mathsf{v}} = 0$, it reduces to $\frac{\partial\tilde{\tau}_{\mathsf{yx}}}{\partial\mathsf{y}} = 0$, with the total shear stress $\tilde{\tau}_{\mathsf{yx}}$ containing the viscose shear stress τ_{yx} and the Reynolds stress $\overline{\rho\mathsf{u}'\mathsf{v}'}$:

$$\tilde{\tau}_{\mathsf{yx}} = \tau_{\mathsf{yx}} - \rho\overline{\mathsf{u}'\mathsf{v}'}\;.\tag{2.75}$$

Combining (2.73) and (2.75), the wall shear stress can be derived by integration as

$$\tau_{\mathsf{w}} = \mu\frac{\partial\bar{\mathsf{u}}}{\partial\mathsf{y}} - \rho\overline{\mathsf{u}'\mathsf{v}'} \qquad \text{or} \qquad \frac{\tau_{\mathsf{w}}}{\rho} = \nu\frac{\partial\bar{\mathsf{u}}}{\partial\mathsf{y}} - \overline{\mathsf{u}'\mathsf{v}'}\tag{2.76}$$

respectively. The unit of the ratio τ_{w}/ρ is the square of velocity and therefore its square root is known as friction velocity

$$\mathsf{u}_\tau = \sqrt{\frac{\tau_{\mathsf{w}}}{\rho}}\;,\tag{2.77}$$

which quantifies the fluctuating velocity of the turbulent flow. By re-arranging (2.76) to

$$1 = \frac{d(\bar{u}/u_\tau)}{d(y\,u_\tau/\nu)} - \frac{\overline{u'v'}}{u_\tau^2} \tag{2.78}$$

the dependence

$$\frac{\bar{u}}{u_\tau} = f\left(y\frac{u_\tau}{\nu}\right) \tag{2.79}$$

and

$$\frac{\overline{u'v'}}{u_\tau^2} = g\left(y\frac{u_\tau}{\nu}\right) \tag{2.80}$$

can be identified. This universal law of the wall in (2.79) and (2.80) was discovered by Ludwig Prandtl (1925) and is valid for all turbulent flow conditions next to the wall which satisfy the above mentioned assumptions. Since the Reynolds stress disappears next to the wall the function f can be derived by a Taylor series expansion from (2.79)

$$\frac{\bar{u}(y^+)}{u_\tau} = y^+\left.\frac{d(\bar{u}/u_\tau)}{dy^+}\right|_{y=0} + (y^+)^2\frac{1}{2}\left.\frac{d^2(\bar{u}/u_\tau)}{(dy^+)^2}\right|_{y=0} + (y^+)^3\frac{1}{6}\left.\frac{d^3(\bar{u}/u_\tau)}{(dy^+)^3}\right|_{y=0} + \dots \;, \tag{2.81}$$

with $\bar{u}(0) = 0$ due to the non-slip condition. Here, y^+ is the dimensionless wall distance defined as

$$y^+ = y\frac{u_\tau}{\nu} \;. \tag{2.82}$$

Due to the vanishing fluctuation at the wall $\overline{u'v'}|_{y=0} = 0$, using (2.78), the first term on the right hand side in (2.81) can be written as:

$$\left.\frac{d(\bar{u}/u_\tau)}{dy^+}\right|_{y=0} = 1 \;. \tag{2.83}$$

Building the first and second derivatives of (2.78), the second and third terms in (2.81) become

$$\left.\frac{d^2(\bar{u}/u_\tau)}{(dy^+)^2}\right|_{y=0} = \frac{1}{u_\tau^2}\frac{d(\overline{u'v'})}{dy}\frac{dy}{dy^+} = \frac{1}{u_\tau^2}\frac{\nu}{u_\tau}\left[\overline{\frac{\partial u'}{\partial y}v'} + \overline{\frac{\partial v'}{\partial y}u'}\right]_{y=0} = 0 \tag{2.84}$$

and

$$\left.\frac{d^3(\bar{u}/u_\tau)}{(dy^+)^3}\right|_{y=0} = \frac{1}{u_\tau^2}\left(\frac{\nu}{u_\tau}\right)^2\left[\overline{\frac{\partial^2 u'}{\partial y^2}v'} + 2\overline{\frac{\partial u'}{\partial y}\frac{\partial v'}{\partial y}} + \overline{\frac{\partial^2 v'}{\partial y^2}u'}\right]_{y=0} = 0 \;. \tag{2.85}$$

These terms also disappear due to the vanishing fluctuating velocity perpendicular to the wall, hence

$$\frac{\bar{u}(y^+)}{u_\tau} = y^+ + O(y^+)^4 \;. \tag{2.86}$$

The influence of fluctuation on the velocity profile depends on the order of the fourth power of the dimensionless wall distance $O(y^+)^4$. In a thin layer next to the wall, the fluctuations do not disappear but the mean velocity is dominated by the viscose shear

stress. Therefore this thin layer is called viscose sublayer. Between the viscose sublayer and the zone with rising influence of the Reynolds stress the transition is smooth.

With a rising distance to the wall, the influence of the viscose stress decreases and the Reynolds stress dominates the velocity profile. For this region, (2.76) can be reduced to

$$\tau_\mathsf{w} = \tau_\mathsf{t} = -\rho(\mathsf{u}'\mathsf{v}') . \tag{2.87}$$

One approach for describing these fluctuations mathematically is provided by the formulation of Boussinesq

$$\tau_\mathsf{t} = -\rho(\mathsf{u}'\mathsf{v}') = \nu_\mathsf{t}\frac{\partial \bar{\mathsf{u}}}{\partial \mathsf{y}} , \tag{2.88}$$

with the eddy viscosity ν_t which e.g. can be set to a constant value. Since the Reynolds stress disappears next to a solid surface, this approach is inappropriate in cases with the influence of walls but can be used for flow conditions without the wall influence.

Another approach is provided by the Mixing Length Model developed by Ludwig Prandtl which considers the turbulent (wall) shear stress τ_t to be:

$$\tau_\mathsf{t} = -\rho(\mathsf{u}'\mathsf{v}') = \rho l^2 \left(\frac{d\bar{\mathsf{u}}}{d\mathsf{y}}\right)^2 \quad \text{or} \quad \tau_\mathsf{t} = \rho l^2 \left|\frac{d\bar{\mathsf{u}}}{d\mathsf{y}}\right|\frac{d\bar{\mathsf{u}}}{d\mathsf{y}} \tag{2.89}$$

respectively. With the mixing length l, the eddy viscosity $\nu_\mathsf{t} = \rho l^2 \left|\frac{d\bar{\mathsf{u}}}{d\mathsf{y}}\right|$ is defined depending on the velocity gradient next to the wall. Although this approach is not an exact solution, the mixing length model produces good results for many practical problems. Since the Reynolds stress has to disappear directly at the wall, the mixing length is chosen to be linear depending on the wall distance with

$$l = \kappa \mathsf{y} . \tag{2.90}$$

For a constant wall shear stress with $\tau_\mathsf{w} = \rho\mathsf{u}_\tau^2$, the mixing length model (2.89) can be written as

$$\mathsf{u}_\tau = \kappa\mathsf{y}\frac{d\bar{\mathsf{u}}}{d\mathsf{y}} . \tag{2.91}$$

By the integration of (2.91) the velocity profile of the logarithmic law of the wall outside the viscose sublayer is obtained:

$$\frac{\bar{\mathsf{u}}}{\mathsf{u}_\tau} = \frac{1}{\kappa}\ln(\mathsf{y}) + \mathsf{C} \tag{2.92}$$

where κ and C are empirical constants. A conversion using $\mathsf{C} = \mathsf{B} + (1/\kappa)\ln(\mathsf{u}_\tau/\nu)$ results in the non-dimensional equation:

$$\frac{\bar{\mathsf{u}}}{\mathsf{u}_\tau} = \frac{1}{\kappa}\ln\left(\mathsf{y}\frac{\mathsf{u}_\tau}{\nu}\right) + \mathsf{B} . \tag{2.93}$$

The constants have been experimentally evaluated and have values of $B = 5.5$ and $\kappa = 0.41$ [76, 80]. A more frequently used form of the logarithmic law of the wall, or the log-law is

$$u^+ = \frac{1}{\kappa}\, \ln(y^+) + B \ , \qquad\qquad (2.94)$$

with the dimensionless velocity $u^+ = \bar{u}/u_\tau$. This log-law is valid at a certain distance from the wall and for a developed explicit turbulent flow. On closer examination, there are three distinct layers next to the wall, which can be defined by the value of y^+ [7, 80]:

Viscous sublayer $0 \leq y^+ \leq 5$**:** There is a linear correlation between wall distance and velocity in the non-turbulent layer $u^+ = y^+$.

Buffer layer $5 \leq y^+ \leq 30$**:** The velocity profile changes with a smooth transition between the viscous sublayer and the logarithmic layer. Neither the linear correlation, nor the logarithmic law of the wall is valid in this layer.

Logarithmic layer $y^+ > 30$**:** A logarithmic correlation between wall distance and velocity can be assumed in this area for a fully developed turbulent flow. Depending on the referenced sources, the log-law is valid above different values of y^+, ranging from $y^+ > 26$ to $y^+ > 60$ [7, 48, 80].
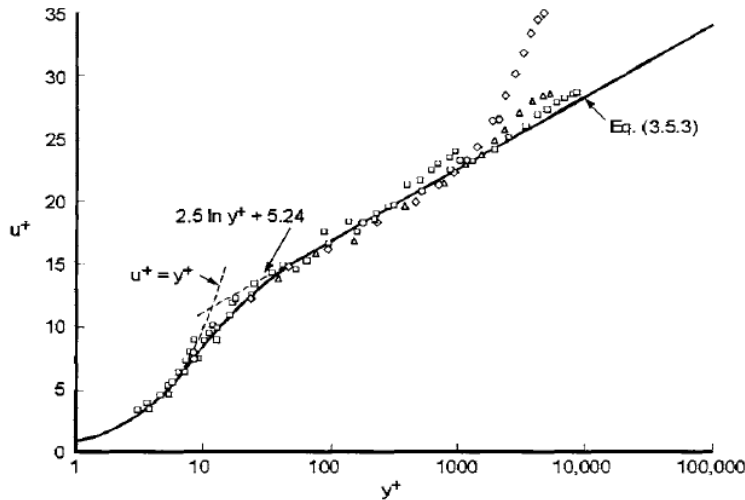

Figure 2.9: Logarithmic law of the wall [17]

2.4   Computational Fluid Dynamics

The Navier-Stokes equations (2.47) can be used for the analytical solution of basic problems under laminar flow conditions. Since the majority of flow problems in engineering are neither laminar nor do they involve simple shaped geometries, a numerical

approach is required. Computational fluid dynamics (CFD) is a general term for numerical calculations of fluid flow problems by dividing the calculation domain into small parts of finite size and basic geometry. With this discretization the conservation equations can be applied to the single finite volumes, which can be solved by different methods. Common methods for the numerical calculation are: the finite difference (FD) method and the finite volume (FV) method.

2.4.1 Discretization

The solution domain is discretized by a mesh whose nodes are used for the calculation and is thereby divided into a finite number of non overlapping control volumes.

The FD method solves the differential form of conservation equations with the node-values of the calculation mesh. This method is easy and effective to implement for structured meshes, and especially with methods of higher order. A major drawback of the FD method is its restriction to structured meshes and therefore to basic geometries. Since FD methods have not been used in this work, they are not described in detail.

Different implementations of the FV method use different strategies for defining the control volume center and hence the valid location of the calculated values. Using the
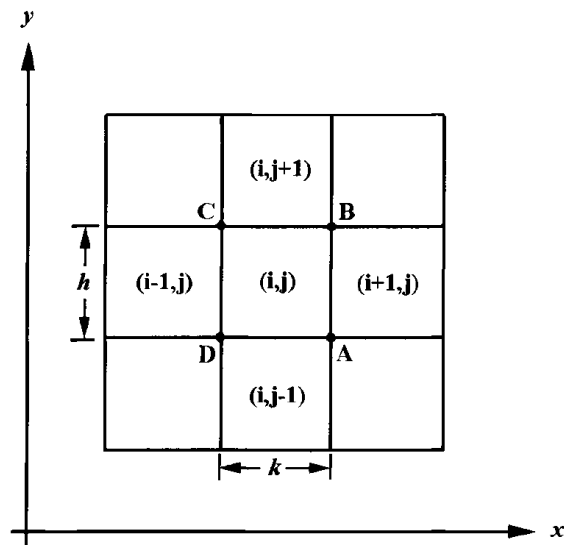

Figure 2.10: Two-dimensional structured finite volume mesh in the xy-plane [17]

mass center of the control volume, as shown in Fig. 2.10, is one way of implementation which is beneficial to the accuracy of the averaged volume values. Values for the faces of control volumes are interpolated between the mass centers of adjacent control volumes. Another implementation of the FV method is the median dual approach which defines the mesh nodes as centers of the control volumes. By using the edge centers and mesh volume centers as corners, an apparent control volume is built around the calculation node. Since the control volume faces are located on the edge center between the mesh

nodes, the interpolated values for faces are more accurate than the ones obtained with the mass center method [4, 22]. The following description, based on derivations in [2,17,23,24], is used for a structured mesh in a two-dimensional xy-plane with control volumes identified by the sequential numbers i and j for the position in the x and y directions, as shown in Fig. 2.10.

Basic CFD methods use the RANS equations introduced in Subsection 2.3.7 to calculate the fluxes of mass, momentum and energy. Due to the fluctuating and therefore time dependent flow parameters and the fine mesh resolution, the calculation of the Reynolds stresses with direct numerical simulation (DNS) is very time consuming, as briefly outlined in Subsection 2.4.3 on page 43. Since the results of time-averaged flow parameters are usually sufficient, it is more feasible to approximate the fluctuations by turbulence models and calculate the flow conditions by the Navier-Stokes equations replacing the molecular viscosity μ by the effective viscosity

$$\mu_{\text{eff}} = \mu + \mu_{\text{t}} \,. \tag{2.95}$$

The turbulent viscosity μ_{t}, on the other hand, can be calculated e.g. by the turbulence models described in Subsection 2.4.4 starting on page 43. With the modelled fluctuations, the calculation mesh for solving the Navier-Stokes equations can be much coarser than for a calculation with DNS reducing the computational effort for the solution.

For the following example, the external heat sources and the body forces $\mathbf{f}^{\text{B}}$ have been neglected, since buoyant or gravity forces have not been assumed. Therefore, the equations for the conservation of momentum (2.41) for two spatial dimensions can be simplified to

$$
\begin{aligned}
\frac{\partial(\rho \mathsf{u})}{\partial \mathsf{t}} + \frac{\partial(\rho \mathsf{u}^2)}{\partial \mathsf{x}} + \frac{\partial(\rho \mathsf{u}\mathsf{v})}{\partial \mathsf{y}} &= -\frac{\partial \mathsf{p}}{\partial \mathsf{x}} + \frac{\partial \tau_{\mathsf{xx}}}{\partial \mathsf{x}} + \frac{\partial \tau_{\mathsf{yx}}}{\partial \mathsf{y}} \\
\frac{\partial(\rho \mathsf{v})}{\partial \mathsf{t}} + \frac{\partial(\rho \mathsf{v}\mathsf{u})}{\partial \mathsf{x}} + \frac{\partial(\rho \mathsf{v}^2)}{\partial \mathsf{y}} &= -\frac{\partial \mathsf{p}}{\partial \mathsf{y}} + \frac{\partial \tau_{\mathsf{xy}}}{\partial \mathsf{x}} + \frac{\partial \tau_{\mathsf{yy}}}{\partial \mathsf{y}} \,.
\end{aligned}
\tag{2.96}
$$

For the same conditions, the conservation of mass in (2.28) can be written as

$$\frac{\partial \rho}{\partial \mathsf{t}} + \frac{\partial(\rho \mathsf{u})}{\partial \mathsf{x}} + \frac{\partial(\rho \mathsf{v})}{\partial \mathsf{y}} = 0 \,. \tag{2.97}$$

The conservation of energy in (2.42) without the body forces and the energy transport over the system boundaries can be written for two spatial dimensions as

$$\frac{\partial \mathsf{E}_{\mathsf{t}}}{\partial \mathsf{t}} + \frac{\partial(\mathsf{u}\mathsf{E}_{\mathsf{t}})}{\partial \mathsf{x}} + \frac{\partial(\mathsf{v}\mathsf{E}_{\mathsf{t}})}{\partial \mathsf{y}} = -\frac{\partial(\mathsf{p}\mathsf{u})}{\partial \mathsf{x}} - \frac{\partial(\mathsf{p}\mathsf{v})}{\partial \mathsf{y}} + \frac{\partial}{\partial \mathsf{x}}(\mathsf{u}\tau_{\mathsf{xx}} + \mathsf{v}\tau_{\mathsf{xy}}) + \frac{\partial}{\partial \mathsf{y}}(\mathsf{u}\tau_{\mathsf{yx}} + \mathsf{v}\tau_{\mathsf{yy}}) + \dot{\mathsf{q}}_{\mathsf{Q}} \,. \tag{2.98}$$

The heat flux in (2.98) written in index notation is generally defined as

$$\dot{\mathsf{q}}_{\mathsf{Q}} = -\lambda \frac{\partial \mathsf{T}}{\partial \mathsf{x}_{\mathsf{i}}} + \mathsf{c}_{\mathsf{p}} \overline{\rho \mathsf{T}' \mathsf{u}'_{\mathsf{i}}} \,, \tag{2.99}$$

and

$$-c_p \overline{\rho T' u_i'} = \lambda_t \frac{\partial T}{\partial x_i} \tag{2.100}$$

with the turbulent conductivity λ_t. The turbulent conductivity is defined with the turbulent Prandtl number $Pr_t = 0.9$ as

$$\lambda_t = \frac{c_p \mu_t}{Pr_t} \ . \tag{2.101}$$

For two dimensional flow, the vector components of $\dot{q}_Q$ are defined as

$$\dot{q}_{Qx} = -\left(\lambda + \frac{c_p \mu_t}{Pr_t}\right) \frac{\partial T}{\partial x}$$
$$\dot{q}_{Qy} = -\left(\lambda + \frac{c_p \mu_t}{Pr_t}\right) \frac{\partial T}{\partial y} \ . \tag{2.102}$$

The shear stresses in (2.96) written in index notation are generally defined as

$$\tau_{ij} = \mu \left(\frac{\partial u_i}{\partial x_j} + \frac{\partial u_j}{\partial x_i} - \frac{2}{3} \delta_{ij} + \frac{\partial u_k}{\partial x_k} \right) - \overline{\rho(u_i'' u_j'')} \tag{2.103}$$

and

$$-\overline{\rho(u_i'' u_j'')} = \mu_t \left(\frac{\partial u_i}{\partial x_j} + \frac{\partial u_j}{\partial x_i} - \frac{2}{3} \delta_{ij} + \frac{\partial u_k}{\partial x_k} \right) - \frac{2}{3} \delta_{ij} k \ , \tag{2.104}$$

with the turbulent kinetic energy k as defined in (2.53). Hence, for the flow calculation in two dimensional domain the shear stresses are defined as

$$\begin{aligned}
\tau_{xx} &= \mu_{eff} \frac{\partial u}{\partial x} - \mu_{eff} \frac{2}{3} \left(\frac{\partial u}{\partial x} + \frac{\partial v}{\partial y} \right) - \frac{2}{3} \rho k \\
\tau_{yy} &= \mu_{eff} \frac{\partial v}{\partial y} - \mu_{eff} \frac{2}{3} \left(\frac{\partial u}{\partial x} + \frac{\partial v}{\partial y} \right) - \frac{2}{3} \rho k \\
\tau_{xy} &= \mu_{eff} \left(\frac{\partial u}{\partial y} + \frac{\partial v}{\partial x} \right) \ .
\end{aligned} \tag{2.105}$$

Since the equations (2.96), (2.97) and (2.98) have an identical structure, they can be

written in vector notation with the flux vectors:

$$\mathbf{Q} = \begin{pmatrix} \rho \\ \rho u \\ \rho v \\ E_t \end{pmatrix} \quad ,$$

$$\mathbf{E} = \begin{pmatrix} \rho u \\ \rho u^2 + p - \tau_{xx} \\ \rho uv - \tau_{xy} \\ (E_t + p - \tau_{xx})u - \tau_{xy}v + \dot{q}_{Qx} \end{pmatrix} \quad ,$$

$$\mathbf{F} = \begin{pmatrix} \rho v \\ \rho uv - \tau_{xy} \\ \rho v^2 + p - \tau_{yy} \\ (E_t + p - \tau_{yy})v - \tau_{xy}u + \dot{q}_{Qy} \end{pmatrix} \quad , \tag{2.106}$$

with the velocities u and v, the total energy E_t and the hydrostatic pressure

$$p = (\gamma - 1)[E_t - 0.5\rho(u^2 + v^2)] . \tag{2.107}$$

Hence, the Navier-Stokes equations in the two dimensional Cartesian coordinate system without external heat or the body forces are in vector notation:

$$\frac{\partial \mathbf{Q}}{\partial t} + \frac{\partial \mathbf{E}}{\partial x} + \frac{\partial \mathbf{F}}{\partial y} = 0 . \tag{2.108}$$

The finite volume method is based on the subdomain method, a special weighted residual method [23]. For three spatial dimensions, the general formulation of the weighted residual methods is

$$\iiint W_m(x, y, z) \, R_{WRM} \, dx \, dy \, dz = 0 \tag{2.109}$$

where W_m is a test function and R_{WRM} the residual. In the subdomain method, the test function is defined as $W_m = 1$ inside the subdomain and $W_m = 0$ outside the subdomain. For equations like the continuity equation (2.97) with first derivatives only, the subdomain method can be written for two spatial dimensions as

$$\iint_{ABCD} 1 \left(\frac{\partial \rho}{\partial t} + \frac{\partial(\rho u)}{\partial x} + \frac{\partial(\rho v)}{\partial y} \right) dx \, dy = 0 . \tag{2.110}$$

By applying Green's theorem, the double integral over the subdomain can be replaced by line integrals:

$$\frac{\partial}{\partial t} \int \rho \, dV + \int_A^B (\rho u) dy - \int_C^D (\rho u) dy + \int_B^C (\rho v) dx - \int_D^A (\rho u) dy = 0 . \tag{2.111}$$

As illustrated in Fig. 2.10, the line integrals in (2.111) can be replaced by the sum of the specific mass fluxes over the elements boundaries, with $h = \mathsf{y_B} - \mathsf{y_A} = \mathsf{y_C} - \mathsf{y_D}$ and $k = \mathsf{x_A} - \mathsf{x_D} = \mathsf{x_B} - \mathsf{x_C}$ [23]:

$$\frac{\partial}{\partial \mathsf{t}}(hk\,\rho_{\mathsf{ij}}) + \sum_{\mathsf{AB}}^{\mathsf{DA}}[(\rho\mathsf{u})h - (\rho\mathsf{v})k] = 0 \ . \tag{2.112}$$

Since the volume hk is independent of time, (2.112) can be divided by hk and the discretized conservation of mass can be written as

$$\frac{\partial \rho_{\mathsf{ij}}}{\partial \mathsf{t}} + \frac{(\rho\mathsf{u})_{\mathsf{AB}} - (\rho\mathsf{u})_{\mathsf{CD}}}{k} + \frac{(\rho\mathsf{v})_{\mathsf{BC}} - (\rho\mathsf{v})_{\mathsf{DA}}}{h} = 0 \ , \tag{2.113}$$

with the flux components $(\rho\mathsf{u})_{\mathsf{AB}}$, $(\rho\mathsf{v})_{\mathsf{BC}}$, $(\rho\mathsf{u})_{\mathsf{CD}}$ and $(\rho\mathsf{v})_{\mathsf{DA}}$. Different finite volume methods can be distinguished by the way of evaluation of the flux terms. An overview of different finite volume methods and methods of flux term calculation can be found i.a. [43] or [44]. One basic method of evaluation is by averaging the fluxes as

$$(\rho\mathsf{u})_{\mathsf{AB}} = \frac{1}{2}[(\rho\mathsf{u})_{\mathsf{i}+1,\mathsf{j}} + (\rho\mathsf{u})_{\mathsf{i},\mathsf{j}}] \qquad \text{and} \qquad (\rho\mathsf{u})_{\mathsf{CD}} = \frac{1}{2}[(\rho\mathsf{u})_{\mathsf{i},\mathsf{j}} + (\rho\mathsf{u})_{\mathsf{i}-1,\mathsf{j}}] \tag{2.114}$$

in x direction and

$$(\rho\mathsf{u})_{\mathsf{BC}} = \frac{1}{2}[(\rho\mathsf{v})_{\mathsf{i},\mathsf{j}+1} + (\rho\mathsf{v})_{\mathsf{i},\mathsf{j}}] \qquad \text{and} \qquad (\rho\mathsf{u})_{\mathsf{DA}} = \frac{1}{2}[(\rho\mathsf{v})_{\mathsf{i},\mathsf{j}} + (\rho\mathsf{v})_{\mathsf{i},\mathsf{j}-1}] \tag{2.115}$$

in y direction. Applying the average fluxes to (2.113), the discretized form of the conservation of mass is

$$\frac{\partial \rho_{\mathsf{ij}}}{\partial \mathsf{t}} + \frac{(\rho\mathsf{u})_{\mathsf{i}+1,\mathsf{j}} - (\rho\mathsf{u})_{\mathsf{i}-1,\mathsf{j}}}{2k} + \frac{(\rho\mathsf{v})_{\mathsf{i},\mathsf{j}+1} - (\rho\mathsf{v})_{\mathsf{i},\mathsf{j}-1}}{2h} = 0 \ . \tag{2.116}$$

The system of equations (2.108) can be solved e.g. implicitly with the Beam and Warming scheme. To implement this scheme to the compressible viscose Navier-Stokes equations, (2.108) changes to

$$\frac{\partial \mathbf{Q}}{\partial \mathsf{t}} = \mathbf{RHS} \ , \tag{2.117}$$

with the spatial derivatives at the right hand side

$$\mathbf{RHS} = -\frac{\partial \mathbf{E}}{\partial \mathsf{x}} - \frac{\partial \mathbf{F}}{\partial \mathsf{y}} = \quad - \quad \frac{\partial}{\partial \mathsf{x}}\left(\mathbf{E}^{\mathsf{i}} - \mathbf{E}_1^{\mathsf{v}}(\mathbf{Q}, \mathbf{Q_x}) - \mathbf{E}_2^{\mathsf{v}}(\mathbf{Q}, \mathbf{Q_y})\right)$$
$$- \quad \frac{\partial}{\partial \mathsf{y}}\left(\mathbf{F}^{\mathsf{i}} - \mathbf{F}_1^{\mathsf{v}}(\mathbf{Q}, \mathbf{Q_x}) - \mathbf{F}_2^{\mathsf{v}}(\mathbf{Q}, \mathbf{Q_y})\right) \ . \tag{2.118}$$

The flux terms in (2.118) are separated into the inviscid fluxes $\mathbf{E}^{\mathsf{i}}$ and $\mathbf{F}^{\mathsf{i}}$ and the viscose therms $\mathbf{E}_1^{\mathsf{v}}$, $\mathbf{F}_1^{\mathsf{v}}$, $\mathbf{E}_2^{\mathsf{v}}$ and $\mathbf{F}_2^{\mathsf{v}}$ by applying (2.105) and (2.102) to (2.106). Therefore, the

flux vectors in (2.106) can be written as

$$
\mathbf{Q} = \begin{pmatrix} \rho \\ \rho u \\ \rho v \\ E_t \end{pmatrix}, \ \mathbf{E}(\mathbf{Q}) = \begin{pmatrix} \rho u \\ \rho u^2 + p \\ \rho uv \\ (E_t + p)u \end{pmatrix}, \ \mathbf{F}(\mathbf{Q}) = \begin{pmatrix} \rho v \\ \rho uv \\ \rho v^2 + p \\ (E_t + p)v \end{pmatrix},
$$

$$
\mathbf{E}_1^v + \mathbf{E}_2^v = \begin{pmatrix} 0 \\ \frac{2}{3}\mu_{\text{eff}}(2u_x - v_y) \\ \mu_{\text{eff}}(u_y + v_x) \\ \mu_{\text{eff}}v(u_y + v_x) + \frac{2}{3}\mu_{\text{eff}}u(2u_x - v_y) + \lambda_t T_x \end{pmatrix},
$$

$$
\mathbf{F}_1^v + \mathbf{F}_2^v = \begin{pmatrix} 0 \\ \mu_{\text{eff}}(u_y + v_x) \\ \frac{2}{3}\mu_{\text{eff}}(2v_y - u_x) \\ \mu_{\text{eff}}u(u_y + v_x) + \frac{2}{3}\mu_{\text{eff}}v(2v_y - u_x) + \lambda_t T_y \end{pmatrix} \quad (2.119)
$$

where the subscripts x, y next to the velocities u, v and the temperature T indicate a derivative with respect to x or y, respectively [83]. The derivatives with respect to the direction x are grouped in $\mathbf{E}_1^v$ and $\mathbf{F}_1^v$ and the derivatives with respect to the direction y are grouped in $\mathbf{E}_2^v$ and $\mathbf{F}_2^v$, respectively [24]. For transient problems, the Beam-Warming scheme uses the following general difference formula for the calculation of the time steps

$$
(1 + \Theta_2)\Delta\mathbf{Q}^n - \Theta_2\Delta\mathbf{Q}^n = \Delta t(\Theta_1\mathbf{RHS}^{n+1} + (1 - \Theta_1)\mathbf{RHS}^n), \quad (2.120)
$$

with $\Delta\mathbf{Q}^{n+1} = \mathbf{Q}^{n+1} - \mathbf{Q}^n$ and $\Delta\mathbf{Q}^n = \mathbf{Q}^n - \mathbf{Q}^{n-1}$ at the time-step n. With the parameters Θ_1 and Θ_2, the stability and accuracy of the difference scheme can be modified [24]. Using the values $\Theta_1 = 1$ and $\Theta_2 = 0$, the compressible Navier-Stokes equations are solved with the Euler implicit scheme, first-order accurate in time. A three-point backward implicit scheme can be applied with $\Theta_1 = 1$ and $\Theta_2 = 0.5$ which is second-order accurate in time [83]. One time-step increment of the right hand side is

$$
\mathbf{RHS}^{n+1} = \mathbf{RHS}^n \ - \ \frac{\partial}{\partial x}(\mathbf{A}\Delta\mathbf{Q}^{n+1} - \mathbf{P}\Delta\mathbf{Q}^{n+1} - \mathbf{R}\Delta\mathbf{Q}_x^{n+1} - \Delta\mathbf{E}_2^{v,n+1})
$$
$$
- \ \frac{\partial}{\partial y}(\mathbf{B}\Delta\mathbf{Q}^{n+1} - \mathbf{T}\Delta\mathbf{Q}^{n+1} - \mathbf{S}\Delta\mathbf{Q}_y^{n+1} - \Delta\mathbf{F}_2^{v,n+1}), (2.121)
$$

with the inviscid Jacobian matrices $\mathbf{A}$ and $\mathbf{B}$ and the derivatives

$$
\mathbf{P} = \frac{\partial\mathbf{E}_1^v}{\partial\mathbf{Q}}, \ \mathbf{T} = \frac{\partial\mathbf{F}_2^v}{\partial\mathbf{Q}}, \ \mathbf{R} = \frac{\partial\mathbf{E}_1^v}{\partial\mathbf{Q}_x}, \ \mathbf{S} = \frac{\partial\mathbf{F}_2^v}{\partial\mathbf{Q}_y}. \quad (2.122)
$$

The right hand side (2.118) can be simplified by introducing

$$
\mathbf{R}\Delta\mathbf{Q}_x^{n+1} = (\mathbf{R}\Delta\mathbf{Q}^{n+1})_x - \mathbf{R}_x\Delta\mathbf{Q}^{n+1}
$$
$$
\mathbf{S}\Delta\mathbf{Q}_y^{n+1} = (\mathbf{S}\Delta\mathbf{Q}^{n+1})_y - \mathbf{S}_y\Delta\mathbf{Q}^{n+1}. \quad (2.123)
$$

The cross-derivatives

$$\Delta \mathbf{E}_2^{v,n+1} = \Delta \mathbf{E}_2^{v,n} + O(\Delta t^2) \qquad \text{and} \qquad \Delta \mathbf{F}_1^{v,n+1} = \Delta \mathbf{F}_1^{v,n} + O(\Delta t^2) \qquad (2.124)$$

can be replaced by the values from the previous time-step with second order accuracy [24]. By introducing (2.121) and (2.124) in (2.120), the system of equations can be written as

$$
\begin{aligned}
\Delta \mathbf{Q}^{n+1} = \Bigg[\mathbf{I} \quad &+ \quad \frac{\Theta_1 \Delta t}{1 + \Theta_2} \left(\frac{\partial}{\partial x} (\mathbf{A} - \mathbf{P} + \mathbf{R}_x)^n - \frac{\partial^2}{\partial x^2} \mathbf{R}^n \right) \\
&+ \quad \frac{\Theta_1 \Delta t}{1 + \Theta_2} \left(\frac{\partial}{\partial y} (\mathbf{B} - \mathbf{T} + \mathbf{S}_y)^n - \frac{\partial^2}{\partial y^2} \mathbf{S}^n \right) \Bigg] \Delta \mathbf{Q}^{n+1} \\
&= \quad \frac{\Delta t\, \mathbf{RHS}^n}{1 + \Theta_2} + \frac{1 + \Theta_2}{\Theta_2} \Delta \mathbf{Q}^n + \frac{\Theta_1' \Delta t}{1 + \Theta_2} \left(\frac{\partial}{\partial x} \Delta \mathbf{E}_2^{v,n} + \frac{\partial}{\partial y} \Delta \mathbf{F}_1^{v,n} \right) \\
&= \quad \Delta \mathbf{Q}^m \,,
\end{aligned}
\qquad (2.125)
$$

with the identity matrix $\mathbf{I}$. For transient problems the constant Θ_1' is equal to Θ_1. Finally, the algorithm of the Beam-Warming scheme is

$$\left\{ \mathbf{I} + \frac{\Theta_1 \Delta t}{1 + \Theta_2} \left(L_x (\mathbf{A} - \mathbf{P} + \mathbf{R}_x)^n - L_x^2 (\mathbf{R})^n \right) \right\} \Delta \mathbf{Q}^* = \Delta \mathbf{Q}^m \,, \qquad (2.126)$$

with

$$\left\{ \mathbf{I} + \frac{\Theta_1 \Delta t}{1 + \Theta_2} \left(L_y (\mathbf{B} - \mathbf{T} + \mathbf{S}_y)^n - L_y^2 (\mathbf{S})^n \right) \right\} \Delta \mathbf{Q}^{n+1} = \Delta \mathbf{Q}^* \,. \qquad (2.127)$$

In (2.126) and (2.127) $\ldots L_x^2(\mathbf{R})^n\}\Delta \mathbf{Q}^*$ implies $\ldots L_x^2(\mathbf{R}\Delta \mathbf{Q}^*)$ and L_x, L_x^2, L_y and L_y^2 are the first and second order three point central differences for the directions x and y, respectively [24].

Due to the central difference discretization, oscillations may occur at locations with discontinuities which can be avoided with an additional dissipation term (damping) to the Beam-Warming scheme:

$$\left\{ \mathbf{I} + \frac{\Theta_1 \Delta t}{1 + \Theta_2} \left(L_x (\mathbf{A} - \mathbf{P} + \mathbf{R}_x)^n - L_x^2 (\mathbf{R})^n - \epsilon_i L_x^2 \right) \right\} \Delta \mathbf{Q}^* = \Delta \mathbf{Q}^m - \epsilon_e (L_x^4 + L_y^4) \mathbf{Q}^n$$

$$(2.128)$$

$$\left\{ \mathbf{I} + \frac{\Theta_1 \Delta t}{1 + \Theta_2} \left(L_y (\mathbf{B} - \mathbf{T} + \mathbf{S}_y)^n - L_y^2 (\mathbf{S})^n - \epsilon_i L_y^2 \right) \right\} \Delta \mathbf{Q}^{n+1} = \Delta \mathbf{Q}^* \,, \qquad (2.129)$$

with

$$0 \le \epsilon_e \le \frac{1 + 2\Theta_2}{8(1 + \Theta_2)} \qquad \text{and} \qquad \frac{\epsilon_e}{\epsilon_i} = 2 \,. \qquad (2.130)$$

A steady-state solution can be achieved with the pseudo-transient method. The idea of the pseudo-transient method is the solution of an equivalent transient problem, solved until the solution reaches a steady-state and the time-steps can be considered

as iteration steps. For the steady-state, the terms $-\mathbf{P} + \mathbf{R}_x$ and $-\mathbf{T} + \mathbf{S}_y$ can be ignored, since the influence of μ and λ on $\mathbf{Q}$ can be neglected. Additionally to this simplification, the solution of the pseudo-transient formulation with the first order accurate Euler implicit scheme is more efficient [24, 83].

Due to the conservative formulation of the FV method, numerical problems are avoided at discontinuous positions e.g. at shock waves. Therefore, the FV method is beneficial for the calculation of problems in fluid dynamics [17, 22]. Since the structure of the momentum equations (2.96) is similar to the structure of the transport equation of turbulence, as shown in (2.137) and (2.142) on page 45, its discretization can be applied in the same way.

2.4.2   Modeling turbulent flow

Most technically relevant flow conditions are turbulent. Since turbulent flow cannot be treated like laminar or inviscid flow, different methods of calculation are required.

A turbulent flow is characterized by a clearly transient behavior of the fluid in microscopic length scales. The chaotic fluctuation of fluid occurs in all three spatial dimensions. Only a mean flow can be represented in two dimension for particular cases. Fluid flow requires permanent charge of power to maintain the movement of the fluids. This automatically causes turbulence under all flow conditions except for laminar flows. The energy type of moving fluid particles is kinetic energy which is converted irreversibly into heat energy by dissipation. Turbulence can be regarded as a permanent process of producing and collapsing eddies in a wide-band length scale which has to be calculated for accurate simulation of fluid flow. [22]

A variety of turbulence models are available today, each having strengths for specific applications. Tab. 2.5 shows some of the commonly available models grouped by the method of modeling turbulence. In this work, only the models which have been used

RANS Eddy-viscosity Models	RANS Reynolds-Stress Models	Eddy Simulation Models (transient)
- Zero Equation model	- LRR Reynolds Stress	- Large Eddy Simulation
- Standard k-ε model	- QI Reynolds Stress	(LES)
- RNG k-ε model	- Special, Sarkar and Gatski	- Detached Eddy Simulation
- Standard k-ω model	Reynolds Stress	(DES)
- Baseline (BSL) zonal	- SMC-ω model	- Scale Adaptive Simulation
k-ω model	- Baseline (BSL) Reynolds'	SST (SAS)
- SST zonal k-ω model	Stress model	
- k-ε model		

Table 2.5: Commonly used turbulence models [4]

during the simulations are explained in detail. The relevant turbulence model is the SST models. This model is based on the popular k-ε and k-ω turbulence models, which also deserve an explanation.

2.4.3 Direct numerical simulation

As outlined in Tab. 2.5, the turbulence models can be categorized in accordance with their ways of resolving turbulent effects. The direct numerical simulation (DNS) is not mentioned in this context. Since this method does not model but resolve turbulence, it is the most expensive simulation method. DNS performs direct calculation without models or averaging and therefore it is numerically the simplest method. The whole flow domain is discretized by a very fine mesh, resolving eddies until they collapse due to shear stress caused by molecular viscosity. The simulation domain must be at least the size of the physical domain or the size of the largest occurring eddy. Due to the absence of a turbulence model, this method must calculate the dissipation of kinetic energy of particle fluctuation. The mesh resolution where dynamic (molecular) viscosity is dominating is defined by the Kolmogorov length scale η, which can be expressed by:

$$\eta = \left(\frac{\nu^3}{\varepsilon}\right)^{1/4} , \tag{2.131}$$

with kinematic viscosity ν and turbulent dissipation rate ε. In the case of air in a technically relevant flow condition, a finite volume size of some micrometers would be required to adequately discretize the flow domain. Even for simple problems, the number of finite volumes and therefore the number of numerical operations would rise dramatically. With a smaller length scale, the time scale would also decrease, requiring a higher number of time steps. These requirements demand high calculation power over a long period of time making DNS uneconomical for engineering purposes. The implementation of steady state methods or two-dimensional simulation is not possible in DNS. Nevertheless, this simulation method is the most accurate method of numeric simulation and is therefore used for solving academic problems. Due to the improvements in computational technology, in the future this method might also become relevant for engineering purposes [22].

2.4.4 RANS models

Surface averaged values are sufficient for most engineering purposes. Detailed information about the flow regime is not necessary if the target values are of acceptable accuracy. In order to reduce calculation costs, the application of turbulence models does make sense. Many popular turbulence models are based on the Reynolds Averaged Navier-Stokes equations, as introduced in Subsection 2.3.7. RANS eddy viscosity models use the idea of Osborne Reynolds by separating flow into an average flow component and a fluctuating component, as shown in (2.48). All unsteady parts can be removed by modeling the fluctuating components, including other transient aspects of the fluid flow. Hence, a steady state simulation is possible if the type of flow is physically in a steady state.

For an incompressible fluid, the conservation of mass (2.30) can be expressed by

the index notation as:

$$\frac{\partial(\rho\overline{u}_i)}{\partial x_i} = 0 \tag{2.132}$$

and the momentum in (2.62) with neglected body forces as

$$\frac{\partial(\rho\overline{u}_i)}{\partial t} + \frac{\partial}{\partial x_j}\left(\rho\overline{u}_i\overline{u}_j + \rho\overline{u_i'u_j'}\right) = -\frac{\partial\overline{p}}{\partial x_i} + \frac{\partial\overline{\tau}_{ij}}{\partial x_j}\ , \tag{2.133}$$

for Cartesian coordinates with the shear stress tensor $\overline{\tau}_{ij} = \mu\left(\frac{\partial\overline{u}_i}{\partial x_j} + \frac{\partial\overline{u}_j}{\partial x_i}\right)$, shown in (2.27) and (2.38), respectively. A mean scalar value $\overline{\phi}$ can be calculated for the flow regime by

$$\frac{\partial(\rho\overline{\phi})}{\partial t} + \frac{\partial}{\partial x_j}\left(\rho\overline{u}_j\overline{\phi} + \rho\overline{u_j'\phi'}\right) = \frac{\partial}{\partial x_j}\left(\Gamma\frac{\partial\overline{\phi}}{\partial x_j}\right)\ , \tag{2.134}$$

with the diffusivity Γ. Since these equations contain the Reynolds shear stress $\rho\overline{u_i'u_j'}$, the system of equations still has too many unknowns for a solution, which is also known as the closure problem of RANS equations. This closure problem can either be solved by approximation with empirical parameters, or by calculating the Reynolds stress tensor with correlation of higher order, again using approximation models. Since it seems impossible to find an exact solution of this closure problem, the introduction of turbulence models is unavoidable. Commonly applied turbulence models use the eddy viscosity ν_t (or turbulent viscosity μ_t respectively) for deriving the Reynolds stress tensor, as shown in (2.52). It is assumed that the turbulent transport of mass, momentum and energy is controlled by the turbulent viscosity μ_t in the same way as laminar flow is controlled by the dynamic viscosity μ in the Navier-Stokes equations (2.47). Due to this assumption the Reynolds stress can be written as

$$-\rho\overline{u_i'u_j'} = \mu_t\left(\frac{\partial\overline{u}_i}{\partial x_j} + \frac{\partial\overline{u}_j}{\partial x_i}\right) - \frac{2}{3}\rho\delta_{ij}k\ . \tag{2.135}$$

with the turbulent viscosity μ_t, the Kronecker symbol δ_{ij} and the turbulence kinetic energy k as shown in (2.53). The scalar values ϕ are derived likewise with the Reynolds flux

$$-\rho\overline{u_i'\phi'} = \Gamma_t\frac{\partial\overline{\phi}}{\partial x_j}\ . \tag{2.136}$$

with eddy diffusivity $\Gamma_t = \mu_t/Pr_t$ which is defined by the turbulent viscosity and the turbulent Prandtl number Pr_t [4, 22].

k-ε turbulence model

A basic definition of turbulence requires at least two dimensions for its characterization, namely the turbulence kinetic energy k (or dimension of velocity) and a dimension of length L. These parameters are related to each other via the dimensionless constant

C_μ. In most turbulence models, the dimension of velocity is defined by the turbulence kinetic energy k which can be derived from the momentum equation:

$$\frac{\partial(\rho k)}{\partial t} + \frac{\partial(\rho \bar{u}_j k)}{\partial x_j} = \frac{\partial}{\partial x_j}\left(\mu \frac{\partial k}{\partial x_j}\right) - \frac{\partial}{\partial x_j}\left(\frac{\rho}{2}\overline{u_j' u_i' u_i'} + \overline{p' u_j'}\right) - \rho\overline{u_i' u_j'}\frac{\partial(\bar{u}_i)}{\partial x_j} - \mu\overline{\frac{\partial u_i'}{\partial x_k}\frac{\partial u_i'}{\partial x_k}} \ .$$

(2.137)

The terms on the left-hand side and the first term on the right-hand side can be calculated directly. Turbulent diffusion is the second term on the right hand-side and describes the transport of turbulence kinetic energy. It has to be modeled and in most cases this is accomplished by gradient induced diffusion:

$$-\left(\frac{\rho}{2}\overline{u_j' u_i' u_i'} + \overline{p' u_j'}\right) \approx \frac{\mu_t}{\sigma_k}\frac{\partial k}{\partial x_j} \ ,$$

(2.138)

with the turbulent viscosity μ_t and the turbulent Prandtl number σ_k of the k-ε model which is a model constant. The third term on the right-hand side in (2.137) is the production rate of turbulent kinetic energy. If the approach of eddy viscosity (2.135) is used for calculating the Reynolds stress tensor, the production term can be approximated by:

$$P_k = -\rho\overline{u_i' u_j'}\frac{\partial(\bar{u}_i)}{\partial x_j} \approx \mu_t\left(\frac{\bar{u}_i}{\partial x_j} + \frac{\bar{u}_j}{\partial x_i}\right)\frac{\bar{u}_i}{\partial x_j}$$

(2.139)

which can be calculated without any further approximations. The last term in (2.137) represents the isotropic dissipation rate ε, as shown in (2.49), which finally leads to the frequently implemented form of the k equation:

$$\frac{\partial(\rho k)}{\partial t} + \nabla\left(\rho u_j k\right) = \nabla\left[\left(\mu + \frac{\mu_t}{\sigma_k}\right)\nabla k\right] + P_k - \rho\varepsilon \ .$$

(2.140)

As mentioned previously, a dimension of length is required for definition of turbulence. The idea of a turbulent equilibrium of production and dissipation and the fact that dissipation participates in the energy equation lead to the following widespread approach of the length scale L:

$$\varepsilon \approx \frac{k^{3/2}}{L} \ .$$

(2.141)

The turbulence dissipation rate can be obtained from the Navier-Stokes equations by modeling the whole right-hand side, but it is more useful to consider the whole equation as a model, which is defined for most k-ε models with:

$$\frac{\partial(\rho\varepsilon)}{\partial t} + \frac{\partial(\rho u_j \varepsilon)}{\partial x_j} = C_{\varepsilon 1} P_k \frac{\varepsilon}{k} - \rho C_{\varepsilon 2}\frac{\varepsilon^2}{k} + \frac{\partial}{\partial x_j}\left(\frac{\mu_t}{\sigma_\varepsilon}\frac{\partial\varepsilon}{\partial x_j}\right) \ .$$

(2.142)

The turbulent viscosity is defined in this model as:

$$\mu_t = \rho C_\mu \sqrt{k}L = \rho C_\mu \frac{k^2}{\varepsilon} \ .$$

(2.143)

The constant values in the equations above are:

$$\mathsf{C}_\mu = 0.09 \ , \quad \mathsf{C}_{\varepsilon 1} = 1.44 \ , \quad \mathsf{C}_{\varepsilon 1} = 1.92 \ , \quad \sigma_\mathsf{k} = 1 \ , \quad \sigma_\varepsilon = 1.3 \ . \tag{2.144}$$

The whole system of equations can be solved by replacing the dynamic viscosity μ with the effective viscosity $\mu_\mathsf{eff} = \mu + \mu_\mathsf{t}$ in the RANS equations [22].

Based on equations (2.137) and (2.146) this turbulence model is denoted as the k-ε model. It is used in a wide band of applications and may be adjusted with minor changes, such as the addition of a term for consideration of the buoyant forces P_kb and $\mathsf{P}_{\varepsilon \mathsf{b}}$

k-ω turbulence model

The k-ω model introduces a second transport equation in addition to the k equation, which includes the turbulence frequency ω. The calculation of the kinetic energy is appropriate to the k equation in the k-ε model above with:

$$\frac{\partial \rho \mathsf{k}}{\partial \mathsf{t}} + \nabla \left(\rho \mathbf{v} \mathsf{k} \right) = \nabla \left[\left(\mu + \frac{\mu_\mathsf{t}}{\sigma_\mathsf{k}} \right) \nabla \mathsf{k} \right] + \mathsf{P}_\mathsf{k} - \beta^* \rho \mathsf{k} \ . \tag{2.145}$$

Instead of dissipation, the k-ω model uses the transport of turbulent frequency ω:

$$\frac{\partial \rho \omega}{\partial \mathsf{t}} + \nabla \left(\rho \mathbf{v} \omega \right) = \nabla \left[\left(\mu + \frac{\mu_\mathsf{t}}{\sigma_\omega} \right) \nabla \omega \right] + \alpha \frac{\omega}{\mathsf{k}} \mathsf{P}_\mathsf{k} - \beta \rho \omega^2 \ , \tag{2.146}$$

with the turbulent viscosity defined by:

$$\mu_\mathsf{t} = \rho \frac{\mathsf{k}}{\omega} \ , \tag{2.147}$$

the turbulence eddy dissipation rate:

$$\varepsilon = \beta^* \omega \mathsf{k} \ , \tag{2.148}$$

and the constant values:

$$\alpha = 0.09, \quad \beta = 1.44, \quad \beta^* = 1.92, \quad \sigma_\mathsf{k}^* = \sigma_\omega^* = 2 \ . \tag{2.149}$$

[22]

Numerically, the k-ω model is very similar to the k-ε model. It shows its strength in calculations regarding the viscose and logarithmic sublayer of the boundary layer close to solid surfaces. In contrast to other models, it is relatively simple and numerically stable, but still it is not able to accurately calculate the asymptotic behavior of the turbulence in the free fluid flow. Another drawback is the inaccurate distribution of the k and ε values in comparison to results from DNS calculations [56].

Shear Stress Transport (SST) model

In the free stream region, the k-ω model has a deficit, which on the other hand is a clear advantage of the k-ε model, compared to DNS results. The combination of the two models with the aid of a blending function $\mathsf{F_1}$ results in a model called baseline (BSL) model. The blending function is designed to be one in the boundary layer next to the wall, where the original k-ω model prevails. In the free stream, the blending function gradually declines to zero and the fluid flow is calculated with the transformed k-ε model. The modification with respect to the transport of the principal turbulent shear stress and the definition of eddy viscosity by

$$\nu_\mathsf{t} = \frac{\mathsf{a_1}\ \mathsf{k}}{\max(\mathsf{a_1}\ \omega, \mathsf{S}\ \mathsf{F_2})} \tag{2.150}$$

with constant value $\mathsf{a_1}$, magnitude of the strain rate S and a second blending function $\mathsf{F_2}$, in addition to the implementation of the baseline model, leads to the shear-stress transport (SST) model [4].

The original and implemented BSL and SST equations for turbulence transport and blending function can be found in the Appendix (B.4).

Scale-adaptive simulation (SAS) model

The SAS turbulence model is based on the k-kL model [73, 74] which includes an exact transport equation for the turbulent length scale. The approach for the length scale in [73] has strong theoretical foundations and provides a quantity which is proportional to the size of the resolved eddies. Since the k-kL model has deficiencies in combination with the logarithmic law of the wall, it did not succeed in commercial applications. One fundamental difference to the SAS turbulence model is the calculation of the length scale with the derivative of the velocity field. By keeping the second derivative of velocity instead of the third derivative, the SAS turbulence model does function in combination with the log-law and the length scale is proportional to the von Kármán length scale [54]. For a two dimensional flow, the von Kármán length scale in x-direction is defined as

$$\mathsf{L_{vK}} = \kappa \left| \frac{\partial \mathsf{u}/\partial \mathsf{y}}{\partial^2 \mathsf{u}/\partial \mathsf{y}^2} \right| \tag{2.151}$$

with the von Kármán constant κ. In standard turbulence models, the length scale is proportional to the thickness of the shear layer adjusting the local flow topology incorrectly and therefore calculates with a higher diffusion [54, 58]. Since the SAS turbulence model can only be used for transient simulations and not for steady state, it requires a higher computational effort if averaged values are required. The transport equations and model constants for the SAS turbulence model can be found in Appendix B.5.

Gamma-Theta transition model

The change from a laminar to a turbulent fluid flow is not a sudden transition but rather a process which depends on various factors. Transition starts above a specific critical Reynolds number which considers the prevailing velocity and the viscosity of the fluid. The influence of other factors like the surface roughness or the upstream turbulence intensity cannot be easily quantified. Since the whole transition process has not yet been completely investigated, it is a current topic in the research of fluid dynamics [34]. Similarly to the transition from laminar to turbulent flow, the reverse process of relaminarization from turbulent to laminar flow is also not fully explainable yet. The transition process can occur anywhere in the fluid flow domain where the required flow conditions are met. Due to its direct connection to attached and separated flow conditions at surfaces and, therefore, to heat transfer problems, the transition in boundary layers is of special interest [55].

In [59] the authors first introduced the Gamma-Theta model as an empirical approach to the simulation of transition. The same transition model has been implemented with a few changes, as presented in [4, 49], in the commercial CFD software package used in this work. It is based on two transport equations which use local information of the calculation domain only. One of the primary variables is the strain-rate (or vorticity) Reynolds number which is defined as

$$\mathsf{Re_S} = \frac{\rho \mathsf{y}^2}{\mu} \frac{\partial \mathsf{u}}{\partial \mathsf{y}} = \frac{\rho \mathsf{y}^2}{\mu} \mathsf{S} \tag{2.152}$$

with the wall distance y, the density ρ, the viscosity μ and the absolute value of strain rate S. Physically, $\mathsf{y}^2\mathsf{S}$ is responsible for the disturbance in the boundary layer and $\nu = \mu/\rho$ is responsible for damping the turbulence. The first transport equation for the intermittency γ is used to locally initiate transition and to enable the production term of the turbulent kinetic energy. The basis of this operation is the ratio of the transition momentum-thickness Reynolds number and the strain-rate Reynolds number. The second transport equation for the transition onset momentum-thickness Reynolds number $\mathsf{Re_\Theta}$ considers the influence of the non-local turbulent intensity close to the wall in the boundary layer. The Gamma-Theta transition ($\gamma - \mathsf{Re_\Theta}$) model can be used in connection with the BSL, SST and SAS turbulence models. A detailed description of the Gamma-Theta model can be found in [49] and [55]. The definition of the transport equations for γ and $\mathsf{Re_\Theta}$ can be found in Appendix B.6.

2.4.5   Boundary conditions

Wall function model

The boundary conditions of the turbulence equations are treated similarly to the boundary conditions of scalar values. Such problems can be avoided by the use of wall-functions which employ the idealized logarithmic-law of the wall (as shown in

Subsection 2.3.10) to approximate the near wall effects. With the assumption of balanced production and dissipation of turbulence, friction velocity can be expressed as:

$$u_\tau = C_\mu^{1/4}\sqrt{k} \ , \tag{2.153}$$

and the wall shear stress can be derived by:

$$\tau_w = \rho u_\tau^2 = \rho C_\mu^{1/4} \kappa \sqrt{k} \frac{u}{\ln(y^+ e^{\kappa B})} \ , \tag{2.154}$$

with the dimensionless distance of the wall y^+, as shown in (2.82), derived by the node-wall distance y_0 and the kinematic viscosity $\nu = \mu/\rho$:

$$y^+ = \frac{\rho y_0 u_\tau}{\mu} \ . \tag{2.155}$$

Tangential forces on the control volume faces can be calculated using the wall shear stress (2.154), which is required for the boundary conditions of the momentum equations. Since the derivative of velocity parallel to the wall with respect to the perpendicular direction $y \to 0$ cannot be calculated from values of the nodes next to the wall, this approximation is unavoidable. When using the wall-function model, the diffusive flux at the wall is set to zero in the k transport equation in order to obtain the boundary conditions for the momentum equations. This means that the derivative of k with respect to the perpendicular direction of the wall is zero, which is equivalent to a Neumann boundary condition. The turbulence kinetic energy k is zero at the surface but can assume a high value in nodes next to the surface. Hence the production rate in the control volume next to the wall also requires a modification:

$$P_k \approx -\rho \overline{u'v'} \frac{\partial(\overline{u})}{\partial y} \approx \tau_w \frac{\overline{u}}{\partial y} \ . \tag{2.156}$$

This modification is valid due to the nearly constant wall shear stress close to the wall, but again requires a differentiation of the wall-parallel velocity. Since this velocity gradient is not linear, a derivative with respect to the wall distance $(\partial u/\partial y)_n$ in the mesh-node next to the wall would be wrong, as shown in Fig. 2.11. In this case a derivative of the logarithmic-law of the wall with the values from the control volume next to the wall can be used:

$$\frac{\partial \overline{u}}{\partial y} = \frac{u_\tau}{\kappa y} = \frac{C_\mu^{1/4}\sqrt{k}}{\kappa y} \ , \tag{2.157}$$

which is equivalent to the re-arranged equation (2.91) before integration to the log-law. By knowing this velocity derivative, the wall shear stress and production rate can be calculated [22].

Dissipation rate is derived by the assumption of balanced production and dissipation of turbulence. In control volumes next to the wall, only the turbulent kinetic
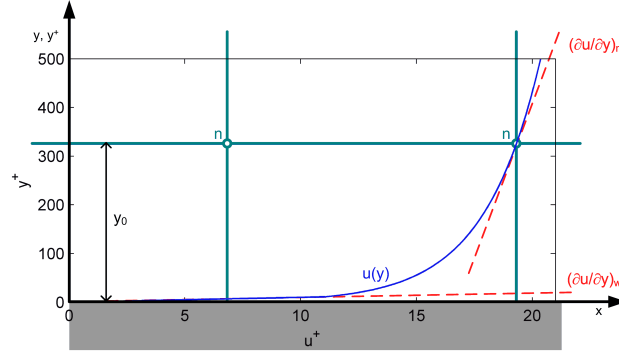
Figure 2.11: Velocity profile u(y) and mesh-nodes n next to the wall with the initial wall-node distance y_0, the velocity gradient at the wall $(\partial u/\partial y)_n$ and the velocity gradient in the mesh-node next to the wall $(\partial u/\partial y)_w$

energy is solved by the turbulence model and the dissipation rate is set proportional to the turbulence kinetic energy:

$$\varepsilon = \frac{C_\mu^{3/4} k^{3/2}}{\kappa y} \ . \tag{2.158}$$

A major drawback of the wall-model approach is its strong connection to the idealized velocity profile of the log-law.

Since the velocity profile at the wall does not always fit the logarithmic profile, e.g. at points of flow separation, the log law does not describe correctly the derivative of velocity. In situations of clearly attached flow conditions, e.g. pipe flow, the wall-model can calculate well approximated values. When using the wall-model approach in situations with much flow separation, the calculation eventually prove to be incorrect.

Resolved near wall region

Close to the wall, the k-ε model, as shown in the last section, can encounter problems due to the numerical oscillation of k and ε which occasionally assume negative values. Since both parameters are physically always positive, this can lead to convergence problems in the solution. These problems can be reduced by refining the mesh, especially in the direction perpendicular to the considered wall. Turbulence kinetic energy at the surface must be zero $k|_{y\to0} = 0$ due to the non-slip-condition, while the turbulence dissipation rate ε, can be approximated by:

$$\varepsilon = \nu \left(\frac{\partial^2 k}{\partial n^2}\right)_{\text{wall}} \quad \text{or} \quad \varepsilon = 2\nu \left(\frac{\partial k^{1/2}}{\partial n}\right)^2_{\text{wall}} \ . \tag{2.159}$$

Since turbulence becomes non-isotropic close to the wall, modified k-ε models are required when resolving the near wall region with a finer mesh. These are denoted as Low-Reynolds turbulence models [22].

Automatic near-wall treatment

A great benefit of the k-ω turbulence model is the availability of an exact solution of the ω value in the viscose sublayer next to a wall. As in the wall function model, the diffusive flux in the k equation is set to zero. The diffusive flux in the momentum equation $\mathsf{F_u}$ is derived by:

$$\mathsf{F_u} = -\rho \mathsf{u}_\tau \mathsf{u}^* \,, \tag{2.160}$$

with

$$\mathsf{u}^* = \sqrt[4]{\left(\sqrt{\frac{\mu}{\rho}\left|\frac{\mathsf{u_0}}{\mathsf{y_0}}\right|}\right)^4 + \left(\sqrt{\mathsf{a_1 k}}\right)^4} \tag{2.161}$$

and the friction velocity

$$\mathsf{u}_\tau = \sqrt[4]{(\mathsf{u}_\tau^{\mathsf{vis}})^4 + (\mathsf{u}_\tau^{\mathsf{log}})^4} \,, \tag{2.162}$$

which contains the friction velocity for the viscose sublayer

$$\mathsf{u}_\tau^{\mathsf{vis}} = \sqrt{\frac{\mu}{\rho}\left|\frac{\mathsf{u_0}}{\mathsf{y_0}}\right|} \tag{2.163}$$

and the friction velocity for the logarithmic layer

$$\mathsf{u}_\tau^{\mathsf{log}} = \frac{\mathsf{u}}{1/\kappa \, \mathsf{log}(\mathsf{y}^+) + \mathsf{B}} \,, \tag{2.164}$$

with the von Kármán constant κ and the log-law constant B. In order to correctly approximate the near-wall effects at locations with a coarse mesh $\mathsf{y}^+ > 11.06$, the automatic near-wall treatment works with a blending function between the logarithmic and the sublayer region. As presented in [57], the blending between these dissipation rates is accomplished by

$$\omega = \sqrt{\omega_{\mathsf{log}}^2(\mathsf{y}^+) + \omega_{\mathsf{vis}}^2(\mathsf{y}^+)} \,. \tag{2.165}$$

The dissipation rate in the logarithmic region is defined by:

$$\omega_{\mathsf{log}} = \frac{\mathsf{u}_\tau}{0.3\kappa\mathsf{y}} \tag{2.166}$$

and the dissipation rate for the sublayer region is:

$$\omega_{\mathsf{vis}} = \frac{6\nu}{0.075\mathsf{y}^2} \,, \tag{2.167}$$

with the non-dimensional wall distance $\mathsf{y}^+ = \mathsf{y} \, \mathsf{u}_\tau/\nu$.

Calculation of heat flux

In [47], the dimensionless near wall temperature profile Θ^+ was evaluated from empirical data for different types of fluids with different Prandtl numbers. The dimensionless near wall temperature profile is defined as

$$\Theta^+ = \frac{\mathsf{T_w} - \mathsf{T_\infty}}{\mathsf{T_\tau}} \, , \tag{2.168}$$

with

$$\mathsf{T_\tau} = \frac{\dot{\mathsf{q}}_\mathsf{w}}{\rho \, \mathsf{c_p} \, \mathsf{u_\tau}} \, . \tag{2.169}$$

Based on this near wall temperature profile, the automatic wall treatment calculates the heat transfer in the boundary layer.

$$\Theta^+ = \mathsf{Pr} \, \mathsf{y}^+ e^{-\Gamma_\mathsf{w}} + \left(2.12 \, \ln(1 + \mathsf{y}^+) + \beta_{\mathsf{Pr}} \right) \, e^{-1/\Gamma_\mathsf{w}} \, , \tag{2.170}$$

with the functions

$$\beta_{\mathsf{Pr}} = (3.85 \, \mathsf{Pr}^{1/3} - 1.3)^2 + 2.12 \, \ln(\mathsf{Pr}) \ \text{and} \qquad \Gamma_\mathsf{w} = \frac{0.01(\mathsf{Pr} \cdot \mathsf{y}^+)^4}{1 + 5 \, \mathsf{Pr}^3 \cdot \mathsf{y}^+} \, , \tag{2.171}$$

the Prandtl number Pr, as defined in Subsection 2.3.9. The automatic wall treatment uses the distance to the first calculation node next to the wall with $\mathsf{y_0} = n_0$. Due to historic and stability reasons the standard and scalable wall treatment use only a quarter of the distance with $\mathsf{y_0} = n_0/4$. This temperature profile is valid for the viscose and the logarithmic sublayer. The definition of the wall heat flux $\mathsf{q_w}$ is:

$$\dot{\mathsf{q}}_\mathsf{w} = \frac{\rho \, \mathsf{c_p} \, \mathsf{u}^*}{\Theta^+}(\mathsf{T_w} - \mathsf{T_\infty}) \, , \tag{2.172}$$

with wall temperature $\mathsf{T_w}$ and fluid temperature $\mathsf{T_\infty}$ [4]. An example for the temperature profile $\Theta^+(\mathsf{y}^+)$ is shown in Fig. 2.12 as published in [47] for air with a Prandtl number of $\mathsf{Pr} = 0.7$ and $\mathsf{y}^* = \mathsf{y}^+$.

2.4.6   Mesh requirements

A mesh used for CFD simulations has to meet certain requirements. Especially if the goal is to predict near-wall effects such as wall shear stress or convective heat transfer, the elements next to the wall require a specific wall to mesh-node distance $\mathsf{y_0}$ depending on the Reynolds number and thus on the local fluid velocity and properties. The approach of the wall function model assumes the validity of the logarithmic law of the wall at solid surfaces, as shown in Fig. 2.11. The log-law itself is not an exact description of the wall effects, but is rather a model. It describes the similarity of fluid flow and turbulence next to a surface between two parallel plates or pipes with circular cross sections and assumes a mean flow parallel to the wall, as shown in Subsection 2.3.10.
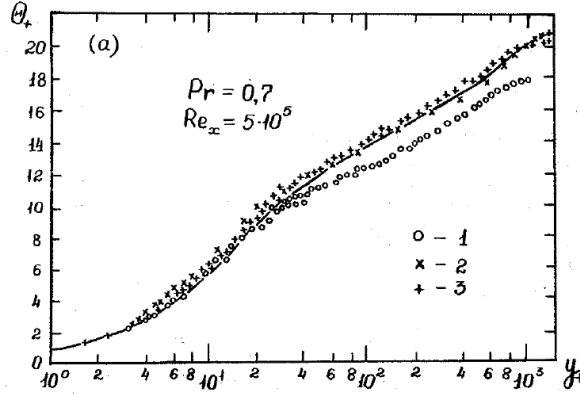
Figure 2.12: Temperature profile Θ^+ over the dimensionless wall distance y^+ in a turbulent flow of air on a plate based on experimental data [47].

The theory of the boundary layer assumes a thin boundary layer with thickness δ compared to the characteristic length L as well as high Reynolds number.

$$\frac{1}{\sqrt{\mathsf{Re}}} \sim \frac{\delta}{\mathsf{L}} = \varepsilon_\mathsf{b} \ll 1 \tag{2.173}$$

Due to the high Reynolds number, the inertial forces prevail over the viscous forces and potential flow[1] can be assumed outside the boundary layer. The viscous forces are relevant directly next to the wall inside the boundary layer. This works as long as the mean flow goes in the direction of a negative pressure gradient along the wall. A problem occurs when the mean flow goes against a positive pressure gradient next to the wall. Compared to the turbulent zone, the viscous layer stores less energy and tends to follow the pressure gradient from higher to lower level of pressure against the direction of the mean flow.

$$\nu \frac{\partial^2 \mathsf{u}}{\partial \mathsf{y}^2} = \frac{1}{\rho} \frac{\partial \mathsf{p}}{\partial \mathsf{x}} < 0 \tag{2.174}$$

In this situation, eddies caused by the return flow expand the boundary layer to a thickness where (2.173) becomes questionable or even invalid and consequently influences all models which are based on this theory [76].

The validity of the simulated heat transfer coefficient with the wall function model depends basically on the logarithmic law of the wall and thus the theory of the boundary layer [37]. Hence the boundary layer of surface areas which are supposed to adjoin separated flow conditions and are relevant for heat transfer results should be resolved with mesh-layers of thin prisms during the meshing procedure [89]. A resolved boundary layer requires a specific height of the first cell next to the surface for the calculation of accurate values for the near wall effects. The use of prismatic cells next to the wall is an established way of resolving the boundary layer, with an initial cell height of $\mathsf{y}^+ \approx 1$ for the first prism-layer. The following prism layers have a layer height growth

---

[1]Potential flow is an idealized frictionless and non-vortical flow [14, 79]

factor of 1.2 times the height of the layer beneath. For a proper resolution of the boundary layer at least ten prism-layers are required. For basic geometries, the value for the height of the first element can be calculated using the *Reynolds* number Re, the characteristic length L and the desired value for y^+ [4]:

$$\mathsf{y_0} = \mathsf{L}\mathsf{y}^+\sqrt{74}\,\mathsf{Re}^{-13/14}\;. \tag{2.175}$$

Due to the small values of $\mathsf{y_0}$, the number of elements rises rapidly when the heat flux of larger areas is investigated.

Depending on the model of near-wall treatment, the approximation of near-wall effects in CFD simulations fits best to empirical data for values of about $\mathsf{y}^+ \approx 1$ for a resolved boundary layer or $\mathsf{y}^+ \approx 30$ for a log-law wall model. As shown in [89], the value of $\mathsf{y}^+ = 11.06$ represents the most unsuitable case and thus the model probably describes the near wall effects with a higher error than above or below this value [42].

Chapter 3

Validation of the simulation setup

Simulating heat transfer by CFD is a time-consuming process due to the high number of finite volume cells requiring a long computation time. The accuracy of the simulation results depends essentially on the models and on the computation mesh used for the simulation. The choice of a turbulence model depends on its accuracy regarding convective wall heat transfer. In order to analyze the end-windings' numerical model with an adequate configuration, the parameters of the numerical simulations have been tested on simple three-dimensional models. To ensure good agreement between the CFD results and the real wall heat flux distribution, numerical models of a cylinder in a cross flow have been investigated with configurations for different Reynolds numbers [42]. Several measurements of this setup have been published in the last decades offering a high reliability of the results. The comparison of the measured and the simulated results provides a good overview of the methods' accuracy.

3.1 Cylinder in a cross flow

Circular cylinders are popular objects in fluid dynamic investigations. Despite their simple geometry, the flow conditions around a circular cylinder vary greatly depending on the circumferential position. It has an attached flow at the forward stagnation point, flow separation at about $80°$ from the forward stagnation point as sketched in Fig. 3.1, and separated turbulent flow in the downstream wake space. The downstream zone of a cylinder has an unsteady but periodical behavior, which is known as the von Kármán vortex street. The pressure and velocity are changing periodically at Reynolds numbers as low as $Re > 90$ [76] creating an alternating force perpendicular to the mean flow and periodical changes in heat transfer with respect to time. Beside its basic shape and the diverse flow conditions, the circular cylinder is important in solving industrial problems connected to structural analysis or heat transfer (e.g. tube bundle heat exchanger). A sketch of the used setup is shown in Fig. 3.1. The Reynolds number Re of this setup can be calculated with (2.65) using the diameter D as characteristic length, as well as the free stream velocity u_∞ and the temperature dependent kinematic viscosity
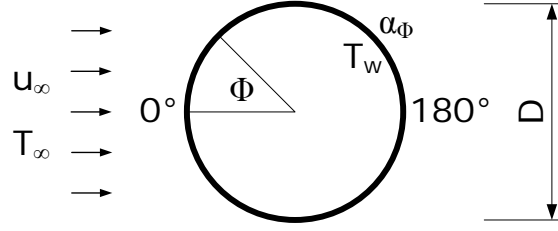
Figure 3.1: Sketch of a cylinder in cross flow with diameter D, local convective heat transfer coefficient α_Φ, wall temperature T_w, fluid temperature T_∞, free stream velocity u_∞ and angle $\Phi = 0°$ at the forward stagnation point

ν. This geometry has been extensively investigated and is therefore used in this work for the validation of the numerical models in CFD. In the following subsections, the empirical approaches are briefly described and compared to the numerical results.

The information about the average heat transfer from a cylinder (pipe) is sufficient for many engineering purposes. Such cases have been investigated by [93, 94] and [97] and give accurate results for a wide range of Reynolds numbers. For the model validation, it is preferable to use local values of the wall heat transfer coefficient at a specific circumferential location. These data can be found in the investigations of [27] dealing with Reynolds numbers from $Re = 70\,800$ to $219\,000$. Investigations of the circumferential variation of the local Nusselt number Nu_Φ at lower Reynolds numbers, starting from $Re = 8\,290$, are available in [77].

The use of the Nusselt number is an established way to specify the heat transfer for a more general expression of wall heat transfer. The local Nusselt number Nu_Φ can be derived by (2.69) using the local heat transfer coefficient α_Φ, the characteristic length D and the thermal conductivity of air λ [42].

3.1.1 Empirical results

White

The wall heat transfer for a wide range of Prandtl numbers $0.7 \leq Pr \leq 300$ and Reynolds numbers $10 \leq Re \leq 10^5$ can be calculated with

$$Nu_D = 0.3 + \frac{0.62\,Re^{1/2}\,Pr^{1/3}}{[1 + (0.4/Pr)^{2/3}]^{1/4}} \left[1 + \left(\frac{Re}{280\,000}\right)^{5/8}\right]^{4/5}, \tag{3.1}$$

where Nu_D denotes the average Nusselt number with the diameter D as characteristic length [94]. The Reynolds number (2.65) and Prandtl number (2.66) are both defined in Subsection 2.3.9.

Whitaker

Considering the different values of the dynamic viscosity for bulk-temperature ('mixing cup temperature') μ_b and for wall temperature μ_0, (3.2) shows a reasonable agreement

with measurements at high-temperature gradients with a dynamic viscosity ratio of $0.25 \leq \mu_b/\mu_0 \leq 5.2$, for the range of Reynolds number $44 \leq \mathsf{Re} \leq 10^5$ and Prandtl number $0.67 \leq \mathsf{Pr} \leq 300$:

$$\mathsf{Nu_D} = \left(0.4\ \mathsf{Re}^{1/2} + 0.06\ \mathsf{Re}^{2/3}\right) \mathsf{Pr}^{0.4} \left(\frac{\mu_b}{\mu_0}\right)^{1/4} . \tag{3.2}$$

Zukauskas

Another empirical formula which gives an average Nusselt number $\mathsf{Nu_D}$ for a cylinder in a cross flow is available in [97]. It can be used for a wider range of Reynolds numbers $1 \leq \mathsf{Re} \leq 10^6$ in comparison to (3.1) and (3.2) and is defined as:

$$\mathsf{Nu_D} = \mathsf{C}\ \mathsf{Re}^m\ \mathsf{Pr}^n \left(\frac{\mathsf{Pr}}{\mathsf{Pr_s}}\right) , \tag{3.3}$$

where $n = 0.37$ for $\mathsf{Pr} < 10$, $n = 0.36$ for $\mathsf{Pr} > 10$ and the values of the constants C and m depend on the used Reynolds number, as shown in Tab. 3.1. All fluid parameters

Table 3.1: Coefficients for (3.3)

Re			C	m
1	–	40	0.75	0.4
40	–	$1 \cdot 10^3$	0.51	0.5
$1 \cdot 10^3$	–	$2 \cdot 10^5$	0.26	0.6
$2 \cdot 10^5$	–	$1 \cdot 10^6$	0.076	0.7

are defined for the free stream temperature $\mathsf{T_\infty}$, except the Prandtl number $\mathsf{Pr_s}$, which is defined for the surface temperature $\mathsf{T_w}$.

Giedt

The aim of the investigation in [27] has been to identify the wall heat transfer coefficient of a circular cylinder made of acrylic glass with an outer diameter of $101.6\ \mathsf{mm}$ and a total length of $1016\ \mathsf{mm}$. Different velocities and angles of attack of the free air stream have resulted in different heat transfer coefficients at different angular positions on the cylinder and thus different surface temperatures. A thin metal tape with a total length of $1651\ \mathsf{mm}$, thickness of $50.8\ \mu\mathsf{m}$ and width of $25.4\ \mathsf{mm}$ has been wrapped helically around the cylinder for five full turns. The metal tape was made of nickel-chrome alloy has an electric resistance of $0.86\ \Omega/\mathsf{m}$ measured at $\mathsf{T} = 21\,°\mathsf{C}$. By applying an electric current I to the metal tape, a uniform heat flux density $\dot{\mathsf{q}}$ has been achieved on the surface of the cylinder. With a constant heat flux density at the surface, the only degree of freedom has been the temperature difference $\Delta\mathsf{T}$ measured by thermocouples. The heat transfer coefficient has hence been obtained as

$$\alpha = \frac{\dot{\mathsf{q}}}{\Delta\mathsf{T}} \propto \frac{\mathsf{I}^2\ \mathsf{R}}{\Delta\mathsf{T}} . \tag{3.4}$$

The prepared cylinder has been exposed to the air flow of a wind tunnel with a 0.9144 m wide nozzle opening. Iron-constantan thermocouples have been applied on one half of the circumference at distances of 12.7 mm to measure the temperature variations. A pressure sensor has been applied to the cylinder and the circumferential static pressures have been measured by revolving the cylinder and placing the sensor at the desired circumferential positions. The ambient temperature T_{ref} has been measured using a shielded iron-constantan thermocouple. The heat flux caused by radiation has been considered analytically with an emission coefficient of $\varepsilon = 0.2$ for the nickel-chrome tape. The Nusselt number has been evaluated with a thermal conductivity λ at an average film temperature of:

$$T_{avg} = T_{ref} + \frac{T_{max} - T_{min}}{2} \; , \tag{3.5}$$

with the maximum surface temperature T_{max} and the minimum surface temperature T_{min}.

   The numerical reconstruction of the setup requires an appropriate ambient temperature for the calculation of the material properties of air in order to obtain accurate air velocities for the Reynolds numbers given in the publication. The ambient temperature is not given but can be estimated by the material properties. Regarding the calculation of the wall heat transfer coefficient from the Nusselt number, a constant value is mentioned in the paper with $\alpha = 0.044 \cdot Nu$, which equals the ratio between the thermal conductivity and the diameter of the cylinder[1] $\lambda/D = 0.25$ W/m^{2}K. For a diameter of $D = 0.1016$ m, the thermal conductivity is $\lambda_{ref} = 0.25 \cdot D = 0.02537$ W/mK. With a thermal conductivity of air $\lambda_{10} = 0.02512$ W/mK at $T = 10°$C and $\lambda_{20} = 0.02587$ W/mK at $T = 20°$C [88], the average film temperature is approximately $T_{avg} = 13.3°$C. Due to the vague factor of λ/D, the film temperatures can only be estimated with an accuracy of $\pm 3.8°$C. This uncertainty has not be considered in the subsequent calculations. The difference between the maximal and the minimal temperature at the surface is shown in the diagram in Fig. 3.2(b) with $\Delta T = T_{max} - T_{min} = 4.9°$F $= 2.7°$C. According to (3.5), the reference temperature is $T_{ref} = T_{avg} - \Delta T/2 = 12°$C. The experiment has been carried out for different velocities of air and hence different Reynolds numbers from $70\,800$ to $219\,000$. The values for the velocities are missing in the publication and they have been re-calculated for the purposes of the present investigation by rearrangement of (2.65). The adequate kinematic viscosity has been linearly interpolated between $\nu_{10} = 1.44 \cdot 10^{-5}$m^2/s and $\nu_{20} = 1.532 \cdot 10^{-5}$m^2/s with $\nu_{12} = 1.457 \cdot 10^{-5}$m^2/s. The resulting velocities according to the Reynolds numbers for a diameter $D = 0.1016$ m of the cylinder can be found in Tab. 3.2 on page 65.

Schmidt

The experimental setup in [77] has had the aim of measuring the wall heat transfer coefficient along the circumference of a circular cylinder but using a different method

---

[1]Converted from $\lambda/D = 0.044$ Btu/(h ft^2 F) with 1 Btu/(h ft^2 F) $= 5.6745$ W/m^{2}K

(a) Wall heat transfer

(b) Temperature distribution
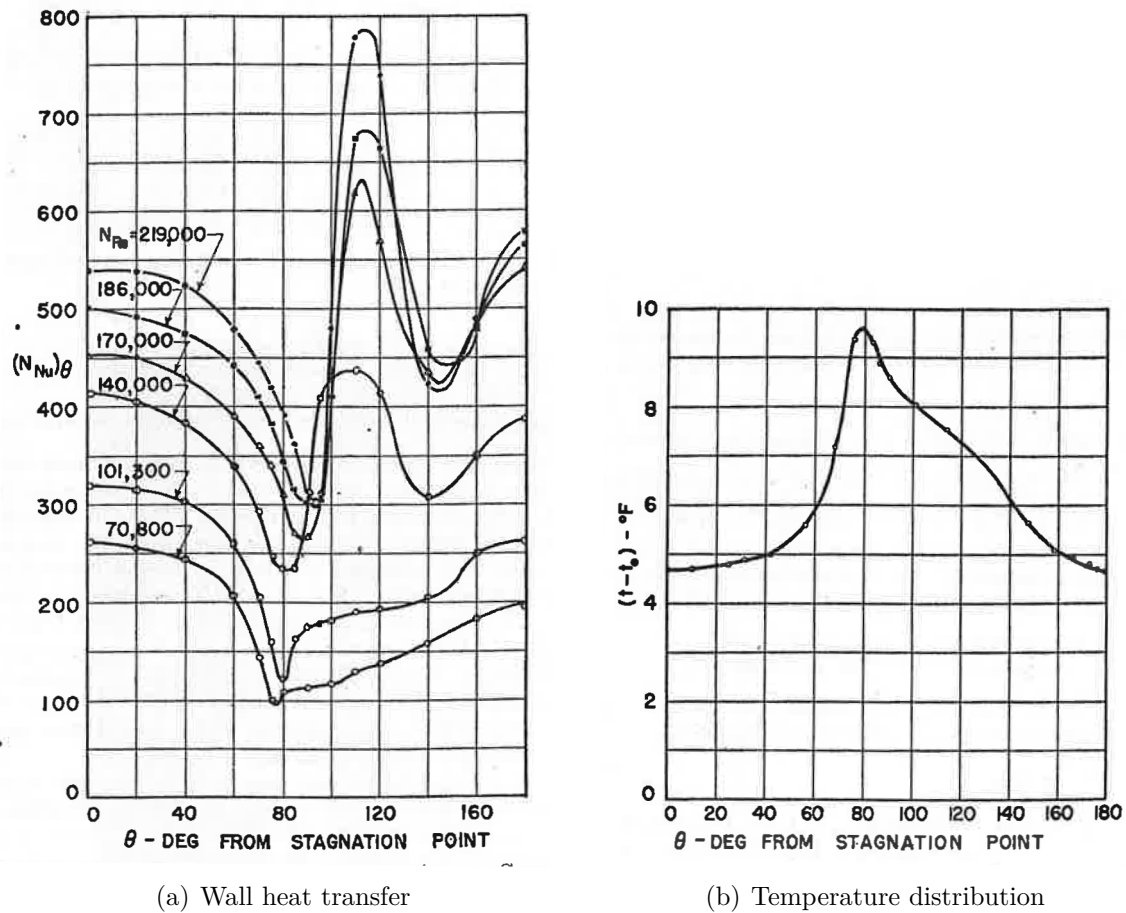
Figure 3.2: Distribution of (a) the wall heat transfer and (b) temperature distribution at the surface with respect to the angle from the forward stagnation point [27]

than the one previously described. In order to investigate low and high Reynolds numbers with the same setup, cylinders with three different diameters $D = 50$ mm, 100 mm and 250 mm have been used.

By constantly feeding the brass cylinder with steam, the surface has been kept at a constant and uniform temperature of 100°C. An electrically heated and thermally insulated copper bar has been embedded into the surface of the cylinder assuring a smooth transition of the surface. By keeping the copper bar at the same temperature as the rest of the cylinder, the wall heat transfer can be calculated using the surface temperature and the supplied electrical power. Conductive heat transport between the copper bar and the brass cylinder has been neglected due to the uniform temperature and the resulting vanishing temperature gradient. Heat flux by radiation has been considered with an emission coefficient of $\varepsilon = 0.1$ for the polished surface of the copper bar.

The investigations have been carried out at an ambient temperature of $T_a = 20°C$

(a)　　　　　　　　　　　　　　　　(b)
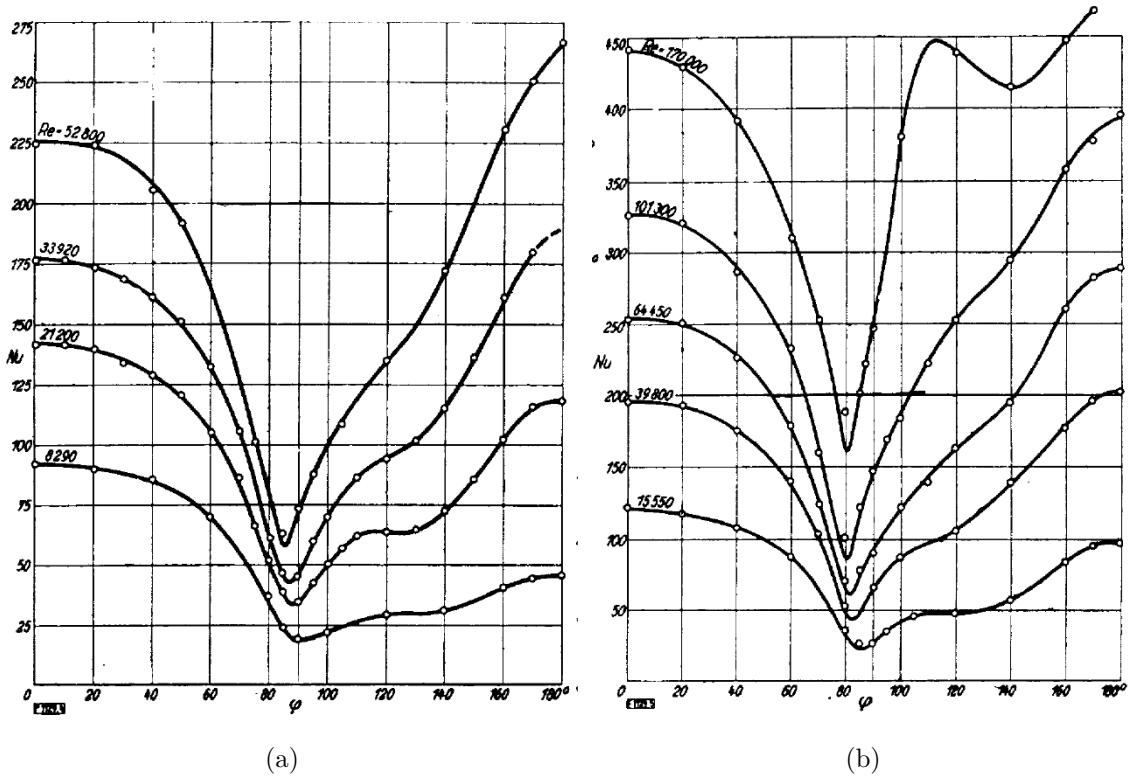
Figure 3.3: Wall heat transfer on two different cylinders with diameters of (a) 50 mm and (b) 100 mm and hence different ranges of Reynolds numbers [77]

to 26°C kept constant within a range of 0.1°C for each test run. For the calculation of the Reynolds and Nusselt numbers, the material properties for thermal conductivity $\lambda = 0.0241$ W/mK and kinematic viscosity $\nu = 1.94 \cdot 10^{-5}$ m^2/s have been used. The cylinders have been placed behind a 600 mm wide and 250 mm high nozzle connecting two chambers with sizes $6 \times 5 \times 3$ m and $6 \times 4 \times 3$ m. The chambers have also been connected with a fan, so the pressure in both of them has changed assuring a steady pressure driven flow through the nozzle. The velocity in the nozzle has been measured using a Prandtl pitot tube and the difference of pressures in the two chambers.

3.2　Fluid properties of the coolant

In order to consider the temperature dependence of the streaming fluid, the material properties of air have been adjusted by calculating the parameters as listed in [88] with a Gauss Newton method. The heat capacity c_p has been approximated by the so called zero pressure polynomial [3]

$$\frac{c_p}{R_s} = t_1 + t_2 \ T + t_3 \ T^2 + t_4 \ T^3 + t_5 \ T^4 \ , \tag{3.6}$$
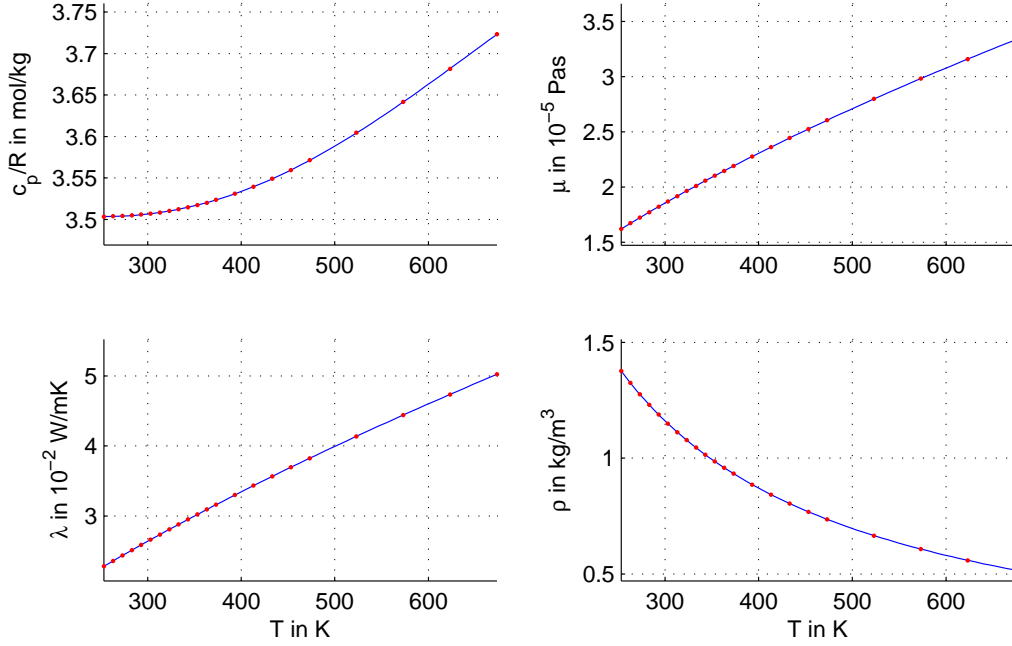
Figure 3.4: Properties of dry air at a pressure of p = 1 bar from [88] (dots) including approximation (line)

with the gas constant for air $R_s = 287.12 \frac{J}{kgK}$, the temperature T in Kelvin and the following coefficients:

$$
\begin{array}{ll}
t_1 = 3.574 & t_2 = 4.269 \; 10^{-4} \; K^{-1} \\
t_3 = -4.185 \; 10^{-8} \; K^{-2} & t_4 = 3.099 \; 10^{-9} \; K^{-3} \\
t_5 = -2.385 \; 10^{-12} \; K^{-4} & .
\end{array}
$$

The values for the dynamic viscosity μ have been approximated by the Sutherland formula

$$
\frac{\mu}{\mu_{ref}} = \frac{T_{ref} + S_\mu}{T + S_\mu} \cdot \left(\frac{T}{T_{ref}} \right)^{n_\mu} , \tag{3.7}
$$

as well as the thermal conductivity λ

$$
\frac{\lambda}{\lambda_{ref}} = \frac{T_{ref} + S_\lambda}{T + S_\lambda} \cdot \left(\frac{T}{T_{ref}} \right)^{n_\lambda} . \tag{3.8}
$$

In these formulae, S_μ and S_λ stand for the Sutherland constant while n_μ and n_λ represent the appropriate exponents. Values for the reference viscosity μ_{ref} and the reference thermal conductivity λ_{ref} have been chosen from a material property table in [88] at the reference temperature $T_{ref} = 325 \; K$ which is close to the mean operating temperature of air in an electrical machine

$$
\begin{array}{lll}
S_\mu = 77.8 \; K & \mu_{ref} = 1.97 \; 10^{-5} \; Pa \; s & n_\mu = 1.57 \\
S_\lambda = 60.7 \; K & \lambda_{ref} = 2.82 \; 10^{-2} \; W/mK & n_\lambda = 1.68 \quad .
\end{array}
$$

With this approach, the material properties have been approximated accurately in a temperature range of about 253 K to 673 K. It is not recommended to use the same parameters above or below this given range of temperature [36].

3.3 Simulation setup of the cylinder in cross flow

Simulations have been carried out with different turbulence models. The models used have been the SST, the SAS, the k-ε and the k-ω models described in Subsection 2.4.4. As shown in Fig. 3.5, the simulations with the SST turbulence model [56] and the

(a) SST and standard k-ε turbulence model 	(b) SAS and k-ω turbulence model
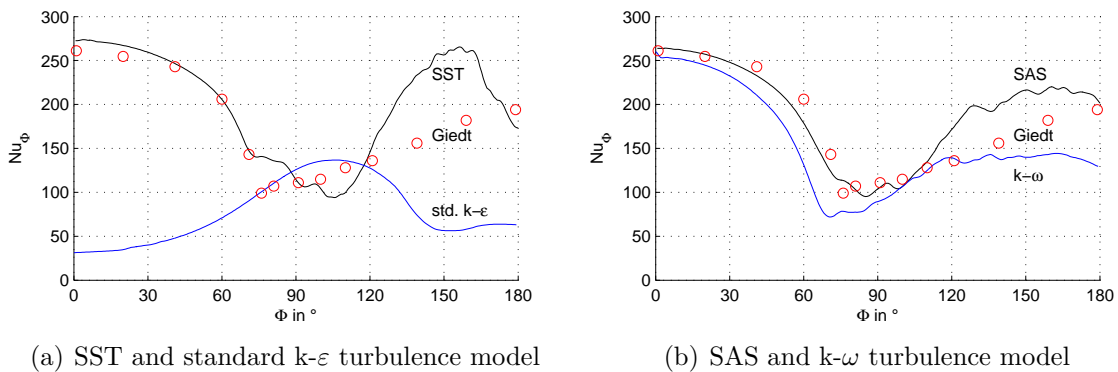
Figure 3.5: Comparison between empirical results in [27] and different turbulence models as implemented in *ANSYS CFX* and calculated in a transient CFD simulation setup for a Reynolds number of Re = 70 800 [42]

SAS turbulence model result in acceptable agreement with Giedt's empiric data up to the break-off point at $\Phi \approx 80°$. Due to an ideally symmetric heat transfer of the top half and the bottom half of the cylinder, the diagrams show only the distribution form $\Phi = 0° \ldots 180°$, which is also valid for $\Phi = 360° \ldots 180°$. After the break-off point, the flow starts to stall and the agreement between the calculated heat transfer with the empiric data is poor. Even though the simulated heat transfer coefficient is not exact, it is more accurate than the one obtained using the k-ω model or the k-ε model. Compared to the empirical data, the numerical simulation with the SST model slightly over-predicts the heat transfer. Even though the curve obtained by the k-ω turbulence model is similar to the empirical data shown in [27], its average value for the Nusselt number is less accurate than the Nusselt number from the SST model. Of the tested models, the standard k-ε turbulence model [95] shows the lowest prediction accuracy. Since the model has been designed for high Reynolds number applications, it is not appropriate for simulating heat transfer for low velocities or small length scales, as also confirmed in [18]. Depending on the Reynolds number, the results computed by the SAS turbulence model are comparable to the results of the SST turbulence model or are sometimes even more accurate, as shown in Fig. 3.5. The heat transfer derived with constant fluid properties has the same circumferential distribution as the heat

transfer derived with temperature-dependent fluid properties. However, the absolute values do not match the empirical data [42]. Since the SAS turbulence model can only be solved in transient simulations, the computational effort is much higher than for the SST turbulence model, which can be used in steady state simulations. Therefore, the SST turbulence model and steady state simulation setup have been chosen for the following investigations.

In order to test the configuration parameters for different Reynolds numbers, more test cases have been examined. The calculated and the simulated results including the used operating parameters of the different test cases are presented in Tab. 3.2. In the same table, the average values for Nu_{D1}, Nu_{D2} and Nu_{D3} which have been calculated with (3.1), (3.2) and (3.3), are compared to the average Nusselt numbers of the data in Fig. 3.2 and Fig. 3.3.

The validation of the simulation setup in the present work has been carried out on three different geometries. The measurement setups described in Subsection 3.1.1 have been modeled using CFD for cylinders with diameters $D = 102$ mm as used by [27] and $D = 50$ mm as well as $D = 100$ mm as used by [77]. The wire-frame of one used geometry is shown in Fig. 3.6, including the streamlines from the model inlet to the model outlet.
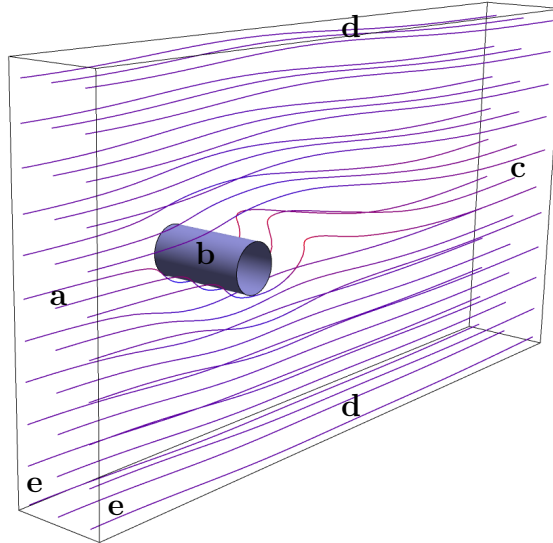
Figure 3.6: Geometry wire-frame and streamlines with (a) the model inlet, (b) the cylinder, (c) the model outlet, (d) the model outflow region and (e) the periodical sectional planes.

The mesh next to the surface of the cylinder has been created with specific properties to achieve a dimensionless wall distance of $y^+ \approx 1$ (see (2.155)) for the highest Reynolds number used with this model. The value of y^+ must be considered during the meshing procedure and defines the initial height y_0 of the cells next to the wall calculated with (2.175). These initial cells have been modeled as a prism layer followed by at least 20 further prism layers with a cell height growth rate of 20% [38]. This

has resulted in a very fine mesh close to the surface of the cylinder and a coarse mesh at other boundaries, illustrated in Fig. 3.7, with a total number of approximately 1.4 million elements and about 0.4 million nodes, respectively.
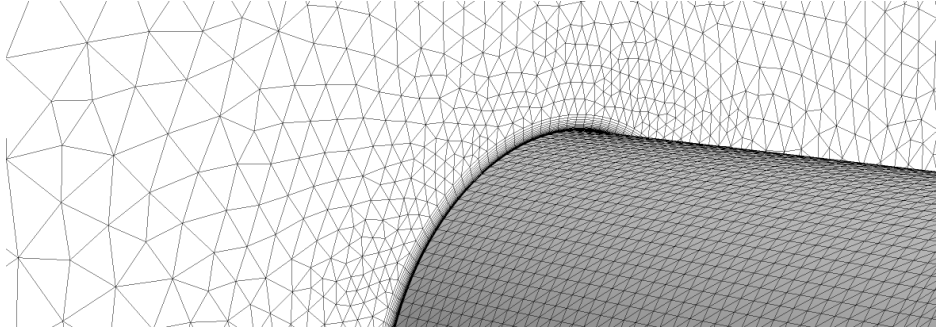
Figure 3.7: Surface mesh of the cylinder and one sectional plane with the inflated mesh on the cylinder.

The surface of the cylinder has been assumed to be a hydraulic smooth wall with non slip condition and a uniform and constant surface temperature of T_w for the test cases shown in [77] or constant wall heat flux $\dot{q}_w$, as used in [27], respectively. The important values for the parameters are listed in Tab. 3.2. A fluid velocity u_∞ normal to the boundary has been defined at the subsonic model inlet with static temperature T_{in} and turbulence intensity I of one percent. The model outflow has been defined as an entrainment with the relative pressure of $p_{out} = 0$ Pa, opening temperature T_{out} and zero gradient turbulence. Test cases which are described in [27] have been modeled with a constant fluid velocity normal to the boundary for the outlet in order to consider the conditions of the wind tunnel. The outlet of the other test cases investigated in [77] has been modeled like the outflow region in order to consider the pressure-driven air flow between the two chambers. Translational periodicity with a general grid interface (GGI) and direct intersection control has been defined for the sectional areas which are perpendicular to the cylinder axis.

The air has been modelled as explained in Section 3.2 with temperature-dependent fluid properties at a referent pressure of $p_{ref} = 10^5$ Pa. The turbulence of the steady state and non buoyant flow simulation has been calculated with the SST turbulence model, including the Gamma-Theta transition model, as introduced in subsection 2.4.4. The transport of energy has been calculated with the total energy equation without calculating the viscose work term. Effects next to the cylinder's wall have been modelled using the automatic wall function which calculates the wall heat flux with (2.172) and resolves the boundary layer according to $y^+ \leq 1$.

The solver has simulated the flow conditions by an upwind advection scheme and high resolution turbulence numerics, using a local time-scale with a factor of five. The solution process has been monitored by the area-weighted average of the wall heat transfer coefficient at the surface of the cylinder. The bulk temperature used for calculating the wall heat transfer coefficient has been set to the same value as the

D	Re	Nu_{avg}	α_{avg}	T_{in}	T_w	$\dot{q}_w$	u_∞	Nu_{D1}	Nu_{D2}	Nu_{D3}	Nu_{CFD}
mm			$\frac{W}{m^2K}$	°C	°C	$\frac{W}{m^2}$	$\frac{m}{s}$	(3.1)	(3.2)	(3.3)	
102	70800	179.3	44.78	12		211	10.15	171.6	181.9	186.1	205.7
102	101300	236.6	59.08	12		211	14.53	217.4	224.1	230.8	268.1
102	140000	360.4	90.00	12		211	20.08			280.2	340.5
102	170000	442.8	110.57	12		211	24.38			314.8	393.8
102	186000	479.6	119.76	12		211	26.67			332.3	422.4
102	219000	515.0	128.59	12		211	31.41			366.4	479.9
050	8290	51.4	24.79	24	100		3.22	48.3	50.9	51.5	61.6
050	21200	93.1	44.85	24	100		8.23	82.0	86.9	90.4	124.2
050	33920	123.9	59.72	24	100		13.16	108.3	113.8	119.9	168.7
050	52800	171.5	82.64	24	100		20.49	142.2	147.0	156.3	225.5
100	15550	74.8	18.03	24	100		3.02	68.6	72.7	75.1	94.9
100	39800	140.7	33.91	24	100		7.72	119.3	124.8	132.0	190.1
100	64450	192.4	46.38	24	100		12.50	161.4	165.1	176.2	261.4
100	101300	265.3	63.94	24	100		19.65	217.2	214.8	231.1	353.3
100	170000	377.3	90.94	24	100		32.98			315.3	498.0
250	39200	119.7	11.54	24	100		3.04	118.2	123.8	130.8	
250	102000	233.5	22.51	24	100		7.92	218.2	215.7	232.1	
250	257600	471.8	45.49	24	100		19.99			411.1	
250	426000	717.9	69.21	24	100		33.06			584.7	

Table 3.2: Parameters according to the investigated Reynolds numbers in [27] and [77] compared to the results of empirical equations of [93, 94] and [97]

ambient temperature T_∞.

3.4 Comparison of simulation results with empirical results

The values of the empirical results discussed in Section 3.1 depend on various parameters of the investigation setup. As described in [27] and [77], the actual setup conditions have been compared to the different approaches of (3.1), (3.2) and (3.3), as shown in Fig. 3.8.

In [27], a wind tunnel brings the fluid in motion and the cylinder is heated electrically, assuring a constant heat flux $\dot{q}_w$ and varying wall temperature T_w at the cylinder's surface. The investigation of [77], on the other hand, uses a pressure driven fluid flow and a constant wall temperature T_w of the cylinder with a varying heat flux $\dot{q}_w$. The fluid properties of air required for the calculation of the air velocities from the Reynolds numbers and for the definition of the Nusselt numbers are available in [77], but they match only partially the fluid properties used in [88]. Compared to [88], the kinematic viscosity of $\nu = 1.94 \cdot 10^{-5}$ corresponds to an average film temperature of $T = 61.7$°C which is the arithmetic average of fluid and wall temperature, but the thermal conductivity of $\lambda = 0.0241$ W/m²K would correspond to a temperature of $T = -3.4$°C. An accurate value for thermal conductivity is required for the calculation

(a) $T_\infty = 12°C$ and $\dot{q}_w = 211\ W/m^2$ (b) $T_\infty = 24°C$ and $T_w = 100°C$
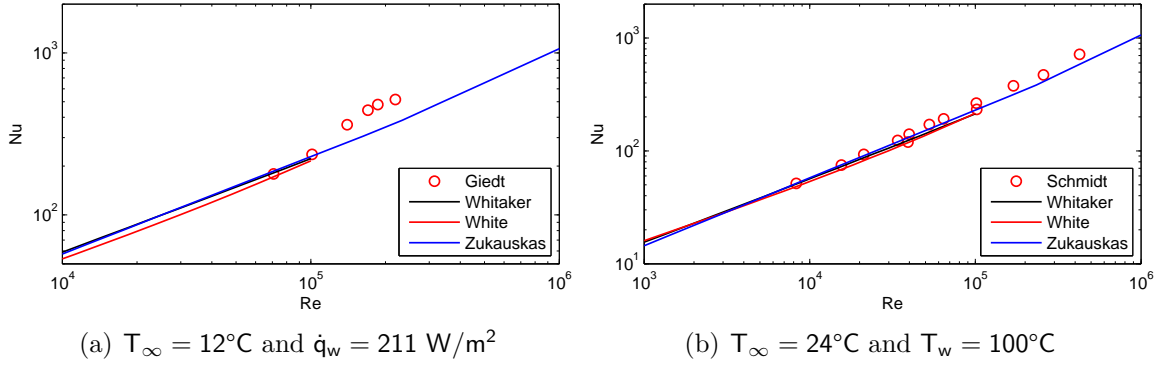
Figure 3.8: Comparison of different empirical results for (a) the setup of Giedt and (b) for Schmidt

of Nusselt numbers comparable to the empirically obtained numbers in [77], hence the thermal conductivity has been changed to a value of $\lambda = 0.0289\ W/m^2K$ corresponding to the same film temperature as the kinematic viscosity. The fluid properties in [27] have not been mentioned and have been calculated from other values. Since the kinematic viscosity ν increases by 74% within the temperature range of $0°C$ to $100°C$ and the thermal conductivity increases by 30%, the lack of precise information about the fluid properties used in these investigations can explain deviations from the simulation results.

(a) $Re = 70\,800$ (b) $Re = 101\,300$
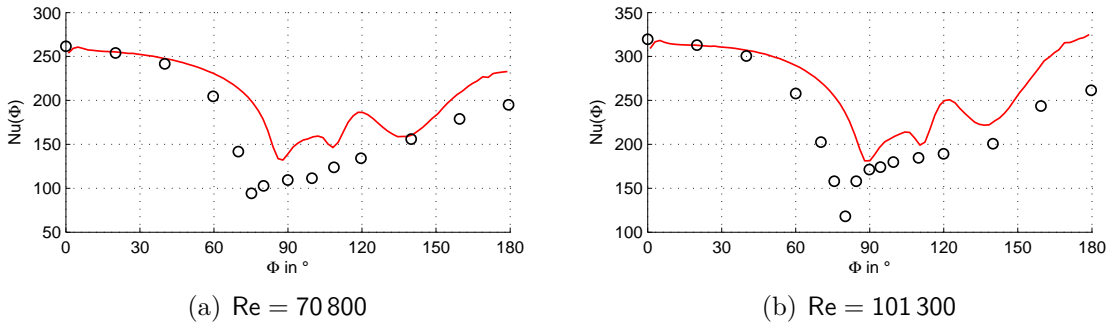
Figure 3.9: Simulation results for different Reynolds numbers shown as solid line compared to the results in [27] shown as circles using a cylinder with a diameter of $D = 102\ mm$

The diagrams in Fig. 3.9 show a comparison between the measured values of [27] and the results simulated by CFD. At the Reynolds numbers of $Re = 70\,800$ and $Re = 101\,300$ the prediction is consistent with the empirical results at the leading stagnation point. The point of flow separation, which can be identified by the lowest Nusselt number at an angle of about $80°$, has been estimated by CFD at a higher angle than measured. The predicted results in the wake area are higher but still comparable. At higher Reynolds numbers of $Re \geq 140\,000$ the prediction starts to get less accurate for both zones: the attached flow at the leading stagnation point and the wake space behind the cylinder.

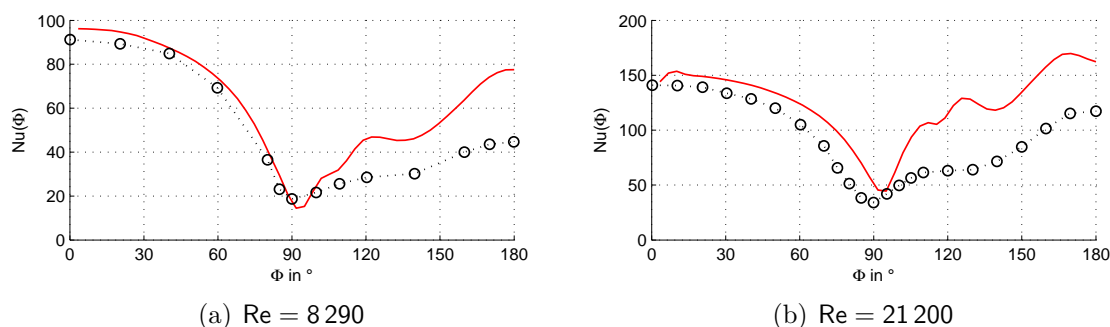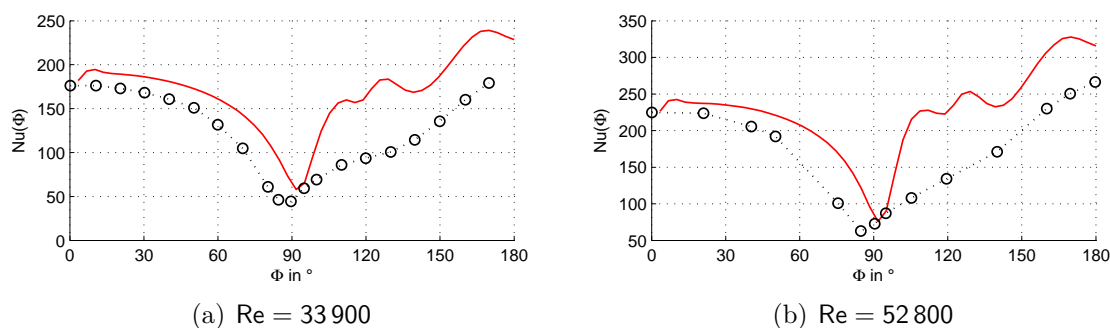(a) Re = 140 000

(b) Re = 170 000
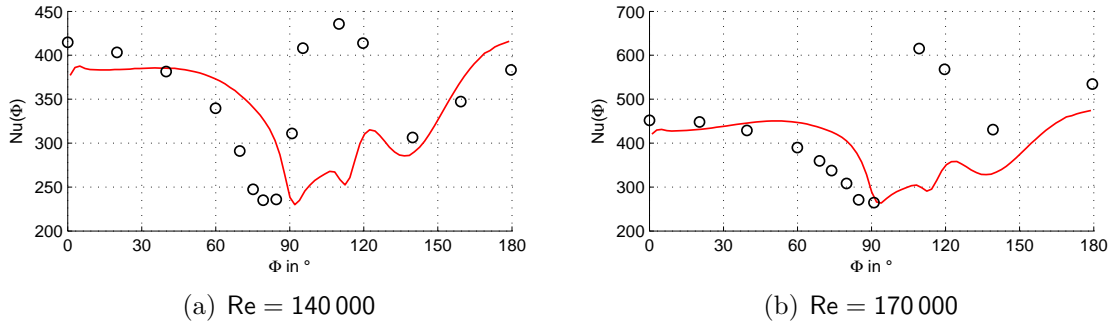
Figure 3.10: Simulation results for different Reynolds numbers shown as solid line compared to the results in [27] shown as circles using a cylinder with a diameter of D = 102 mm
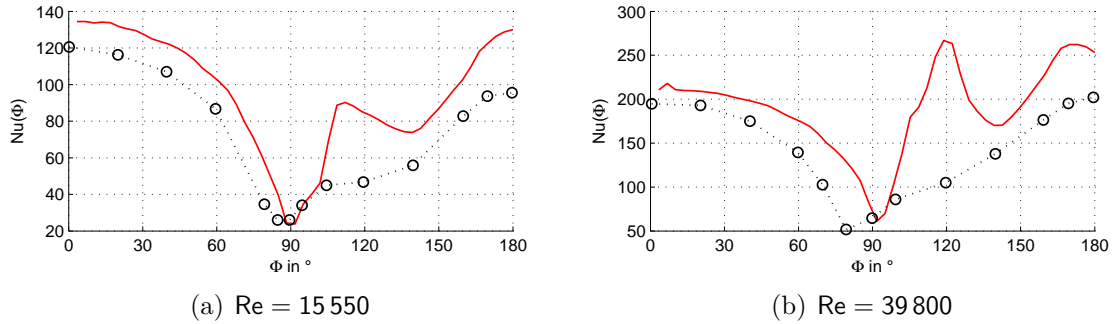

(a) Re = 186 000

(b) Re = 219 000
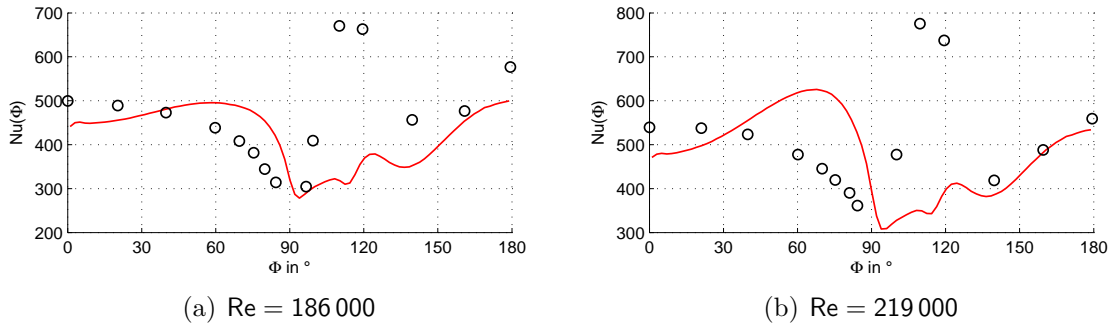
Figure 3.11: Simulation results for different Reynolds numbers shown as solid line compared to the results in [27] shown as circles using a cylinder with a diameter of D = 102 mm

Compared to the investigations of [77], the prediction with CFD shows good agreement at very low Reynolds numbers as shown in Fig. 3.12. The difference between the measured and the simulated results at the leading stagnation point can be explained with incomplete or incorrect information about the used fluid parameters in [77]. Even the angle where flow separation occurs matches the measured results and the Nusselt number is predicted with an accurate magnitude. In the wake area, the values become less consistent with the empirical data with an over-prediction of magnitude.

At higher Reynolds numbers, the consistency between simulated and measured values of the point of flow separation deteriorates. The simulation tends to estimate the separation point about 10° behind the measured point but the magnitude of heat transfer at this point is estimated with good accuracy even for higher Reynolds numbers. Regarding the mean heat transfer in the downstream area of fluid flow, the relative error of simulated and measured results is smaller for higher Reynolds numbers as shown in Fig. 3.13 than it is for lower Reynolds numbers as shown in 3.12.

Since the characteristic length is not as obvious for the end-windings of an electrical machine as it is for a cylinder, a single Reynolds number for a certain rotational speed can hardly be specified. Basically, two different flow conditions can be identified at the end-windings of the investigated type of motor, where a Reynolds number can be

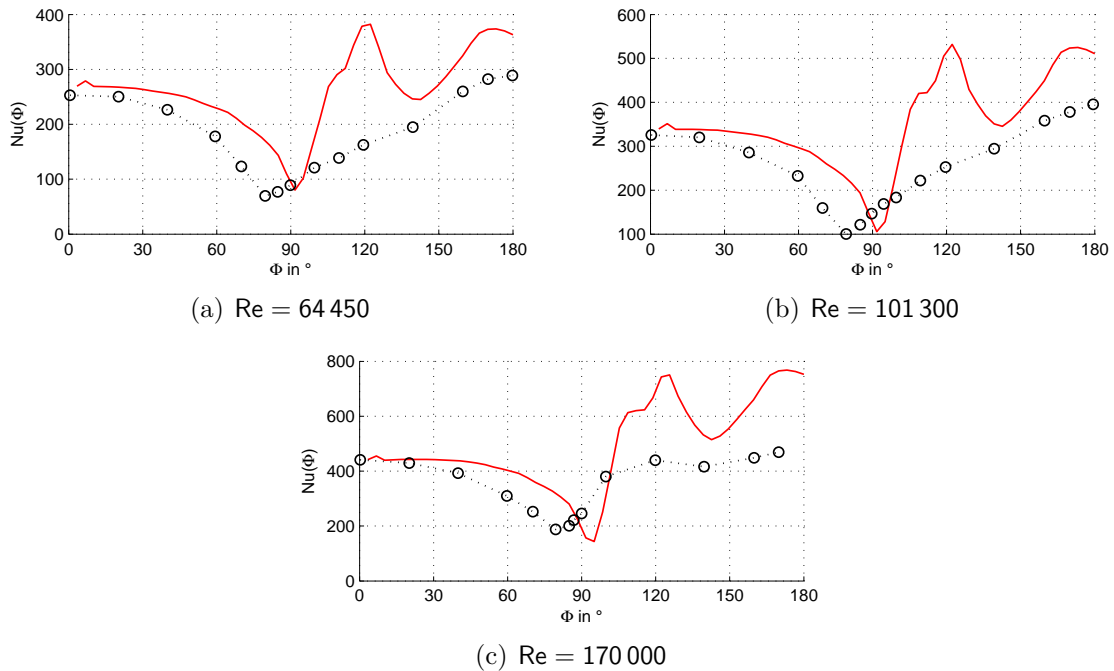(a) Re = 8 290

(b) Re = 21 200

Figure 3.12: Simulation results for different Reynolds numbers shown as solid line compared to the results in [77] shown as circles using a cylinder with a diameter of D = 50 mm

(a) Re = 33 900

(b) Re = 52 800

Figure 3.13: Simulation results for different Reynolds numbers shown as solid line compared to the results in [77] shown as circles using a cylinder with a diameter of D = 50 mm

defined theoretically by comparing the flow conditions with a flow parallel to a plate. On the one hand, the angular speed of the rotor is causing a high velocity of air next to the end-windings. In this azimuthal direction, the width of the conductors can be chosen as characteristic length. On the other hand, the air coming from the cooling ducts flows in axial direction over the end-windings. In this case, the overhang of the end-windings is a proper characteristic length. Considering these two flow conditions independently, the maximum Reynolds number will not exceed the value of Re = 10^5.

(a) Re = 15 550

(b) Re = 39 800

Figure 3.14: Simulation results for different Reynolds numbers shown as solid line compared to the results in [77] shown as circles using a cylinder with a diameter of D = 100 mm

(a) Re = 64 450

(b) Re = 101 300

(c) Re = 170 000

Figure 3.15: Simulation results for different Reynolds numbers shown as solid line compared to the results in [77] shown as circles using a cylinder with a diameter of D = 100 mm

3.5 Global-local domain decomposition method

As shown in the previous section, the calculation of the wall heat transfer requires a very fine resolution of the mesh close to the surface. Due to the large surface area, a properly resolved mesh of the whole end region of the investigated induction motor would contain about 12 million finite volume cells which might exceed the computational possibilities. In order to adopt the convective heat transfer problem to the computational resources, a method is required which can simulate the heat transfer problem piece by piece. This leads to the idea of the global-local domain decomposition method, allowing simulation of fluid flow on a coarse mesh and simulation of the wall heat transfer coefficient on a fine mesh but only at specific locations. In order to test its validity, the heat transfer coefficient of the same cylindrical geometry has been calculated as in Section 3.3 by using the global-local domain decomposition method. Both the global and the local models are shown in Fig. 3.16. The global model on the

(a) Global model with boundary mesh of local model   (b) Local model
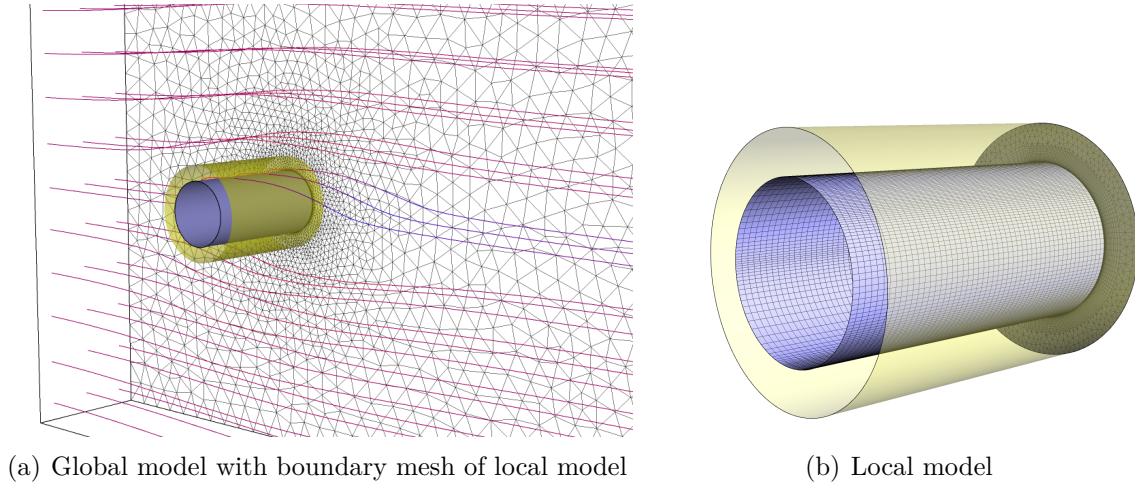
Figure 3.16: (a) Streamline, cylinder and boundary area from local model in the global model and (b) cylinder in the local model

left hand side shows streamlines starting from the model inlet (left), the surface mesh of the back sectional plane, the cylinder and the location of the boundary mesh from the local model. On the right hand side of Fig. 3.16, the local model is shown with the shaded boundary interface and the surface meshes of the back sectional plane and the cylinder.

The boundary conditions for the fine local mesh are taken from the flow simulation on the coarse global mesh by transferring the velocity components for all Cartesian coordinates u, v, w, the temperature T, the turbulence kinetic energy k and the turbulence eddy dissipation ε from the coarse mesh to the boundary of the fine mesh. Once a solution for the coarse mesh is available, the boundary node coordinates of the fine mesh can be used for a user defined area to export the velocity, temperature and turbulence variables to boundary condition profiles, as shown in Fig. 3.17.

(a) Velocities u, v, w

(b) Temperature T

(c) Turbulence kinetic energy k

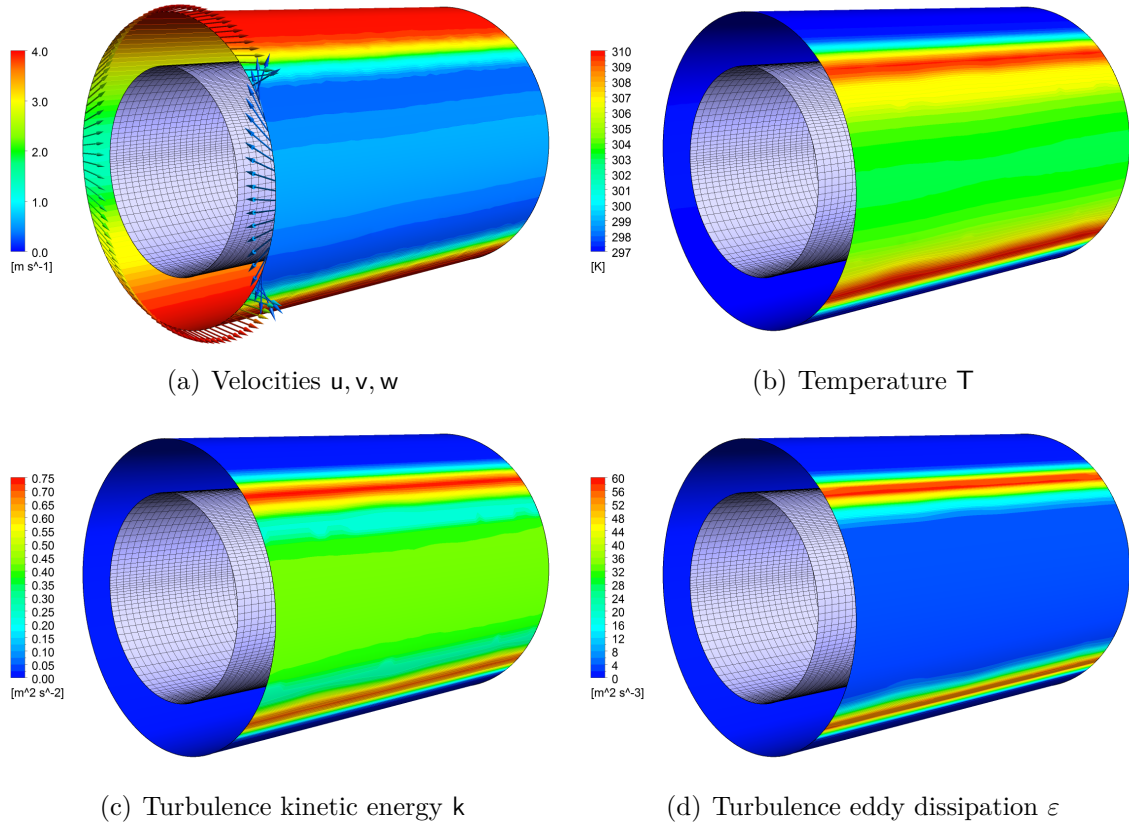(d) Turbulence eddy dissipation ε

Figure 3.17: Boundary conditions transfer from the global to the local model for a Reynolds number of $Re = 15\,550$

The local model has been solved with the configuration described in Section 3.3. Due to the fine mesh resolution but small total size of the local mesh, the convective wall heat transfer coefficient can be simulated with acceptable accuracy in a reasonable period of time. The results of simulated wall heat transfer coefficients are shown in Fig. 3.18 and Fig. 3.19, respectively.

The diagrams shown in Fig. 3.19 compare the results of the domain decomposition method with the results from the simulation in 3.4 and the empirical results. A noticeable detail is the higher wall heat transfer coefficient between the angles of $\Phi = 20°$ and $\Phi = 70°$. Nevertheless, the results of the domain decomposition method in the wake area reproduce the empirical results with higher accuracy than without domain decomposition. Especially at low Reynolds numbers, this method generates good results with small errors, as shown in Fig. 3.19 (a).
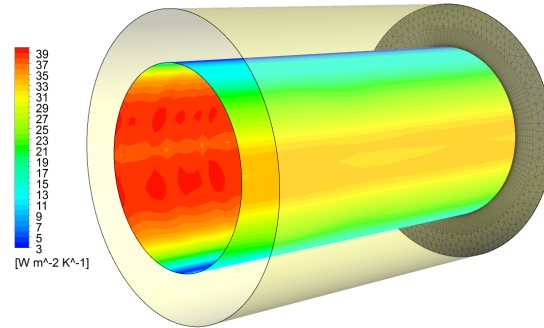
Figure 3.18: Simulated wall heat transfer coefficient at the cylindric surface of the local model with Reynolds number of $\mathsf{Re} = 15\,550$

(a) $\mathsf{Re} = 15\,550$

(b) $\mathsf{Re} = 38\,900$

(c) $\mathsf{Re} = 64\,450$

(d) $\mathsf{Re} = 101\,300$
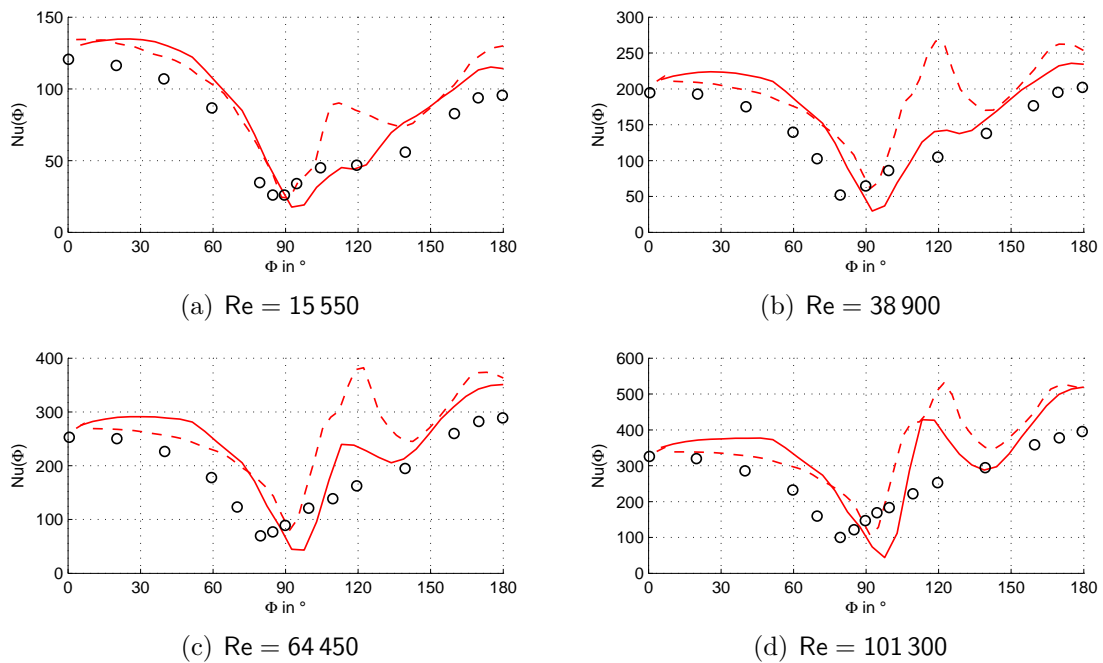
Figure 3.19: Results of global-local domain decomposition calculation for different values of the Reynolds number (solid lines), results calculated without domain decomposition (dashed lines) and empirical results as published in [77] (circles)

Chapter 4

Measurements at the end-region

Despite the opportunities presented in the previous chapters, a totally reliable model for predicting the convective heat transfer coefficient is not available yet. It is still necessary to validate the derived values under certain operating conditions by measurements. On the one hand, the results of this chapter are required for specifying accurate operation parameters for the simulations. On the other hand, the measured heat transfer values are necessary for the validation of numerical results. Since the investigated fluid flow is inside the closed cooling cycle of an induction machine, the operation parameters for the simulation such as mass flow or temperature cannot be obtained easily. By measuring the static pressure inside one cooling duct of the induction machine, the air velocity inside this cooling duct has been identified for different rotational speeds of the motor. For these different operational conditions, the wall heat fluxes at several positions on the end-windings have been measured to obtain points of comparison for the simulations presented in Chapter 5.

4.1   Investigated motor

The measurements have been carried out on an induction motor designed to be used as a traction motor in a tramway, as sketched in Fig. 4.1. The motor with a rated power of 120 kW at a rated speed of 2290 rpm has been designed to work in the whole range of rotational speeds up to 4230 rpm in both rotational directions. The cooling type of the machine is a so called double air cooled system (DACS) or IC 5A1A1, respectively, as presented in Subsection 2.1.4. The cooling of the machine under investigation is based on an inner air-circuit consisting of cooling ducts which pass through the rotor as well as the stator and driven by an axis-mounted fan. This is a closed circuit and thus protects the rotor and the stator end-region from contaminating dust. By means of this circuit, the rotor losses and the losses in the end-winding region of the machine are transferred to the stator yoke. Another axis-mounted fan discharges air through a set of cooling ducts which are located radially outward of the inner-circuit ducts. The air flow of this path is loaded with the iron losses and copper losses of the stator and
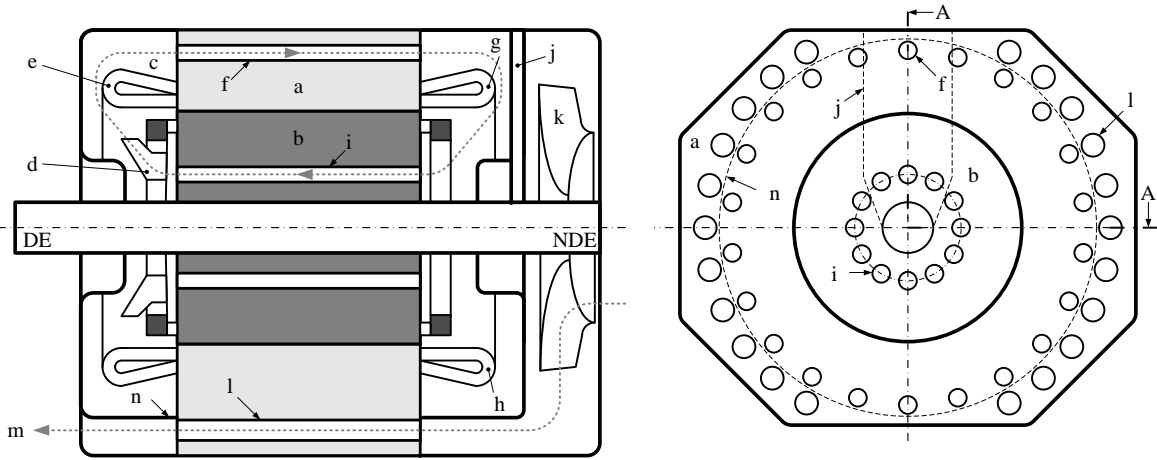
73

Figure 4.1: Longitudinal section (A-A) and cross section of the investigated DACS motor with (a) stator iron, (b) rotor iron, (c) path of inner cooling circuit, (d) fan of the inner cooling circuit, (e) end-windings of the motors drive end, (f) cooling ducts of the inner cooling circuit in the stator, (g,h) end-windings of the motors non drive end, (i) cooling ducts of the inner cooling circuit in the rotor, (j) waste grease drain, (k) fan of the outer cooling circuit, (l) stator cooling ducts of outer cooling circuit in the stator, (m) path of outer cooling circuit and (n) separation between inner and outer cooling circuit

the losses handed over from the inner circuit. This is an open cooling circuit which releases the heated air to the environment. In this investigation, only the inner cooling circuit on the non drive end side (NDE) has been examined. The separation between the inner and the outer cooling cycle is indicated by a dashed line on the right hand side of Fig. 4.1. Due to the asymmetric shape of the end-shield, differences in the heat flux of different conductors can be expected. The heat flux has been measured on eight different conductors of the end-windings with four pairs of heat flux sensors, each pair mounted at identical positions on different conductors. Two of these positions are labeled (g) and (h) in Fig. 4.1. The waste grease drain which causes the asymmetry of the end-shield is labeled (i) [36, 41, 42].

4.2 Determining the air mass flow in the machine

It is necessary to know the air mass flow $\dot{m}$ in the cooling duct, in order to use it as operation parameters in the simulation of the heat transfer values, presented in Chapter 5. By measuring the loss of static pressure in the cooling ducts, the velocity and hence the air mass flow can be calculated. Since the cooling ducts of the present machine are parts of the laminated stator and rotor iron, a specific roughness exists at their surfaces. Therefore the ducts cannot be considered as hydraulically smooth and their roughness has to be taken into account in the calculation of the air mass flow $\dot{m}$.

4.2.1 Determining the duct roughness

Due to the lamination of the stator sheets, the surfaces of the inner and outer cooling ducts have the same absolute roughness k_s in m [88]. The roughness has been determined by measuring the pressure loss along one outer cooling duct and the total air mass flow $\dot{m}_{to}$ of the outer cooling circuit. Uniform flow conditions in all cooling ducts of the same size of the outer cooling circuit have been assumed and manufacturing tolerances have been neglected. The used measuring setup is shown in Fig. 4.2. It allows the measurement of the total air mass flow of the outer cooling circuit. The ambient
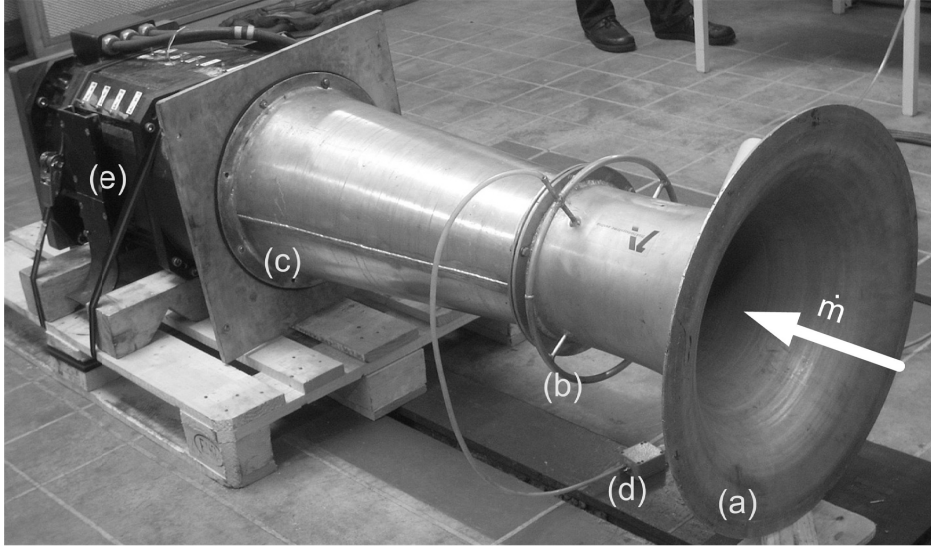
Figure 4.2: Setup for measuring the total air mass flow $\dot{m}_o$ of the outer cooling circuit with (a) the air inlet, (b) four pressure probes at the narrowest position of the cone, connected by a ring-like pipe, (c) the air inlet, (e) the investigated traction motor and (d) the pressure transducer, which has been connected to an analog digital converter. The measurements have been carried out at *Traktionssysteme Austria GmbH*

temperature and ambient pressure have remained constant during the measurements at values of $T_a = 28°C$ and $p_a = 95\,600$ Pa respecitvely. Using the ideal gas law

$$\rho = \frac{p}{R_s \cdot T} \ , \tag{4.1}$$

the density $\rho = 1.106$ kg/m^3 has been calculated with the ideal gas constant for air $R_s = 287.12$ J/kgK and the prevailing temperature. The kinematic viscosity $\nu = 1.608 \cdot 10^{-5}$ m^2/s has been obtained for the specific temperature by interpolating listed values for dry air in [88].

The outer cooling circuit consists of two different types of cooling ducts with diameters d_{oA} and d_{oB}, total numbers n_{oA} and n_{oB} and cross sectional areas A_{oA} and A_{oB}, respectively[1]. Since the measurements have been taken at a cooling duct with

---

[1]Since most calculation steps have to be accomplished for both types of ducts, the index of the variables has been changed to ox for these steps, to represent oA or oB.

diameter d_{oA}, the iterative calculation of the roughness is based on cooling ducts of type A. The initial value for the air mass flow $\dot{m}_{ox}$ and hence the velocity v_{ox} in the cooling ducts have been determined by the total air mass flow $\dot{m}_{to}$, density ρ and the total sum of cross sectional areas of all cooling ducts.

$$v_{ox}^{(0)} = \frac{\dot{m}_{to}}{\rho(n_{oA}A_{oA} + n_{oB}A_{oB})} \; . \tag{4.2}$$

The iterative solution of the roughness starts with the calculation of the Reynolds numbers $Re_{ox}^{(i)}$ for both types of cooling ducts with (2.65) for all rotational speeds using the hydraulic diameters d_{ox} and velocities v_{ox} as parameters. Since the pressure losses have been measured between positions along the cooling duct, the pressure loss coefficients for the inlet and the outlet can be disregarded. Without these additional losses at the inlet and the outlet the pressure losses in these cooling ducts can be described by the Darcy-Weissbach equation [14]

$$\Delta p_o = \lambda_{fo} \frac{l}{d_o} \frac{\rho}{2} v_o^2 \; , \tag{4.3}$$

with the pipe length l between the considered positions for the pressure difference Δp_o and the Darcy friction factor of the pipe-flow λ_{fox}. The friction factor has been calculated by re-arranging (4.3):

$$\lambda_{fox}^{(i)} = \frac{2 \, \Delta p_o \, d_{ox}}{l \, \rho \left(v_{ox}^{(i)}\right)^2} \tag{4.4}$$

and hence the roughness k_s has been solved by the re-arranged Colebrook and White equation [88] with the values for the cooling circuit of type A

$$k_s^{(i)} = \frac{d_{oA}}{2} \left(10^\gamma - \frac{18.574}{Re_{oA}^{(i)} \sqrt{\lambda_{foA}^{(i)}}}\right) \qquad \text{with} \qquad \gamma = 0.5 \left(1.7384 - \frac{1}{\sqrt{\lambda_{foA}^{(i)}}}\right) \; . \tag{4.5}$$

Since the roughness and the friction factor of a cooling duct do not change with the operational conditions, the mean values for the various operational conditions $\bar{k}_s^{(i)}$ and $\bar{\lambda}_{foA}^{(i)}$ have been used for iteratively re-calculating the friction factor with the Colebrook and White equation:

$$\frac{1}{\sqrt{\bar{\lambda}_{fox}^{(j+1)}}} = 1.7384 - 2 \log \left(\frac{2 \, \bar{k}_s^{(i)}}{d_{ox}} + \frac{18.574}{Re_{ox}^{(i)} \sqrt{\bar{\lambda}_{fox}^{(j)}}}\right) \; . \tag{4.6}$$

The new velocity for the type B cooling ducts has been calculated by

$$v_{oB}^{(i)} = \sqrt{\frac{2 \, \Delta p_o \, d_{oB}}{l \, \rho \, \bar{\lambda}_{foB}^{(i)}}} \; , \tag{4.7}$$

and the velocity of the type A cooling ducts by subtracting the air mass flow in the type B ducts from the total air mass flow $\dot{m}_{to}$

$$v_{oA}^{(i)} = \frac{\dot{m}_{to}/\rho - n_{oB}\,A_{oB}\,v_{oB}^{(i)}}{n_{oA}\,A_{oA}} \ . \tag{4.8}$$

Using these new velocities, the next iteration step can be derived by re-starting with the calculation of the Reynolds numbers and the friction factor in (4.4).

The roughness has been calculated using the pressure probe values between the first and the fourth, the second and the fourth and the first and third positions. According to the positions, the values of the lengths have been changed to $l = 0.112$ m (for II-IV and I-III) and $l = 0.168$ m (for I-IV), respectively. The obtained average value of the

f	v_{oB}	v_{oA}	Re_{oA}	I-IV			II-IV			I-III			
				Δp	λ_{foA}	k_s	Δp	λ_{foA}	k_s	Δp	λ_{foA}	k_s	
Hz	m/s	m/s		Pa	10^{-2}	mm	Pa	10^{-2}	mm	Pa	10^{-2}	mm	mm
50	13.5	15.6	25357	37	4.32	0.333	21	3.68	0.188	25	4.38	0.347	
60	16.4	19.1	31176	54	4.17	0.305	30	3.48	0.159	35	4.06	0.278	
70	19.4	22.6	36903	75	4.14	0.302	44	3.64	0.196	49	4.05	0.283	
80	21.7	25.8	42121	94	3.98	0.271	52	3.30	0.139	62	3.94	0.262	
90	24.5	29.0	47251	119	4.00	0.279	68	3.43	0.165	79	3.99	0.275	
100	27.3	32.0	52084	147	4.07	0.297	83	3.45	0.170	97	4.03	0.287	
110	30.2	34.4	56151	180	4.29	0.349	102	3.64	0.209	122	4.36	0.367	
$\bar{k}_s$ in mm						0.305			0.175			0.300	0.260

Table 4.1: Calculation of the average roughness of cooling ducts

cooling duct roughness $\bar{k}_s$ is the arithmetic mean value of all derived values in Tab. 4.1. Since, for the calculation of the air mass flow, the inner and the outer cooling ducts have been assumed to be uniform, the average roughness can be used for the cooling ducts of the inner and the outer cooling cycle [42].

4.2.2 Air mass flow in the inner cooling cycle

The parts of the inner cooling circuit are encapsulated by the end-shields and cannot be accessed during the operation of the machine. A particular construction is necessary in order to obtain values which characterize the air mass flow in the inner cooling circuit. This construction is sketched in Fig. 4.3.

Four holes have been drilled at equidistant positions along one cooling duct labeled (f) in Fig. 4.1. Other cooling ducts of the inner cooling cycle and the same type, at different circumferential positions, are not accessible during operation of the machine. Beside the holes offering access to the cooling duct, two holes have been drilled in each end-shield. Pressure probe pipes have been placed in these drill holes, in order to measure the static pressure in the positions shown in Fig. 4.3. The pressures have been measured at certain rotational speeds of the motor, with a fully signal-conditioned pressure transducer measuring in the range of ± 500 Pa with non-linear properties and
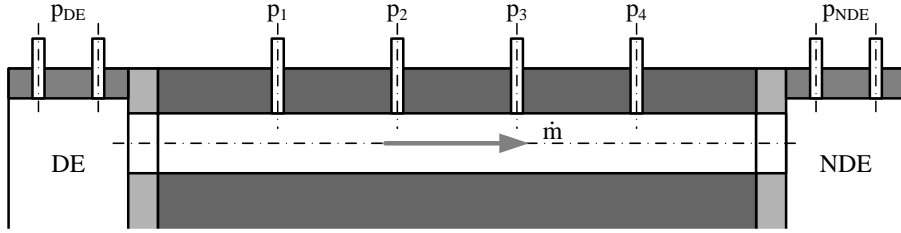
Figure 4.3: Longitudinal section of a cooling duct with attached pressure probes. The air mass flow $\dot{m}$ inside the duct can be derived by the measured pressure loss $\Delta p = p_1 - p_4$

hysteresis of 0.1%. By electronically collecting more than 100 pressure values within a time period of about 10 seconds, a mean value of the relative pressure between the pressure probes shown in Tab. 4.2 has been estimated for further calculations. As shown in Fig. 4.4, the loss of static pressure inside the cooling ducts changes linearly in relation to the position along the length of the ducts even for turbulent flow conditions, allowing extrapolation of the static pressure at the inlet of the cooling duct.
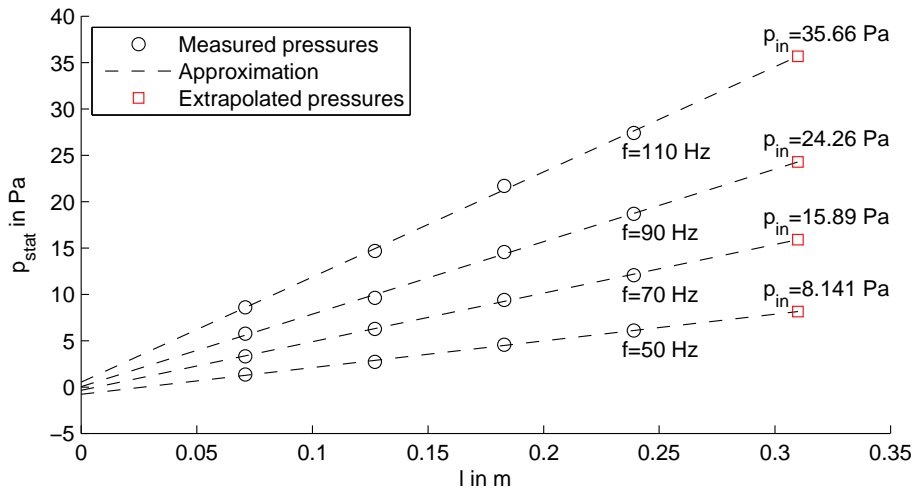
Figure 4.4: Loss of static pressure along the cooling ducts for different frequencies f of supply current and corresponding rotational speeds.

For the calculation of the air mass flow in the inner circuit, it is necessary to determine the pressure loss $\Delta p_i = p_{i1} - p_{i4}$ inside the cooling duct, as well as the diameter d_i of the cooling duct, the distance l between the pressure probes of p_{i1} and p_{i4}, the kinematic viscosity ν of air at fluid temperature T_f and the roughness k_s of the inner surface of the cooling duct. With an initial estimation of the velocity $v_i^{(0)}$ in the cooling duct, the air mass flow has been calculated by an iterative refinement of the velocity

$v_i^{(k)}$. One iteration step k consists of the calculation of the Darcy friction factor

$$\lambda_{fi}^{(k)} = \frac{2 \, \Delta p_i \, d_{ki}}{l \rho \left(v_i^{(k)} \right)^2} \, , \tag{4.9}$$

the Reynolds number

$$Re_i^{(k)} = \frac{v_i^{(k)} \, d_{ki}}{\nu} \, , \tag{4.10}$$

the Darcy friction factor $\lambda_{fi}^{(k+1)}$ by the Colebrook-White equation

$$\frac{1}{\lambda_{fi}^{(k+1)}} = \left(1.7384 - 2 \log \left(\frac{2 \, k_s}{d_{ki}} + \frac{18.574}{Re_i^{(k)} \sqrt{\lambda_{fi}^{(k)}}} \right) \right)^2 \tag{4.11}$$

and the velocity inside the cooling ducts with

$$v_i^{(k+1)} = \sqrt{\frac{2 \, \Delta p_i \, d_{ki}}{\lambda_{fi}^{(k+1)} \, l \, \rho}} \, . \tag{4.12}$$

Once the change of the friction factor between two consecutive iterations is below a tolerance (this usually occurs in less than ten iterations), the air mass flow in one cooling duct of the inner cooling cycle $\dot{m}_i$ can be calculated by

$$\dot{m}_i = v_i \, \rho \, A_i \, , \tag{4.13}$$

where ρ is the density of air at a certain temperature and A is the cross-sectional area of the cooling duct [42]. The results for air velocity and air mass flow in one cooling duct is listed in correspondence with the measured pressures in Tab. 4.2.

				static pressure probes					calculated			
f	T_a	T_m	p_a	p_{i1}	p_{i2}	p_{i3}	p_{i4}	p_{DE}	ρ	Re	v	$\dot{m}_i$
Hz	°C	°C	hPa	Pa	Pa	Pa	Pa	Pa	kg/m^3		m/s	g/s
50	29.0	76.3	945	1.35	2.72	4.57	6.10	24.27	0.942	3 159	4.13	0.782
70	25.1	75.1	944	3.32	6.27	9.39	12.07	48.11	0.944	4 417	5.74	1.089
90	28.1	70.5	956	5.75	9.63	14.55	18.69	80.00	0.969	5 503	6.98	1.360
110	28.1	67.0	956	8.60	14.67	21.70	27.41	118.00	0.979	6 796	8.47	1.667

Table 4.2: Relative static pressure at different positions of the inner cooling cycles cooling duct compared to the static pressure p_{NDE} in the end-shield of the non drive end side including flow properties at average temperature $T_m = (T_f + T_w)/2$.

4.3 Heat flux measurement

The heat flux density $\dot{q}$ from the end-windings to the surrounding air has been measured using thermopiles as heat flux sensors at specific positions of eight end-winding conductors at the non drive end side of the motor.

Due to the size of the investigated motor, the end-windings offer some areas where heat flux sensors can be applied. Depending on the type of sensor, it is either permitted to only slightly bend the sensor for application or it is recommended not to bend it at all. Therefore, the application surface has to offer a planar area where the sensor can be applied which, in this case, has dimensions of 10×30 mm or 5×60 mm, respectively. A smaller sensor would be desirable, but due to the measuring principle, a certain sensor area is necessary to achieve a gaugeable signal. The heat flux sensors have been fixed to the surface with a special type of glue which withstands operational temperatures of up to 150°C [51].

Due to the asymmetry of the end-shield, the two heat flux sensors in each pair have been placed at identical positions on different conductors as sketched in Fig. 4.1 where measuring point HFS-5 is labeled (g) and measuring point HFS-6 is labeled (h). For an accurate calculation of the heat transfer coefficient α, the fluid temperatures T_f
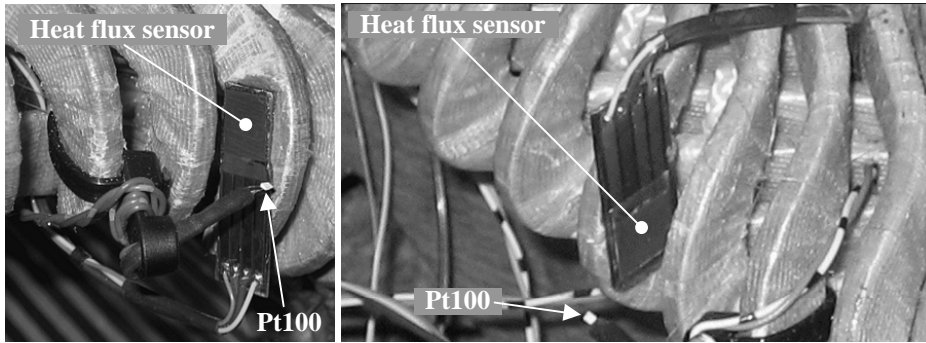
Figure 4.5: Measuring points HFS-5 and HFS-6 at opposite conductors of the end-windings

have been measured by Pt100 temperature sensors next to the surface of the heat flux sensors. The wall temperatures T_w have been measured by separate thermocouples inside the heat flux sensors shown in Fig. 4.5. Based on these measured values, the convective heat transfer coefficient α can be derived as

$$\alpha = \frac{\dot{q}}{T_w - T_f},\tag{4.14}$$

if forced convection and homogeneous wall and fluid temperature can be assumed [33].

4.3.1 Heat flux sensor

The used heat flux sensors consist of a polymeric plate as a substrate with known thickness h and thermal resistance R_{th}. As shown in Fig. 4.6, the top and bottom sides of this plate are covered by thermocouples individually connected through the substrate to a thermopile. The heat flux sensors shown in Fig. 4.5 and used in this investigation utilize Type-T thermocouples for measurement. The sensitivity of the heat flux sensor depends on the number of thermocouples in the thermopile and thus
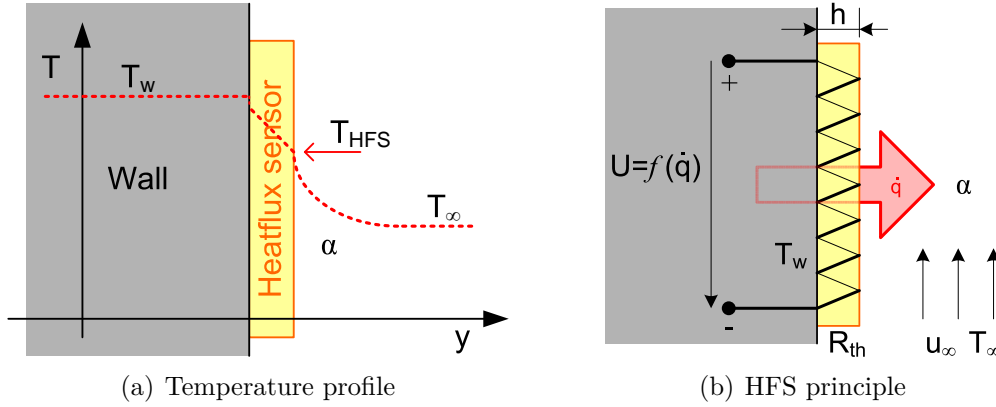
(a) Temperature profile   (b) HFS principle

Figure 4.6: Schematic sketch of a heat flux sensor in cross-sectional view with free stream velocity u, free stream temperature T_∞ (= T_f), wall temperature T_w, thermal resistance R_th, sensor thickness h, sensor output voltage U and heat flux $\dot{\mathsf{q}}$

the sensor area. In this investigation, sensors with areas of $100~\mathsf{mm}^2$ and $250~\mathsf{mm}^2$ and sensitivities of about $\mathsf{K}_\mathsf{HFS} = 0.6\mu\mathsf{V}/(\mathsf{W}/\mathsf{m}^2)$ and $\mathsf{K}_\mathsf{HFS} = 1.5\mu\mathsf{V}/(\mathsf{W}/\mathsf{m}^2)$, respectively, have been used. One separate Type-T thermocouple inside the heat flux sensors, which is not connected to the thermopile, is used to measure the surface temperature T_w. This value is necessary for the calculation of the convective wall heat transfer coefficient α from the measured heat flux $\dot{\mathsf{q}}$ as in (4.14) [37].

4.3.2 Power supply

The measurements have been completed for several different rotational velocities of the rotor, operated in no-load conditions. In order to achieve higher temperatures in the end-region, the motor has been overexcited.

Since the used heat flux sensors generate a signal in the range of some millivolts and are connected to the measuring amplifier by a two-wire circuit, they are sensitive to induced interference voltages. In order to avoid such interferences, the operation has been accomplished without an inverter for the power supply. As shown in Fig. 4.7, the operation power has been generated by a machine unit with Ward Leonard Speed Control System, which is capable of generating three-phase sinusoidal voltage of up to $\mathsf{U}_\mathsf{m} = 630~\mathsf{V}$ and a frequency up to $\mathsf{f} = 100~\mathsf{Hz}$. The induction motor on the left hand side of Fig. 4.7 is connected to the public electric network. It mechanically drives a DC generator which, in turn, supplies a DC motor. A synchronous generator creates the electric power for the investigated motor shown on the right hand side of Fig. 4.7. The frequency f has been changed by regulating the excitation of the DC motor, while the voltage U_m has been controlled with the excitation of the synchronous generator.

Using a 30 channel data acquisition system, all signals for temperature and heat flux have been simultaneously measured, digitally converted and stored including a time stamp for each time step of $4~\mathsf{s}$. In order to collect approximately one hundred
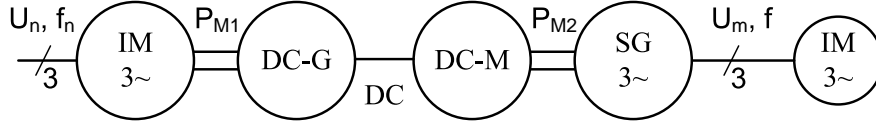
Figure 4.7: Schematic diagram of the power converting machine unit with Ward Leonard Speed Control System

sets of data for each operating point of the machine, the voltage and frequency have been held constant for several minutes.

4.3.3   Thermal resistance of the sensor

As generally known, any sensor affects the measured physical value. In the present case, the heat flux density is measured by the temperature difference between the top and bottom surface of the heat flux sensor, which means that the measured wall temperature deviates from the real wall temperature. This difference is necessary to measure the heat flux through the sensor, but it leads to an error in the calculation of the heat transfer coefficient.

The thermal resistance from the conductors surface to the environmental air consists of the thermal resistance of the insulation $R_{th\,I}$ and the thermal resistance of the convective heat transfer $R_{th\,C}$. Assuming that the used glue has approximately the same thermal conductivity as the conductors' insulation (resin), the thermal resistance of the heat flux sensor $R_{th\,H}$ will additionally affect a small portion of the conductors' surface where the heat flux sensor is mounted. Therefore the overall thermal resistance of the conductor is $R_{th1} = R_{th\,I} + R_{th\,C}$, and $R_{th2} = R_{th\,I} + R_{th\,H} + R_{th\,C}$ for the sensor area, respectively. As the heat transfer coefficient α increases, the thermal resistance of convection decreases. However, due to the rising heat flux density $\dot{q}$, the influence of the thermal resistance of the heat flux sensor $R_{th\,H}$ becomes ascending, resulting in greater errors for higher heat transfer coefficients.

The surface area not covered by the heat flux sensor has been assumed to be five times higher than the area of the heat flux sensor. A relative thermal resistance of the heat flux sensor has been specified by the manufacturer with $r_{thH} = 4 \cdot 10^{-4}$ Km^2/W. Assuming the thermal conductivity of the insulation is $\lambda_I = 0.25$ W/mK and its thickness is $l_I = 1$ mm, one can calculate the total thermal resistance $R_{th\,wH}$ with the heat flux sensor and $R_{th\,woH}$ without the heat flux sensor with:

$$R_{th} = \frac{r_{th}}{A} = \frac{l}{A\,\lambda} = \frac{1}{A\,\alpha} = \frac{\Delta T}{P_{th}} \tag{4.15}$$

The higher the value of the convective heat transfer coefficient α, the greater the relative error of the thermal resistance $E_{Rth} = (R_{thwH} - R_{thwoH})/R_{thwoH}$, as shown in Tab. 4.3.

α	$R_{th\,C1}$	$R_{th\,C2}$	$R_{th\,wH}$	$R_{th\,woH}$	E_{Rth}
W/m^{2}K	K/W	K/W	K/W	K/W	%
10	200	1000	173.44	173.33	0.064
200	10	50	15.11	15.00	0.714

Table 4.3: Example of the relative error of thermal resistance at high and low values of the heat transfer coefficient
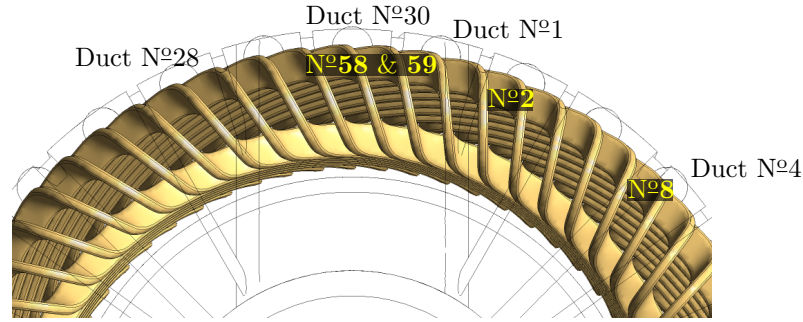
4.3.4 Sensor positions

Figure 4.8: Front view at the end-windings with numbering order of cooling ducts and conductors

In order to identify the positions of the sensors, the conductors have been numbered from №1 to №60 and the cooling ducts from №1 to №30, respecively. Looking axially at the end-windings, the numbering of the cooling ducts starts next to the top position counting clockwise, as shown in Fig. 4.8. The conductors are numbered in the same way as the cooling ducts and according to the stator slots starting next to the stator slot at the top position.

Four pairs of heat flux sensors have been applied to the end-windings. The two heat flux sensors in each pair have been fixed at identical positions on two different conductors as shown in Fig. 4.9 to Fig. 4.12. Each of these figures show one pair of heat flux sensors applied to identical positions for all four positions HFS-A to HFS-D, as shown in the next chapter in Fig. 5.5. In order to obtain reliable information about the air-temperatures next to the sensors, they have been measured by Pt100 sensors positioned next to the heat flux sensors as shown in 4.5. The sensors HFS-5 and HFS-6 have been applied to the tips of the end-windings by adapter plates made of copper to accomplish a more homogeneous distribution of wall temperature and to provide flat surfaces for sensor application. Measurements at the opposite side of the end-windings' tips have been taken by the sensors HFS-9 and HFS-10 directly glued to the conductors' insulation. At the position on the end-windings conductors close to the rotors end-ring, high values of heat transfer have been expected. In this position the sensors HFS-11 and HFS-12 have been glued to the conductors with thermally conducting tape. Measurements at the position of the conductors which are close to the outlets of the cooling ducts have been taken by the sensors HFS-13 and HFS-14. The temperature of the fluid entering the end-region has been measured by two
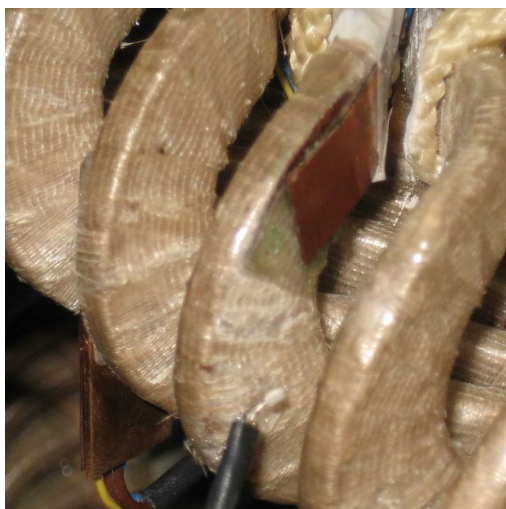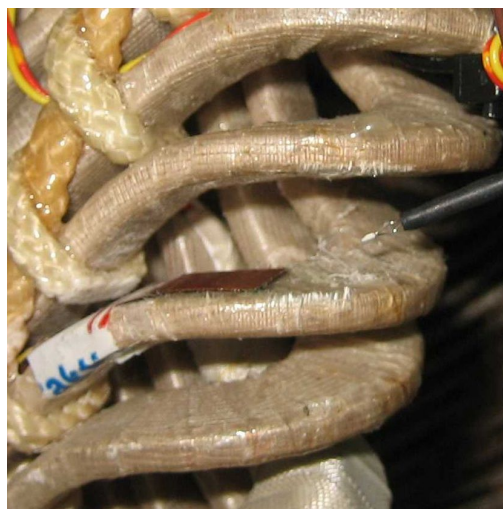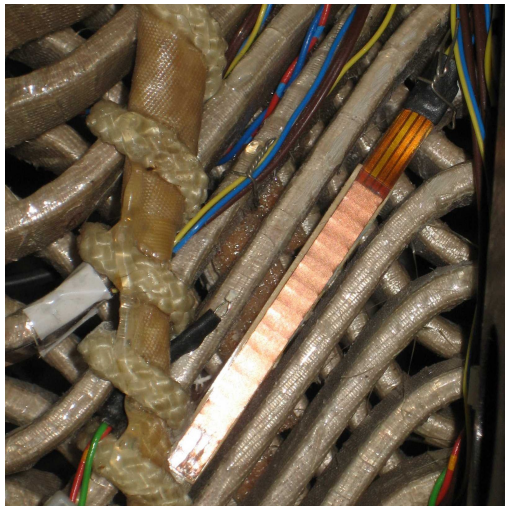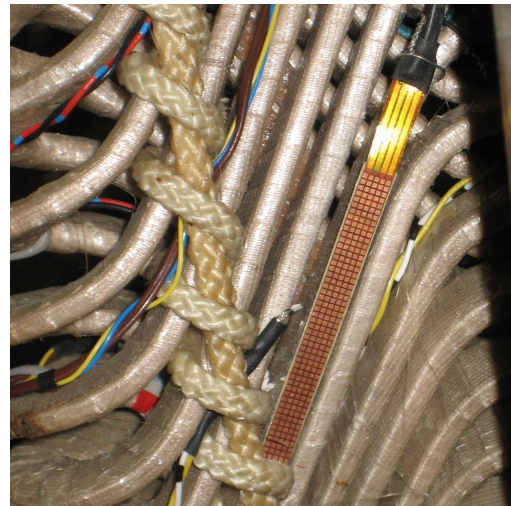
(a) HFS-5 at conductor №58

(b) HFS-6 at conductor №27

Figure 4.9: Heat flux sensors applied at position HFS-A on the end-windings

(a) HFS-9 at conductor №59

(b) HFS-10 at conductor №45

Figure 4.10: Heat flux sensors applied at position HFS-B on the end-windings

separate Pt100 sensors at the outlets of cooling ducts №4 and №28, as shown in Fig. 4.13. A complete wiring list of the used measurement amplifier can be found in Appendix C.1.

4.3.5   Measured heat flux

In Fig. 4.14 to Fig. 4.17, the values measured by all heat flux sensors are shown as boxplots, depending on the frequency of the power supply and the respective rotational

(a) HFS-11 at conductor №22   (b) HFS-12 at conductor №11

Figure 4.11: Heat flux sensors applied at position HFS-C on the end-windings

(a) HFS-13 at conductor №2   (b) HFS-14 at conductor №8

Figure 4.12: Heat flux sensors applied at position HFS-D on the end-windings

speed. The upper and lower levels of the boxes are calculated with the upper and lower quartile of the measured values. One quartile contains a quarter of measured values above or below the median for one specific operation point. The horizontal line in the box is the value of the median from the data recorded at the specific operation point. The whiskers above and below the box show the value range of the rest of the data with the maximum range of the inter-quartile length. Outliners which are outside the inter-quartile range above or below the box are shown as crosses. The ordinates of the diagrams have been limited to a minimum wall heat transfer coefficient of $\alpha_{\mathsf{min}} = 0 \ \mathsf{W/m^2K}$ and a maximum value of $\alpha_{\mathsf{max}} = 450 \ \mathsf{W/m^2K}$, since negative values or coefficients above this range are assumed to be non-physical.

As shown in the figures, the values measured are wide spread at many operation
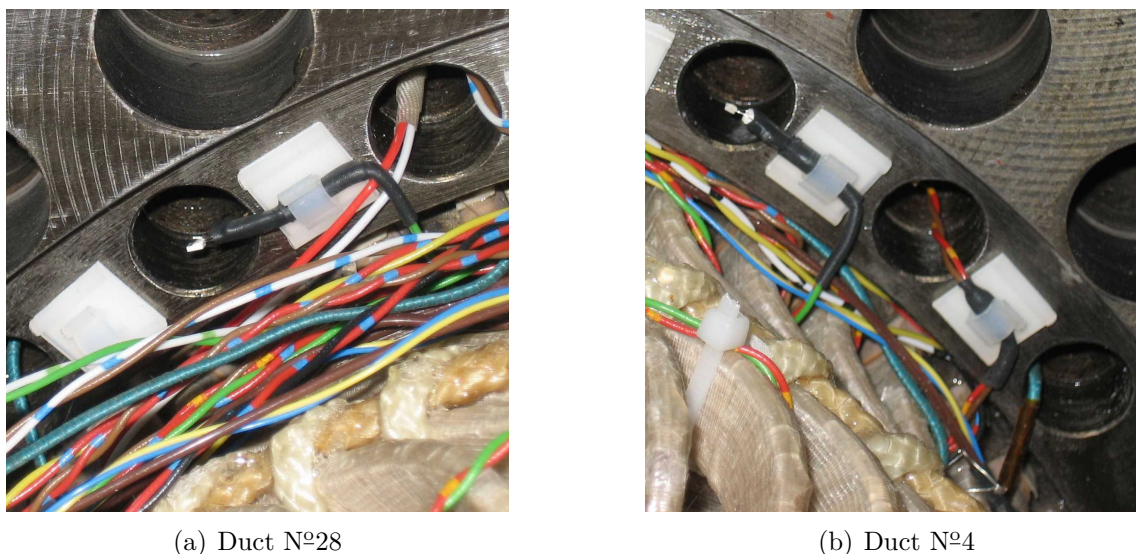
(a) Duct №28
(b) Duct №4

Figure 4.13: Pt100 sensors measuring the air-temperature at the outlets of two cooling ducts of the inner cooling cycle

points. This measuring error can be explained with the following reasons. As mentioned above, the heat flux sensors gain a signal caused by the heat flux in the range of some millivolts and are glued directly to the conductor, separated only by a thin layer of insulation. Each heat flux sensor and temperature sensor is connected to the measuring equipment by an unshielded two-wire circuit. The temperature gradient between conductor and fluid is small, especially at higher revolution speeds with higher air mass flow and hence better cooling of the conductors. This small gradient causes a small signal of the heat flux sensor and increases the relative error of the temperature difference measurements, since the values of wall and fluid temperature are close. In this case, effects mentioned in Subsection 2.2.4 cause an unphysical behavior of the wall heat transfer coefficient. Due to the asymmetric (non rotation-symmetric) shape of the end-shield, as well as to the difference in the number of stator ducts and slots, the measured values of the pairs of heat flux sensors at identical measuring points differ from each other, as shown in some diagrams in Fig. 4.14 to Fig. 4.17.
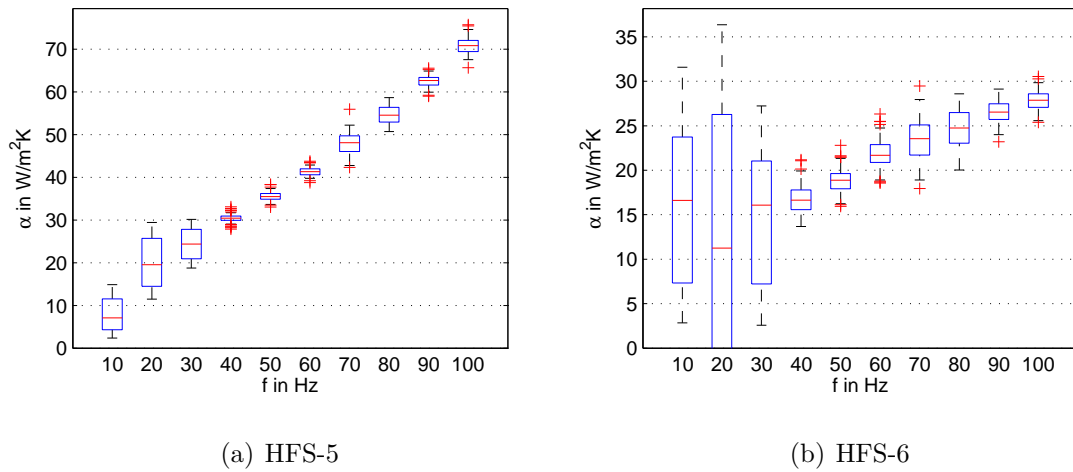
(a) HFS-5   (b) HFS-6

Figure 4.14: Measured wall heat transfer coefficient at different frequencies of supply power

(a) HFS-9   (b) HFS-10
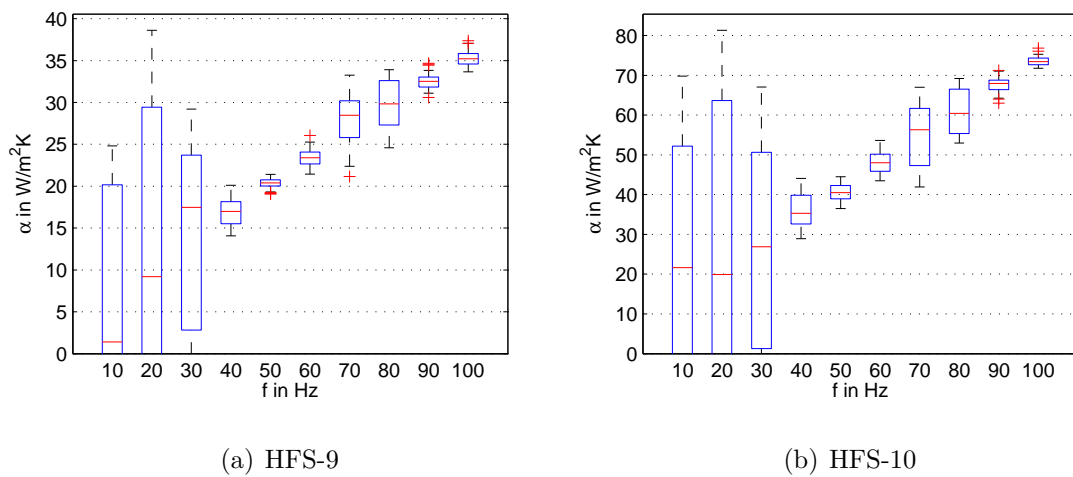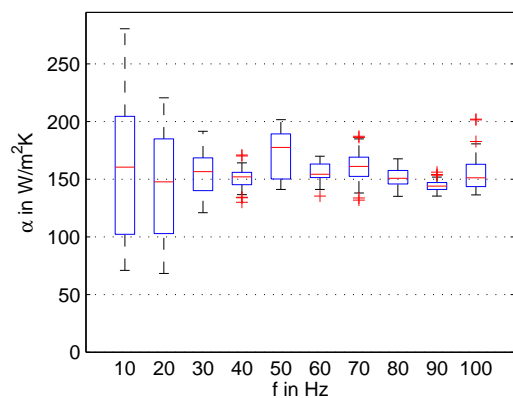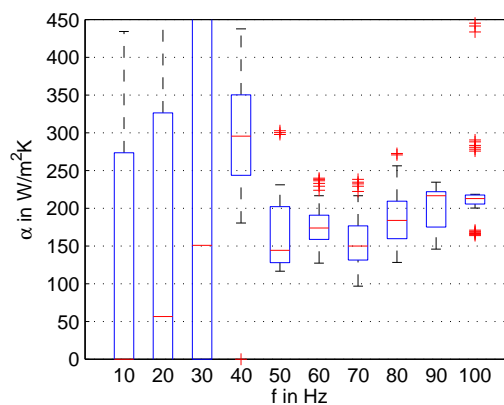
Figure 4.15: Measured wall heat transfer coefficient at different frequencies of supply power
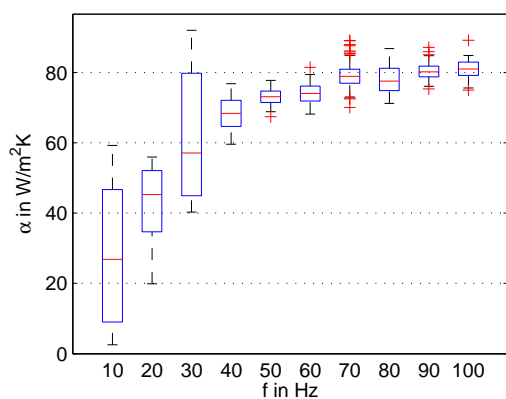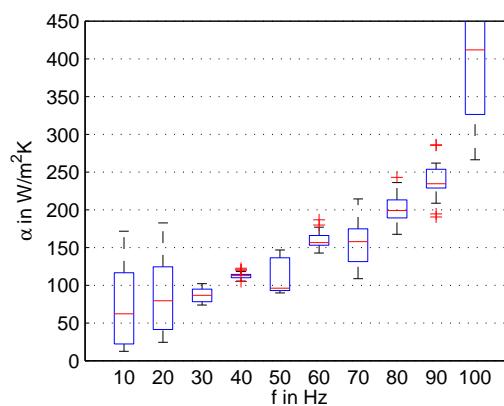
(a) HFS-11

(b) HFS-12

Figure 4.16: Measured wall heat transfer coefficient at different frequencies of supply power

(a) HFS-13

(b) HFS-14

Figure 4.17: Measured wall heat transfer coefficient at different frequencies of supply power

Chapter 5

Simulated heat transfer of the end region

The geometry of the induction machine on which the measurements in Chapter 4 have been carried out has been used for the present simulations. As shown in Fig. 4.1, this type of machine consists of two separate cooling circuits with a separate fan for each circuit. To obtain detailed information about the heat transfer at the end-windings inside the closed inner cooling circuit, measurements alone are not sufficient but are required for validation. For further use in heat transfer calculations, the average values of the heat transfer coefficients are required, rather than coefficients at certain positions with small areas of heat flux sensors, as collected in Chapter 4. In order to obtain reliable coefficients for a heat transfer characterization (see Chapter 6), the simulation of wall heat transfer coefficients has been validated in the present chapter. The measured heat transfer values at the end-windings can only be compared to areas in the simulation setup which correspond to the positions where the heat flux sensors of the actual measurements have been placed. Due to its non-symmetric shape, the end region cannot be split into periodic regions as a whole, but as explained in the meshing procedure in Subsection 5.1.1, a separation into a periodic and a non-periodic volume is possible. As presented in Subsection 2.4.6, the mesh at the surface has to resolve the boundary layer to accurately simulate the wall heat transfer. Since the number of finite volumes would be too high with a resolved boundary layer at the whole end-windings surface, the simulation in this chapter has been carried out with the global-local domain decomposition method, as explained in Section 3.5.

The investigation presented in this chapter has been accomplished in connection to previous research published in [37–39] and [41, 42].
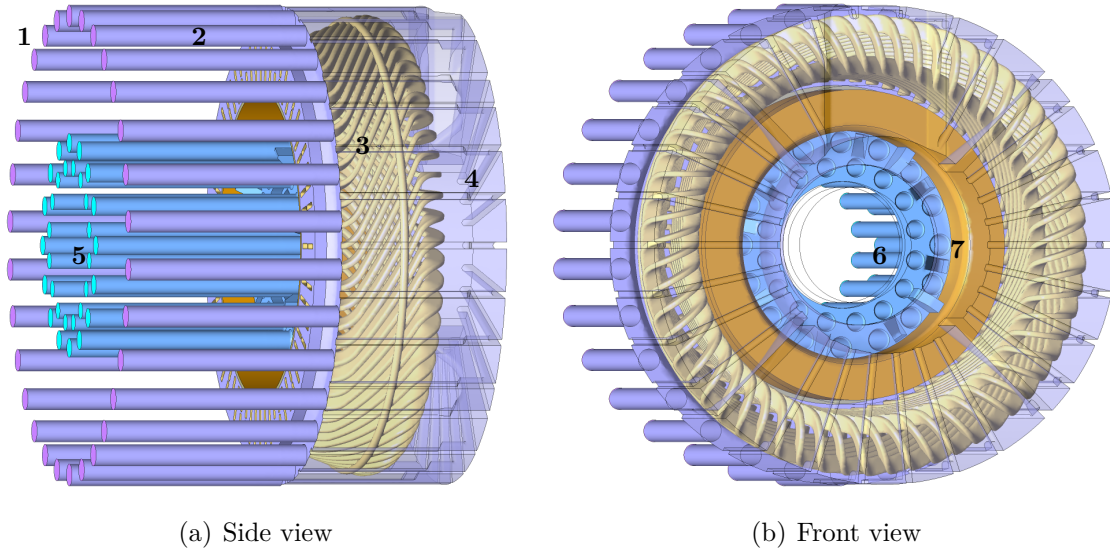
(a) Side view

(b) Front view

Figure 5.1: Global model of the NDE end region with (1) the model air inlets, (2) cooling ducts of the inner cooling circuit in the stator, (3) the end-windings, (4) the end-shield, (5) the model air outlets, (6) cooling ducts inside the rotor iron and (7) the end-ring.

5.1   Domain decomposition global model

5.1.1   Global model geometry and mesh

Like the measurements, the CFD simulation is focused on the end region of the non-drive-end (NDE) side of the same induction machine's inner cooling circuit, as described in Section 4.1. As shown in Fig. 5.1(a), the stator domain of the model contains the surfaces of the end-windings, the end-shield and the half length of the inner cooling circuits ducts of the stator iron. The rotor domain contains the surfaces of the half length of the cooling ducts inside the rotor iron, the end-ring and the shaft. Since the air gap between the rotor iron and the stator iron is 1-2 millimeters wide, it has been assumed that it is not relevant to the flow conditions around the end-windings and it has not been modeled or meshed in the present model.

Some details of the end-shield are shown in Fig. 5.2 as e.g. the waste grease drain which renders a segmentation of the end-shield into equal parts of rotational periodicity impossible. The end region contains four bracings reaching deeper into the end region than the cooling fins. As shown in the results, these bracings influence the flow conditions and, consequently, the heat transfer.

The end-windings shown in Fig. 5.1(a) obviously have a periodic structure which can simplify the simulation model. Since the end-shield shown in Fig. 5.2 cannot be simplified with the same periodicity as the end-windings, the stator domain has been split into a periodic part with the end-winding and a non-periodic part with the end-shield and stator cooling ducts.
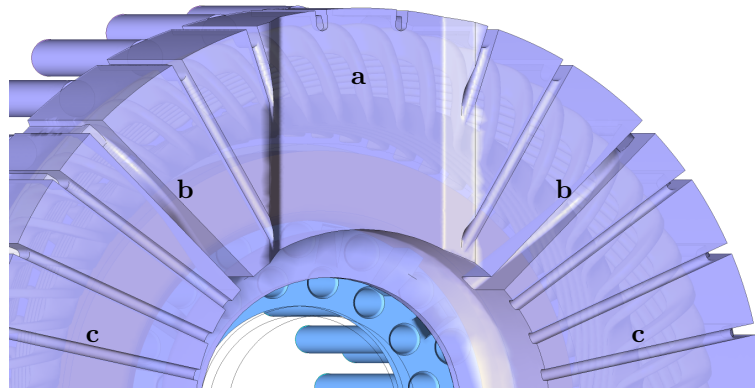
Figure 5.2: Perspective view of the air volume shaped by the inner surface of the end-shield with (a) the waist grease drain (b) two of a total of four bracings and (c) cooling fins

The stator and rotor dimensions have been taken from the original engineering drawings. One conductor of the end-windings has been modeled with the software package *CATIA V5* and has been imported into *ANSYS Workbench*. All other end-windings have been copied from the single imported end-winding. Due to the manufacturing process of the stator windings, the tolerance of the end-winding dimensions is in the range of several millimeters and does not fit exactly to the used model. This imprecision may lead to a difference between the measured and the simulated heat transfer values. Since the whole circumference of the end-shield has been modeled without simplification, realistic flow conditions in the end region can be expected.

In order to compare the results of different conductors independent of changing mesh quality, an identical mesh for each conductor is required. Since a free-mesh-algorithm would create different surface meshes on different conductors and consequently a different volume mesh, a periodical mesh sector has been created for the angle of one single conductor, as shown in 5.3(a). As visible in the same figure, the surface of the end-windings has been meshed by four layers of prismatic cells to assure at least nine mesh elements between adjacent conductors.

(a) Periodical mesh of the end-winding   (b) End-winding mesh   (c) Total stator mesh
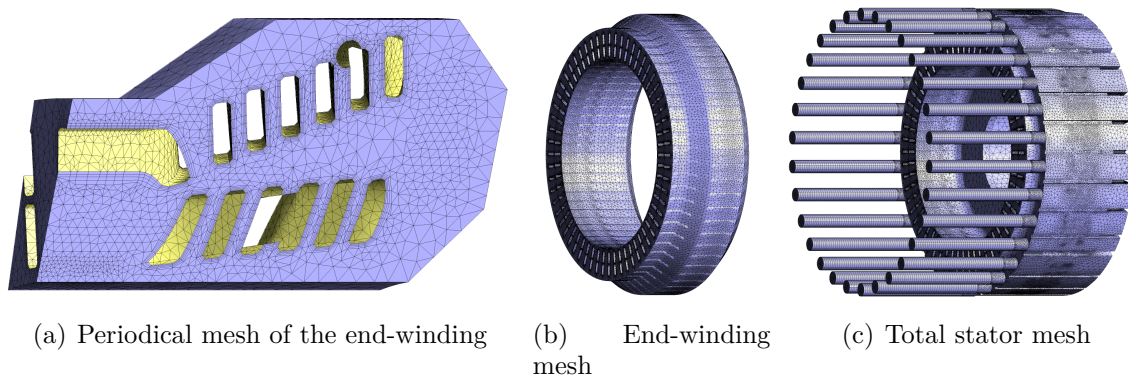
Figure 5.3: Periodical sector and assembled mesh of the end-windings and mesh of the whole stator

This periodical mesh has been copied for each further conductor in azimuthal direction to create the total mesh of the end-windings, as shown in 5.3(b). Based on the end-windings' surface mesh in 5.3(b), the rest of the volume inside the end-shield has been created using a tetrahedral free mesh, shown in Fig. 5.3(c)

The rotor of the induction machine has been created in a similar way. As shown in Fig. 5.4(a), the periodical shape of the rotor has been used to create the mesh of one quarter of the circumference of the rotor. By copying and rotating this mesh three times, the whole rotor domain has been created, as shown in 5.4(b)

(a) Periodical mesh sector of the rotor mesh   (b) Total rotor mesh
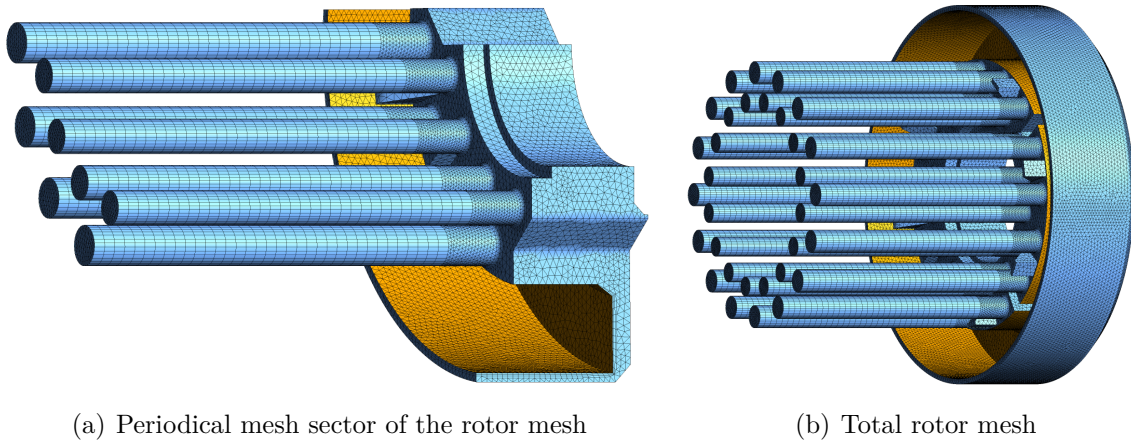
Figure 5.4: Periodical sector and assembled mesh of the rotor

The cooling ducts of the stator and the rotor have been created by sweeping the surface mesh of the cooling ducts' cross-sectional area into the axial direction of the machine. After copying the periodical mesh parts in both domains, covering mesh nodes have been merged to obtain a consistent mesh for the stator domain and the rotor domain.

5.1.2   Global model simulation setup

For the simulation setup, the stator domain shown in Fig. 5.3(c) and the rotor domain shown in Fig. 5.4(b) have been connected by a frozen rotor general grid interface (GGI) linking the stationary to the rotating domain. The simulation has been started for the same rotational speeds n which have also been used during the measurements. All ventilation ducts in Fig. 5.3(c), which are connected to the stator, represent the model air inlets. The inlets in the stator domain have been configured with an opening pressure of $p_{in} = 0$ Pa and inlet fluid temperatures T_{in} for different rotational velocities n, in accordance with the measured results, as listed in Tab. 5.1. In addition to the inlet fluid temperature T_{in}, the wall temperature T_w of the end-windings has also been adjusted for the different simulations with different rotational speeds, also listed in Tab. 5.1. All other surfaces of the stator and the rotor domains have been assumed to be adiabatic walls. The measurements of the air mass flow have been taken at one

f	n	T_{in}	T_w	$\dot{m}_{tot}/\dot{m}_{mon}$
Hz	min^{-1}	K	K	
50	1503	346	353	30.54
60	1800	346	353	30.58
70	2104	345	352	30.63
80	2400	343	349	30.67
90	2700	341	346	30.71
100	3007	338	342	30.76

Table 5.1: Variated operating parameters

single cooling duct, as presented in Subsection 4.2.2. Due to the non-symmetric end-shield, the flow conditions in the end region are changing with the azimuthal angle. Consequently the air mass flow in the single stator cooling duct is varying depending on its angular position. To consider this, the air mass flow of the same cooling duct examined during the measurements has been monitored and adjusted during the CFD simulations. The total air mass flow has been set to the model air outlets which are parts of the rotor domain shown in Fig. 5.4. The ratio between the total air mass flow $\dot{m}_{tot}$ and the air mass flow of the monitored cooling ducts $\dot{m}_{mon}$ is listed in Tab. 5.1 for all used rotational speeds. Due to the linear correlation between the air mass flow in the cooling ducts and the rotational speed of the machine, the air mass flow of the monitored (and measured) cooling duct has been calculated by linear interpolation between zero and maximal air mass flow at maximum speed

$$\dot{m}_{mon} = \frac{\dot{m}_{max} \cdot n}{n_{max}} \ . \tag{5.1}$$

The surfaces of the cooling ducts and the end-windings have been set to rough wall with a sand grain roughness height of $k_{s\ duct} = 0.26$ mm for the cooling ducts which has been determined by measurements as described in Section 4.2. The environmental pressure of $p_0 = 956$ hPa has not changed during the measurements. Therefore, a reference pressure of $p_{ref} = p_0$ has been set for all simulations [42].

The transport of enthalpy has been solved with the total energy equation which includes the kinetic energy effects. Compared to sonic speed, the velocities of air around the end-windings are relatively low, hence a rise of air temperature due to dissipation has not been assumed. Dissipation is viscose work and is a part of the conservation of energy in the Navier-Stokes equations. Since the influence of dissipation is negligible, it has been disabled for the solution. Due to the relatively high rotational velocity of the rotor compared to velocities, which can be caused by free convection, buoyant forces caused by gravity have been neglected during the numerical calculation. Compared to the convective heat transfer inside the end-shield and the low temperature difference between walls, the heat transfer by radiation is relatively low and has been neglected as well.

The configuration of turbulence models has been set in accordance with the validation setup for the global local domain decomposition method presented in Section 3.5.

5.2 Domain decomposition local model

5.2.1 Local model geometry and mesh

The local model has been used to calculate the flow around the single conductors on a refined mesh, using boundary conditions calculated in the global model. Fig. 5.5 shows one conductor as it has been examined with the positions HFS-A to HFS-D where heat flux sensors have been applied to some conductors. As shown in the measurements,

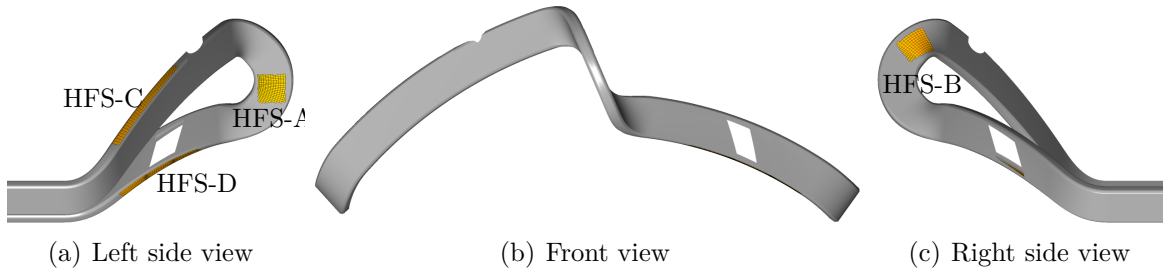(a) Left side view   (b) Front view   (c) Right side view

Figure 5.5: Conductor of local domain with the different positions of heat-flux sensors HFS-A to HFS-D

four pairs of heat flux sensors have been applied on eight different conductors. Each pair of sensors has been fixed at an identical position HFS-A to HFS-D. In order to obtain identical calculation meshes for all conductors, one single conductor has been meshed and the mesh of all other conductors has been obtained by transformation of the mesh coordinates with an angle of six degrees for the remaining 59 conductors. Consequently, each of the four sensor positions is available on all 60 conductors but only 24 of them have been used for comparison with the measurements presented in Chapter 4.

The mesh for the local model has been created by first building an envelope area around the conductor as sketched in Fig. 5.6. This envelope area must not touch or
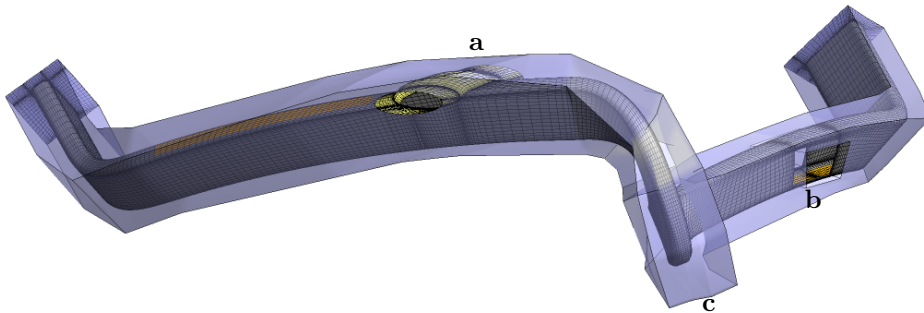

Figure 5.6: Local model of the conductor with (a) the cord, (b) the resin-impregnated support and (c) the envelope area

cross any surfaces of adjacent conductors or the end-shield. The volume between the conductor's surface and the envelope area has been filled with a block-structured mesh

with refined hexahedral cells at the conductor's surface. This provides a dimensionless wall distance of $y^+ \leq 1$ with an initial finite volume cell height of $y_0 = 10 \ \mu m$ next to the surface.

5.2.2 Local model simulation setup

As already presented in Section 3.5, the boundary conditions of the local model have been taken from the solution of the global model. By importing the envelope area as

| (a) Side view | (b) Front view |
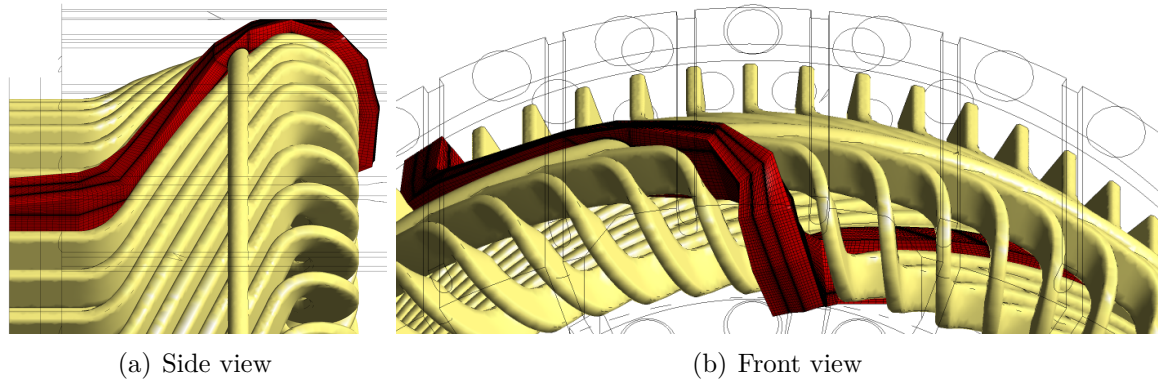
Figure 5.7: Envelope area of the conductor's №54 local domain imported into the global domain for definition of the local domain's boundary conditions

shown in Fig. 5.7 into the global model, the relevant variables of velocity, turbulence and temperature for each calculation node at the local model's envelope surface have been exported into a boundary condition profiles file. This file has been created for all 60 conductors and each of the six investigated rotational speeds. The boundary condition profiles at the envelope include the temperature T, the velocity magnitude $|\mathbf{u}|$, the turbulence kinetic energy k and the turbulence dissipation rate ε as shown in Fig. 5.8.

(a) Temperature

(b) Velocity magnitude

(c) Turbulence kinetic energy

(d) Turbulence eddy dissipation

Figure 5.8: Boundary conditions for the envelope area of the local domain at a rotational speed of $n = 3007$ min^{-1}

5.3 Results of the global local decomposition model

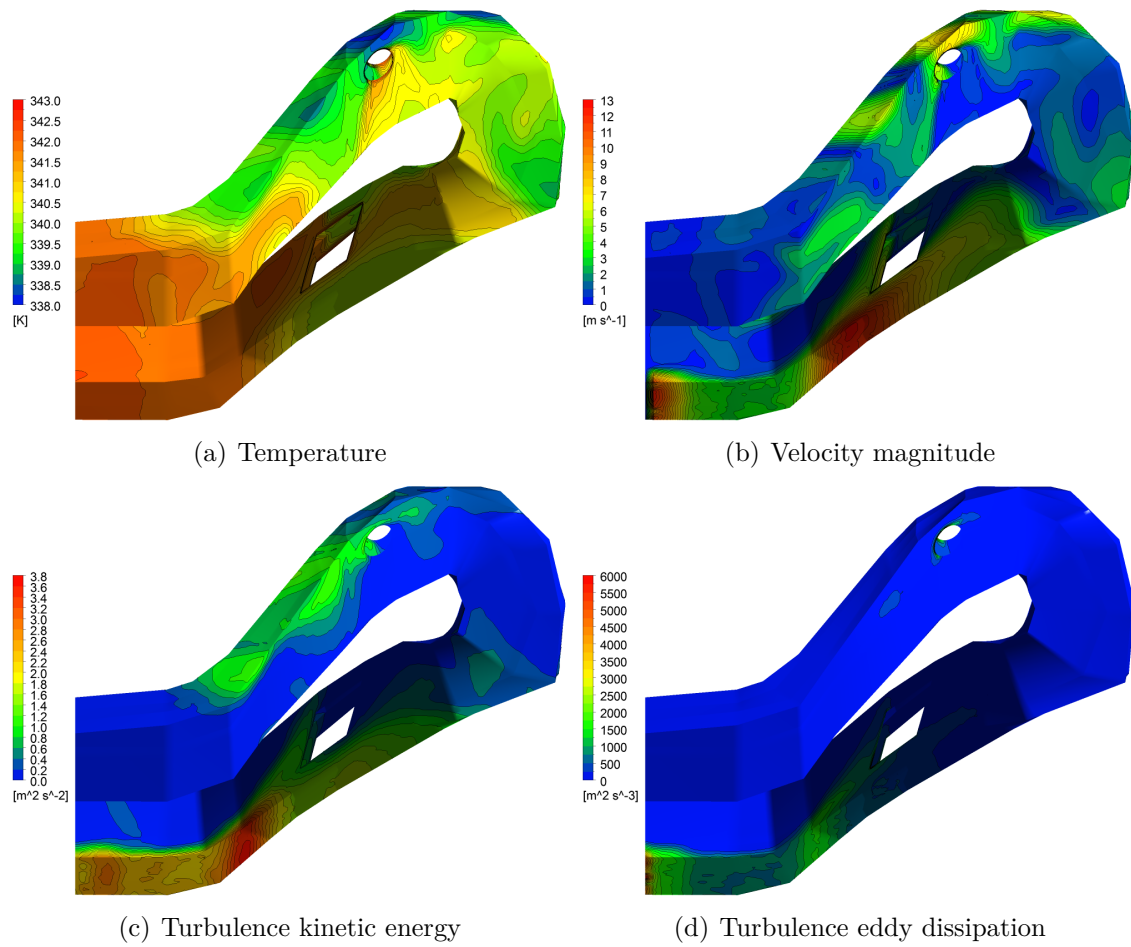As seen in the example presented in Chapter 3, a reliable heat transfer coefficient can only be obtained if the condition $\mathsf{y}^+ \leq 1$ is satisfied (see Section 3.5). This cannot be achieved with acceptable computational demand in a global model, therefore, a global local decomposition has been applied. The simulation of the global model has been executed with the solution of the total energy equation (2.42) included in order to obtain valid temperature values for the local domains boundary conditions. Since the energy equation also includes the solution of the heat flux, an analysis of the wall heat transfer coefficient can easily be performed, even though it has been derived with the logarithmic law of the wall. The absolute quantity of the wall heat transfer coefficient may not be accurate, nevertheless, a qualitative illustration is informative. The contour plot in Fig. 5.9 shows the local wall heat transfer coefficient α, where the blue areas designate its lowest values and the red areas the highest. The cooling
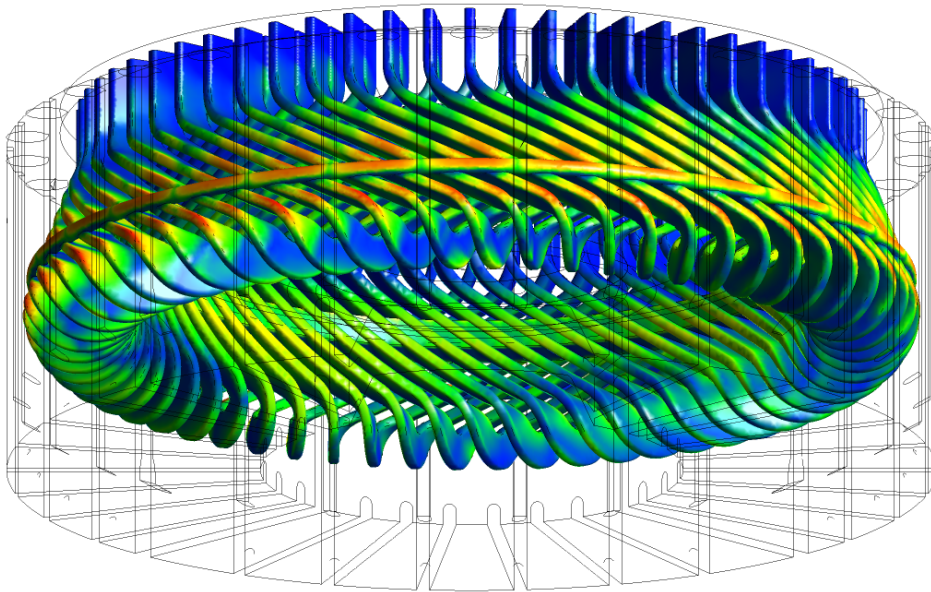
Figure 5.9: Convective wall heat transfer coefficient at the end-windings with the end-shield sketched as a wire-frame obtained from the global model

ducts of the stator generate a jet flow condition after the ducts' outlet which causes a locally higher heat transfer coefficient at the end-windings. This locally increased heat transfer is shown in Fig. 5.9 as yellow contours, recurring azimutally with the same periodicity as the cooling ducts. The averaged values of the wall heat transfer coefficients at the global meshes, as shown in Fig. 5.9 are listed in Tab. 5.2, including minimum, average and maximum values of the dimensionless wall distance y^+.

In creating the local models, care has been taken to get values of $\mathsf{y}^+ \leq 1$ next to the conductors surfaces. In order to obtain comparable results, identical meshes of all

n	α	y^+_{avg}	y^+_{min}	y^+_{max}
min^{-1}	$W/m^{-2}K$			
1503	13.40	1.63	0.06	5.94
1800	14.86	1.87	0.07	6.99
2104	16.59	2.07	0.06	7.57
2400	18.86	2.35	0.09	8.00
2700	20.76	2.60	0.08	8.81
3007	22.55	2.90	0.14	10.10

Table 5.2: Simulated wall heat transfer coefficient obtained from the global model

conductors have been developed. The only difference between the separate conductors is the transformed coordinate system and the individual boundary conditions for each conductor obtained from the global mesh, as shown in Fig. 5.8. Each of the 60 conductors has been simulated for six different rotational speeds using the respective boundary conditions profile obtained from the global models. One example of the simulation on the local model is illustrated in Fig. 5.10 and shows the wall heat transfer coefficient on conductor №54 for a rotational velocity of $n = 3007 \text{ min}^{-1}$.

| (a) Left view | (b) Front view | (c) Right view |
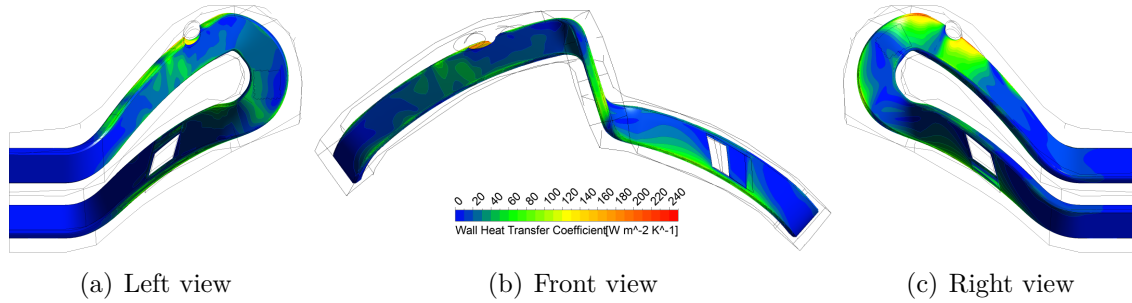
Figure 5.10: Local wall heat transfer coefficient on the surface of conductor №54 for a rotational velocity of $n = 3007 \text{ min}^{-1}$

The values of the average wall heat transfer coefficients for each conductor and each rotational speed are shown in the diagrams in Fig. 5.11. The results for each conductor are shown as circles. Also, the wall heat transfer coefficients of all conductors have been averaged for each rotational speed and are presented in the right bottom corner of the diagrams. These are average values of the whole end-windings calculated in the local meshes and thus can be compared with the results from the global mesh, shown in Tab. 5.2. It is evident that the results of the global and local mesh match with a relative error of less than 2%. This shows that for this particular problem, the y^+ values used in the global model shown in Tab. 5.2 are also sufficient. This can be explained as follows.

Obviously, the heat transfer at the end-windings is caused by an attached flow parallel to the wall, rather than by a highly turbulent separated flow next to the wall. Therefore, the logarithmic law of the wall is valid at most locations of the end-windings and the wall heat transfer can be calculated with good accuracy with the log-law. A

comparison between adjacent conductors for the different rotational velocities shows an alternating behavior from one conductor to the next. As shown in Fig. 5.9, the jet flow of the cooling ducts causes a higher heat transfer at specific locations. Since the number of conductors of this machine is two times greater than the number of cooling ducts, it is obvious that the heat transfers of every second conductor are comparable and thus altering from one to the next conductor.

The diagrams in Fig. 5.12 show a comparison of the simulated values, shown as circles, to the values measured in Chapter 4, shown as squares. These values have been examined on the conductors equipped with heat flux sensors during the measurements and at identical positions on the adjacent conductors, shown as triangles in the diagrams. The heat flux at identical positions is spread widely between some neighboring conductors, e.g. as shown in Figs. 5.12(a), 5.12(c) or 5.12(g). On the one hand, this is caused by the unequal number of cooling ducts and conductors. On the other hand, the air flow inside the end-shield is disturbed by the waste grease drain and the bracings shown in Fig. 5.2.

In some diagrams in Fig. 5.12, poor congruence between simulated and measured results can be observed. Beside errors caused by CFD, the measurements also exhibit a certain error. The manufacturer of the used Pt100 temperature sensors ensures an accuracy of DIN class A between $-90°C$ and $300°C$ in the DIN EN 60751 standard [19]. For a measured temperature of $80°C$ this error class guarantees an absolute temperature accuracy of $0.31°C$. Although all sensors have been calibrated at the environmental temperature, an absolute error of less than $0.1°C$ cannot be guaranteed. Since the difference between fluid and wall temperature is below $8°C$ for all rotational speeds, the measuring error can have high influence on the wall heat transfer coefficient, as also discussed in Subsection 2.2.4. As shown at the end of Chapter 4, the measured results presented here are average values of sometimes widely spreading measuring data of the same sensor. The wider the measuring samples spread, the more samples would be necessary to get statistically significant values. For some operation points of the machine, the number of collected samples is too small. Nevertheless, the average values fit into the general trend of steadily rising heat transfer with increasing rotational speed.

Another source of error is the accuracy of the conductors' manufacture. The real end-windings do not satisfy an exact periodicity due to manufacturing tolerances which can cause e.g. an azimutal offset of the heat flux sensors' position of some degrees. In the model, on the other hand, the conductors have been rotated and copied by an angle of exacly six degrees. As already mentioned, the heat flux at identical positions on adjacent conductors can differ widely, hence a misplaced conductor in the real machine can have a different heat flux compared to the simulated conductor.

(a) n = 1503 min^{-1}

(b) n = 2104 min^{-1}

(c) n = 2104 min^{-1}

(d) n = 2400 min^{-1}

(e) n = 2700 min^{-1}

(f) n = 3007 min^{-1}
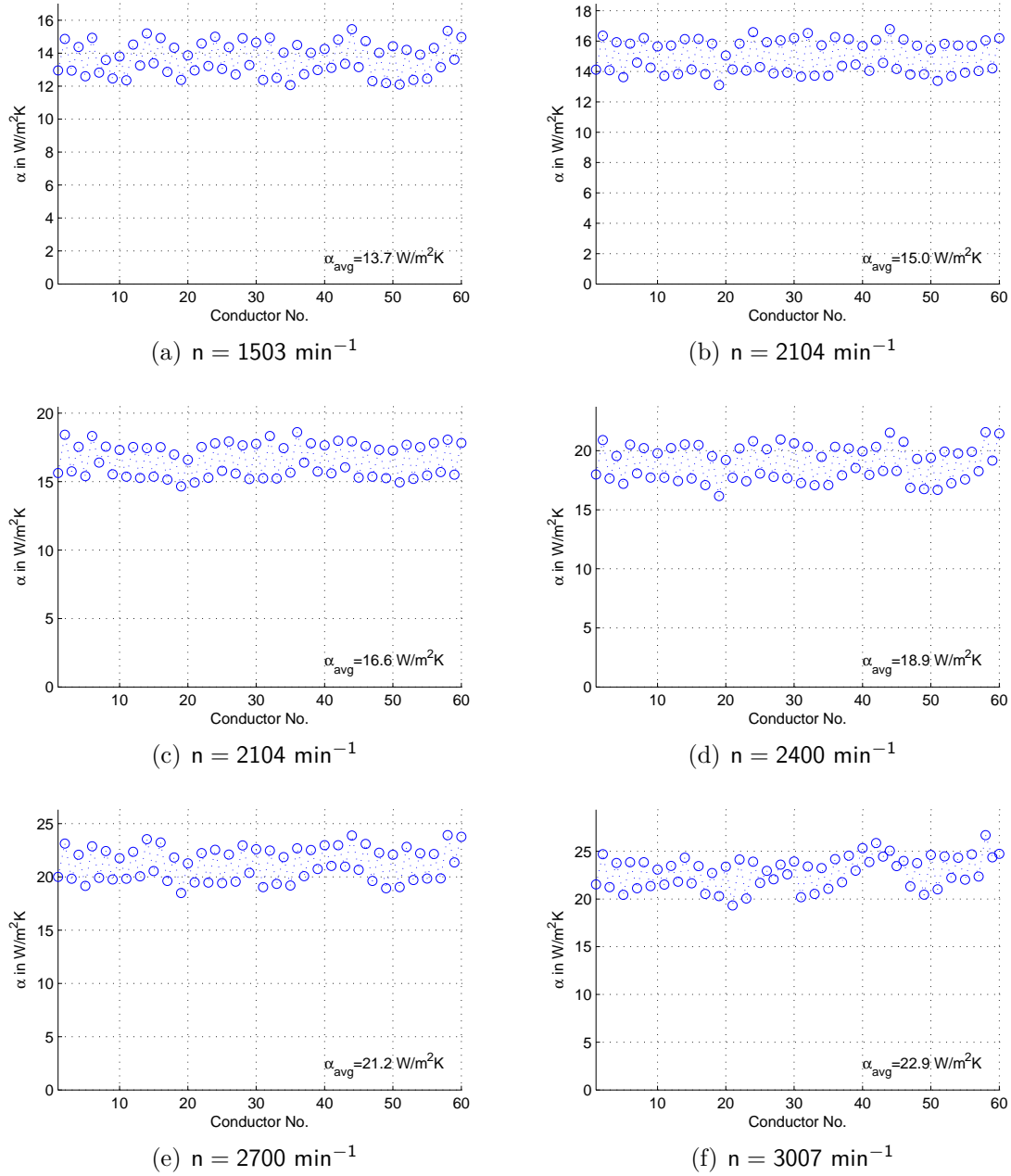
Figure 5.11: Averaged values of the wall heat transfer coefficient for all conductors at different rotational speeds
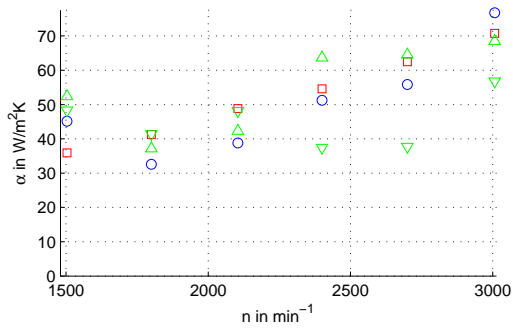
(a) HFS-05 at position HFS-A
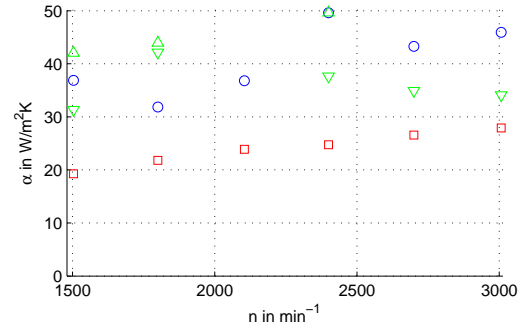
(b) HFS-06 at position HFS-A
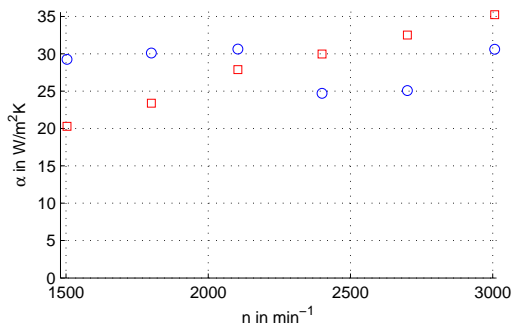
(c) HFS-09 at position HFS-B
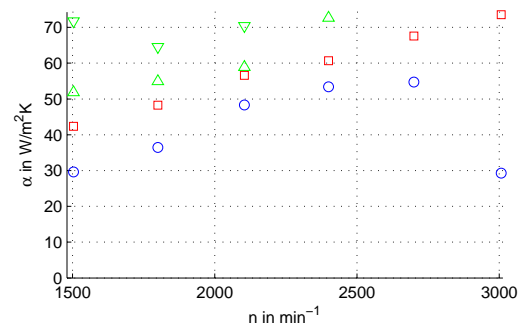
(d) HFS-10 at position HFS-B
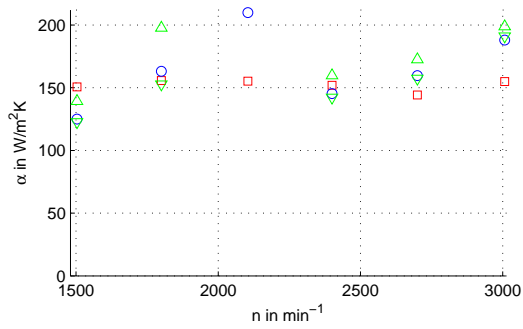
(e) HFS-11 at position HFS-D
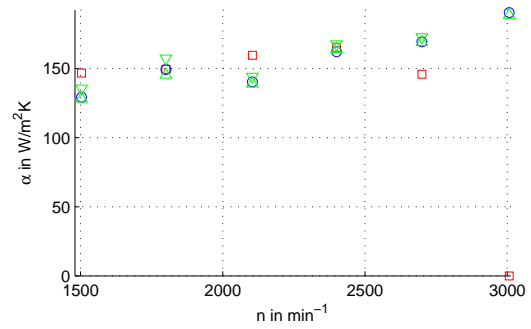
(f) HFS-12 at position HFS-D
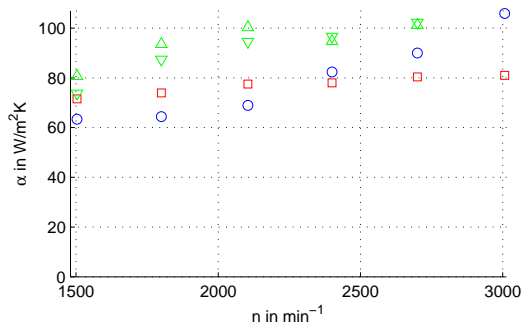
(g) HFS-13 at position HFS-C
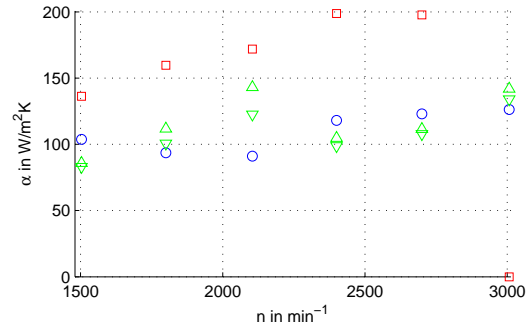
(h) HFS-14 at location HFS-C

Figure 5.12: Simulated results of the local wall heat transfer coefficients (circles) compared to the measured results (squares) and at identical positions on two neighboring conductors (triangles)

Chapter 6

Characterizing the heat transfer

Predicting the thermal behavior of complex geometric shapes by calculating the thermal field inside solid materials depends on the availability of proper values of the wall heat transfer coefficient. Simulation of the heat transfer at the end-windings of an electric machine is often restricted by the quality of the coefficients used in the simulation model.

Since this coefficient depends basically on the usually turbulent fluid flow, there is practically no way of calculating it exactly in any case. Earlier investigations on heat transfer problems used experimental setups to obtain non-dimensional correlations from the measured heat transfer values, as outlined in [93]. The correlations of such publications have been defined for simple geometries like flat plates or pipes and have been listed in works of reference, e.g. in [88]. Since the geometry of the end-windings depends on a range of parameters, a large number of geometry-variations are necessary and thus measurements on varied geometries would be very costly. Hence measurement based correlations can hardly be found in literature for such geometries.

A correlation between tangential velocity and the wall heat transfer coefficient has been found for totally enclosed fan cooled motors, as shown in [8]. Since electrical machines of a higher power class have typically other cooling systems, different correlations are necessary. In [70], an electrical machine has been investigated extensively which has a comparable cooling system to the machine investigated in this work. Since the measurements have been taken on a single geometry, only a correlation to the rotational speed would be possible. The investigation in this chapter has been accomplished in addition to former research published in [36] and [40].

The non-dimensional descriptions of correlations have the benefit of scalability depending on specific characteristic lengths. A characteristic length can be the diameter of a pipe in the case of a pipe-flow or the length of a plate in the case of a fluid flow parallel to a flat plate. In case of a more complex shape, as that of the end-windings of an electric machine, the characteristic length is not obvious.

The data for correlations of the wall heat transfer coefficient had been collected by measurements in the past. Today the progress in computer and simulation technology provides tools for replacing the majority of measurements on experimental setups. By

using CFD, it has become possible to simulate the fluid flow including the relevant effects, like the convective wall heat transfer. This technology cannot be considered an exact method, since it is based on non-exact models to some extent. Nevertheless, it provides sufficient accuracy for most engineering applications.

The following chapter gives an outline of obtaining correlations between the convective wall heat transfer coefficient of the end-windings and geometrical as well as operational conditions. The heat transfer values of a variety of geometries have been computed by CFD before correlating them to the known conditions with the Gauss-Newton method.

The result is a set of characterization parameters which allows the calculation of the wall heat transfer coefficient by a simple formula which can be applied e.g. to a thermal network model for drive cycle simulations of traction motors. This characterization provides a way of calculating values for the convective wall heat transfer coefficient depending on specific degrees of freedom for the rotational speed of the rotor and the geometry of the end-shield. Due to the conversion into dimensionless numbers, the result is also applicable on scaled geometries.

6.1 Dimension analysis and Pi-Theorem

A physical magnitude has three attributes: value, unit and dimension. Dimension is an agreement with the purpose of quantifying a natural principle with a value. This is a convention about the principle and not a result of the principle. The dimensions of a specific system are categorized as fundamental dimensions and derived dimensions. For example, in a dynamic system, the fundamental dimensions are length, time and mass. The derived dimensions for this system can be force, velocity and acceleration, which are products of powers of fundamental dimensions. The choice of the fundamental dimensions is a matter of agreement but still has to satisfy the following two criteria:

- No fundamental dimension can be derived from other fundamental dimensions.

- Each derived dimension of the considered problem can be obtained from the fundamental dimensions.

Units are classified as fundamental or derived units, according to their dimensions [34]. The Pi-Theorem [34] can be used to calculate a common solution for any correlation as a function of a specific number of dimensionless values. For the correlation of n variables a_i with m fundamental dimensions with

$$f(a_1, a_2, \ldots, a_n) = 0 \, , \tag{6.1}$$

the solution of the correlation has the common form

$$F(\Pi_1, \Pi_2, \ldots \Pi_{n-m}) = 0 \, . \tag{6.2}$$

The Π_i values in (6.2) represent a set of $(n - m)$ independent and dimensionless values. Depending on the actual problem, a specific set of fundamental dimensions is required. A system of the three fundamental dimensions length (L), time (Z) and mass (M) turns out to be reasonable for finding solutions to dynamic problems. Since this system is not able to define a value of heat energy, an additional dimension for the temperature is required. Hence heat transfer problems can be defined from the thermodynamic point of view by the dimensions of length (L), time (Z), mass (M) and temperature (T).

The main task in the dimension analysis is the definition of relevant values and a target value which are specific to the problem. A list of relevance separates the values into five categories, from R1 to R5, and each value has to be controlled depending on its influence on the target value. If the change of a value might change the target value it should be included in the list of relevance, as shown in Tab. 6.1.

R1	Target value	Value to be determined
R2	Geometric values	Characteristic geometrical values
R3	Process values	Characteristic values for the intensity of the process
R4	Material properties	Material properties which can be relevant for the process
R5	Constants	Constant values of physical relations

Table 6.1: List of relevance

6.2 Simulation

The focus of this investigation has been on the end-windings of the non drive-end side of various variations of the induction motor examined in Chapter 4, as shown in the outlined detail A in Fig. 6.1. The analyzed motor type in this chapter is the same
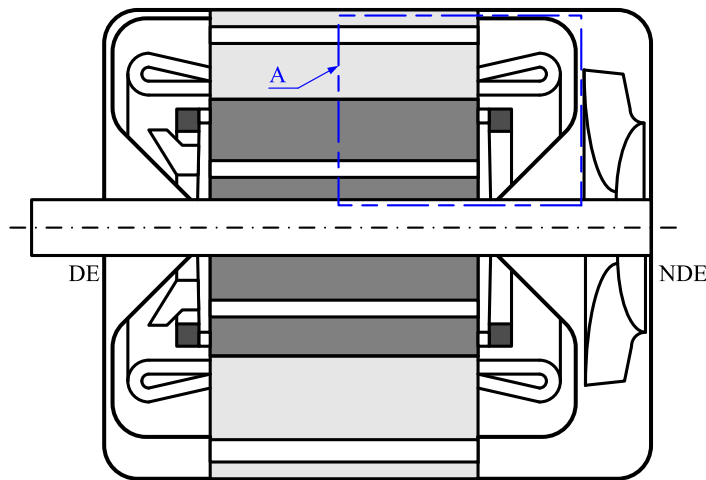
Figure 6.1: Longitudinal section of the investigated induction motor with the outlined detail A [40]

type as the analyzed motor used for the measurements in Chapter 4 and simulations in Chapter 5 and is described in detail in Section 4.1. This motor type is used as a traction motor and operates in the whole velocity range up to the maximal rotational speed. Since the values of convective heat transfer are changing with the rotational speed, these speed dependent values of the cooling cycle are of interest.

6.2.1 Geometry

The analysis of the convective heat transfer with CFD programs requires a very fine mesh at the surface of the end-windings. Hence the number of degrees of freedom increases dramatically and it becomes necessary to focus the simulation on just one certain part of the machine. Since a principle solution of this problem is required, not the whole circumference of the end-region containing the stator and the rotor has been modeled. In contrast to the motor presented in Chapters 4 and 5, a rotational periodicity has been assumed. The number of stator slots is an integer multiple of the number of the cooling ducts which are equally spaced over the whole circumference. On this account, a sector has been considered for the investigations by CFD which covers only one cooling duct and two conductors. The rotor of this machine features an equal number of cooling ducts on two different pitch circles. Like the stator, the rotor has been simplified by a section containing one pair of cooling ducts, one duct from the outer pitch circle and one duct from the inner pitch circle. One drawback of this simplification is the inaccurate modelling of the end-shield. In the real machine it does not have the same rotational periodicity as the end-windings or stator cooling ducts. The geometry which has been used for the CFD investigations is shown in Fig. 6.2, which also explains the parts of this model. Starting at the model's air inlet, the
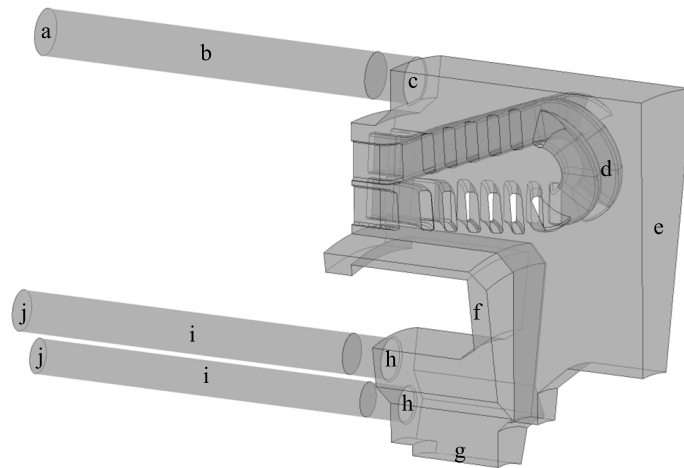
Figure 6.2: Used sectors for the CFD simulation with the stator-volume containing (a) model air inlet, (b) cooling duct of the stator, (c) stator duct outlet, (d) end-windings and (e) end-shield. The rotor-volume contains the, (f) short circuit ring, (g) shaft, (h) rotor duct inlets, (i) rotor cooling ducts and (j) model air outlet.

coolant flows through the stator cooling duct, passes the end-windings, the end-shield and the short circuit ring and flows through the rotor cooling ducts to the model's air outlet.

6.2.2 Variations

Modifications of the end-shield geometry lead to a change of the local fluid velocity around the end-windings. Due to this change of velocity, the value of the convective heat transfer at the end-windings' surface is affected. In order to investigate the correlations of geometric variations to the heat transfer, the geometry of the end-region has been modified. The three geometric dimensions end-shield hight l_V, end-shield diameter l_H and overhang of the end-windings l_A, as shown in Fig. 6.3, have been changed and 16 different geometries and calculation meshes, respectively, have been created. All other dimensions have been kept constant for all geometric variations, but have been used for the correlations. In order to consider the heat transfer on the scaled
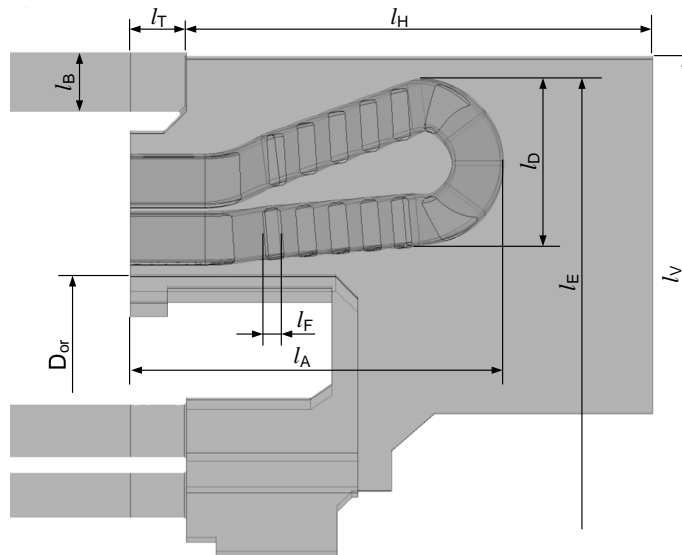
Figure 6.3: Geometric dimensions which have been used for this investigation. The dimensions l_V, l_E and l_K represent radii measured from the rotational axis of the machine.

end-regions, the 16 different geometries have been converted to larger geometries scaled by 20%. The scaled geometries have been re-meshed with the same mesh properties as the original geometries. With four different rotational speeds of the rotor and two different values for the air mass flow in the stator cooling ducts each, a total number of 256 CFD simulations on 32 different meshes have been accomplished to obtain the calculation of the correlation.

In order to achieve a proper wall treatment at the surface of the end-windings by CFD, thin inflated mesh layers have been created at the the end-windings' surface-mesh. With ten layers of prismatic cells, a growth factor of 1.2 and a total thickness

of 1 mm for all layers, a dimensionless cell height of $y^+ < 1$ has been achieved, even for the highest rotational velocity of the rotor.

6.2.3 Boundary conditions

The wall heat transfer coefficients have been identified by CFD simulations with different boundary conditions determined by varying revolution speeds n of the rotor and air mass flows $\dot{m}_{in}$ through the stator cooling ducts at a constant air temperature. At the rotor's circumference, the revolution speed causes a maximum angular velocity w which can be calculated from the revolution speed n expressed in revolutions per minute and the outer diameter D_{or} of the rotor iron or end-ring, respectively:

$$w = \frac{D_{or}\ \pi\ n}{60}\ .$$

(6.3)

Each model has been analyzed with four different rotational velocities to achieve a correlation with the heat transfer.

A certain mean velocity v in the stator cooling ducts is caused by the air mass flow at the inlet $\dot{m}_{in}$ which can be obtained as

$$v = \frac{\dot{m}_{in}}{\rho\ A}$$

(6.4)

where ρ is the density of air at atmospheric conditions and A denotes the cross sectional area of the stator cooling ducts [36].

In the real machine, the air mass flow $\dot{m}_{in}$ is a function of rotational speed n and is affected by the pressure to mass flow characteristics of the fan of the inner cooling cycle. For a general description of the machine it should be independent of the fan to provide more freedom in the design process. To achieve this, the functional relationship between air mass flow $\dot{m}_{in}$ and rotational speed n is split and the two variables are given as separate and independent parameters. Since the air mass flow through the cooling ducts $\dot{m}$ depends linearly on the rotational speed n, the ratio $\dot{m}/n$ of these values is a constant value for a specific fan. In order to make the correlations dependent on the fan characteristics two different ratios of air mass flow to rotational speed $\dot{m}/n$ have been investigated. Their used values including the resulting values of wall heat transfer coefficient can be found in Tab. 6.2 for the non scaled geometry and in Tab. 6.3 for the scaled geometries, respectively.

Since the heat transfer of the scaled geometries should be comparable to the results of the original geometries, the rotational speed and the velocity in the stator cooling ducts has to be adjusted to achieve equal Reynolds numbers inside the machine. For the same Reynolds numbers of scaled and original geometry the velocity w and hence the rotational speed n has to be adjusted by the same factor of $s_f = 1.2$ as the geometry, since the kinematic viscosity ν can be assumed to be constant. Decreasing the circumferential velocity by the scaling factor requires a reduction of the rotational

speed by the square of the scaling factor with

$$n_{scaled} = \frac{n_{original}}{s_f^2} \tag{6.5}$$

The air mass flow of a fan rises with the third power of the diameter and thus with the scaling factor at equal rotational speed. Since the rotational speed is reduced by the square of the scaling factor and the cross section rises with the square of the scaling factor, the resulting velocity in the cooling ducts decreases linearly achieving equal Reynolds numbers in the cooling ducts for the original and scaled geometry:

$$v_{scaled} = \frac{v_{original}}{s_f} \tag{6.6}$$

The temperature of air at the model's air inlet, labeled (a) in Fig. 6.2, has been set to $T_{in} = 350 \text{ K}$. The air has been modeled with temperature dependent fluid properties and with a constant density of

$$\rho = \frac{p_0}{R_s \, T_{in}} \, , \tag{6.7}$$

with the reference pressure p_0, the ideal gas constant for air $R_s = 287.12 \text{ J/kgK}$ and the temperature at the model's air inlet T_{in} in K. The heat capacity c_p has been approximated by a so called zero pressure polynomial and the thermal conductivity λ and dynamic viscosity μ have been modeled by the Sutherland formula, as described in Section 3.2. The wall temperature has been defined as $T_{ew} = 360 \text{ K}$ for the end-windings and $T_{es} = 330 \text{ K}$ for the end-shield. All other walls of the simulation model has been assumed to be adiabatic. The model's air outlets, labeled as (j) in Fig. 6.2, have been set to a subsonic entrainment with 0 Pa relative pressure.

As mentioned above, the model has been simplified to a small sector, in order to reduce the computational effort. Due to this simplification, sectional areas evolve for the stator and the rotor, which have been defined as interfaces with rotational periodicity. Since the number of cooling ducts in the stator and the rotor is not equal, the sector-angle of the rotor-volume is different from the sector-angle of the stator-volume. For this reason, the volumes of stator and rotor have been connected by a frozen rotor interface, which supports this pitch change.

Thermal radiation is a phenomenon in which the heat flux rises with the fourth power of temperature difference. Since this temperature difference between surface and environment has been expected to be not higher than 10 K the total amount of transported heat energy by radiation has been assumed to be small and therefore neglected in this investigation.

6.2.4 Simulation results

In order to achieve acceptable results for the convective wall heat transfer coefficient, a CFD simulation setup with the Shear-Stress-Transport (SST) turbulence model for a steady state simulation has been chosen, as described in [37]. The configuration of

the models have been set according to the validation setup, as described in Section 3.3. After solving the CFD simulation of all model variations, the convective wall heat transfer coefficients α have been obtained by calculating the area weighted average of the heat transfer coefficient over all surfaces of the end-windings. The results have been listed in Tab. 6.2 and 6.3, respectively. Knowing the wall heat transfer coefficient α, one can easily calculate the corresponding Nusselt number with (2.69), as shown in Section 6.3.

n in min^{-1}			1000	2000	3000	4000	1000	2000	3000	4000
$\dot{m}$ in 10^{-3} kg/s			0.260	0.521	0.781	1.041	0.545	1.090	1.635	2.180
l_V	l_H	l_A		α				α		
mm	mm	mm		W/m^{2}K				W/m^{2}K		
175	80	90	9.4	16.0	21.5	26.7	15.5	25.5	34.8	43.1
175	90	100	9.6	16.3	22.2	27.6	15.1	24.7	32.7	39.8
175	95	90	6.9	13.5	18.2	24.3	11.4	20.0	26.8	33.1
175	95	95	8.6	15.4	20.9	26.4	12.8	21.8	29.4	36.0
175	95	100	8.4	15.0	21.1	26.3	13.3	22.6	30.2	37.1
175	125	90	6.9	11.4	14.8	18.3	11.1	19.1	25.6	31.7
175	125	100	6.6	10.9	16.6	19.8	11.0	19.3	26.1	32.4
180	95	90	7.6	13.9	19.9	25.6	11.3	20.0	27.4	34.0
180	95	95	7.8	14.9	20.8	26.8	12.3	21.6	29.6	36.5
180	95	100	7.9	14.6	20.4	25.6	13.0	22.8	31.0	38.1
185	80	90	9.1	15.9	20.9	26.5	15.0	25.2	33.9	41.5
185	90	100	8.9	15.7	22.1	27.1	14.9	25.1	33.3	40.6
185	95	90	6.8	12.7	17.1	23.3	10.7	19.4	26.3	32.8
185	95	100	7.5	14.1	20.2	25.2	12.4	21.8	29.5	36.2
185	125	90	5.3	11.5	12.8	16.0	9.9	18.0	24.5	30.8
185	125	100	4.9	11.1	12.4	15.9	9.6	17.6	24.1	30.2

Table 6.2: Area weighted average of the convective wall heat transfer coefficient α at the end-windings depending on rotational velocity of the rotor for the variations of the original geometry.

6.3 Characterization of the wall heat transfer coefficient

Since an analytical calculation of the convective wall heat transfer coefficient fails in the case of the convoluted shape of the end-windings, an alternative approach is required.

6.3.1 Non-dimensional approach

An alternative solution has been found in the dimension analysis by correlating variations of boundary conditions and geometric modifications to the convective heat transfer coefficient on the end-windings. In fluid dynamics, the use of dimension analysis is a common method, as shown on the example of the Reynolds number (2.65). By

n in min^{-1}			694	1389	2083	2778	694	1389	2083	2778
$\dot{m}$ in 10^{-3} kg/s			0.312	0.625	0.937	1.250	0.654	1.308	1.962	2.616
l_V	l_H	l_A	α				α			
mm	mm	mm	W/m^{2}K				W/m^{2}K			
210	96	108	8.2	13.5	17.9	22.3	12.6	20.4	26.9	32.6
210	108	120	8.4	13.9	18.6	23.3	13.0	20.9	27.5	33.4
210	114	108	6.9	11.9	16.3	21.2	9.9	17.0	23.0	28.3
210	114	114	7.2	12.4	17.2	21.7	10.6	18.0	24.2	29.7
210	114	120	7.7	13.1	17.6	22.4	11.7	19.3	25.7	31.4
210	150	108	6.5	10.9	14.7	18.1	9.6	16.4	22.2	27.4
210	150	120	6.6	11.2	15.1	19.0	9.8	16.8	22.6	27.8
216	114	108	6.2	12.0	16.9	21.6	9.5	16.9	23.2	28.8
216	114	114	6.5	12.3	17.1	21.8	10.1	17.9	24.4	30.1
216	114	120	7.0	13.1	17.9	22.6	11.3	19.4	26.2	32.2
222	96	108	8.1	14.6	19.3	23.7	13.3	21.4	28.4	34.6
222	108	120	8.1	14.1	19.1	23.8	13.1	21.7	28.7	34.9
222	114	108	6.3	12.3	17.2	22.0	9.7	17.1	23.4	29.0
222	114	120	7.2	12.9	18.3	23.1	11.6	19.8	26.6	32.6
222	150	108	4.7	9.2	12.8	19.2	9.0	15.8	21.8	27.1
222	150	120	5.1	10.4	14.4	20.4	8.9	16.0	22.2	27.6

Table 6.3: Area weighted average of the convective heat transfer coefficient α at the end-windings depending on rotational velocity of the rotor for the scaled geometry.

relating the velocity and length to the viscosity, the quotient becomes a criterion about the extent of turbulence.

Like the Reynolds number the Nusselt number (2.69) describes a physical phenomenon by making the convective wall heat transfer coefficient α dimensionless.

As shown in [48], there is also a correlation between the Nusselt number and other dimensionless numbers, as for instance:

$$\mathsf{Nu} = F(\mathsf{Re}, \mathsf{Pr}, \mathsf{Ec}, \mathsf{Gr}) . \tag{6.8}$$

In the case of air as coolant and the common temperature range inside an electric machine, the Prandtl number (see (2.66)) remains almost constant at about $\mathsf{Pr} = 0.7$ and can be included in a constant factor. The Eckert number Ec becomes relevant for supersonic fluid flow, which does not occur in the investigated electric motor. If the fluid flow is caused by buoyant forces, the Grashof number Gr dominates, which can be assumed at zero rotational velocity. Buoyant forces cannot be used with the simplified model, since the direction of gravity has no rotational periodicity. Since the Eckert number can be neglected in subsonic problems and the Grashof number due to the forced flow conditions, the correlation between Nusselt and Reynolds numbers can be simplified to:

$$\mathsf{Nu} = F(\mathsf{Re}) = \mathsf{C} \cdot \mathsf{Re}^\mathsf{n} \tag{6.9}$$

6.3.2 Method

The aim of this work is finding a correlation between the Nusselt number, which describes the convective wall heat transfer and the flow conditions around the end-windings. In this particular case it is assumed that the heat transfer depends on the flow conditions of air only, since the fluid properties remain almost constant but are still temperature dependent. According to (6.1) the relevant variables of the heat transfer problem can be identified as

$$\alpha = f(\mathsf{v}, \mathsf{w}, l_\mathsf{V}, l_\mathsf{H}, l_\mathsf{A}, l_\mathsf{F}, \nu, \lambda) \ , \tag{6.10}$$

with wall heat transfer coefficient α, the velocities v and w, the geometric dimensions l_V, l_H, l_A and l_F the kinematic viscosity ν and the thermal conductivity λ. The conductor width l_F is a geometric dimension which only depend on the geometry scaling factor $\mathsf{s_f}$. A list of relevance is shown in Tab. 6.4 with $\mathsf{h} = 9$ relevant variables. The

Relevance	Derived dimension	Unit	SI unit
R1:	α	$\mathsf{Wm^{-2}K^{-1}}$	$\mathsf{kgs^{-3}K^{-1}}$
R2:	$l_\mathsf{V}, l_\mathsf{H}, l_\mathsf{A}, l_\mathsf{F}$	m	m
R3:	v, w	$\mathsf{ms^{-1}}$	$\mathsf{ms^{-1}}$
R4:	ν	$\mathsf{m^2s^{-1}}$	$\mathsf{m^2s^{-1}}$
R5:	λ	$\mathsf{Wm^{-1}K^{-1}}$	$\mathsf{kgms^{-3}K^{-1}}$

Table 6.4: List of relevant variables

transfer problem requires $\mathsf{m} = 4$ fundamental dimensions length (in m), time (in s), mass (in kg) and temperature (in K) for a suitable characterization. For the set of $\mathsf{n} - \mathsf{m} = 5$ independent variables, the characterization must satisfy (6.2). Since dimensionless numbers for turbulence and heat transfer are available with the Reynolds number and the Nusselt number, the procedure in the dimension analysis of making the variables dimensionless is obsolete. The correlation according to (6.9) is sufficient but a description of C, Re and q is required in accordance with

$$\Pi_\mathsf{5} = F(\Pi_\mathsf{1}, \Pi_\mathsf{2}, \Pi_\mathsf{3}, \Pi_\mathsf{4}) \ . \tag{6.11}$$

The flow conditions and velocities next to the end-windings depend on the angular velocity $\mathsf{w_i}$ of the short circuit ring or the rotor and the velocity $\mathsf{v_i}$ in the stator cooling ducts, respectively. The angular velocity can be derived by the rotational speed $\mathsf{n_i}$ and the diameter of the short circuit ring $\mathsf{D_{or}}$ with (6.3). By using the air mass flow $\dot{\mathsf{m}}$ and cross-sectional area of the stator cooling ducts A, the velocity in the cooling ducts can be calculated with (6.4). These velocities have been considered by the Reynolds number at the end-windings close to the stator cooling ducts outlets

$$\Pi_\mathsf{1i} = \frac{\mathsf{v_i} \ \mathsf{L_{vi}}}{\nu} = \mathsf{Re(v)} \ , \tag{6.12}$$

with the characteristic length L_{vi} and the Reynolds number at the end-windings close to the short circuit ring by

$$\Pi_{2i} = \frac{w_i \ L_{wi}}{\nu} \ , \tag{6.13}$$

with the characteristic length L_{wi}. The characteristic length L_{vi} is the overhang of the end-windings, labeled l_{Ai} in Fig. 6.3 and the characteristic length L_{wi} is the width of a conductor, labeled l_{Fi} in Fig. 6.3. The index i denotes one of the 256 CFD simulations.

On the other, hand the fluid flow around the end-windings is influenced by sectional areas in the flow path which has to be passed by the coolant. In the present case especially those sectional areas are of interest which represent a bottleneck in the flow path and constrain the air to a higher velocity. Such possible constricted cross-sectional areas can be found on two locations around the end-windings, one in radial and one in axial direction between end-windings and end-shield, as shown in Fig. 6.4. The
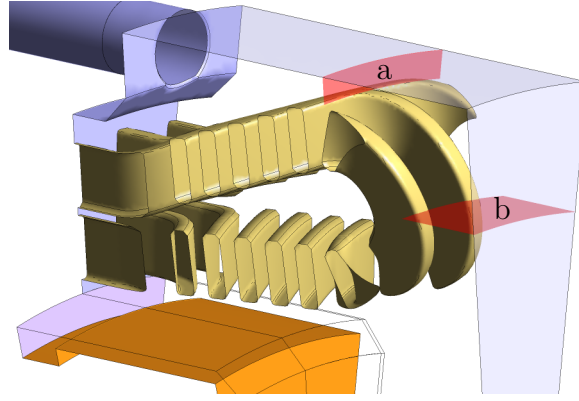
Figure 6.4: Bottlenecks in the air flow path between end-windings and end-shield (a) in radial direction and (b) in axial direction

hydraulic diameter d_h is an established parameter in fluid dynamics, which describes the influence of the cross-sectional area to the flow conditions. It is defined as

$$d_h = \frac{4 \cdot A_h}{U_h} \tag{6.14}$$

which is a ratio of four times the wetted area A_h and the wetted circumference U_h of the cross-sectional area. By calculating these hydraulic diameters of the bottlenecks with

$$L_{zi} = 2(l_{Hi} + l_{Ti} - l_{Ai}) \tag{6.15}$$

and

$$L_{ri} = 4(l_{Vi} - l_{Ei}) \ , \tag{6.16}$$

and taking them as the characteristic length in the calculation of the Reynolds number, the third and the fourth dimensionless factors can be calculated as

$$\Pi_{3i} = \frac{v \ L_{zi}}{\nu} \tag{6.17}$$

and

$$\Pi_{4i} = \frac{\mathsf{v}\ \mathsf{L_{ri}}}{\nu}\ . \tag{6.18}$$

The fifth dimensionless factor is the Nusselt number which can be calculated with (2.69) using the wall heat transfer coefficient α from the CFD simulation and the characteristic length $\mathsf{L_{ui}}$. During the investigation, a characteristic length $\mathsf{L_{ui}}$ for the end-windings of

$$\mathsf{L_{ui}} = l_{\mathsf{Ai}} + \frac{l_{\mathsf{Di}}\ \pi}{2} \tag{6.19}$$

has proved to be reasonable.

By combining the values Π_{1i} to Π_{4i}, the most important parameters are expected to be covered in order to calculate the Nusselt number:

$$\mathsf{Nu_{aprx\ i}} = \Pi_{1i}^{\mathsf{q_1}} \cdot \Pi_{2i}^{\mathsf{q_2}} \cdot \Pi_{3i}^{\mathsf{q_3}} \cdot \Pi_{4i}^{\mathsf{q_4}} \cdot \mathsf{q_5}\ . \tag{6.20}$$

6.3.3 Approximation

By using the Gauss-Newton method, the coefficients $\mathsf{q_1} \ldots \mathsf{q_5}$ have been adjusted to minimize the error between (6.20) and the values simulated with CFD, shown in Tab. 6.2 and 6.3, respectively. The resulting characterization parameters for the approximation of the wall heat transfer coefficient at the end-windings are presented in Tab. 6.5. The results of this approximation have been plotted in Fig. 6.5 to 6.8 as functions

Table 6.5: Characterization parameters

$\mathsf{q_1}$	$\mathsf{q_2}$	$\mathsf{q_3}$	$\mathsf{q_4}$	$\mathsf{q_5}$
0.6764	0.2161	-0.1307	-0.0034	0.0638

of the Reynolds numbers of the cooling ducts $\mathsf{Re}(\mathsf{v})$ which have been calculated with the CFD simulations. Compared to the computed values of the wall heat transfer coefficient by CFD, the average relative error of the approximation can be specified for this data set with $\mathsf{e_{Nu}} = 5.4\%$ and the maximum relative error with $max(\mathsf{e_{Nu}}) = 53\%$.

Revising the results of the approximation, one has to be careful concerning the physical validity of the values $\mathsf{q_1}$ to $\mathsf{q_5}$, since the Gauss-Newton method might find solutions which are mathematically optimal but physically invalid. The Nusselt number on a flat plate rises with the length and with the Reynolds number of the plate. Since the flow conditions along the overhang l_{Ai} of the end-windings can be compared to the conditions of a flat plate the Nusselt number must rise with a rising overhang l_{Ai} and the factor $\mathsf{q_1}$ has to be positive. The Nusselt number should rise with rising rotational speed, hence the factor $\mathsf{q_2}$ must have positive values. For a preset air mass flow, the fluid velocity should rise if the cross-sectional area and hydraulic diameter in (6.15) and (6.16) becomes smaller, hence it is more likely that the factors $\mathsf{q_3}$ and $\mathsf{q_4}$ have negative values. Since the Reynolds and the Nusselt numbers are positive, the factor $\mathsf{q_5}$ has to be positive as well.

6.3.4   Application

With the availability of the end-windings' heat transfer characterization, the wall heat transfer coefficient α can be obtained easily for similar geometries analyzed in this work. Once the geometry and operational parameters are available for a specific motor the Pi-values can be calculated with (6.12), (6.13), (6.17) and (6.18). By knowing the Pi-values the Nusselt number of a specific operation point can be calculated by (6.20) including the characterization parameters in Tab. 6.5. Rearranging (2.69), the wall heat transfer coefficient α can the be obtained with the characteristic length $\mathsf{L_u}$ as calculated in (6.19) and the thermal conductivity of air λ for the prevailing temperature. Applying this characterization to the geometry investigated in chapters 4 and 5 the approximated heat transfer coefficients α_{aprx} can be calculated, as shown in Tab. 6.6. The approximated wall heat transfer coefficients have been compared with the simulated values from the global model α_{glob} in Tab. 5.2 and the results of the local model α_{loc} in Section 5.3, also shown in Tab. 6.6. Since this characteriza-

n	w	$\dot{m}$	v	Π_3	Π_4	Nu	α_{aprx}	α_{glob}	α_{loc}
min^{-1}	m/s	kg/s	m/s	–	–	–		W/m^{2}K	
1503	18.1	7.6E-04	4.00	2915	4127	61.4	13.8	13.4	13.7
1800	21.7	9.2E-04	4.79	3492	4943	70.4	15.9	14.9	15.0
2104	25.3	1.1E-03	5.59	4081	5778	79.3	17.9	16.6	16.6
2400	28.9	1.2E-03	6.38	4655	6591	87.6	19.7	18.9	18.9
2700	32.5	1.4E-03	7.18	5237	7414	95.8	21.6	20.8	21.2
3007	36.2	1.5E-03	7.99	5833	8258	103.9	23.4	22.6	22.9

Table 6.6: Application of characterization to the geometry investigated in the chapters 4 and 5 including a comparison of the results

tion is based on a specific range of geometric dimensions and operational conditions, the interpolation inside these ranges is safe. Heat transfer coefficients calculated for geometries or operational conditions which were extrapolated outside these ranges, might be calculated with a much higher error than estimated in here.

6.3.5   Discussion

With the aid of dimension analysis it has been possible to extract a set of parameters which allow the characterization of the average convective wall heat transfer coefficient on the end-windings of a traction motor. The characterization with a non-dimensional correlation has the benefit of scalability depending on specific characteristic lengths.

In the present chapter the procedure of obtaining correlations of the convective wall heat transfer coefficient of the end-windings and geometrical plus operational conditions has been outlined. The employment of CFD allows the simulation of the fluid flow including the according effects, like the convective wall heat transfer. In the present case 32 different geometries with two different values for the air mass flow in the stator cooling ducts and each with four different rotational speeds of the

rotor have been investigated. Out of these 256 CFD simulation cases the data for the correlation of heat transfer and operational conditions have been extracted. The computed heat transfer values of the varied geometries have been correlated to the known boundary conditions and geometric dimensions with the Gauss-Newton method. Interpreting the obtained characterization parameters in Tab. 6.5, one can see that the Reynolds numbers affect the heat transfer to a higher extent than the geometric ratios. Especially the fluid flow from the stator cooling ducts has a large influence to the overall heat transfer. In Fig. 6.5 to Fig. 6.8, the simulated results have been compared to the approximations. Each diagram contains the average heat transfer as Nusselt number obtained from eight different CFD simulations with two different ratios of rotational speed n to stator cooling duct mass flow $\dot{m}$. The two different ratios $\dot{m}_1/n$ and $\dot{m}_2/n$ have been approximated with the obtained characterization parameters of this chapter, shown as solid lines in the diagrams. Additionally to these results, the relative errors between the simulated and approximated Nusselt numbers have been plotted together with the corresponding simulation results. Each pair of the left and right hand side diagrams refer to a non-scaled and a scaled pair of geometries. Since the CFD simulations of one pair of non-scaled and scaled geometry has been accomplished with boundary conditions for theoretically equal Reynolds numbers, the corresponding Nusselt numbers in the diagrams in Fig. 6.5 to 6.8 should match each other. In all these pairs of diagrams the results differ more or less. Especially the results of the diagram-pairs in Fig. 6.8(e) to Fig. 6.8(h) stray widely up to a maximum error of 53%. Since these are comparisons of equal simulation setups, this difference can be identified as an error of the CFD simulation. Therefore this difference can be identified partially as an error of the CFD simulation, which was also experienced during the CFD simulations by non properly converging residuals. The average error on the other hand remains mostly below 10% which is sufficient for most engineering purposes.

The benefit of this parameter set is a more flexible way of calculating the wall heat transfer coefficents. Compared to other approaches, this method allows more degrees of freedom regarding the basic end-shield dimensions and a scalability of the geometry as a whole.

Additional results of models with more variations of geometry and additional dimensionless ratios can be appended to the existing data, in order to make the presented method more flexible to other geometries.

(a) $l_V = 175$ mm, $l_H = 80$ mm, $l_A = 90$ mm

(b) $l_V = 210$ mm, $l_H = 96$ mm, $l_A = 108$ mm

(c) $l_V = 175$ mm, $l_H = 90$ mm, $l_A = 100$ mm

(d) $l_V = 210$ mm, $l_H = 108$ mm, $l_A = 120$ mm

(e) $l_V = 175$ mm, $l_H = 95$ mm, $l_A = 90$ mm

(f) $l_V = 210$ mm, $l_H = 114$ mm, $l_A = 108$ mm

(g) $l_V = 175$ mm, $l_H = 95$ mm, $l_A = 95$ mm

(h) $l_V = 210$ mm, $l_H = 114$ mm, $l_A = 114$ mm

Figure 6.5: Simulated results and approximation of the *Nusselt* number for variations of geometry including the relative error in percent

(a) $l_V = 175$ mm, $l_H = 95$ mm, $l_A = 100$ mm

(b) $l_V = 210$ mm, $l_H = 114$ mm, $l_A = 120$ mm

(c) $l_V = 175$ mm, $l_H = 125$ mm, $l_A = 90$ mm

(d) $l_V = 210$ mm, $l_H = 150$ mm, $l_A = 108$ mm

(e) $l_V = 175$ mm, $l_H = 125$ mm, $l_A = 100$ mm

(f) $l_V = 210$ mm, $l_H = 150$ mm, $l_A = 120$ mm

(g) $l_V = 180$ mm, $l_H = 95$ mm, $l_A = 90$ mm

(h) $l_V = 216$ mm, $l_H = 114$ mm, $l_A = 108$ mm
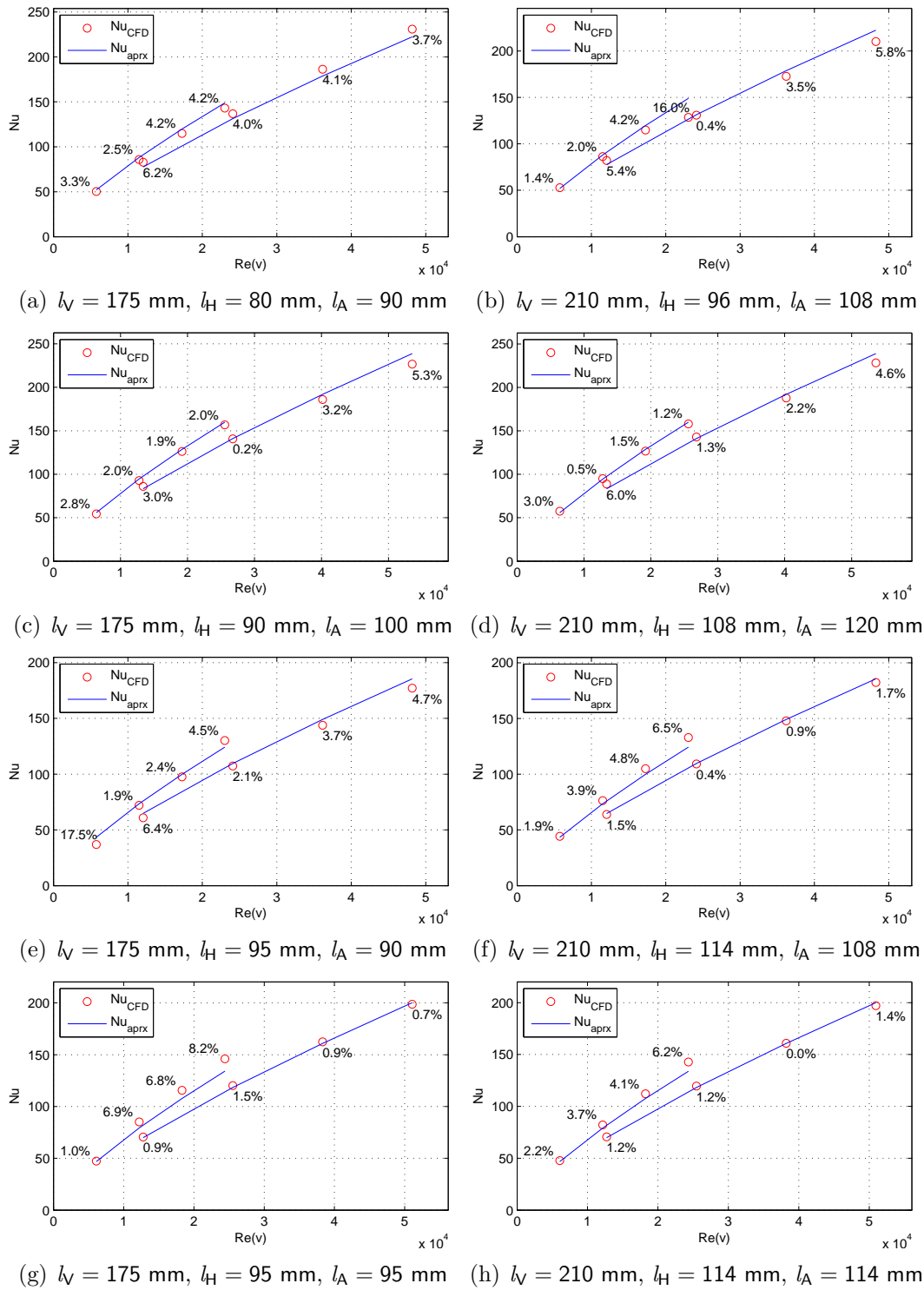
Figure 6.6: Simulated results and approximation of the *Nusselt* number for variations of geometry including the relative error in percent

(a) $l_V = 180$ mm, $l_H = 95$ mm, $l_A = 95$ mm　(b) $l_V = 216$ mm, $l_H = 114$ mm, $l_A = 114$ mm

(c) $l_V = 180$ mm, $l_H = 95$ mm, $l_A = 100$ mm　(d) $l_V = 216$ mm, $l_H = 114$ mm, $l_A = 120$ mm

(e) $l_V = 185$ mm, $l_H = 80$ mm, $l_A = 90$ mm　(f) $l_V = 222$ mm, $l_H = 96$ mm, $l_A = 108$ mm

(g) $l_V = 185$ mm, $l_H = 90$ mm, $l_A = 100$ mm　(h) $l_V = 222$ mm, $l_H = 108$ mm, $l_A = 120$ mm
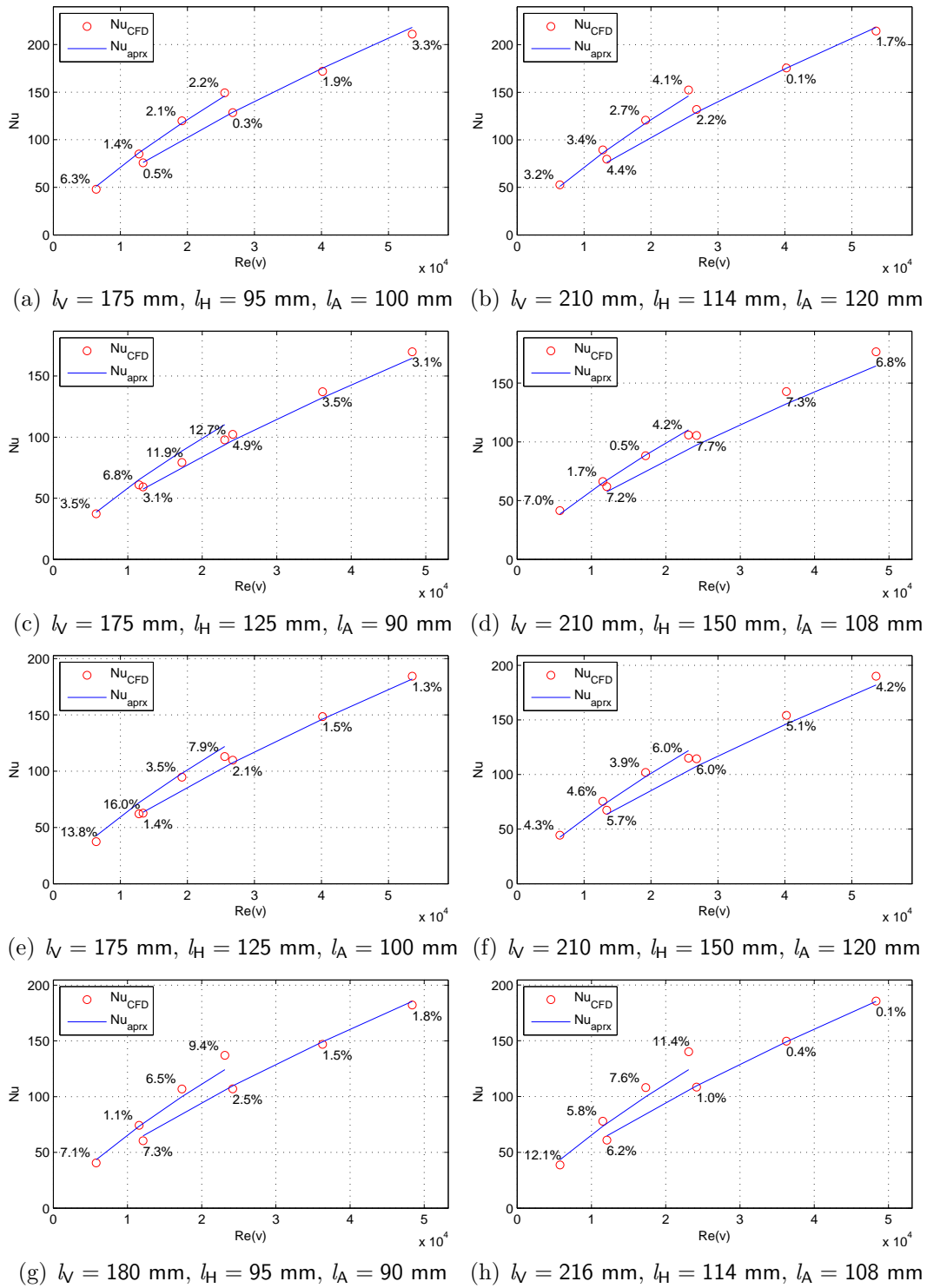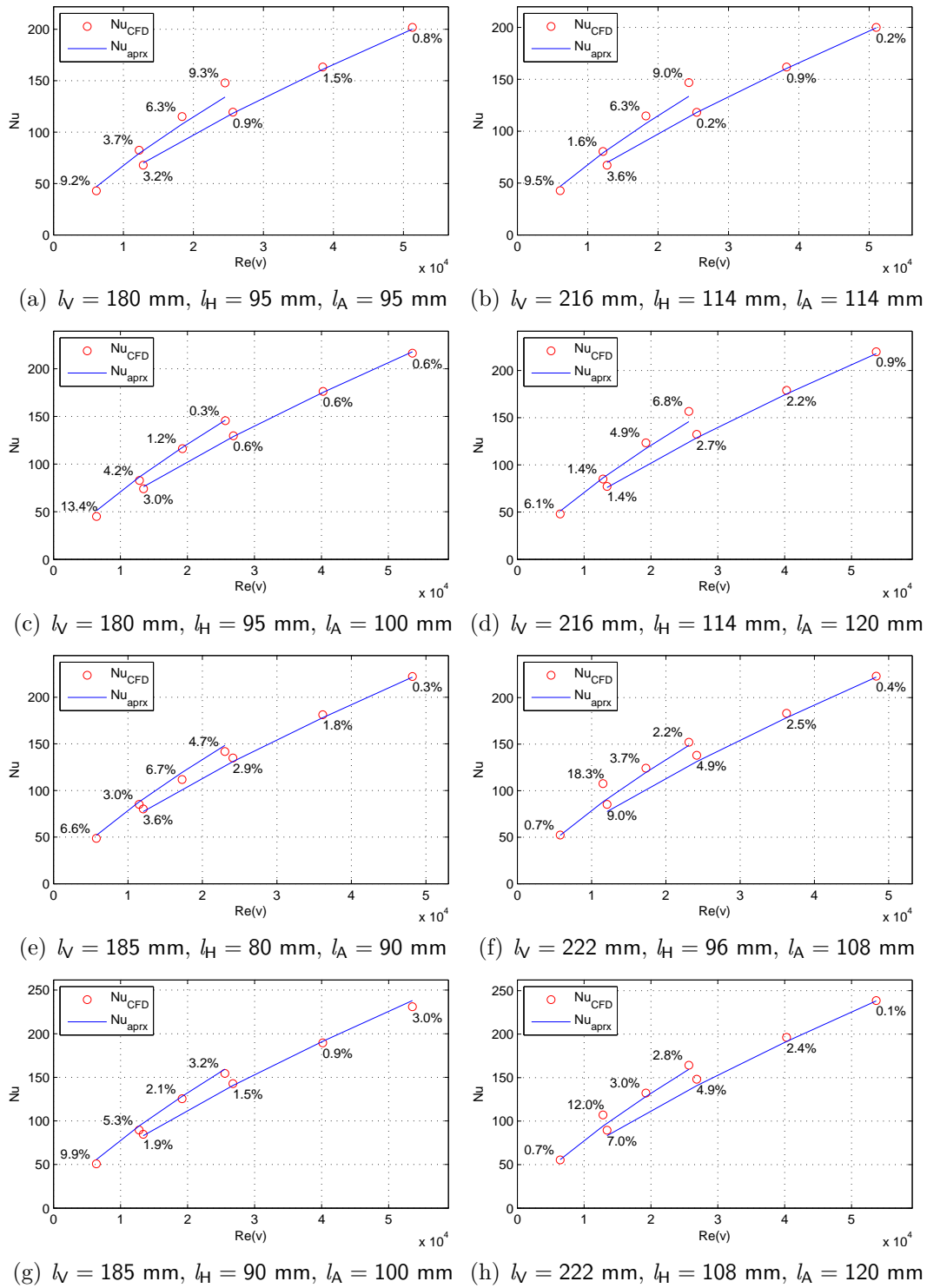
Figure 6.7: Simulated results and approximation of the *Nusselt* number for variations of geometry including the relative error in percent

(a) $l_V = 185$ mm, $l_H = 95$ mm, $l_A = 90$ mm

(b) $l_V = 222$ mm, $l_H = 114$ mm, $l_A = 108$ mm

(c) $l_V = 185$ mm, $l_H = 95$ mm, $l_A = 100$ mm

(d) $l_V = 222$ mm, $l_H = 114$ mm, $l_A = 120$ mm

(e) $l_V = 185$ mm, $l_H = 125$ mm, $l_A = 90$ mm

(f) $l_V = 222$ mm, $l_H = 150$ mm, $l_A = 108$ mm

(g) $l_V = 185$ mm, $l_H = 125$ mm, $l_A = 100$ mm

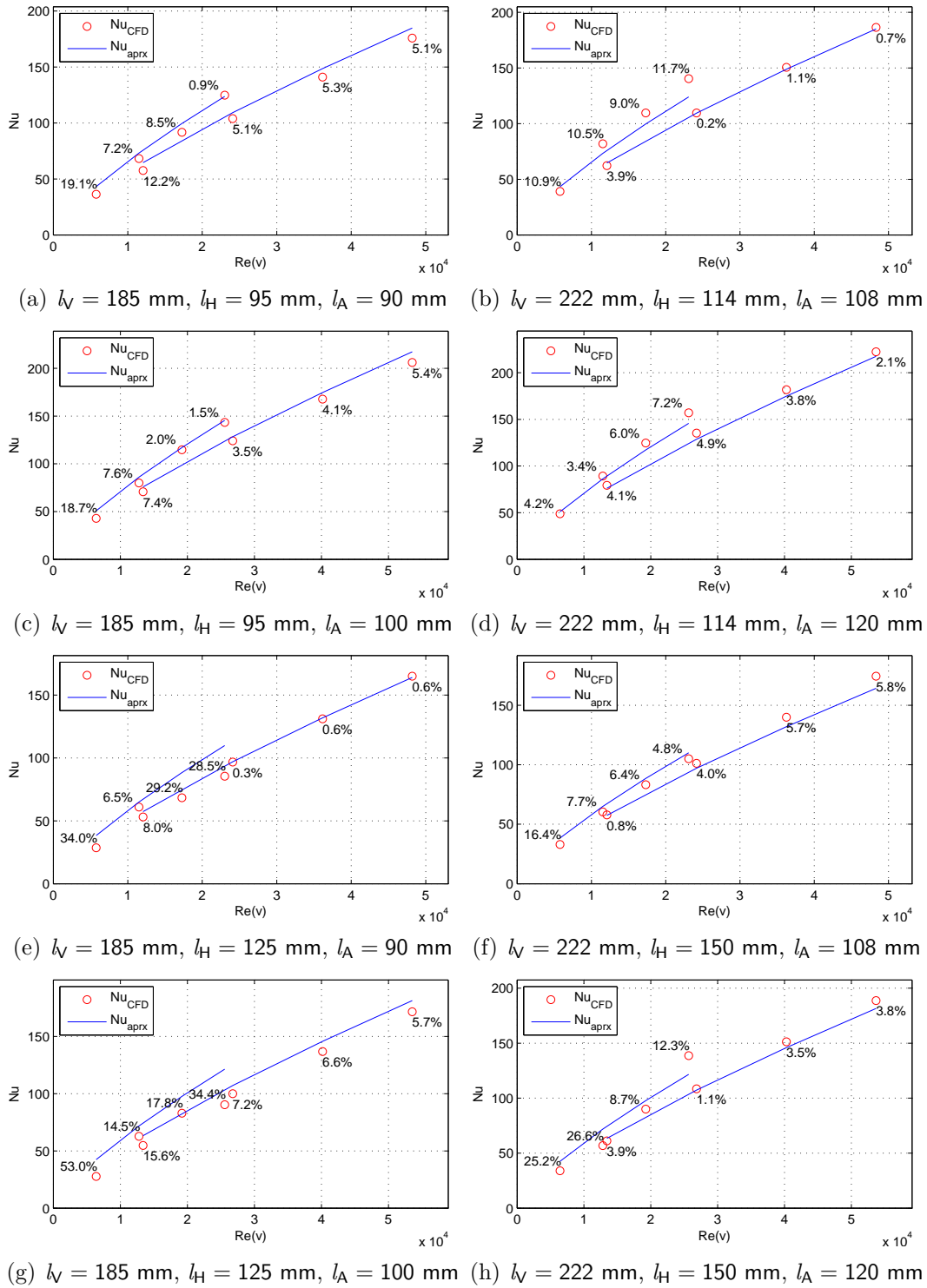(h) $l_V = 222$ mm, $l_H = 150$ mm, $l_A = 120$ mm

Figure 6.8: Simulated results and approximation of the *Nusselt* number for variations of geometry including the relative error in percent

Chapter 7

Results and Conclusion

7.1 New scientific results

Investigations known from the literature are focused, with some exceptions, on TEFC motors. Due to a different cooling strategy of traction motors with DACS, empirical models for the convective wall heat transfer coefficient of the end-windings of TEFC motors cannot be used for DACS motors. The recent advances in CFD, e.g. [49, 56], allow the numerical calculation of the convective wall heat transfer coefficient with acceptable accuracy. Hence, the approach of this thesis is based on CFD and on measurements for validation.

The capability of CFD for predicting the convective wall heat transfer coefficient has been identified on a cylinder in a cross-flow. It has been shown that the prediction of the convective wall heat transfer coefficient with the SST turbulence model is not exact but correlates with the empirical results with acceptable accuracy. The simulation has been accomplished with different velocities showing that the agreement is better for low Reynolds numbers which are more likely in the end-region of the investigated machine.

Due to the non-periodical shape of the end-region of the measured motor, the CFD simulations have taken into account the whole circumference of the end-region. In order to obtain accurate values of the wall heat transfer coefficient, the simulations have been carried out with a resolved boundary layer mesh using the global-local domain decomposition method. The results have shown that the local models have led to no significant improvements in this particular case. The simulated values of the wall heat transfer coefficient have been validated by locally measured values.

A transient thermal network for calculating the thermal management of a traction motor requires a fast way of calculating the convective wall heat transfer coefficient. The implementation of a rough approximation is more useful in this case than the computationally costly CFD method. Therefore, a characterization of the convective wall heat transfer coefficient has been created in this thesis which allows the variation of rotational speed, cooling duct air mass flow, end-windings overhang, end-shield

diameter and end-shield height, as well as a variation by a total scaling of the geometry.

7.2 Conclusion

In order to efficiently deploy the available resources in the manufacturing process of electrical machines, a comprehensive understanding of the utilization of each single part of the machine is valuable. By visualizing various physical mechanisms, simulations support this understanding to a large extent.

For the simulation of the thermal management of an electrical machine, boundary conditions like the convective wall heat transfer coefficient are required. The accuracy of the thermal management simulation depends highly upon the accuracy of these boundary conditions. The quantity of transferred heat depends on the coolant (fluid) and on the flow conditions next to the heated surface. In the case of a self ventilated motor, the flow conditions depend exclusively on its rotational speed. Traction motors have to operate in the full range of rotational speed, from zero at start conditions to the highest rotational speed at the vehicle's maximum velocity. Since the flow conditions depend on the rotational speed and thus on the operation cycle of the traction motor, an accurate transient simulation of the heat management requires convective wall heat transfer coefficients depending on the rotational speed.

The heat transfer inside the cooling ducts is comparable to a pipe flow, which has been investigated satisfactorily in the past and the results are available in reference books as [88] for a large number of different flow conditions and fluids. These flow conditions can often be reduced to 2-D problems and some of them can even be solved analytically. Due to the convoluted shape of the end-windings, the prediction of the convective wall heat transfer coefficient on their surfaces requires a more sophisticated approach. Regarding traction motors, a variety of different cooling methods with different shapes of end-windings and end-shields are feasible. Therefore it is unlikely to find a common solution for all types of end-windings, hence this work is focusing on one specific type of traction motor. The method used in this work, on the other hand, is applicable to any type of cooling method and shape of end-region, respectively.

The investigation of the convective wall heat transfer has been carried out using computational fluid dynamics (CFD), briefly described in Section 2.4. The velocity of air and its turbulence next to a wall is a major factor for its convective heat transfer coefficient. With the method of CFD it is possible to gather velocity information about fluid conditions which were hardly gaugeable in the past. The underlying models of CFD are able to calculate accurate results within certain limits but may yield wrong results, if the limits of one model are disregarded. To ensure proper use of these CFD models, the simulation setup has been validated on a circular cylinder by comparing the simulation results to previously published measurements. In Chapter 3 this validation has been carried out in accordance with established investigations.

One type of end-windings has been investigated with measurements at specific positions. Due to the shape of the end-windings and the size of the used heat flux

sensors, local values of the convective wall heat transfer coefficient have been measured rather than values averaged over the whole end-windings' surfaces. Heat flux sensors with a larger sensing area would gain a more averaged result and would hence be beneficial to such investigations. Since it is not possible to bend the used type of heat flux sensors, the application of larger sensors to the convoluted surface of the end-windings is impossible.

The end-windings of the investigated traction motor are cooled by a closed cooling circuit, which are not accessible during operation without modifications of the motor. In order to obtain values of the air mass flow inside the cooling ducts, the loss of static pressure along the cooling ducts has been measured. The air mass flow depends not only on the static pressure but also on the roughness of the surface inside the cooling ducts. This roughness has also been evaluated by measuring the static pressure inside the cooling ducts of the outer cooling circuit. Since this is an open cooling circuit, values of the total air mass flow have been available during the operation. By measuring the total air mass flow of the machine, the air mass flow inside the single cooling ducts of the outer cooling cycle have been available. These measurements including the corresponding calculations are presented in Chapter 4.

On the one hand, CFD is very helpful to get a survey of the heat transfer over the whole surface. On the other hand, measurements can be performed at certain spots only, but are indispensable to validate the simulation results [42]. The end-region of a real induction machine has no strict rotational periodicity. Some non-periodic shapes as waste grease drain, bracings and fins whose numbers are not equal to the number of the end-windings can cause different flow conditions on different end-winding conductors. Hence, the convective wall heat transfer coefficient varies azimuthally at the conductors. Obviously a more accurate comparison between measurements and simulation can be achieved by modeling the whole circumference of the machines end-region, rather than a single sector. Since CFD simulations of convective heat transfer problems require a very fine calculation mesh, a computable limit on contemporary computers can be reached very fast.

Despite the permanent improvement of commercial CFD software, the prediction of convective heat transfer coefficients is still a demanding subject. Especially for cooling purposes, the examined geometry is rarely optimized for fluid flow and thus causes flow separation and re-attachment, which can not always be simulated accurately by CFD, the choice of the turbulence model is essential, as presented in [42]. In Chapter 5 the measured results of the local convective wall heat transfer coefficients have been compared to the simulated results. These simulations have been carried out for the whole circumference of the end-windings with the global-local domain decomposition method to appropriately consider the shape of the end-region.

With this validated simulation setup, a characterization of the end-windings' convective wall heat transfer coefficient has been carried out. By the use of CFD, a number of different end-winding geometries and different operational conditions have been investigated to find the different values of the convective wall heat transfer coefficient at the end-windings.

With the aid of the Pi-Theorem, a correlation between the convective wall heat transfer coefficient and the operational conditions, as well as the geometrical changes of the end-shield has been found. The result is a flexible approximation of the Nusselt number dependent on operational conditions. The Nusselt number is, as customary, a function of the Reynolds number but adapted by additional parameters, as shown in Chapter 6. It is not only a function of the rotational speed and the mass flow through the cooling vents but also a function of some basic geometric values [35]. With the dimensionless Reynolds numbers and Nusselt numbers the result is also applicable to scaled geometries with similar shapes. The attained characterization of the convective wall heat transfer coefficient provides an easy and fast way to forecast the heat flux from the end-windings and is, therefore, well suitable for transient simulations with thermal network models. Describing the air mass flow through the cooling vents with the rotational speed of the rotor, the performance of the ventilator can be considered. This also provides an improvement for optimizing the properties of the ventilator [36].

The surface of the real end-windings is partially smooth and partially rough, due to resin impregnated bandages wrapped around the conductors. These investigations have been made on hydraulically smooth surfaces, since measurements have been carried out with heat flux sensors with smooth surfaces. The conditions at the end-windings' surface depend on the manufacturing processes to a high extent and are therefore subject to statistical distribution of smooth and rough regions on the surface. Therefore a number of identical motors would be required to find a statistically significant result.

Bibliography

[1] Eugene F. Adiutori. Origins of the heat transfer coefficient. In *Mechanical Engineering*, pages 46–50. West Chester, Ohio, 1990.

[2] John D. Anderson. *Computational Fluid Dynamics - The Basics with Applications*. McGraw-Hill, New York, 1995.

[3] AnsysWB. *Release 11.0 Documentation for ANSYS Workbench*. Ansys, Inc., Southpointe 275 Technology Drive Canonsburg, PA 15317, 2007.

[4] AnsysWB. *Release 13.0 Documentation for ANSYS Workbench*. SAS IP, Inc., Southpointe 275 Technology Drive Canonsburg, PA 15317, 2010.

[5] A.F. Armor and M.V.K. Chari. Heat flow in the stator core of large turbine-generators, by the method of three-dimensional finite elements part II: Temperature distribution in the stator iron. *IEEE Transactions on Power Apparatus and Systems*, 95(5):1657 – 1668, 1976.

[6] Hans Dieter Baehr and Stephan Kabelac. *Thermodynamik - Grundlagen und technische Anwendungen*. Springer, Berlin Heidelberg, 14th edition, 2009.

[7] Hans Dieter Baehr and Karl Stephan. *Wärme- und Stoffübertragung*. Springer, Heidelberg London New York, 6th edition, 2008.

[8] A. Boglietti and A. Cavagnino. Analysis of the endwinding cooling effects in TEFC induction motors. *IEEE Transactions on Industry Applications*, 43(5):1214–1222, 2007.

[9] A. Boglietti, A. Cavagnino, and D. Staton. Determination of critical parameters in electrical machine thermal models. *IEEE Transactions on Industry Applications*, 44(4):1150–1159, 2008.

[10] A. Boglietti, A. Cavagnino, D. Staton, M. Shanel, M. Mueller, and C. Mejuto. Evolution and modern approaches for thermal analysis of electrical machines. *IEEE Transactions on Industrial Electronics*, 56(3):871–882, 2009.

[11] A. Boglietti, A. Cavagnino, D.A. Staton, M. Popescu, C. Cossar, and M.I. McGilp. End space heat transfer coefficient determination for different induction motor enclosure types. *IEEE Transactions on Industry Applications*, 45(3):929–937, 2009.

[12] Craig F. Bohren. Comment on "Newton's law of cooling—A critical assessment," by Colm T. O'Sullivan. *American Journal of Physics*, 59:1044, 1991. Department of Meteorology, Pennsylvania State University, University Park, Pennsylvania 16802.

[13] Günther Brenn. *Strömungslehre und Wärmeübertragung I*. TU Graz, 2004.

[14] Leopold Böswirth. *Technische Strömungslehre*. Vieweg, Wiesbaden, 2007.

[15] Edgar Buckingham. The principle of similitude. *Nature*, 96(2406):396–397, 1915.

[16] N.J. Carew. Experimental determination of heat transfer co-efficients of salient pole rotors. In *IEE Colloquium on Thermal Aspects of Machines*, pages 8/1 –8/8, London, UK, October 27 1992.

[17] Tuncer Cebeci, Jian Shao, Fassi Kafyeke, and Eric Laurendeau. *Computational Fluid Dynamics for Engineers From Panel to Navier-Stokes Methods with Computer Programs*. Springer, Berlin Heidelberg, 2005.

[18] K. Dhinsa, C. Bailey, and K. Pericleous. Investigation into the performance of turbulence models for fluid flow and heat transfer phenomena in electronic applications. *IEEE Transactions on Components and Packaging Technologies*, 28(4):686 – 699, 2005.

[19] DIN-EN-60751. Industrial platinum resistance thermometers and platinum temperature sensors (iec 60751:2008), 2009.

[20] E. Farnleitner and G. Kastner. Moderne Methoden der Ventilationsauslegung von Pumpspeichergeneratoren. *E&I Elektrotechnik und Informationstechnik*, 127:24– 29, 2010.

[21] Ernst Farnleitner. *Computational Fluid Dynamics Analysis for Rotating Electrical Machinery*. PhD thesis, University of Leoben, Austria, 1999.

[22] Joel H. Ferziger and Milovan Peric. *Numerische Strömungsmechanik*. Springer, Berlin Heidelberg, 2008.

[23] C.A.J. Fletcher. *Computational Techniques for Fluid Dynamics*, volume 1. Springer, Berlin Heidelberg New York, 2nd edition, 2006.

[24] C.A.J. Fletcher. *Computational Techniques for Fluid Dynamics*, volume 2. Springer, Berlin Heidelberg New York, 2nd edition, 2006.

[25] Fluent. *FLUENT 6.0 User's Guide*. Fluent Inc., Centerra Resource park, 10 Cavendish Court, Lebanon, NH 03766, 2001.

[26] Jean Baptiste Joseph Fourier. *The Analytical Theory of Heat*. Cambridge University Press, 1878.

[27] W. H. Giedt. *Investigation of Variation of Point Unit-Heat-Transfer Coefficient around a Cylinder Normal to an Air Stream*, volume 71. Trans.ASME, 1949.

[28] G. Gilson, S.J. Pickering, D.B. Hann, and C. Gerada. Analysis of the end winding heat transfer variation with altitude in electric motors. In *IECON '09. 35th Annual Conference of IEEE Industrial Electronics*, pages 2545 –2550, Porto, Portugal, November 3-5 2009.

[29] Gottfried Gotter. *Erwärmung und Kühlung elektrischer Maschinen*. Springer-Verlag, Berlin Göttingen Heidelberg, 1954.

[30] J. Hak. Der Luftspalt-Wärmewiderstand einer elektrischen Maschine. *Electrical Engineering (Archiv für Elektrotechnik)*, 42(5):257–272, 1956.

[31] J. Hak. Lösung eines Wärmequellen-Netzes mit Berücksichtigung der Kühlströme. *Electrical Engineering (Archiv fur Elektrotechnik)*, 42(3):137–154, 1956.

[32] K. Hattori, K. Ide, K. Takahashi, K. Kobashi, H. Okabe, and T. Watanabe. Performance assessment study of a 250 MVA air-cooled turbo-generator. In *IEMDC'03. IEEE International Electric Machines and Drives Conference, 2003.*, volume 1, pages 124 – 128, Madison, Wisconsin, June 1-4 2003.

[33] Heinz Herwig. Kritische Anmerkungen zu einem weitverbreiteten Konzept: der Wärmeübergangskoeffizient α. *Forschung im Ingenieurwesen*, 63:13–17, 1997.

[34] Heinz Herwig. *Strömungsmechanik - Eine Einführung in die Physik und die mathematische Modellierung von Strömungen*. Springer, Berlin Heidelberg, 2nd edition, 2006.

[35] Martin Hettegger, Alice Reinbacher-Köstinger, and Oszkár Bíró. Characterizing the convective wall heat transfer on convoluted shapes in the end-region of an induction machine. In *XX International Conference on Electrical Machines (ICEM), 2012*, pages 1–8, Marseille, France, September 2–5 2012.

[36] Martin Hettegger, Bernhard Streibl, Oszkár Bíró, and Harald Neudorfer. Characterizing the heat transfer on the end-windings of an electrical machine for transient simulations. In *MELECON 2010 - 15th IEEE Mediterranean Electrotechnical Conference*, pages 581–586, Valetta, Malta, April 26–28 2010.

[37] Martin Hettegger, Bernhard Streibl, Oszkár Bíró, and Harald Neudorfer. Identifying the heat transfer coefficients on the end-windings of an electrical machine by measurements and simulations. In *XIX International Conference on Electrical Machines (ICEM)*, pages 1–5, Rome, Italy, September 6–8 2010.

[38] Martin Hettegger, Bernhard Streibl, Oszkár Bíró, and Harald Neudorfer. Measurements and simulations of the heat transfer on end windings of an induction machine. In *14th International IGTE Symposium*, pages 97–100, Graz, Austria, September 19–22 2010.

[39] Martin Hettegger, Bernhard Streibl, Oszkár Bíró, and Harald Neudorfer. Measurements and simulations of the heat transfer on end windings of an induction machine. In *Sixth International PhD & DLA Symposium*, page C:116, Pécs, Hungary, October 25–26 2010.

[40] Martin Hettegger, Bernhard Streibl, Oszkár Bíró, and Harald Neudorfer. Characterizing the heat transfer on the end-windings in an electrical machine depending on geometrical properties of the end-region. In *ISEF 2011 - XV International Symposium on Electromagnetic Fields in Mechatronics, Electrical and Electronic Engineering*, pages 1–8, Funchal, Portugal, September 1–3 2011.

[41] Martin Hettegger, Bernhard Streibl, Oszkár Bíró, and Harald Neudorfer. Measurements and simulations of the heat transfer on end windings of an induction machine. *COMPEL*, 30(6):1727–1736, 2011.

[42] Martin Hettegger, Bernhard Streibl, Oszkár Bíró, and Harald Neudorfer. Measurements and simulations of the convective heat transfer coefficients on the end-windings of an electrical machine. *IEEE Transactions on Industrial Electronics*, 59(5):2299–2308, 2012.

[43] Charles Hirsch. *Numerical Computation of Internal and External Flows Fundamentals of Computational Fluid Dynamics*. Elsevier Science & Technology Books, Burlington, 2nd edition, 2007.

[44] Klaus A. Hoffmann and Steve T. Chiang. *Computational Fluid Dynamics*, volume 2. Engineering Education System, Wichita, Kansas, 4th edition, 2000.

[45] IEC60034-1. Rotating electrical machines - part 1: Rating and performance, 2004.

[46] IEC60034-6. Rotating electrical machines - part 6: Methods of cooling, 1991.

[47] B.A. Kader. Temperature and concentration profiles in fully turbulent boundary layers. *International Journal of Heat and Mass Transfer*, 24(9):1541 – 1544, 1981.

[48] Frank Kreith and Mark S. Bohn. *Principles of Heat Transfer*. Thomson, 6th edition, 2001.

[49] R.B. Langtry and F.R. Menter. Transition modeling for general CFD applications in aeronautics. Technical report, ANSYS Germany GmbH, 2005.

[50] Weili Li, Junci Cao, and Xiaochen Zhang. Electrothermal analysis of induction motor with compound cage rotor used for PHEV. *IEEE Transactions on Industrial Electronics*, 57(2):660 –668, 2010.

[51] Loctite. *Technical Data Sheet - Loctite 603.* Henkel Technologies, 2004.

[52] Yiping Lu, Wenhao Yin, Pengfei Chen, and Weili Li. Mechanism research on air mass flow rate distribution in rotor radial ducts of turbo generator with sub-slot ventilation. In *WAC 2008. World Automation Congress*, pages 1–5, Waikoloa, Hawaii, September 28 - October 2 2008.

[53] Yiping Lu, Wenhao Yin, Jiade Han, Weili Li, and Pengfei Chen. Effect of insulation property and distribution of turbo generator rotor on temperature field. In *WAC 2008. World Automation Congress*, pages 1–5, Waikoloa, Hawaii, September 28 - October 2 2008.

[54] F. Menter and Y. Egorov. The scale-adaptive simulation method for unsteady turbulent flow predictions. part 1: Theory and model description. *Flow, Turbulence and Combustion*, 85:113–138, 2010.

[55] F. Menter, R. Langtry, and S. Völker. Transition modelling for general purpose CFD codes. *Flow, Turbulence and Combustion*, 77:277–303, 2006.

[56] F. R. Menter. Two-equation eddy-viscosity turbulence models for engineering applications. *AIAA Journal*, 32:1598–1605, 1994.

[57] Florian Menter, Jorge Carregal Ferreira, Thomas Esch, and Brad Konno. The SST turbulence model with improvedwall treatment for heat transfer predictions in gas turbines. In *Proceedings of the International Gas Turbine Congress*, pages 1–7, Tokyo, Japan, November 2-7 2003.

[58] F.R. Menter and Y. Egorov. A scale adaptive simulation model using two-equation models. In *43rd AIAA Aerospace Sciences Meeting and Exhibit*, AIAA-2005-1095, Reno, NV, January 10–13 2005.

[59] F.R. Menter, R.B. Langtry, S.R. Likki, Y.B. Suzen, P.G. Huang, and S. Völker. A correlation based transition model using local variables part 1 - model formulation. In *ASME-GT2004-53452, ASME TURBO EXPO 2004*, Vienna, Austria, June 14–17 2004.

[60] C. Micallef, S.J. Pickering, K. Simmons, and K. Bradley. Improvements in air flow in the end region of a large totally enclosed fan cooled induction motor. In *IEEE International Conference on Electric Machines and Drives*, pages 579–584, San Antonio, Texas, May 15-18 2005.

[61] C. Micallef, S.J. Pickering, K.A. Simmons, and K.J. Bradley. Improved cooling in the end region of a strip-wound totally enclosed fan-cooled induction electric machine. *IEEE Transactions on Industrial Electronics*, 55(10):3517 –3524, 2008.

[62] Germar Müller. *Grundlagen elektrischer Maschinen*. VCH-Verl.-Ges., Weinheim, 1994.

[63] Germar Müller and Bernd Ponick. *Allgemeine Betrachtungen über rotierende elektrische Maschinen*, pages 203–281. Wiley-VCH Verlag GmbH & Co. KGaA, Weinheim, 2006.

[64] J. Mugglestone, S.J. Pickering, and D. Lampard. Effect of geometric changes on the flow and heat transfer in the end region of a TEFC induction motor. In *Ninth International Conference on Electrical Machines and Drives*, pages 40–44, Canterbury Christ Church College, UK, September 1-3 1999.

[65] J. Mugglestone, S.J. Pickering, and D. Lampard. Prediction of the heat transfer from the end winding of a TEFC strip-wound induction motor. In *Ninth International Conference on Electrical Machines and Drives*, pages 484–486, Canterbury Christ Church College, UK, September 1-3 1999.

[66] Isaac Newton. A scale of the degrees of heat. *Proceedings of the Royal Society of London*, 22:1–4, 1701.

[67] Colm T. O'Sullivan. Newton's law of cooling-a critical assessment. *American Journal of Physics*, 58(10):pp. 956–960, 1990.

[68] S. Pickering, F. Thovex, P. Wheeler, and K. Bradley. Thermal design of an integrated motor drive. In *32nd Annual Conference of the IEEE Industrial Electronics*, pages 4794–4799, Paris, France, November 7-10 2006.

[69] S.J. Pickering, D. Lampard, N. Hay, and T.F. Roylance. Heat transfer from the stator end-windings of a low voltage concentric-wound induction motor. In *Seventh International Conference on Electrical Machines and Drives*, pages 477–481, Southampton, UK, September 11-13 1995.

[70] S.J. Pickering, D. Lampard, N. Hay, and T.F. Roylance. Heat transfer in a through-ventilated induction motor. *IEE Proceedings on Electric Power Applications*, 145(5):429–433, 1998.

[71] Rudolf Pischinger, Manfred Klell, and Theodor Sams. *Thermodynamik der Verbrennungskraftmaschine*. Springer, Vienna, 2009.

[72] Rudolf Richter. *Elektrische Maschinen*. Springer, Berlin, 1967.

[73] Julius C. Rotta. Über eine Methode zur Berechnung turbulenter Scherströmungen. Technical Report Rep. 69 A14, Aerodynamische Versuchsanstalt, Göttingen, 1968.

[74] Julius C. Rotta. *Turbulente Strömungen - Eine Einführung in die Theorie und ihre Anwendung.* Teubner, Stuttgart, 1972.

[75] H. Schlichting. Wärmeübergang an einer längsangeströmten ebenen Platte mit veränderlicher Wandtemperatur. *Forschung auf dem Gebiete des Ingenieurwesens*, 17:1–8, 1951.

[76] Hermann Schlichting and Klaus Gersten. *Grenzschicht-Theorie.* Springer, Berlin Heidelberg, 2006.

[77] Ernst Schmidt and Karl Wenner. Heat transfer over the circumference of a heated cylinder in transverse flow. *Forschung auf dem Gebiete des Ingenieurwesens*, 12(2):65–73, 1943.

[78] Wladimir Schuisky. *Berechnung elektrischer Maschinen.* Springer, Wien, 1960.

[79] Herbert Sigloch. *Technische Fluidmechanik.* Springer, Berlin Heidelberg, 2012.

[80] Joseph H. Spurk and Nuri Aksel. *Strömungslehre Einführung in die Theorie der Strömungen.* Springer, Berlin Heidelberg, 8th edition, 2010.

[81] D. Staton, A. Boglietti, and A. Cavagnino. Solving the more difficult aspects of electric motor thermal analysis. In *IEMDC'03. IEEE International Electric Machines and Drives Conference*, volume 2, pages 747–755, Madison, Wisconsin, June 1-4 2003.

[82] D. Staton, A. Boglietti, and A. Cavagnino. Solving the more difficult aspects of electric motor thermal analysis in small and medium size industrial induction motors. *IEEE Transactions on Energy Conversion*, 20(3):620–628, 2005.

[83] John C. Tannehill, Dale A. Anderson, and Richard H. Pletcher. *Computational Fluid Mechanics and Heat Transfer.* Taylor & Francis, Philadelphia, 2nd edition, 1997.

[84] M. Tari, K. Yoshida, S. Sekito, J. Allison, R. Brutsch, A. Lutz, and N. Frost. A high voltage insulating system with increased thermal conductivity for turbo generators. In *Electrical Insulation Conference and Electrical Manufacturing Coil Winding Technology Conference*, pages 613 – 617, Brigham, UT, September 23-25 2003.

[85] M. Tari, L. Yoshida, S. Sekito, R. Brutsch, J. Allison, and A. Lutz. HTC insulation technology drives rapid progress of indirect-cooled turbo generator unit capacity. In *IEEE Power Engineering Society Summer Meeting*, volume 3, pages 1427 – 1432, Vancouver, Canada, July 15-19 2001.

[86] G. Traxler-Samek, B. Jordan, and A. Schwery. Kühlung von luftgekühlten Wasserkraftgeneratoren bei verschiedenen Betriebszuständen. *E&I Elektrotechnik und Informationstechnik*, 128:181–187, 2011.

[87] G. Traxler-Samek, R. Zickermann, and A. Schwery. Cooling airflow, losses, and temperatures in large air-cooled synchronous machines. *IEEE Transactions on Industrial Electronics*, 57(1):172 –180, 2010.

[88] VDI, editor. *VDI Heat Atlas.* Springer, Berlin Heidelberg, 10th edition, 2006.

[89] W. Vieser, T. Esch, and F. Menter. Heat transfer predictions using advanced two-equation turbulence models. Technical report, AEA Technology, 2002.

[90] H.Y. Wang, P.S. Su, and X.H. Wang. Calculation on the thermal field of the water cooling stator of three-gorge hydro-generator. In *ICEMS 2005. Proceedings of the Eighth International Conference on Electrical Machines and Systems*, volume 3, pages 2231 –2235, Nanjing, China, September 27-29 2005.

[91] Li Weili, Chai Feng, and Zhao Fen. Study on eddy current loss and heat-transfer character of stator windings in synchronous generator. In *ICEMS 2008. International Conference on Electrical Machines and Systems*, pages 479 –484, Wuhan, China, October 17-20 2008.

[92] Li Weili, Zhou Feng, and Chi Liming. Calculation of rotor ventilation and heat for turbo-generator radial and tangential air-cooling system. In *POWERCON '98. Proceedings of International Conference on Power System Technology*, volume 2, pages 1030 –1033, Beijing, China, August 18-21 1998.

[93] Stephen Whitaker. Forced convection heat transfer correlations for flow in pipes, past flat plates, single cylinders, single spheres, and for flow in packed beds and tube bundles. *AIChE Journal*, 18(2):361–371, 1972.

[94] Frank M. White. *Heat and mass transfer.* Addison-Wesley series in mechanical engineering. Addison-Wesley, 1988.

[95] David C Wilcox. *Turbulence modeling for CFD : Solutions manual.* DCW Industries, La Canada, CA, 1994.

[96] Jürgen Zierep. *Ähnlichkeitsgesetze und Modellregeln der Strömungslehre.* G. Braun, Karlsruhe, 1972.

[97] A. A. Zukauskas. *Heat Transfer from Tubes in Cross Flow*, volume 8. Academic Press, 1972.

Appendix A

Fundamentals

A.1 Wall heat transfer coefficient classification

A.1.1 Models of cooling of thermal systems

In [67] the author arranges the different models chronologically and named it by their inventors.

Newtonian cooling

It is the first known approach describing the principle of cooling of a solid body.

$$\frac{1}{A}\frac{dQ}{dt} = \dot{q} = \alpha(T_w - T_\infty) \tag{A.1}$$

Under certain circumstances the so called Newton's law of cooling is valid if the following conditions are satisfied:

- The ratio α/c_p of the wall heat transfer coefficient α and the specific heat for constant pressure c_p remains constant.

- The surface of the observed solid has a uniform temperature T_w.

- The ambient temperature T_∞ of the fluid remains constant during the considered period of time.

- No internal sources of heat generation inside the solid body.

Dulong-Petit cooling

Under circumstances of mixed cooling principles, the linearized approach in (A.1) is potentially insufficient. For a combination of cooling by radiation, conduction and convection with low velocity, the following power-law relationship is applicable:

$$\dot{q} = g(T_w - T_\infty)^n \tag{A.2}$$

The factors g and n can be identified by fitting (A.2) to empirical results.

Newton-Stefan cooling

Introducing the findings of Stefan and Boltzmann, a more theoretical approach than
(A.2) can describe the cooling of solid bodies with mixed cooling principles:

$$\dot{q} = \alpha(T_w - T_\infty) + \epsilon\sigma(T_w^4 - T_e^4) \, , \tag{A.3}$$

with the environmental temparature T_e of radiating solid surfaces.

A.2 IEC-60034-6 Tables

Abbr.	Circuit arrangement
0	Free cooling cycle
1	Cooling cycle with pipe or duct as coolant inlet
2	Cooling cycle with pipe or duct as coolant outlet
3	Cooling cycle with pipe or duct as coolant inlet and outlet
4	Surface cooling
5	Built in heat exchanger with environmental fluid as secondary coolant
6	Attached heat exchanger with environmental fluid as secondary coolant
7	Built in heat exchanger with externally supplied fluid as secondary coolant
8	Attached heat exchanger with externally supplied fluid as secondary coolant
9	Heat exchanger separated from the machine and externally supplied fluid as secondary coolant

Table A.1: Denotation of cooling circuit arrangement in IEC 60034-6 standard

Abbr.	Medium	Abbr.	Medium	Abbr.	Medium
A	Air	F	Frigen	H	Hydrogen
N	Nitrogen	C	Carbon dioxid	W	Water
U	Oil	S	Others	Y	Not yet defined

Table A.2: Denotation of coolant for primary and secondary cooling cycle in IEC 60034-6 standard

Abbr.	Conveying type
0	Buoyant free convection
1	self ventilated, depending on rotational speed of machine
5	Forced ventilation by an integrated module independent from rotational speed of machine
6	Forced ventilation by an attached module independent from rotational speed of machine
7	Separated independent driven cooling module
8	Relative movement of the coolant (machine is moving or fluid flow of coolant)
9	Other methods than mentioned obove

Table A.3: Denotation of conveying type in IEC 60034-6 standard

Appendix B

Fundamentals CFD

B.1 Vector-variable form of the Navier Stokes equations

$$\frac{\partial \mathbf{Q}}{\partial t} + \frac{\partial \mathbf{E}}{\partial x} + \frac{\partial \mathbf{F}}{\partial y} + \frac{\partial \mathbf{G}}{\partial z} = \mathbf{S} \tag{B.1}$$

$$\mathbf{Q} = \begin{pmatrix} \rho \\ \rho u \\ \rho v \\ \rho w \\ \rho(e + \frac{V^2}{2}) \end{pmatrix} \qquad \mathbf{S} = \begin{pmatrix} 0 \\ \rho g_x \\ \rho g_y \\ \rho g_z \\ \rho(u g_x + v g_y + w g_z) + \rho \dot{q} \end{pmatrix} \tag{B.2}$$

$$\mathbf{E} = \begin{pmatrix} \rho u \\ \rho u^2 + p - \tau_{xx} \\ \rho uv - \tau_{xy} \\ \rho uw - \tau_{xz} \\ \rho(e + \frac{V^2}{2}) + pu - u\tau_{xx} - v\tau_{xy} - w\tau_{xz} + \dot{q}_x \end{pmatrix} \tag{B.3}$$

$$\mathbf{F} = \begin{pmatrix} \rho v \\ \rho uv - \tau_{xy} \\ \rho v^2 + p - \tau_{yy} \\ \rho vw - \tau_{yz} \\ \rho(e + \frac{V^2}{2}) + pv - u\tau_{xy} - v\tau_{yy} - w\tau_{yz} + \dot{q}_y \end{pmatrix} \tag{B.4}$$

$$\mathbf{G} = \begin{pmatrix} \rho w \\ \rho uw - \tau_{xz} \\ \rho vw - \tau_{yz} \\ \rho w^2 + p - \tau_{zz} \\ \rho(e + \frac{V^2}{2}) + pw - u\tau_{xz} - v\tau_{yz} - w\tau_{zz} + \dot{q}_z \end{pmatrix} \tag{B.5}$$

B.2 k-ε model

Turbulence transport equations:

$$\frac{\partial \rho k}{\partial t} + \frac{\partial}{\partial x_j}(\rho u_j k) = \frac{\partial}{\partial x_j}\left[\left(\mu + \frac{\mu_t}{\sigma_k}\right)\frac{\partial k}{\partial x_j}\right] + P_k - \rho\varepsilon + P_{kb} \tag{B.6}$$

$$\frac{\partial \rho \varepsilon}{\partial t} + \frac{\partial}{\partial x_j}(\rho u_j \varepsilon) = \frac{\partial}{\partial x_j}\left[\left(\mu + \frac{\mu_t}{\sigma_\varepsilon}\right)\frac{\partial \varepsilon}{\partial x_j}\right] + \frac{\varepsilon}{k}(C_{\varepsilon 1}P_k - C_{\varepsilon 2}\rho\varepsilon + C_{\varepsilon 1}P_{\varepsilon b}) \tag{B.7}$$

Model constants and other equations for k-ε model:

$\sigma_k = 1$	$\sigma_\varepsilon = 1.3$	$C_{\varepsilon 1} = 1.44$	$C_{\varepsilon 2} = 1.92$
$C_\mu = 0.09$	$\sigma_\rho = 0.9$ or 1	$\kappa = 0.41$	$C_3 = 1$

$P_{\varepsilon b} = C_3 \cdot \max[0, P_{kb}]$ production and dissipation option

$\mu_t = C_\mu \rho \frac{k^2}{\varepsilon}$ eddy viscosity

$\varepsilon = \nu \overline{\frac{\partial u_i'}{\partial x_k}\frac{\partial u_i'}{\partial x_k}}$ isotropic dissipation rate

B.3 k-ω model

Turbulence transport equations:

$$\frac{\partial \rho k}{\partial t} + \frac{\partial}{\partial x_j}(\rho u_j k) = \frac{\partial}{\partial x_j}\left[\left(\mu + \frac{\mu_t}{\sigma_k}\right) + \frac{\partial k}{\partial x_j}\right] + P_k - \beta'\rho k\omega + P_{kb} \tag{B.8}$$

$$\frac{\partial \rho \omega}{\partial t} + \frac{\partial}{\partial x_j}(\rho u_j \omega) = \frac{\partial}{\partial x_j}\left[\left(\mu + \frac{\mu_t}{\sigma_\omega}\right)\frac{\partial \omega}{\partial x_j}\right] + \alpha\frac{\omega}{k}P_k - \beta\rho\omega^2 + P_{\omega b} \tag{B.9}$$

Model constants and other equations for k-ω model:

$\beta' = 0.09$	$\alpha = 5/9$	$\beta = 0.075$	$\sigma_k = 2$
$\sigma_\omega = 2$	$\kappa = 0.41$	$C_3 = 1$	

$P_{\omega b} = \frac{\omega}{k}((\alpha + 1)C_3 \cdot \max[0, P_{kb}] - P_{kb}$ production and dissipation option

$\mu_t = \rho\frac{k}{\omega}$ eddy viscosity

$L = \frac{\sqrt{k}}{\omega}$ turbulent length scale

$\omega = \frac{1}{C_\mu}\frac{\varepsilon}{k}$ turbulence eddy frequency

Other equations for k-ε and k-ω model:

$P_k = \mu_t\left(\frac{\partial u_i}{\partial x_j} + \frac{\partial u_j}{\partial x_i}\right)\frac{\partial u_i}{\partial x_j} - \frac{2}{3}\frac{\partial u_k}{\partial x_k}\left(2\mu_t\frac{\partial u_k}{\partial x_k} + \rho k\right)$ production rate of turbulence

$P_{kb} = -\frac{\mu_t}{\rho\sigma_\rho}g_i\frac{\partial\rho}{\partial x_i}$ full buoyancy model

$P_{kb} = -\frac{\mu_t}{\rho\sigma_\rho}\rho\beta g_i\frac{\partial T}{\partial x_i}$ Boussinesq buoyancy model

B.4   Baseline and Shear Stress Transport Model

B.4.1   Original BSL and SST equations:

Model equations as published in [56]

Original k-ω model:

$$\frac{\mathrm{d}\rho k}{\mathrm{dt}} = \tau_{ij}\frac{\partial u_i}{\partial x_j} - \beta^*\rho\omega k + \frac{\partial}{\partial x_j}\left[(\mu + \sigma_{k1}\mu_t)\frac{\partial k}{\partial x_j}\right] \tag{B.10}$$

$$\frac{\mathrm{d}\rho\omega}{\mathrm{dt}} = \frac{\gamma_1}{\nu_t}\tau_{ij}\frac{\partial u_i}{\partial x_j} - \beta_1\rho\omega^2 + \frac{\partial}{\partial x_j}\left[(\mu + \sigma_{\omega 1}\mu_t)\frac{\partial\omega}{\partial x_j}\right] \tag{B.11}$$

Transformed k-ε model:

$$\frac{\mathrm{d}\rho k}{\mathrm{dt}} = \tau_{ij}\frac{\partial u_i}{\partial x_j} - \beta^*\rho\omega k + \frac{\partial}{\partial x_j}\left[(\mu + \sigma_{k2}\mu_t)\frac{\partial k}{\partial x_j}\right] \tag{B.12}$$

$$\frac{\mathrm{d}\rho\omega}{\mathrm{dt}} = \frac{\gamma_2}{\nu_t}\tau_{ij}\frac{\partial u_i}{\partial x_j} - \beta_2\rho\omega^2 + \frac{\partial}{\partial x_j}\left[(\mu + \sigma_{\omega 2}\mu_t)\frac{\partial\omega}{\partial x_j}\right] + 2\rho\sigma_{\omega 2}\frac{1}{\omega}\frac{\partial k}{\partial x_j}\frac{\partial\omega}{\partial x_j} \tag{B.13}$$

Blending function F_1:

$$F_1 = \tanh(\text{arg}_1^4) \tag{B.14}$$

$$\text{arg}_1 = \min\left(\max\left(\frac{\sqrt{k}}{\beta'\omega y};\frac{500\nu}{y^2\omega}\right);\frac{4\rho k}{\text{CD}_{kw}\sigma_{\omega 2}y^2}\right) \tag{B.15}$$

$$\text{CD}_{kw} = \max\left(2\rho\frac{1}{\sigma_{\omega 2}\omega}\frac{\partial k}{\partial x_j}\frac{\partial\omega}{\partial x_j};1.0\cdot 10^{-10}\right) \tag{B.16}$$

Blending function F_2:

$$F_2 = \tanh(\text{arg}_2^2) \tag{B.17}$$

$$\text{arg}_2 = \max\left(\frac{\sqrt{k}}{\beta'\omega y};\frac{500\nu}{y^2\omega}\right) \tag{B.18}$$

Blending the model constants:
$\phi_1 = (\sigma_{k1},\dots)$, $\phi_2 = (\sigma_{k2},\dots)$ and $\phi = (\sigma_k,\dots)$:

$$\phi = F_1\phi_1 + (1 - F_1)\phi_2 \tag{B.19}$$

BSL and SST k transport equation:

$$\frac{\mathrm{d}\rho k}{\mathrm{dt}} = \tau_{ij}\frac{\partial u_i}{\partial x_j} - \beta^*\rho\omega k + \frac{\partial}{\partial x_j}\left[(\mu + \sigma_k\mu_t)\frac{\partial k}{\partial x_j}\right] \tag{B.20}$$

BSL and SST ω transport equation:

$$\frac{\mathrm{d}\rho\omega}{\mathrm{dt}} = \frac{\gamma}{\nu_t}\tau_{ij}\frac{\partial u_i}{\partial x_j} - \beta\rho\omega^2 + \frac{\partial}{\partial x_j}\left[(\mu + \sigma_\omega\mu_t)\frac{\partial\omega}{\partial x_j}\right] + 2\rho\sigma_{\omega 2}\frac{1}{\omega}\frac{\partial k}{\partial x_j}\frac{\partial\omega}{\partial x_j} \tag{B.21}$$

Model constants and other equations for BSL and SST model:
Constant values for (B.10) and (B.11):

$$\sigma_{k1} = 0.5 \qquad \sigma_{\omega 1} = 0.5 \qquad \beta_1 = 0.075 \qquad \beta^* = 0.09 \qquad \kappa = 0.41$$

$$\gamma_1 = \beta_1/\beta^* - \sigma_{\omega 1}\kappa^2/\sqrt{\beta^*}$$

Constant values for (B.12) and (B.13):

$$\sigma_{k2} = 1 \qquad \sigma_{\omega 2} = 0.856 \qquad \beta_2 = 0.0828 \qquad \beta^* = 0.09 \qquad \kappa = 0.41$$

$$\gamma_2 = \beta_2/\beta^* - \sigma_{\omega 2}\kappa^2/\sqrt{\beta^*}$$

BSL and SST transport equations as implemented in *ANSYS CFX v13* [4]

$$\frac{\partial(\rho k)}{\partial t} + \frac{\partial(\rho u_j k)}{\partial x_j} = \frac{\partial}{\partial x_j}\left[\left(\mu + \frac{\mu_t}{\sigma_k}\right)\frac{\partial k}{\partial x_j}\right] + P_k - \beta^*\rho\omega k + P_{kb} \tag{B.22}$$

$$\frac{\partial(\rho\omega)}{\partial t} + \frac{\partial(\rho u_j \omega)}{\partial x_j} = \frac{\partial}{\partial x_j}\left[\left(\mu + \frac{\mu_t}{\sigma_\omega}\right)\frac{\partial \omega}{\partial x_j}\right] + (1 - F_1)\frac{2\rho}{\sigma_{\omega 2}\omega}\frac{\partial k}{\partial x_j}\frac{\partial \omega}{\partial x_j} + \alpha\frac{\omega}{k}P_k - \beta\rho\omega^2 + P_{\omega b} \tag{B.23}$$

B.5 Scale Adaptive Simulation (SAS) Transport model

Turbulence transport equations as implemented in *ANSYS CFX v13* [4]:

$$\frac{\partial\rho k}{\partial t} + \frac{\partial(\rho u_j k)}{\partial x_j} = \frac{\partial}{\partial x_j}\left[\left(\mu + \frac{\mu_t}{\sigma_k}\right)\frac{\partial k}{\partial x_j}\right] + P_k - \rho C_\mu k\omega \tag{B.24}$$

$$\frac{\partial\rho\omega}{\partial t} + \frac{\partial(\rho u_j \omega)}{\partial x_j} = \frac{\partial}{\partial x_j}\left[\left(\mu + \frac{\mu_t}{\sigma_\omega}\right)\frac{\partial \omega}{\partial x_j}\right] + (1 - F_1)\frac{2\rho}{\sigma_{\omega 2}\omega}\frac{\partial k}{\partial x_j}\frac{\partial \omega}{\partial x_j} + \alpha\frac{\omega}{k}P_k - \rho\beta\omega^2 + Q_{SAS} \tag{B.25}$$

Model constants

$$\zeta_2 = 3.51 \qquad \sigma_\Phi = 2/3 \qquad C = 2 \qquad C_S = 0.11$$

Other equations
SAS source term:

$$Q_{SAS} = \max\left[\rho\zeta_2\kappa S^2\left(\frac{L}{L_{vK}}\right)^2 - C\frac{2\rho k}{\sigma_\Phi}\max\left(\frac{1}{\omega^2}\frac{\partial \omega}{\partial x_j}\frac{\partial \omega}{\partial x_j}, \frac{1}{k^2}\frac{\partial k}{\partial x_j}\frac{\partial k}{\partial x_j}\right), 0\right] \tag{B.26}$$

$P_k = \mu_t S^2$ production term

$P_k = \min(P_k, C_{lim}\rho\varepsilon)$ limiting production term with clip factor C_{lim}

$S_{ij} = \frac{1}{2}\left[\frac{\partial u_i}{\partial x_j} + \frac{\partial u_j}{\partial x_i}\right]$ strain rate tensor

$S = \sqrt{2 S_{ij} S_{ij}}$ magnitude of strain rate

$L = \dfrac{\sqrt{k}}{c_\mu^{1/4}\cdot\omega}$ \hspace{3cm} length scale of modeled turbulence

$L_{vK} = \dfrac{\kappa S}{u''}$ \hspace{3cm} the von Kármán length scale

$|u''| = \sqrt{\dfrac{\partial^2 u_i}{\partial x_k^2}\dfrac{\partial^2 u_i}{\partial x_j^2}}$ \hspace{2cm} second derivative of velocity

B.6   Gamma-Theta transition model

The formulation of the $\gamma - Re_\Theta$ transition model as presented in [49]:
Transport equation for intermittency γ:

$$\frac{\partial(\rho\gamma)}{\partial t} + \frac{\partial(\rho u_j\gamma)}{\partial x_j} = P_{\gamma 1} - E_{\gamma 1} + P_{\gamma 2} - E_{\gamma 2} + \frac{\partial}{\partial x_j}\left[\left(\mu + \frac{\mu_t}{\sigma_\gamma}\right)\frac{\partial\gamma}{\partial x_j}\right] \; , \tag{B.27}$$

Transition sources:

$$P_{\gamma 1} = F_{\text{length}}c_{a1}\rho S(\gamma F_{\text{onset}})^{c_\alpha} \qquad \text{and} \qquad E_{\gamma 1} = c_{e1}P_{\gamma 1}\gamma \tag{B.28}$$

Destruction or relaminarization sources:

$$P_{\gamma 2} = c_{a2}\rho\Omega\gamma F_{\text{turb}} \qquad \text{and} \qquad E_{\gamma 2} = c_{e2}P_{\gamma 2}\gamma \tag{B.29}$$

Transport equation for transition momentum-thickness Reynolds number Re_Θ:

$$\frac{\partial(\rho Re_\Theta)}{\partial t} + \frac{\partial(\rho u_j Re_\Theta)}{\partial x_j} = P_{\Theta t} + \frac{\partial}{\partial x_j}\left[\sigma_{\Theta t}(\mu + \mu_t)\frac{\partial Re_\Theta}{\partial x_j}\right] \tag{B.30}$$

Model constants for $\gamma - Re_\Theta$ model:

$c_{e1} = 1.0 \qquad c_{a1} = 2.0 \qquad c_\alpha = 0.5 \qquad c_{e2} = 50 \qquad c_{a2} = 0.06 \qquad \sigma_\gamma = 1.0$

S \hspace{1cm} strain rate magnitude

F_{length} \hspace{0.5cm} empirical correlation controlling the length of the transition region

Ω \hspace{1cm} vorticity magnitude

Appendix C

Measurement

C.1   Measurements of heat flux

Chan.	Sens. Type	Label	Position
1	PT100	T-D5-in	Duct 5 inlet
2	PT100	T-D4-out	Duct 4 outlet
3	PT100	T-D29-in	Duct 29 inlet
4	PT100	T-D28-out	Duct 28 outlet
5	PT100	Tf-13	Conductor 2 HFS-C
6	HFS	U-13	Conductor 2 HFS-C
7	TC/T	Tw-13	Conductor 2 HFS-C
8	PT100	Tf-12	Conductor 8 HFS-D
9	HFS	U-12	Conductor 8 HFS-D
10	TC/T	Tw-12	Conductor 8 HFS-D
11	PT100	T-ESNDE	End shield NDE
12	PT100	Tf-5	Conductor 58 HFS-A
13	HFS	U-5	Conductor 58 HFS-A
14	TC/T	Tw-5	Conductor 58 HFS-A
15	PT100	Tf-14	Conductor 11 HFS-C
16	HFS	U-14	Conductor 11 HFS-C
17	TC/T	Tw-14	Conductor 11 HFS-C
18	PT100	Tf-11	Conductor 22 HFS-D
19	HFS	U-11	Conductor 22 HFS-D
20	TC/T	Tw-11	Conductor 22 HFS-D
21	PT100	Stator	
22	PT100	Tf-10	Conductor 45 HFS-B
23	HFS	U-10	Conductor 45 HFS-B
24	TC/T	Tw-10	Conductor 45 HFS-B
25	PT100	Tf-9	Conductor 59 HFS-B
26	HFS	U-9	Conductor 59 HFS-B
27	TC/T	Tw-9	Conductor 59 HFS-B
28	PT100	Tf-6	Conductor 27 HFS-A
29	HFS	U-6	Conductor 27 HFS-A
30	TC/T	Tw-6	Conductor 27 HFS-A

Table C.1: Wiring list for YOKOGAWA DC-100 measurement amplifier